Final Technical Report

For project entitled:

Large Eddy Simulation of Cirrus Clouds

Contract No.NAG1-1703

Submitted to:
NASA - FIRE
Langley Research Center
Hampton, Va 23681-0001

From:
William R. Cotton, Principal Investigator
Colorado State University
Dept. of Atmospheric Science
Fort Collins, CO 80523-1371
Telephone: (970) 491-8593
e-mail: cotton@atmos.colostate.edu

July 28, 1999

The Regional Atmospheric Modeling System (RAMS) with mesoscale interactive nested-grids and a Large-Eddy Simulation (LES) version of RAMS, coupled to two-moment microphysics and a new two-stream radiative code were used to investigate the dynamic, microphysical, and radiative aspects of the November 26, 1991 cirrus event. Wu (1998) describes the results of that research in full detail and is enclosed as Appendix 1.

The mesoscale nested grid simulation successfully reproduced the large scale circulation as compared to the Mesoscale Analysis and Prediction System's (MAPS) analyses and other observations. Three cloud bands which match nicely to the three cloud lines identified in an observational study (Mace et al., 1995) are predicted on Grid # 2 of the nested grids, even though the mesoscale simulation predicts a larger west-east cloud width than what was observed.

Large-eddy simulations (LES) were performed to study the dynamical, microphysical, and radiative processes in the 26 November 1991 FIRE II cirrus event. The LES model is based on the RAMS version 3b developed at Colorado State University. It includes a new radiation scheme developed by Harrington (1997) and a new subgrid scale model developed by Kosovic (1996).

The LES model simulated a single cloud layer for Case 1 and a two-layer cloud structure for Case 2. The simulations demonstrated that latent heat release can play a significant role in the formation and development of cirrus clouds. For the thin cirrus in Case 1, the latent heat release was insufficient for the cirrus clouds to become positively buoyant. However, in some special cases such as Case 2, positively buoyant cells can be embedded within the cirrus layers. These cells were so active that the rising updraft induced its own pressure perturbations that affected the cloud evolution.

Vertical profiles of the total radiative and latent heating rates indicated that for well developed, deep, and active cirrus clouds, radiative cooling and latent heating could be comparable in magnitude in the cloudy layer. This implies that latent heating cannot be neglected in the construction of a cirrus cloud model.

The probability density function (PDF) of w was analyzed to assist in the parameterization of cloud-scale velocities in large-scale models. For the more radiatively-driven, thin cirrus case, the PDFs are approximately Gaussian. However, in the interior of the deep, convectively unstable case, the PDFs of w are multi-modal and very broad, indicating that parameterizing cloud-scale motions for such clouds can be very challenging.

The results of this research are described in detail in a paper submitted to the Journal of Atmospheric Science (Wu and Cotton, 1999), which is enclosed as Appendix 2.

Using soundings extracted from a mesoscale simulation of the November 26, 1991 cirrus event, the radiative effects on vapor deposition/sublimation of ice crystals was studied using a two-dimensional cloud-resolving model (CRM) version of RAMS, coupled to an explicit bin-resolving microphysics.

The CRM simulations of the November 26, 1991 cirrus event demonstrate that the radiative impact on the diffusional growth (or sublimation) of ice crystals is significant. In this case, the ice particles experienced radiative warming. Model results show that radiative feedbacks in the diffusional growth of ice particles can be very complex. Radiative warming of an ice particle will restrict the particle's diffusional growth. In the case of radiative warming, ice particles larger than a certain size will experience so much radiative warming that surface ice saturation vapor pressures become large enough to cause sublimation of the larger crystals, while smaller crystals are growing by vapor deposition. However, ice mass production can be enhanced in the case of radiative cooling of an ice particle. For the November 26, 1991 cirrus event, radiative feedback results in significant reduction in the total ice mass, especially in the production of large ice crystals, and

consequently, both radiative and dynamic properties of the cirrus cloud are significantly affected. A complete description of this research has been submitted as a paper to the Journal of Atmospheric Science (Wu et al., 1999), and included as Appendix 3.

References

Harrington, J.Y., 1997: The effects of radiative and microphysical processes on simulated warm and transition-season Arctic stratus. Ph.D. dissertation, Colorado State University, Fort Collins, CO, 270 pp.

Kosovic, B., 1996: Subgrid-scale modeling for the large-eddy simulation of stably stratified boundary layers. Ph.D. thesis, Dept. of Aerospace Engineering Sciences, University of Colorado, Boulder, CO, 253 pp.

Mace, G.G., D. O'C. Starr, T.P. Ackerman, and P. Minnis, 1995: Examination of coupling between an upper-tropospheric cloud system and synoptic-scale dynamics diagnosed from wind profiler and radiosonde data. *J. Atmos. Sci.*, **52**, 4094-4127.

Wu, Ting, 1998: Numerical modeling study of the November 26, 1991 cirrus event. Ph.D. dissertation, Colorado State University, Dept. of Atmospheric Science, Fort Collins, CO 80523, 188 pp.

Wu, T., and W.R. Cotton, 1999: Radiative effects on the diffusional growth of ice particles in cirrus clouds. Submitted to *J. Atmos. Sci.*

Wu, T., W.R. Cotton, and W.Y.Y. Cheng, 1999: Large-eddy simulations of the 26 November 1991 FIRE II cirrus case. Submited to *J. Atmos. Sci.*

APPENDIX 1

DISSERTATION

NUMERICAL MODELING STUDY OF THE NOVEMBER 26, 1991 CIRRUS EVENT

Submitted by

Ting Wu

Department of Atmospheric Science

In partial fulfillment of the requirements

for the degree of Doctor of Philosophy

Colorado State University

Fort Collins, Colorado

Spring 1999

COLORADO STATE UNIVERSITY

November 17, 1998

WE HEREBY RECOMMEND THAT THE DISSERTATION PREPARED UNDER OUR SUPERVISION BY TING WU ENTITLED NUMERICAL MODELING STUDY OF THE NOVEMBER 26, 1991 CIRRUS EVENT BE ACCEPTED AS FULFILLING IN PART REQUIREMENTS FOR THE DEGREE OF DOCTOR OF PHILOSOPHY.

Committee on Graduate Work

Michael T Montgomery

Qiang-yu Liu

Stephen K. Cox

William R Cotton
Adviser

Stephen K. Cox
Department Head

ABSTRACT OF DISSERTATION

NUMERICAL MODELING STUDY OF THE NOVEMBER 26, 1991 CIRRUS EVENT

The Regional Atmospheric Modeling System (RAMS) with mesoscale interactive nested- grids and a Large-Eddy Simulation (LES) version of RAMS, coupled to two-moment microphysics and a new two-stream radiative code are used to investigate the dynamic, microphysical, and radiative aspects of the November 26, 1991 cirrus event. The mesoscale nested grids successfully simulate the large scale circulation which compares very well to the Mesoscale Analysis and Prediction System's (MAPS) analyses and some other observations. Three cloud bands which match nicely to the three cloud lines identified in observational study (Mace et al.) are predicted on Grid # 2 of the nested grids, even though the mesoscale simulation predicts a larger west-east cloud width than what was observed.

Initialized with soundings extracted from the mesoscale nested- grids, the LES successfully predicts a single cloud layer corresponding to an inactive and shallow cloud band. With a simulated sounding extracted from a deep and active cloud band, the LES simulates a two-layer cloud structure which matches very well to the observed deep cloud system. The LES studies demonstrate that interaction among various processes (dynamic, microphysical, and radiative) can be very complex and active turbulent motions can be supported, especially deep in the cloud layer. They also suggest that latent heating effects can be a significant factor in modulating cirrus cloud evolution.

Radiative effects on ice particle's diffusional growth (or sublimation) are studied using a two- dimensional cloud- resolving model (CRM) version of RAMS, coupled to an explicit bin resolving microphysics. The CRM results demonstrate that the radiative impact on the diffusional growth (or sublimation) of ice crystals is significant. For the November 26, 1991

cirrus event, radiative feedbacks in the diffusional growth calculations result in significant reduction in the total ice mass, especially in the production of large ice crystals, and consequently, both radiative and dynamic properties of the cirrus cloud are significantly affected.

Ting Wu
Department of Atmospheric Science
Colorado State University
Fort Collins, Colorado 80523
Spring 1999

ACKNOWLEDGEMENTS

First and foremost, I would like to express my gratitude to my adviser, Professor William R. Cotton for his encouragement, guidance, and scientific insight through this research. I'm also grateful to my committee members, Professors Stephen Cox, Mike Montgomery, and Joe She whose constructive remarks have made the improvement of this work. Special thanks are to Professor Mike Montgomery. The courses he taught have helped me a lot in my research into the dynamics of cirrus clouds.

Bob Walko and Brian Gaudet are thanked for helping me in understanding the basics of RAMS. Jerry Harrington, Tamir Reisin, Graham Feingold, and Sue Van Den Heever are thanked for very needed discussions on RAMS Level 5.

Finally, I would like to thank my wife, Zongjun and my daughter, Ingrid for their unconditional support through this journey.

This work was sponsored by the NASA under contracts #NAG-1-1703 and #NAG-1-2045.

DEDICATION

This thesis is dedicated to my family.

CONTENTS

LIST OF FIGURES

LIST OF TABLES

Chapter 1

INTRODUCTION

The climatic importance of cirrus clouds has been recognized for a long time. Cirrus clouds, which cover about 20% of the globe on average, are believed to have profound impacts upon the planetary energy budget due to their radiative effects. Even though the radiative properties of cirrus in the infrared spectral region are of special interest, absorption of solar radiation by cirrus may also significantly influence the stratification of the upper troposphere. As it was noted by Liou (1986), high level cirrus clouds, which contain a significant amount of large, nonspherical ice crystals, are normally optically thin and nonblack and the influence of optically thin and nonblack cirrus on the radiation field of the earth-atmosphere system, and hence on weather and climate components, depends on both the solar and thermal IR radiative properties which, in turn, are modulated by the compositions and physical locations of the cirrus in the atmosphere. In order to assess the validity of cloud predictions from global general circulation models, and also, in general, to better understand the effects of cloud radiative forcing and feedbacks on climate, investigation of cirrus cloud properties is urgent (Sassen, et al., 1995). But this investigation is not an easy task because cirrus clouds represent a particularly difficult cloud category to detect and categorize due to their special compositions and locations in the atmosphere.

As is well known, the radiative properties of a cloud are determined by the cloud microphysical characteristics (e.g., cloud particle size, shape, phase, number concentration and distribution) and the microphysical properties of a cloud are essentially controlled by the dynamical processes taking place within the cloud system. Knowledge of cirrus cloud dynamics is essential in our understanding of the climatic impact of cirrus clouds.

These dynamics include the environment and processes responsible for cirrus formation, maintenance, and dissipation.

1.1 Observational Studies of Cirrus

The study of the microstructure of cirrus clouds was initially carried out in the early 70s. Based on observational measurements in the early 70s, Heymsfield and Knollenberg (1972) found that the average ice crystal concentration for crystals longer than $15\mu m$ in cirrus generating cells was $10-25L^{-1}$. The mean crystal length from their observation was found to be $60-1000\mu m$ with an ice water content of $0.15-0.25gm^{-3}$. The predominant particle habits were found to be columns, bullets, rosettes, and plates.

In a series of research papers, Heymsfield (1975a, 1975b, 1975c, 1977) reported observations of ice characteristics for cirrus uncinus and cirrostratus. According to his study, the predominant ice crystal types were polycrystalline bullet rosettes, single bullets, banded columns, and plates. The ice water content was found to be generally less than $0.2gm^{-3}$. Strong evidence for the temperature dependence of particle sizes and concentrations was suggested. He also illustrated that the ice water content and mean length of the ice crystal could be correlated with temperature. Also based on some comprehensive aircraft measurements, Heymsfield suggested several plausible physical mechanisms for the formation of cirrus uncinus clouds and Heymsfield and Platt (1984) depicted parameterization equations for the ice crystal concentration as a function of the maximum dimension and temperature for a $5^{o}C$ interval from $-20^{o}C$ to $-60^{o}C$. The results derived from their analyses has had a significant impact on the research in this field from the point of view of radiative transfer computations as well as the computation of ice content in a numerical model.

Liou (1986) reviewed and documented the understanding and knowledge of the composition and structure of cirrus clouds before the middle 80s. He pointed out that cirrus clouds are one of the most important, yet least understood atmospheric elements in our weather and climate system. He also pointed out that in order to construct a reliable numerical model for weather and climate prediction, the dynamic and radiative properties of cirrus clouds must be treated accurately within the context of a model setting.

Since the middle of 1980s, observations from FIRE I (First ISCCP (International Satellite Cloud Climatology Project) Regional Experiment) and FIRE II have greatly increased our knowledge of cirrus cloud properties and characteristics. In situ and remote sensing instruments have demonstrated some important microphysical, radiative, and dynamical properties of cirrus clouds (Journal of the Atmospheric Science, vol. 52, 1995 special issue).

FIRE sponsored an intensive field observation (IFO) for cirrus in Wisconsin during October of 1986 (FIRE I). Results from this experiment were described in detail in the special November 1990 issue of the *Monthly Weather Review*. In this special issue, researchers described the rawinsonde- resolved meteorological conditions associated with a succession of five distinct mesoscale cirrus cloud regimes (Starr and Wylie, 1990), a five lidar overview of the cloud structure and evolution (Sassen et al., 1990), cloud microstructure (Heymsfield et al., 1990), cloud optical and radiative properties (Grund and Eloranta, 1990; Spinhirne and Hart, 1990; Minnis et al., 1990), comparison of radiative transfer theory with observations (Wielicki et al., 1990), cloud spectral properties (Ackerman et al., 1990), and cirrus dynamic properties (Smith et al., 1990).

The most significant field observations of cirrus in the early 1990s, FIRE II IFO, was carried out near Coffeyville, Kansas, during November and December of 1991. One objective of this field experiment was to quantify the capabilities and limitations of methods for retrieving physical and optical cirrus cloud properties from satellite observations (Ou et al., 1995). During the period from late November to early December of 1991, a total of 11 cirrus days were observed. For IFO, the November 26 and December 3 -5 cases were well documented (Journal of the Atmospheric Science, vol. 52, 1995 special issue).

Following a separate path but with similar motivation, extensive observations of cirrus have also been conducted in Europe in the 1980s and early 1990s. During the intensive International Cirrus Experiment conducted over the North Sea in the fall of 1989, natural cirrus and contrail-induced cirrus were observed and analyzed from in situ and remote sensing measurements (lidar and infrared radiometer). Gayet et al. (1996) reported that these two cloud types primarily formed at the same range of altitude ($\sim 8200m$, $-37^{o}C$). Their analyses of the measurements depicted distinctive microphysical and optical properties in these two types of cirrus. Natural cirrus exhibits sheared fallstreaks of ice crystals

up to $750\mu m$ in size near the base level. From the top to the base of the natural cirrus, the mean values of ice water content and particle concentrations increase from 15 to $50mgm^{-3}$ and from 26 to 60 L^{-1}, respectively. The corresponding visible optical depth for natural cirrus is around 2.0. However, greater particle concentrations and smaller ice crystals are measured at all levels in contrails leading to an optical depth of 0.8 in the denser contrails despite an ice water content that never exceeds 18 mgm^{-3}. EUCREX 108 was another very representative and well- observed cirrus case in Europe. The experiment was conducted in 1993. Small scale convective cells were the most prominant feature of this cirrus case. The observations showed that some convective cells had vertical velocities on the order of $1 - 2ms^{-1}$. No layered structure was observed. The background ice particle number concentration was about $50L^{-1}$. The generating cells were very distinct with high ice particle number concentrations and small particle mean sizes. The ice water content (IWC) was about $60mgm^{-3}$ near the cloud base. The maximum IWC was found to be larger than $100mgm^{-3}$. The mean particle size was found to be about $90 - 100\mu m$.

1.2 Dynamics of Cirrus

Cirrus clouds which are usually sandwiched between stable layers below and above assume a variety of forms, depending on the mean vertical velocity, wind shear, relative humidity, and static stability (Cotton and Anthes, 1989; Heymsfield, 1975). The dynamic processes that control the formation and evolution of cirrus clouds are as varied as the forms of cirrus themselves. Cirrus clouds can form via upper level frontal lifting, the vertical motions associated with jet streams, upward propagating orographic waves, ascending motions in extra-tropical cyclones, and outflow from convective cells. Dense layers of cirrostratus occur under conditions of gentle, uniform upward motion, saturated air, and high static stability. With less stability and in the presence of weaker mean upward motion, convection may form cirrus uncinus which are dense patches of cirrus which produce ice crystals large enough to acquire appreciable terminal velocities (Cotton and Anthes, 1989).

Observational results and theories have suggested that the atmospheric energy spectrum is at least partly produced by quasi-two-dimensional turbulence, especially in the upper troposphere and stratosphere (Lilly, 1983; 1989). The extreme environmental stability

associated with the development of cirrus clouds in the upper troposphere and stratosphere leads to the hypothesis of two-dimensional turbulence in cirrus clouds.

Two-dimensional turbulence has been studied in the laboratory with a stably stratified fluid. The properties of 2D turbulence can be summarized as (Flatau et al., 1990):

- Small scale turbulence undergoes a transition to a quasi two- dimensional motion under the action of stratification.
- The quasi two-dimensional motion can persist for a long time.
- The vertical motion mode is suppressed in comparison with horizontal components.
- Because the cloud shrinks vertically, it may get very thin.
- Motions of individual layers in the fluid are decoupled. There is a tendency towards layering.
- Since horizontal layers are decoupled and their motion is not correlated, they may produce intermittent turbulent patches.

Even though 2D turbulence is often associated with cirrus clouds, the cloud existence can make the turbulent properties in cirrus clouds different (maybe slightly) from pure 2D turbulence in a stratified fluid. Certainly, the external source of diabatic heat flux providing the energy for mixing, so dominant in the boundary processes, is hard to find in the case of cirrus clouds. However, as it is well known, once ice crystals have formed, they provide a mechanism for the continuous mixing due to interaction with shortwave and longwave radiative field, latent heat release, and turbulent transport.

Field observations have indeed shown some indication of 2D turbulent structures such as layered structure and small vertical perturbation velocity variance in cirrus clouds. On the other hand, as expected, observations have also indicated that three dimensional turbulent features are very obvious for small scale motions. Besides these, the dominance of the energy containing eddies with sizes on the order of 10 km suggests the importance of gravity waves.

The available observations suggest that turbulence in cirrus clouds is basically governed by the dynamics of two-dimensional turbulence and gravity waves, with horizontal spectra of horizontal motions determined by 2D turbulent effects, and vertical spectra and vertical motions mostly controlled by wave dynamics. Gravity wave motions can be triggered by either convective activity associated with locally unstable or neutral (large scale forcing generally exists) profiles or wind shear. Radiative effects of cirrus clouds can modify the turbulent structures, but these effects need to be estimated before a representation of radiation can be formulated.

1.3 Modeling Studies of Cirrus

Modeling studies of cirrus have been believed to be very difficult due to our limited knowledge of the processes occurring in cirrus. However, numerical models of middle- and high-level clouds are useful to determine the quantitative roles of dynamics, microphysics, and radiation in the life cycle of these clouds (Cotton and Anthes, 1989). Cirrus cloud modeling studies were initiated in the late 1960s. Harimaya (1968) constructed a microphysical model coupled with assumed horizontal winds to quantitatively compute the shape of cirrus uncinus. Based on numerical computations, he concluded that the shape of cirrus uncinus depended upon the mass of ice particles and vertical wind shear.

In the middle of 1980s, Starr and Cox (1985) developed a two-dimensional model for the simulation of the evolution of cirrus clouds. In addition to accounting for dynamic and thermodynamic processes including phase changes of water, effects due to microphysical composition and radiative processes were also explicitly incorporated into their model. They found that the structure of cirrus varies dramatically from nighttime to daytime because radiative processes affect the organization and bulk properties of the cloud. Simulations of thin cirrus under midday and nighttime conditions showed, with all other environmental factors being the same, daytime cirrus takes on a cellular structure with pockets of high ice water content (IWC) surrounded by regions of considerably lower IWC while nighttime cirrus exhibits a more layered structure with IWC varying much less within a given layer. The simulated pattern of long-wave radiative cooling above and warming

below is the key factor in modulating the vertical stability, especially for nighttime cirrus. However, for daytime cirrus, the combination of long-wave and short-wave radiation modulates not only the vertical stability but also the horizontal cloud structure because the presence of pockets of higher IWC results in enhanced absorption of solar radiation, warming the pocket and inducing more ascending motion (more cellular structure) than at nighttime.

Lilly (1988) proposed the application of radiative-convective mixed-layer models to cirrus clouds. In his study, Lilly made an assumption that latent heating effects can be ignored because, in cirrus clouds, radiative heating is believed to be the greatest source of destablization of the cloud layer and result in the production of turbulent kinetic energy in the cloud layer. Using a theoretically- predicted radiative heating rate profile for a cloud of 2 km thickness with its top at the level of the tropical tropopause, 17 km, and with an IWC of 0.02 gm^{-3}, he estimated vertical velocity and time scales for radiatively-induced cirrus turbulence, which suggested that they can support active turbulence comparable to boundary layer clouds.

Modeling studies of cirrus has been more active in the 1990s. Some simulation results have been very promising (Heckman and Cotton, 1993; Thompson, 1993; Jensen et al., 1994). Using the nonhydrostatic version of the Regional Atmospheric Modeling System (RAMS) developed at Colorado State University, Heckman and Cotton (1993) simulated the 28 October 1986 FIRE case. Their simulation resulted in very good agreement between observed and model predicted dynamics and cloud fields. Jensen et al. (1994) studied the development of a cirrus cloud event observed on November 1, 1986 during the FIRE intensive field observations by using a cirrus cloud model which included microphysical, dynamical, and radiative processes. Sulfate aerosols, solution drops, ice crystals, and water vapor were all treated as interactive elements in their model. Compared with aircraft microphysical measurements made over Wisconsin, their simulation generated reasonable ice water contents, but the predicted ice number densities were too low, especially for particles with radii less than about $50\mu m$.

Westphal et al. (1996) used observations from a wide variety of instruments and platforms to validate many different aspects of a three-dimensional mesoscale simulation of

the dynamics, cloud microphysics and radiative transfer of the November 26, 1991 FIRE II cirrus case. The simulation was conducted using the mesoscale model version four (MM4) developed at Penn State University and the National Center for Atmospheric Research (NCAR). A simplified bulk water cloud scheme and a detailed spectral model of radiative transfer were utilized in their study. Detailed comparison of their simulation with radar, lidar, GOES-retrieved cloud top height, aircraft data, etc., showed that the simulated distribution and concentration of ice compared favorably with the observations. Direct comparison was done between the radiative transfer simulation and data from broadband and spectral sensors and inferred quantities such as cloud albedo, optical depth, top-of-the-atmosphere $11\mu m$ brightness temperature, and the $6.7\mu m$ brightness temperature. Comparison was also made with theoretical heating rates calculated using the rawinsonde data and measured ice water size distributions near the central observational site. They pointed out that the differences between the observed and predicted radiative quantities were due to errors in the prediction of ice water contents, and not due to the optical properties or the radiative transfer solution technique.

The interaction of clouds with the general circulation is generally agreed to be the most important physical process requiring improvement in today's climate model. This makes cirrus cloud parameterization very important topic in the development of general circulation models. Nebuda (1995) developed a one-dimensional, upper-level cloud model which can be nested in time and space in a localized area with limited frequency. The adaptive cloud model can provide microphysical and radiative information for the large scale model. As modeling studies of cirrus clouds proceeds, some other issues become so important that they must be addressed in order for models to perform realistically in the simulation of cirrus clouds. Since cirrus clouds are located high above the PBL, TKE dissipation due to friction may not be as important as horizontal redistribution through wave activities. Vertical redistribution of TKE is suppressed due to stable stratification of the environmental atmosphere. These features may imply that the horizontal boundary conditions are very important in numerical simulation of turbulence in cirrus clouds. Also, the turbulent parameterization schemes developed for boundary layer processes may not

be simply applied to the study of cirrus clouds due to the marked difference in forcing mechanisms.

1.4 Motivations

Cirrus cloud research has taken two paths (Heckman and Cotton. 1993):

- research into the radiative effects
- exploration of cirrus dynamics

However, these two paths are closely tied together. In order to simulate cirrus clouds successfully, these two aspects should be combined and represented in numerical models. This research is motivated by the following prominent questions associated with cirrus clouds.

- What are the properties of small scale dynamic activity (that is turbulence for large scale models) in cirrus clouds? The potential importance of the dynamical processes on scales too small to be resolved by mesoscale models and GCMs is an obvious uncertainty. Based on analysis of high-frequency observations in cirrus, Quante et al (1990) concluded that waves, quasi-two-dimensional motions and intermittent turbulence were present. Flatau et al. (1990) also showed that the dominant scales of motion in cirrus clouds are between 1 and 10 km.

- What is the role of small scale motions in the dynamical processes responsible for the layered structure frequently observed in cirrus clouds? The tendency for multilayered cloudiness conflicts with the assumption of a single cloud layer that is often invoked in the design of cloud retrieval algorithms for application to satellite observations. Furthermore, if the tendency for multilayered structure and shallow cloud generation layers is widely prevalent, there are important ramifications for modeling cirrus (Starr and Wylie, 1990). Observations have indicated that two-dimensional motions under the action of stratification may be responsible for the suppressed vertical motion and resultant multilayer structure in cirrus clouds. However, observations have also

indicated that small scale motions have obviously both two- and three- dimensional turbulent properties (Dmitriyev, et al., 1986; Gultepe and Starr, 1994). By the way, field observations are generally too coarse to resolve even smaller (smaller than several hundreds of meters) scale motions. Beside these, the dominance of the energy containing eddies with sizes on the order of 10 km suggests the importance of gravity wave activity. The impact of the small scale turbulent motions and gravity waves on the larger scale (resolvable) environment can be very important (but not known) in the generation of layered structures in cirrus. Also, what may be equally important in the generation of layered cloud structure is the evaporative process associated with precipitation of ice particles. Harrington's simulations of Arctic stratus suggest that evaporation of precipitating ice particles can be responsible for the development of a moist layer below the precipitating cloud layer above. This moist layer can be favorable for the development of second cloud layer (Harrington, 1997).

- What are the dynamical processes responsible for cellular structures within cirrus clouds? Maintenance of these structures, likely initiated by shear-induced small scale waves, may result from the effects of latent and radiative heating patterns (Starr and Wylie, 1990). But, it is important to note that cellular convective-appearing structure does not always indicate the presence of free convection although it often does. This indicates that some other small scale dynamical processes embedded in the environment may play an important role in the generation of cellular structures within cirrus clouds.

- The last question, the one which is least tested, is what is the importance of radiative effects on the diffusional growth and sublimation of ice particles in cirrus clouds. Clouds play a dual role in the heat budget of the earth and atmosphere. On the one hand, their high albedo reflects incoming solar radiation in the visible wavelengths, thus cooling the earth. On the other hand, clouds are often opaque to infrared (IR) radiation and their presence reduces the loss of IR radiation to space, thus warming the earth (Cotton and Anthes, 1989). The effect of changes in cloud cover on climate depends critically on the cloud temperature, season, and latitude at which

the changes occur and on the optical properties of the clouds. Central to the issue of climate change is the so-called cloud- climate feedback problem. One of the important aspects of this feedback is the way in which clouds are modulated by their surrounding environment. Thus studies of cloud evolution, which ultimately involve the physics of the growth of cloud particles, hold a special place in cloud-climate studies (Stephens, 1983). An important consequence of the growth of ice crystals in the atmosphere lies in their contribution to the total diabatic heating or cooling of the atmospheric environment. Since cirrus clouds, especially thin cirrus, have a large amount of small ice crystals (smaller than $50\mu m$), diffusional growth, which is essential to the growth of small ice crystals, cannot be considered independent of the radiative transfer that occurs between the ice crystal and its surrounding environment.

Chapter 2

THE NOVEMBER 26, 1991 CIRRUS EVENT

Detailed observational descriptions of this cirrus event have been presented by some researchers during the past years (JAS special issue, 1995). This chapter is dedicated to a summary of the synoptics and kinematics associated with the cirrus formation and evolution, the microphysical properties of the cirrus cloud bands, and the small scale dynamics associated with the cloud system.

2.1 Synoptic settings

The cirrus cloud system that was observed on the 26th of November, 1991 developed in the region of a mobile upper tropospheric trough that was associated with the dynamics of the exit region of an upper tropospheric jet stream. A meteorological overview for this cirrus case was discussed in details by Mace et al. (1995). The synoptic setting for the cloud system is shown in Figure 2.1. Early on the 26th of November 1991, a small amplitude ridge-trough pattern was established over North America. Northwesterly flow in the upper troposphere ahead of the offshore ridge existed over the West Coast, while a broad diffluent trough was over the central United States. A strong jet was embedded in the northwesterly flow over the western third of the United States. A speed maximum of more than $60 m.s^{-1}$ was observed by radiosondes in southwestern Wyoming and the Pacific Northwest. In the Kansas- Oklahoma region, wind speeds decreased substantially compared to the west and the flow became diffluent in the upper troposphere. At the surface the western United States was dominated by a region of high pressure, while low pressure and an associated frontal system were situated in the central United States.

By 1200 UTC of 26 November the right, eastern exit region of the jet and an associated upper level trough entered the western part of Kansas. By 0000 UTC of November 27,

a general amplification of the long-wave pattern was noted. Heights were rising over the Rocky Mountain states at 300 mb, while height falls occurred over the Pacific coast and the central United States. A well developed trough was evident at both 400 mb and 300 mb extending from the western Gulf of Mexico into southern Canada. The northwesterly jet had became firmly established in the region of rising heights over the Rocky Mountain states. The exit region of the jet had propagated into the region of intensive observations, and a strong wind gradient existed from east Texas northward to the Dakotas. At the surface, the low in the north-central United States and the associated frontal system had propagated eastward and filled slightly.

2.2 Cloud fields derived from satellite and surface data

Mace et al. (1995) described this cloud event both regionally and locally based on the GOES satellite imagery of the cloud band as it progressed over central and eastern Kansas and Oklahoma from 1800 UTC of the November 26 to 0000 UTC of the November 27. At 1800 UTC, the cloud system appeared as a linear feature oriented approximately south-north from central Texas through Oklahoma and into eastern Kansas where the system broadened into a fairly extensive cloud system centered over Iowa. In north Texas the band appeared to be composed primarily of middle-level clouds, while the clouds became progressively brighter and more cirriform in nature from central Oklahoma northward. The horizontal width of the band increased from approximately 100 km in central Oklahoma to more than 250 km in northeastern Kansas. Skies cleared considerably in western Kansas and the panhandle region of Oklahoma and Texas. The system propagated roughly at the phase speed of the dynamical pattern.

Mace et al. (1995) also calculated the high cloud optical depths at 1800 UTC by using visible GOES-7 data and the technique of Minnis et al. (1993) (Figure 2.2). Their results were in good agreement with the results shown in Minnis et al. (1993) (Figure 2.5). Optically thin cirrus was diagnosed along much of the band through central Oklahoma. Optical depths increased substantially in southern Kansas.

By 2100 UTC, the entire cloud structure had progressed eastward. The leading edge of the main cloud band in the infrared imaginary was identified in eastern Texas and

Oklahoma. Farther north in northeastern Oklahoma and southeast Kansas, a series of three southwest-northeast oriented cloud lines were identified. These lines became increasingly brighter with time, indicating active cirrus generation, and propagating southeastward toward the leading edge of the primary cloud system. Mace et al. (1995) pointed out that cloud generation was apparently occurring in a wavelike pattern oriented nearly parallel to the weak southwesterly flow aloft. The southwestern portion of these active generation regions tended to be advected faster toward the east by the advancing jet streak than the northeastern segments.

By 0000 UTC of the November 27, the leading edge of the main cloud band had passed eastward into Arkansas and Missouri. The trailing portions of the band were identified over southeastern Kansas and eastern Oklahoma. The region of clear skies had also progressed eastward into central Oklahoma and Kansas.

Using a combination of surface and satellite cloud observations during FIRE cirrus phase II, Minnis et al. (1993) derived the cloud fields of the November 26, 1991 cirrus event. Some of their results are summarized in Figures 2.3, 2.4 and 2.5. The cloud data from surface reports indicated overcast conditions over much of Nebraska, Iowa, central and eastern Kansas, and central Texas and Oklahoma. The lowest cloud ceilings observed from the surface varied from 2000 ft to 25000 ft. Midlevel clouds were the lowest observed cloud decks over much of Kansas, while high clouds were the only cloud type reported over central Arkansas, the Texas panhandle, and the area just north of Coffeyville, Kansas. Cloud fraction derived from GOES data at the same time (Figure 2.3) shows a somewhat similar picture. A combination of the satellite and surface data yields the contours in Figure 2.4 which show midlevel clouds extending as far south as central Missouri and covering much of Kansas. Low clouds were also found over much of Iowa and Nebraska.

Minnis et al. (1993) also derived total and high cloud optical depths from GOES data at 1800 UTC. The results are shown in Figure 2.5. The western and northern portions of the large area of satellite-derived high cloudiness where midlevel clouds were observed from the surface have very high optical depths. The optical depths for the high-cloud-only regions are less than 4. Thus, they pointed out that the larger high-cloud optical depths were caused by thick cloud layers underneath the highest cirrus layer.

2.3 Microphysical observations

Intrieri et al. (1995) reported microphysical observations of the developing cloud system. The initial cirrus cloud was detected by Doppler lidar at approximately 1615 UTC with the cloud base located at 10 km above ground level and cloud thickness measuring 200 m in depth. Within the ensuing one hour and 15 minutes, from the initial returns of Doppler lidar until 1730 UTC, the lidar observations showed that the cirrus cloud gradually deepened with cloud base descending to 9 km above ground level (AGL). The cirrus system was first picked up by both lidar and radar at around 1800 UTC. By about 1930 UTC the base of the cirrus deck descended to about 6 km and retained its top at around 9 km. After about 2100 UTC the cloud base descended to between 2 and 3 km. According to Intrieri et al. (1995), observations of this cirrus case were divided into three discrete subsets that were determined by differences in the simultaneous lidar and radar backscatter returns as follows:

- *Period I (1610-1730 UTC).* Lidar backscatter returns with no corresponding radar return. This period was characterized by high, thin, visible (but not detectable by radar) cirrus clouds.

- *Period II (1730-1900 and 2100-2130 UTC.* Lidar and radar backscatter returns in agreement on cloud boundaries. The first part of this period was characterized by cirrus clouds, and the second part was characterized by deeper mid-level clouds.

- *Period III (1900-2100 UTC).* Radar returns with corresponding lidar signal attenuation. This period was characterized by mid-level mixed phase clouds.

During the first period, the integrated liquid water amount was approximately $0.05mm$. which is very near the noise level of its retrieval from microwave data. The retrieved values of water vapor were approximately $1.0cm$.

During the times between 1735 and 1900 UTC, and again from 2100 to 2130 UTC, the lidar and radar received geometrically similar cloud returns with general agreement

in detected cloud top and base heights. Using techniques developed at NOAA's Environmental Technology Laboratory (ETL), Intrieri et al. (1995) estimated the cirrus particle sizes for the time period between 1815 and 1855 UTC. They showed that particles with the largest effective radii (r_e), between 80 and 90 μm, were located in three regions: 1) at cloud bottom; 2)in the generator cell or turretlike feature indicative of active cirrus cloud growth; 3) in the ensuing fall streak feature as the cirrus began to precipitate. Particles having the smallest sizes, between 20 and 30 μm, were located predominantly at cloud top.

Period three was marked by circumstances in which the radar observed most of or the full extent of the cloud and the lidar signal was attenuated before reaching the cloud top. This period also contains the only times during this case study when liquid water was observed by the microwave radiometer. During this period, the cloud deepened in vertical extent from approximately 1.2 to 2.4 km. The size information obtained for a time period between 2045 and 2054 UTC when the cloud was optically thick showed that the largest particles (diameter $\sim 250\mu m$) were located in the lower region of the cloud, and the smallest-sized particles (diameter $< 100\mu m$) were located in the cloud top region.

The cirrus cloud microphysical properties were also retrieved from radar and lidar observations by Matrosov et al. (1993) and Intrieri and Feingold (1993). They showed that particle concentrations near cloud top were in excess of $1000l^{-1}$ while concentrations near cloud base were less than $10l^{-1}$. Particles with small mean diameters of about $50\mu m$ were associated with higher concentrations near cloud top while the low concentrations near cloud base were associated with larger mean diameter ($\sim 400\mu m$) particles. As it would be expected, they also showed that usually smaller ice water content (IWC) was associated with smaller particles with higher concentrations near cloud top and usually higher IWC (up to $0.04gm^{-3}$) was associated with larger particles near cloud base.

2.4 Kinematics and dynamics

Using data from the wind profiler demonstration network (WPDN) and a temporally and spatially augmented radiosonde array, Mace et atl (1995) diagnosed and explained the evolution of the kinematically- derived ageostrophic vertical circulations and correlated

the circulation with the forcing of an extensively sampled cloud field. The 10-km profiler-derived wind field (Figure 2.6) indicates a strong speed gradient associated with the exit region of the northwesterly jet. A well-defined minimum in horizontal wind speeds can be seen in association with the trough axis that extended through central Oklahoma and Kansas at 1800 UTC. By 2700 UTC, the main feature in the wind field at 10 km had propagated eastward. The region of sharpest cyclonic turning in the wind field at this time was in extreme western Missouri and Arkansas. The jet axis was identifiable extending through Colorado into the panhandle region of Oklahoma, and the intense isotach gradient between the jet core and trough axis was squarely within the wind profiler network. It was evident that air exiting the jet core in western Oklahoma experienced rapid deceleration as it flowed southeastward toward the trough axis.

As it is seen in Figure 2.7, at 1800 UTC, a maximum in positive vorticity was located over the panhandle of Oklahoma with positive values extending eastward to western Missouri and Arkansas. The trough axis that situated in eastern Oklahoma at 1800 UTC was not clearly delineated in the vorticity field. By 2700 UTC, however, the north-south oriented axis of positive vorticity was more clearly aligned with the trough axis identifiable in the wind field. Values near the trough axis had increased during the previous 6 hours, indicating an overall amplification of the upper-tropospheric wave pattern.

The horizontal divergence at 10 km was also closely coupled to the advancing jet streak and to the shortwave trough (Figure 2.7). At 1800 UTC, an axis of positive horizontal divergence was oriented through central Oklahoma. As can be expected, convergence was diagnosed in the speed gradient from the panhandle region northward. At 2700 UTC, the southern portion of the divergence axis at 10 km had shifted eastward with the propagating and evolving wind field, while the more northerly portions had remained stationary. This is consistent with the jet core advancing into Oklahoma and the trough axis moving eastward. Since the horizontal divergence is closely coupled to the ageostrophic motions and vertical velocity, it is critical to cirrus cloud formation on that day.

Mace et. al. (1995) further analyzed the ageostrophic winds and their associated natural coordinate components at 10 km. They found that a thermodynamically indirect

vertical circulation existed in association with a jet streak exit region. The circulation was displaced to the cyclonic side of the jet axis due to the orientation of the jet exit between a deepening diffluent trough and a building ridge. The cloud line formed in the ascending branch of the vertical circulation, with the most concentrated cloud development occurring in conjunction with the maximum large-scale vertical motion. The derived maximum mesoscale kinematic vertical velocity was only slightly greater than $5cms^{-1}$ over Coffeyville, Kansas.

Gultepe et al. (1995) analyzed the vertical velocity fluctuation (Figure 2.8) and studied the dynamical characteristics of the cloud system in micro- and meso-γ scales by using aircraft and radar observations. They made calculations at two different scales because of significant dynamic activity in the micro ($<$ 1 km) and meso-γ ($<$ 25 km) scales within the cloud. Scale separation was chosen to be about 1 km. Coherent structures (e.g., cells, vortex) that transferred significant heat, moisture, and turbulence were analyzed. Results showed that dynamic activity, including w about $\pm 1.5ms^{-1}$, and mean sensible heat fluxes and latent heat fluxes $\sim 10Wm^{-2}$, was estimated for this cirrus case. The size of coherent structures was estimated from aircraft and radar measurements to be about 0.5 and 3.5 km.

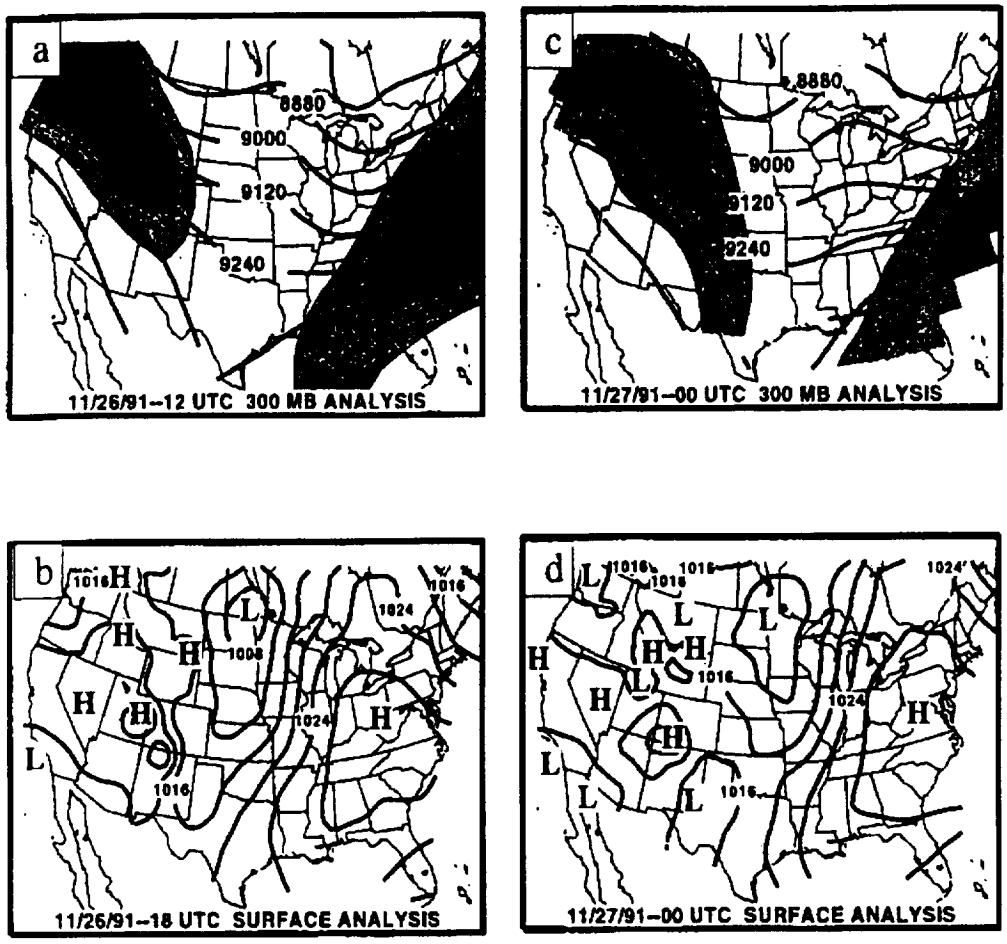

Figure 2.1: The synoptic setting for the case study. (a) 300-mb heights and isotachs at 1200 UTC 26 Nov. 1991. (b) Surface pressure analysis at 1800 UTC 26 Nov. 1991. The contour interval is 4 mb for the surface pressure and 120 m for the thickness. (c) 300-mb heights isotachs at 0000 UTC 27 Nov. 1991. Plotting convention as in (a). (d) Surface pressure at 0000 UTC 27 Nov. 1991. Plotting convention as in (b) (From Mace et al., 1995).

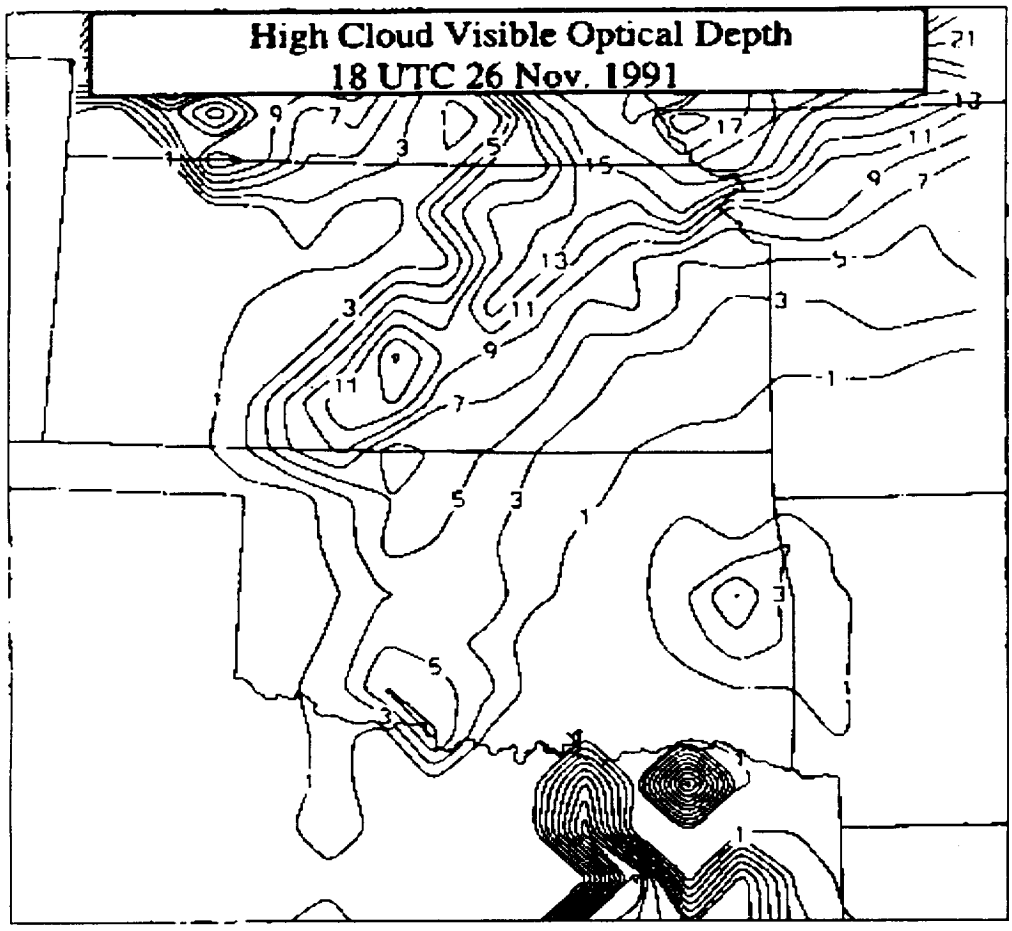

Figure 2.2: High cloud visible optical depths derived from GOES data at 1800 UTC 26 Nov. 1991 (From Mace et al., 1995).

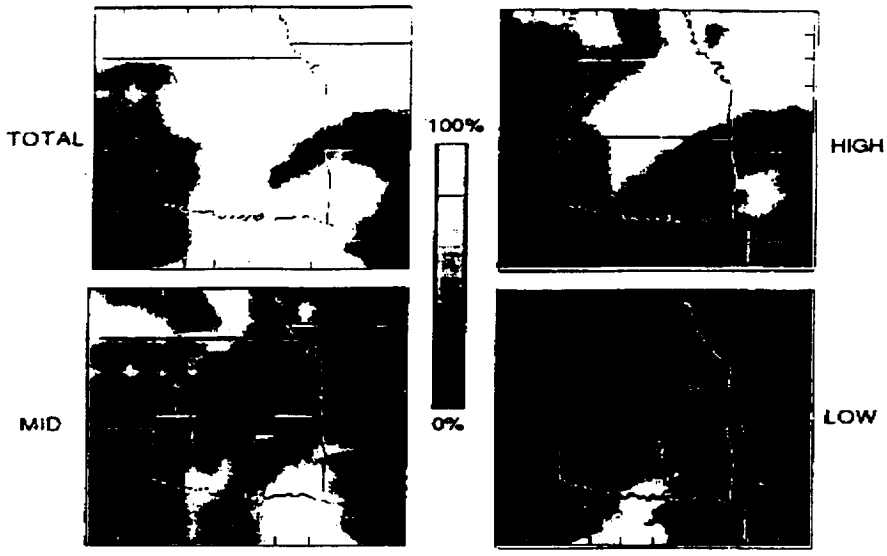

Figure 2.3: Cloud fraction derived from GOES data at 1800 UTC on November 26, 1991. The black areas indicate cloud fractions less than 1% (From Minnis et al., 1993).

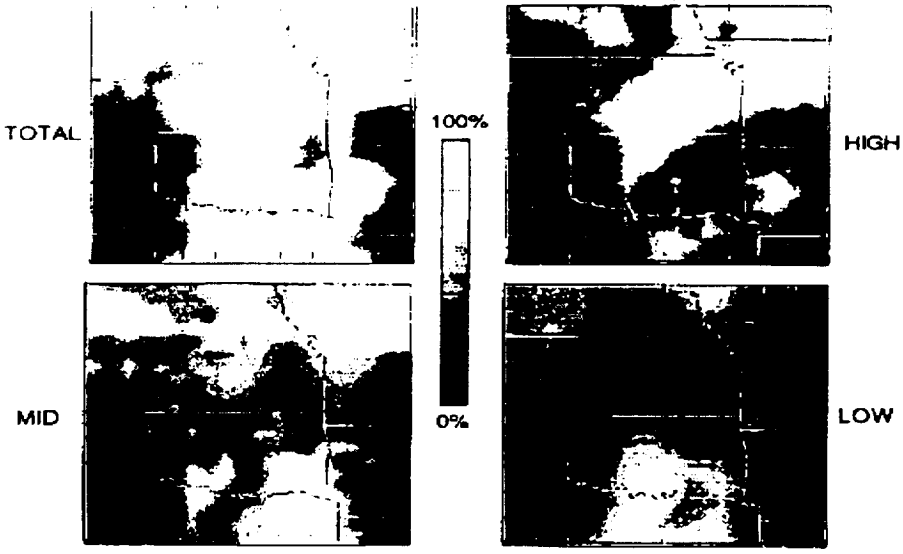

Figure 2.4: Combined satellite and surface derived cloud fraction for November 26, 1991 at 1800 UTC. The black areas denote cloud fractions less than 1% (From Minnis et al., 1993).

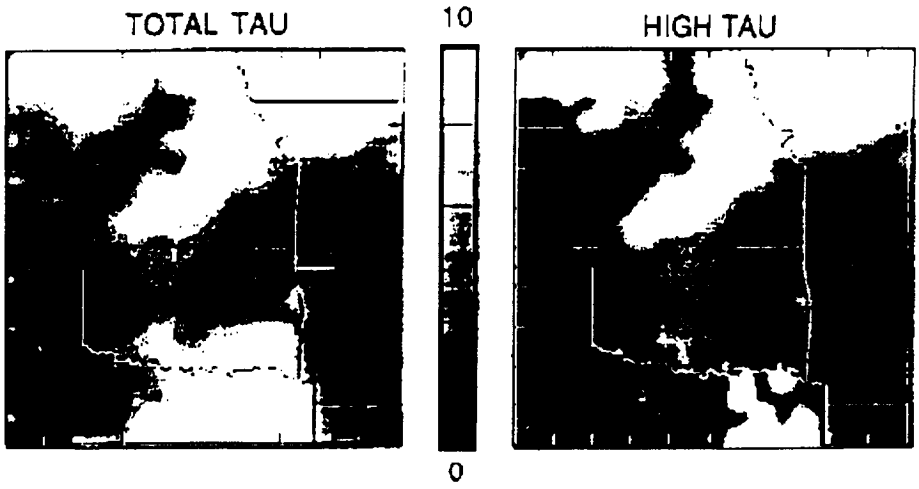

Figure 2.5: Total and high cloud optical depths derived from GOES data at 1800 UTC on November 26, 1991. The black areas denote cloud fractions less than 1% (From Minnis et al., 1993).

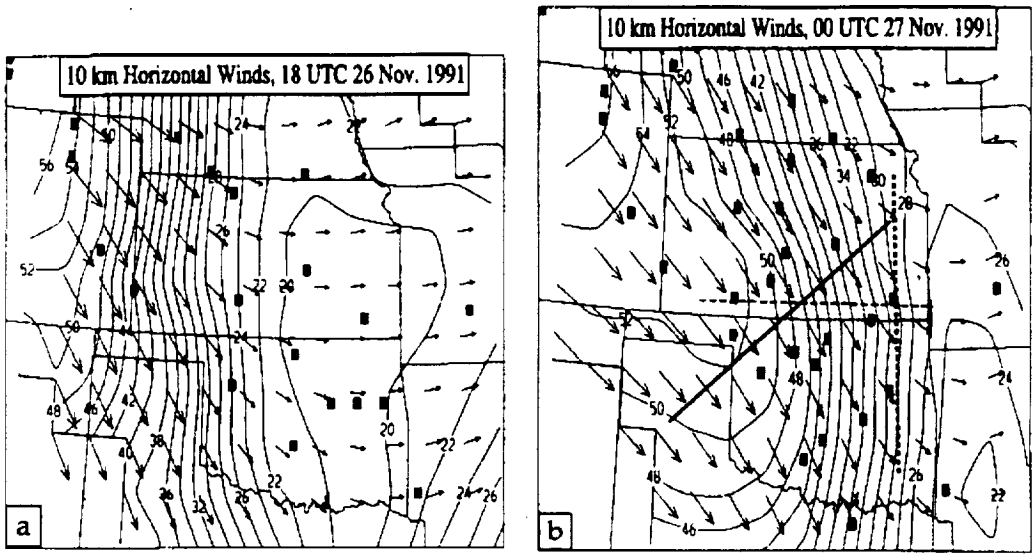

Figure 2.6: Horizontal wind vectors and speeds analyzed from the time-space converted WPDN data at (a) 1800 UTC 26 Nov. 1991 and (b) 0000 UTC 27 Nov. 1991. The wind vectors are compass direction, and the vector lengths are proportional to wind speed. The contours are of wind speed in ms^{-1}. The contour interval is $2ms^{-1}$. The solid squares denote the location of wind profiler observations used in the objective analysis (From Mace et al., 1995).

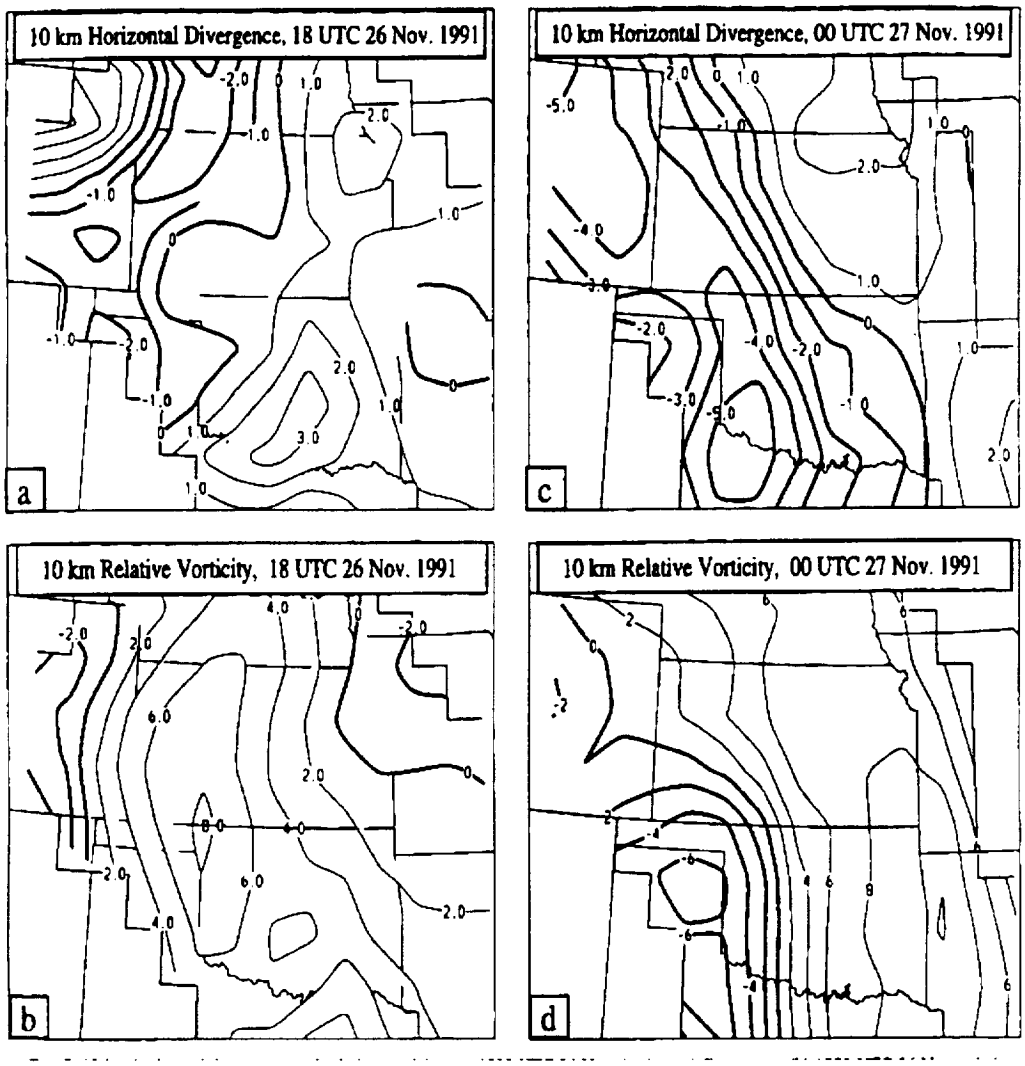

Figure 2.7: 10-km horizontal divergence and relative vorticity: (a) 1800 UTC 26 Nov. horizontal divergence, (b) 1800 UTC 26 Nov. relative vorticity, (c) 0000 UTC 27 Nov. horizontal divergence, and (d) 0000 UTC 27 Nov. relative vorticity. The contour interval in (a) and (c) is $1 \times 10^{-5} s^{-1}$ and in (b) and (d) $4 \times 10^{-5} s^{-1}$. Thick solid lines denote negative contours (From Mace et al., 1995).

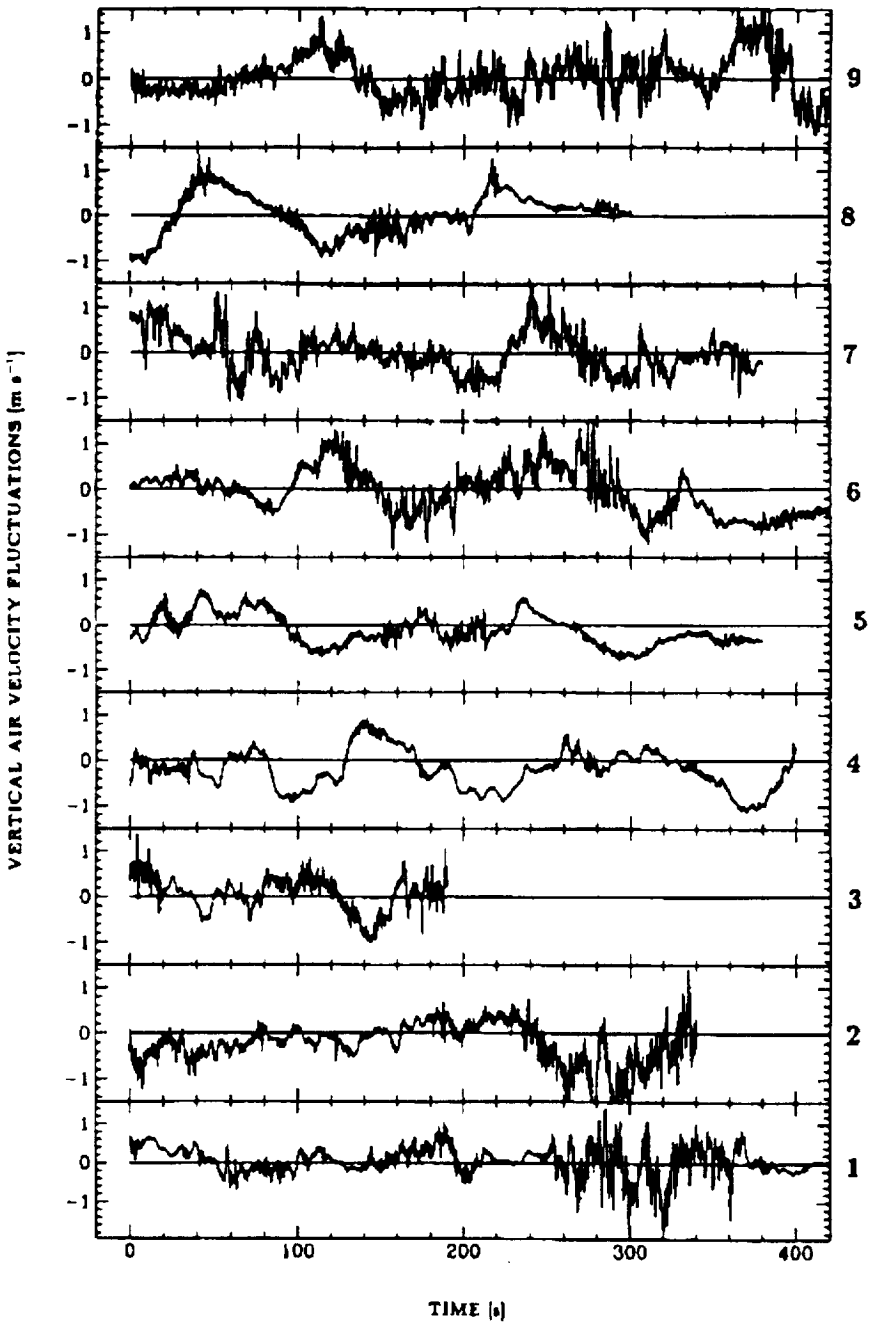

Figure 2.8: Time series of vertical air velocity fluctuations for the 26 Nov. cirrus case after removing mean and large-scale trend. Leg number are shown on the right side of each box (From Gultepe et al., 1995).

Chapter 3

MESOSCALE SIMULATIONS OF THE 26 NOVEMBER 1991 FIRE II CIRRUS CASE

3.1 Brief model description

The numerical model used throughout this research is the Regional Atmospheric Modeling System (RAMS) developed at Colorado State University. A general description of RAMS can be found in Tripoli and Cotton (1982), Cotton et al. (1982), Tremback et al. (1985), Tripoli (1986), Tremback (1990), and Pielke et al. (1992). RAMS is ideal for this research because it has the ability to represent a large-scale area and then to nest progressively to smaller scales. More than one set of telescoping nests can be specified within a larger-scale grid and user- specified and movable grids can be activated. RAMS has a non-hydrostatic option so that all meteorologically relevant spatial scales can be represented.

RAMS uses a standard Arakawa-C grid which is staggered in both the vertical and horizontal directions. A hybrid time differencing scheme has been used throughout this research. According to this hybrid time differencing scheme, velocity components and pressure are updated using leapfrog differencing, and all other prognostic variables are advanced using forward differencing. Sound-wave terms along with the pressure equation are time-split and integrated on a short time-step. Radiation calculations are generally done less frequently, although heating/cooling rates are applied at each time-step. RAMS utilizes a polar stereographic horizontal coordinate. Vertically, RAMS uses a sigma-z terrain-following system. The turbulence scheme used in the mesoscale simulations is the Smagorinsky deformation formulation in which the horizontal diffusion coefficients are calculated as the product of horizontal deformation rate and a length scale squared, and the

vertical diffusion is computed from a one-dimensional analog of the Smagorinsky scheme in which vertical deformation is evaluated from vertical gradients of horizontal wind.

A new two-moment microphysical parameterization scheme described by Meyers (1995) is used throughout the mesoscale simulations. This new microphysical parameterization scheme predicts the mixing ratio and number concentration of rain, pristine ice crystals, snow, aggregates, graupel and hail. The general gamma distribution function is the basis function used for each hydrometeor species. Some highlights of the new microphysical model include

- r_c is diagnosed as $r_t - r_{liq} - r_{ice} - r_{vs}$ (here, $r_c, r_t, r_{liq}, r_{ice}$, and r_{vs} are cloud water mixing ratio, total cloud mixing ratio, liquid water mixing ratio, ice water mixing ratio, and saturation water vapor mixing ratio, respectively).

- pristine ice crystals ($D_m < 125\mu m$) can only convert to snow by vapor deposition (no riming) based on an analytical flux equation.

- heterogeneous ice nucleation follows Meyers et al. (1992) and homogeneous ice nucleation of cloud and haze particles follows DeMott et al. (1994).

- predictive equations are used for ice nuclei.

- crystal habit is diagnosed based on temperature and saturation.

- all mass and number tendencies due to collection are solved by look-up tables from the analytical solutions of the stochastic collection equation.

- collection of pristine ice crystals, snow crystals and or aggregates results in a source for the aggregates.

- evaporation and melting of each species assume that the smallest particles completely disappear first.

- graupel is defined as a low density, heavily rimed crystal (density of $0.4gcm^{-3}$) and hail is high density frozen drops (density of $0.85 - 0.90gcm^{-3}$).

- melting graupel is a source for both rain and hail.
- graupel and hail must be large to shed ($0.5cm$), have a critical mass of water over the ice core's surface before shedding commences, and sizes of drops shed are assumed to be $1.0mm$.

This microphysical parameterization package includes various improvements over the old versions of the RAMS microphysics. It is believed that this parameterization improves the performance in the simulations of cirrus cloud systems (Harrington, 1994).

3.2 Initialization

RAMS includes the Isentropic Analysis package (RAMS/ISAN) as an option in the initialization capability which performs the data analysis tasks for the initial and boundary conditions for larger-scale horizontally inhomogeneous (or variable initialization) runs. RAMS/ISAN has the ability to combine or blend several data sets in the data analysis and its modular structure simplifies insertion of nonstandard data sets. The currently standard RAMS/ISAN code supports the National Meteorological Center (NMC) global-analysis data set, the ECMWF 2.5^o global-analysis data set, and NMC rawinsonde and surface observation data sets, all of which are archived at the National Center for Atmospheric Research (NCAR), as standard data sources. In this study, RAMS/ISAN code has been modified to also support the Mesoscale Analysis and Prediction System (MAPS) data sets from the NOAA Forecast Systems Laboratory (FSL).

MAPS is both a data assimilation system and a primitive equation model. A full description of MAPS' formulation can be found in Benjamin et al. (1991). The MAPS datasets contain the following variables: grid relative wind components, pressure, potential temperature, condensation pressure, and Montgomery streamfunction. Although MAPS is a primitive equation model, only MAPS analyses are used in this study.

The MAPS currently operates on a 3-h analysis cycle and utilizes observations from commercial aircraft and wind profilers in addition to those from the regular synoptic observing network. The biggest advantage of the MAPS data sets over the National Meteorological Centre (NMC) products is the resolution. MAPS is a hybrid sigma-isentropic

dataset with 60 km horizontal grid spacing, while the NMC's datasets have much coarser resolution.

Another advantage of the MAPS datasets is the isentropic coordinate system. Isentropic coordinate system has inherent advantages over other coordinate systems. As it is known, in the absence of diabatic processes (water phase change, radiation, conduction, vertical mixing), air flows and mixes along isentropic surfaces. Because of this, atmospheric features such as fronts, jet streams, and moist and dry tongues usually appear with greater coherence when viewed in the isentropic framework. The isentropic coordinate system also has the advantage of providing extra resolution near fronts, and therefore, near associated wind maxima and moisture features. These characteristics are advantageous not only for quality control and analysis of data but also for numerical modeling (Benjamin et al., 1991).

Because isentropic coordinates are deficient in their resolution of the boundary layer, also in order to provide a dynamically optimal setting for incorporating the additional aircraft and wind profiler information, the numerical prediction model serving as the primary space-time data integrator in the assimilation package is formulated in "hybrid" vertical coordinate, a combination of isentropic and terrain-following (isentropic/sigma) coordinates. The sigma vertical coordinate exists as six levels in the lowest 150 mb thus retaining highly detailed planetary boundary layer information.

Ingesting the MAPS data into RAMS is accomplished in the following manner. First, MAPS variables are converted to true east and north wind components, potential temperature, relative humidity and Montgomery streamfunction. Then a horizontal interpolation is performed transforming variables from MAPS' horizontal grid to RAMS' horizontal grid. Variables are then vertically- interpolated to RAMS' sigma vertical coordinate system. This is first performed for the first 6 sigma levels of MAPS, then for the isentropic surfaces, beginning with the first isentrope above the top sigma level. In a given column, any isentropic level information is ignored if the isentrope crosses into the sigma levels below. Finally, Exner function ($\pi = (p/p_0)^{R/C_p}$) values are obtained by a hydrostatic integration from the MAPS 360 K objectively analyzed streamfunction.

3.3 Nudging boundary conditions

Assuming the atmosphere does not remain steady-state for long periods, the expected atmospheric state at later times must be communicated to the model's lateral boundaries (Thompson, 1993). This is necessary because meteorological conditions outside the model domain of which the model has no information often influence the meteorological conditions on the model boundaries which have influence on the interior of the model domain. Hence, the model of limited domain must be told what the boundary tendencies are with time. This is referred to as time-dependent lateral boundary conditions.

In this study using variable initializations, time-dependent boundary conditions are accomplished by a method called nudging or Newtonian relaxation (Davies, 1983). In the nudging scheme, an extra tendency term is added to each prognostic equation which forces the predicted variable towards the available observation

$$\frac{\partial x}{\partial t} = F(x) + N(x, y, z, t) \cdot (x_0 - x) \tag{3.1}$$

where x is a model prognostic variable, $F(x)$ is the model's physics, $N(x, y, z, t)$ is the nudging weight, and x_0 the observation of the model variable (Pielke et al., 1992).

For simplicity, if we drop the physical forcing term $F(x)$ from the above equation and assume that the observational analysis is perfect and time invariant, then

$$\frac{\partial x}{\partial t} = N(x, y, z, t) \cdot (x_0 - x) \tag{3.2}$$

which has the solution

$$x = x_0 + (x_i - x_0)e^{-N(t-t_i)} \tag{3.3}$$

where x_i is the initial value of x at the start of the nudging period (at t_i). Therefore, the model state approaches the observed state exponentially with an e-folding time of $T = \frac{1}{N}$. This implies that very high frequency fluctuations in the data, as might be available from wind profilers or Doppler radars will not be retained well unless N is much greater; but then the nudging term may not be small compared to some terms of the physical forcing.

The mesoscale simulations of this study use MAPS analyses as the observations for the nudging boundary conditions. It should be noted that nudging is only applied to the boundaries of the coarse grid and interior nudging is not used. Extensive tests demonstrate that a nudging time scale of 300 seconds is appropriate for this study.

3.4 Simulation Overview

RAMS mesoscale model with interactively nested grids is used to simulate the 26 November 1991 FIRE II cirrus case. Atmospheric variables are initialized using a combination of the MAPS analysis data, NWS rawinsonde data at 0000 UTC of November 26, 1991. The data used in the initialization processes is obtained from NASA Langley Distributed Active Archive Center (DAAC). Lateral boundary conditions for the outer five grid points on the coarse grid are provided by a linear time series created from the data mentioned above. Topography, vegetation type, land percentage, and sea surface temperature are read into the grids from RAMS archived datasets.

Mesoscale nested grid simulations with three and four grids have been performed. For these two simulations, Grids # 1 and 2 have the same configurations. However, the third grid is centered at different locations in order for the finer grids to focus on different special areas. Plots of these grids are shown in Figure 3.1. Model setups are shown in Table 3.1. A variable vertical grid spacing is used for all the grids which have identical vertical domain as well as vertical levels. A vertical grid spacing of 500 m is used near the surface and the model top, while a spacing of 200 m is used within the cloud layer (Table 3.2).

The model is initialized with only one grid, the coarse grid (Grid #1). Grid #2 is spawned after 6 hours into the simulation. As mentioned above, two-way interactive nesting is used for the nested grids. Grid #3 is nested in at 12 hours into simulation. Grid # 4 (for Case 1) is activated at 16 hours and runs through the simulation thereafter with all the other three grids. The first simulation (Case a) which uses four nested grids is set up to study a weak cloud band associated with the leading portion (the southeast part) of the observed cloud system. For this case, Grids #3 and #4 are centered at the observational site, Coffeyville, Kansas. By doing so, the mesoscale structures of the weak leading band are expected to be well resolved by RAMS.

	Case 1	Case 2
number of grids	4	3
x grid points	50, 50, 47, 46	50, 50, 47
y grid points	40, 42, 47, 46	40, 42, 47
z grid points	65, 65, 65, 65	65, 65, 65
horizontal grid spacings (km)	80, 20, 4, 1	80, 20, 4
vertical grid spacings (m)	200 to 500	200 to 500

Table 3.1: Model setups for Case 1 and Case 2. The vertical grid spacing is the same for every grid.

0.0	300.0	600.0	900.0	1200.0	1500.0
1800.0	2100.0	2400.0	2700.0	3000.0	3300.0
3600.0	3900.0	4100.0	4300.0	4500.0	4700.0
4900.0	5100.0	5300.0	5500.0	5700.0	5900.0
6100.0	6300.0	6500.0	6700.0	6900.0	7100.0
7300.0	7500.0	7700.0	7900.0	8100.0	8300.0
8500.0	8700.0	8900.0	9100.0	9300.0	9500.0
9700.0	9900.0	10100.0	10300.0	10600.0	10900.0
11200.0	11500.0	11800.0	12200.0	12600.0	13000.0
13400.0	13800.0	14200.0	14600.0	15000.0	15500.0
16000.0	16500.0	17000.0	17500.0	18000.0	

Table 3.2: Vertical levels used in the mesoscale simulations (in m).

The other simulation (Case b) with three nested grids is set to focus on a deep cloud system following the leading cloud band. This system was observed to the northwest of the weak cirrus band and observations showed that the deep cloud system had large high-cloud optical depths which was believed to be caused by thick cloud layers underneath the highest cirrus. This case is intended to predict the middle latitude multilayered cirrus cloud. We feel that the high model resolution combined with the detailed microphysics can yield a thorough investigation of the dynamical and microphysical processes responsible for the cloud evolution and development.

Since the Large-Eddy Simulations (LES) and cloud- resolving modeling (CRM) study of this cirrus event (to be discussed in latter chapters) will be extensions of the mesoscale modeling study, it is vitally important to show that the mesoscale simulations can rea-

sonably predict the observed cloud fields in order for the LES and CRM studies to have credibility for further analyses.

The six-hour model forecast of geopotential heights at 300 mb, 400 mb, and 500 mb is shown in Figure 3.2. A ridge is predicted at the west coast, while a large northeast-southwest oriented trough is sitting over the eastern part of the United States. A strong upper level jet associated with the northwesterly flow in the east side of the ridge covers many of the western States from Oregon to the western part of Colorado. The jet has a maximum wind speed of $60.3m/s$ which is predicted at 300 mb. Model- predicted wind speeds decrease substantially in the eastern part of Colorado and Arizona compared to the west.

Also shown in this Figure, a short trough extending from the US-Canada border to north-central US has propagated to Montana and Wyoming by this time. Large areas of diffluent flow ahead of the short trough imply that this trough will experience amplification as it propagates eastward.

Figure 3.3 shows the 6-hour model prediction of snow particle number concentration on Grid #1 at 300 and 400 mb. Several regions of nonzero snow particle number concentration are displayed. Associated with the short trough discussed above, there is a broad area of snow particle number concentration centered near the western border of South Dakota. The maximum snow concentration within this region is less than $3liter^{-1}$. However, there are no snow particles seen corresponding to the short trough location at 300 mb, meaning that the cloud system associated with that trough is still quite shallow and the cloud top has not reached $9000m$ level by this time.

The short trough propagates slowly eastward. By 1200 UTC, it has moved to the border between Montana and the Dakotas (Figure 3.4). Associated with this trough, the 7040 m contour on 400 mb has reached the southwest corner of North Dakota, a clear indication of amplification of that trough during the past several hours. The northwesterly jet stream has been very steady with a maximum speed of $59.2ms^{-1}$ predicted at 300 mb. The mesoscale vertical velocity predicted at this time on Grid #1 varies from -14 to $12cms^{-1}$.

In association with the trough movement on the coarse grid, the short wave disturbance has propagated into the northwest corner of Grid #2 by 1200 UTC (Figures not shown). Corresponding to the disturbance, areas of ice particle concentration have occupied part of the northwest quarter of Grid #2 (Figure 3.5). PI concentration is generally less than $6liter^{-1}$ while snow particle number concentration can be as high as $29liter^{-1}$. Higher mixing ratios of snow is predicted at lower levels with a maximum value of 2.9×10^{-5} at 500 mb while PI has its maximum value of 4.0×10^{-6} at 400 mb. Vertical velocities on this grid range from -5 to $12cms^{-1}$.

By 24 hours into the simulation, a predicted ridge dominates the western US as shown on the coarse grid while a deep trough is predicted over the central US extending from the US-Canada border to the Gulf of Mexico. The leading edge of the northwesterly jet has reached the panhandle region. Figures 3.6 and 3.7 compare the 24 hour model prediction of the 400 and 500 mb circulations on the coarse grid (Grid #1) with the corresponding MAPS analyses at 0000 UTC of the November 27, 1991. As can be seen, the mesoscale model simulation is quite realistic in predicting the observed large scale features associated with this cloud system. The model- predicted ridge-trough location is nearly identical to the corresponding MAPS analyses at the same time. Also evident both in the model prediction and in the observations is the existence of a strong northwesterly flow at the upper levels over the central west United States. The Kansas- Oklahoma region is in the exit region of this strong upper tropospheric jet, resulting in a strong horizontal wind speed gradient in the observational area. The predicted maximum wind vector on Grid #1 is within $2ms^{-1}$ of the observations. It is also amazing that the model even predicts almost the same geopotential height fields as the MAPS analyses. The consistency between the model prediction and the observation indicates that indirect vertical circulations induced by transverse ageostrophic flow in the jet exit region (as it was analyzed in Mace et al. (1995)) was precisely what occurred in the present cirrus scenario.

3.5 Detailed simulation results

3.5.1 Short-wave disturbances on finer grids

The average height on Grid #2 is about 7200 m which is near the midlevel of the cloud layer. Shown in Figure 3.8, two weak short- wave troughs are discernible near the north boundary of this grid domain at 1800 UTC. As time goes on, the trailing stronger short-wave amplifies while the leading one propagates eastward without noticeable development. By 0000 UTC of November 27, 1991, the model has simulated a dominant trailing short-wave trough to the north of Oklahoma and the leading trough has propagated to east-northeast, nearly out of the domain of Grid #2. In response to the short waves, two distinct bands are predicted with the band to the west showing very active small scale cells, indicating active cloud development. At times, the strong band to the west can be seen to be composed of two tightly related bands (see Figures 3.9 through 3.13).

Figure 3.14 compares the model- predicted snow mixing ratio field on Grid #2 at 1800 UTC with the retrieved total and high-cloud optical depths at the same time. Generally speaking, the predicted cloud macrostructure is consistent with satellite and ground-based remotely sensed cirrus observations for the day. Thin cirrus is simulated over the Coffeeville, Kansas, while a thick cloud layer is simulated in southwest to northeast-oriented bands further to the west. As also can be seen in the top panel of this Figure, three distinct cloud bands are identified. Two tightly connected bands of the three are associated with the main cloud system. These predicted bands are also in agreement with the observational analyses done by Mace et. al. (1995) who identified three cloud lines associated with the cloud system. However, as it is also obviously seen in this Figure the model- predicted cloud system is too extensive in the east-west direction compared with the observational analyses. The predicted cloud width in the east-west direction is about 200 km larger than the observed system, even though the synoptic-scale dynamics for the cloud environment is well simulated. We believe that this shortcoming in the numerical prediction is mainly due to the uncertainties in the initialization of the moisture field in the upper troposphere and lower stratosphere. It may also be partially because of the Rocky Mountain effects which are not well represented in the MAPS analyses used to initialize the model.

The vertical velocity fields shown in Figure 3.13 indicate very active cells associated with the strong cloud band. These convective cells spawn a wide range in spectrum from the model resolvable scale of about 50 km to about several hundred kilometers. The maximum vertical air velocity is $1.6ms^{-1}$ and the strongest sinking motion is $-40cms^{-1}$. It is interesting to note that by 0000 UTC of the November 27, 1991, cells associated with the trailing cloud band have aligned to establish a well defined updraft band with sinking motions sitting at its front and rear sides.

It is important to point out that the short-wave pattern predicted on this grid can not be tracked either in the MAPS analyses or in the circulation predicted on Grid #1. The cloud system predicted on Grid#2 follows closely to the short- wave pattern in the wind fields. Since the simulated cloud system is in good agreement with the available observations, it is reasonable to speculate that the short-wave circulation pattern is in fact what happened that day, even though this feature was not captured in the synoptic observation network (maybe because the observational network is too coarse to capture this smaller scale circulation feature). Considering the fact that Grid #2 has a domain size of 1000 km in west- east direction, the short waves predicted have a wave length of about 400 km or less. As discussed in the previous Chapters, Mace et al. attributed the cloud bands observed to gravity wave activities involved in the cloud development.

Some of the model prediction on Grid #2 at 300 mb are shown in Figures 3.15 through 3.20. Similar circulation features are seen at this pressure level as well as at 400 mb, indicating that the short- wave pattern is a deep dynamic disturbance (Figure 3.20 vs. Figure 3.13). Higher PI number concentration and mixing ratio are found at this pressure level than at 400 mb while it is opposite for snow. Maximum PI concentration of as large as $2100liter^{-1}$ at 1800 UTC compares well to the observed maximum value of more than $1000liter^{-1}$ (discussed in Chapter 2). As expected, snow particle number concentration at this level which is on the order of ten is much less than that of PI. PI mixing ratio contributes dominantly to the total ice mass. The strength of updraft at this level is generally less than $80cms^{-1}$ while the strongest downward motion is about $-18cms^{-1}$.

Figures 3.21 through 3.25 shows the model prediction of PI concentration and mixing ratio, snow particle concentration and mixing ratio, and vertical velocity fields on Grid #3

at 1900 UTC for Case a and Case b. Since Grid #3 has a domain size of $184 \times 184 km^2$, the model prediction on this grid is nothing interesting but some fractions of the cloud bands predicted on Grid #2. The inefficiency of diffusion when the grid size is getting small also results in some accumulation of small scale noise near the outflow boundary, especially in the vertical velocity field (Figure 3.25). Because of the inefficiency in diffusion with the finer grids, we feel that much of the effort should be devoted to the detailed analyses of the model results on Grid #2.

3.5.2 East-west cross sections along Coffeyville, Kansas

Figures 3.26 through 3.30 show east-west cross sectional plots (along Coffeyville, Kansas) of the model- predicted snow particle concentration, snow mixing ratio, pristine ice number concentration, pristine ice mixing ratio, and vertical velocity fields at 2000 UTC of the November 26 and 0000 UTC of the November 27. Coffeyville, Kansas is located at about 500 km along the horizontal coordinate. The middle cloud band seen on the pressure surfaces shown in the previous Sections can not be seen in these cross sections because its south boundary is far to the north of this latitude. The leading edge of the first band has moved to Coffeyville at about 1600 UTC. By 0000 UTC of the November 27, the weak band has already moved out of Coffeyville and propagated to the east while the trailing band is about to be observed at the observational site.

During the simulation period, the weak band confines its top and bottom boundaries to be within 5 and 10 km MSL (mean sea level). Snow particles which are generally converted from pristine ice crystals exist throughout the cloud layer, while as can be expected, large amounts of pristine ice particles are suspended near the top level of the cloud. As simulation time goes on, sedimentation of larger ice particles can be traced by the descending of the cloud base as well as the secondary center of snow particle number concentration (shown at 2000 UTC) located at about 6 km above the ground. Some indication of multilayer features can also be identified, especially in the pristine ice field.

Associated with this weak cloud band, the maximum snow number concentration is usually less than $4L^{-1}$; the maximum snow mixing ratio is about 3×10^{-2} g/kg; the maximum pristine ice number concentration is less than $100L^{-1}$; the maximum pristine

mixing ratio is less than 7×10^{-3} g/kg; and the maximum mesoscale vertical velocity is only about 5 cm/s.

The trailing cloud band (main cloud system) is quite distinct. Even though the prediction of this system lags behind the observations on that day, the model prediction indeed reflects the properties of the main cloud system to the northwest of the weak cloud band. As shown in these cross-sectional plots, the main system is much stronger than the weak band. This system which extends from 2 km to 10 km shows several peaks in particle number concentration and mixing ratio in the vertical, a possible indication of multilayered structures. The maximum snow particle number concentration is less than $40L^{-1}$; the maximum snow mixing ratio is about 0.22 g/kg; the maximum pristine ice particle concentration is $1800L^{-1}$; and the maximum pristine ice mixing ratio is about 0.119 g/kg. Several distinct convective-like cells can be identified in the vertical velocity field at 0000 UTC. However, the maximum mesoscale vertical velocity is only about 44 cm/s.

3.6 Brief summary

Using RAMS mesoscale nested grids, we have simulated the November 26, 1991 cirrus event. The model accurately simulates the dynamics associated with the cloud formation and evolution except that the second short-wave disturbance which modulates the evolution of the deep cloud system, persists too long. The persistence of that short-wave disturbance results in a wider west-east direction cloud coverage than the observed cloud system.

The indirect vertical circulations induced by transverse ageostrophic flow in the jet exit region provided the favorable meso-scale environment for cirrus cloud development. However, the RAMS simulations reveal that the short-wave disturbances which are predicted on the finer grid (Grid # 2) are the direct driving force for cloud formation and evolution, even though these disturbances were not captured in the observational network, nor predicted in the previous mesoscale simulation of the same case (Westphal et al., 1996). The model-predicted cloud bands which are modulated by the short-wave disturbance pattern are consistent with the cloud lines identified in the observational studies (Mace et al., 1995).

The RAMS simulations also demonstrate that adding more nested grids to the simulations does not gain much, especially for this cirrus case. In fact, the lack of a suitable subgrid- scale model when the resolution is getting higher and higher reduces the credibility of prediction on the finer grids with horizontal resolutions better than several kilometers. The second grid which has a horizontal grid spacing of 20 km is capable of resolving the dynamical properties of this cirrus event.

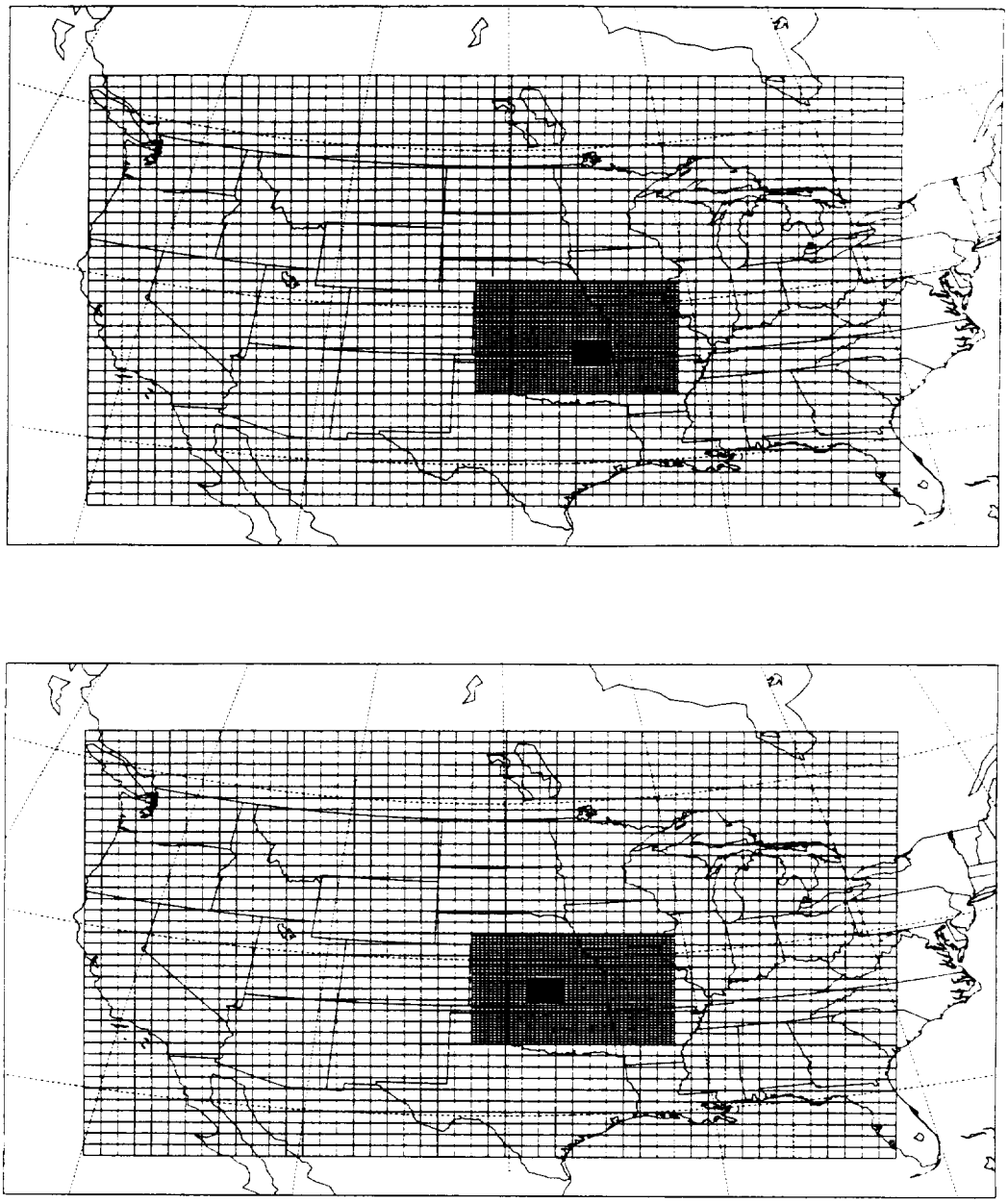

Figure 3.1: Grid configurations used for Case I (top) and Case II (bottom).

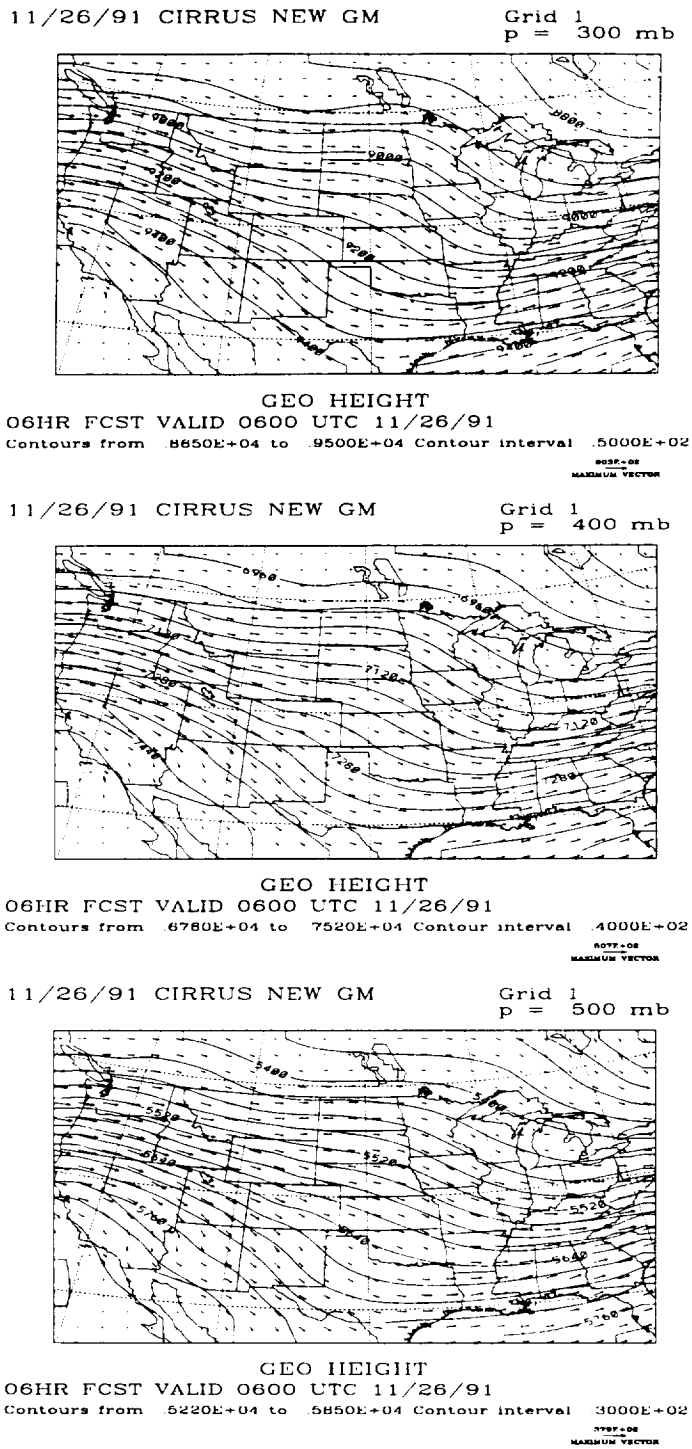

Figure 3.2: Model predicted geopotential heights at 300 mb, 400 mb, and 500 mb on Grid #1 at 6 hours into simulation.

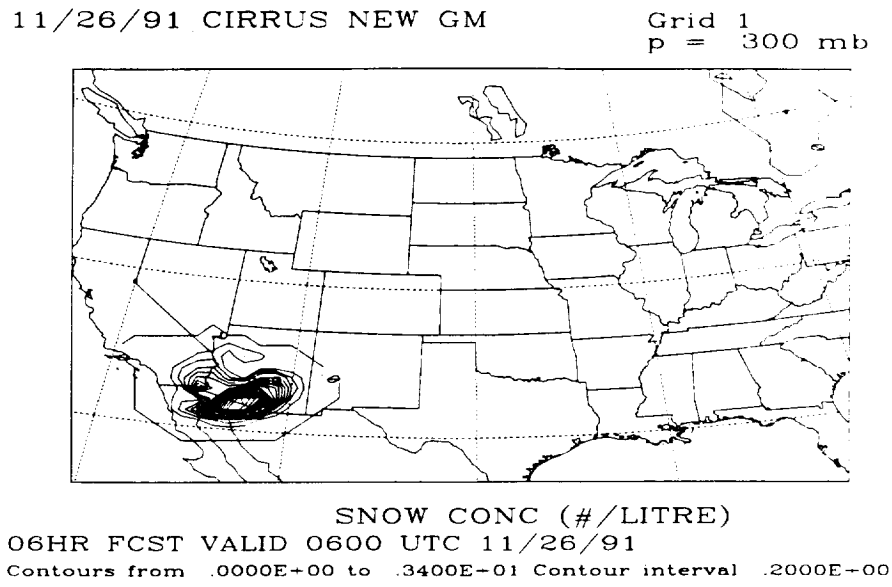

Figure 3.3: 6-hour model prediction of snow particle number concentration on Grid #1 at 300 and 400 mb.

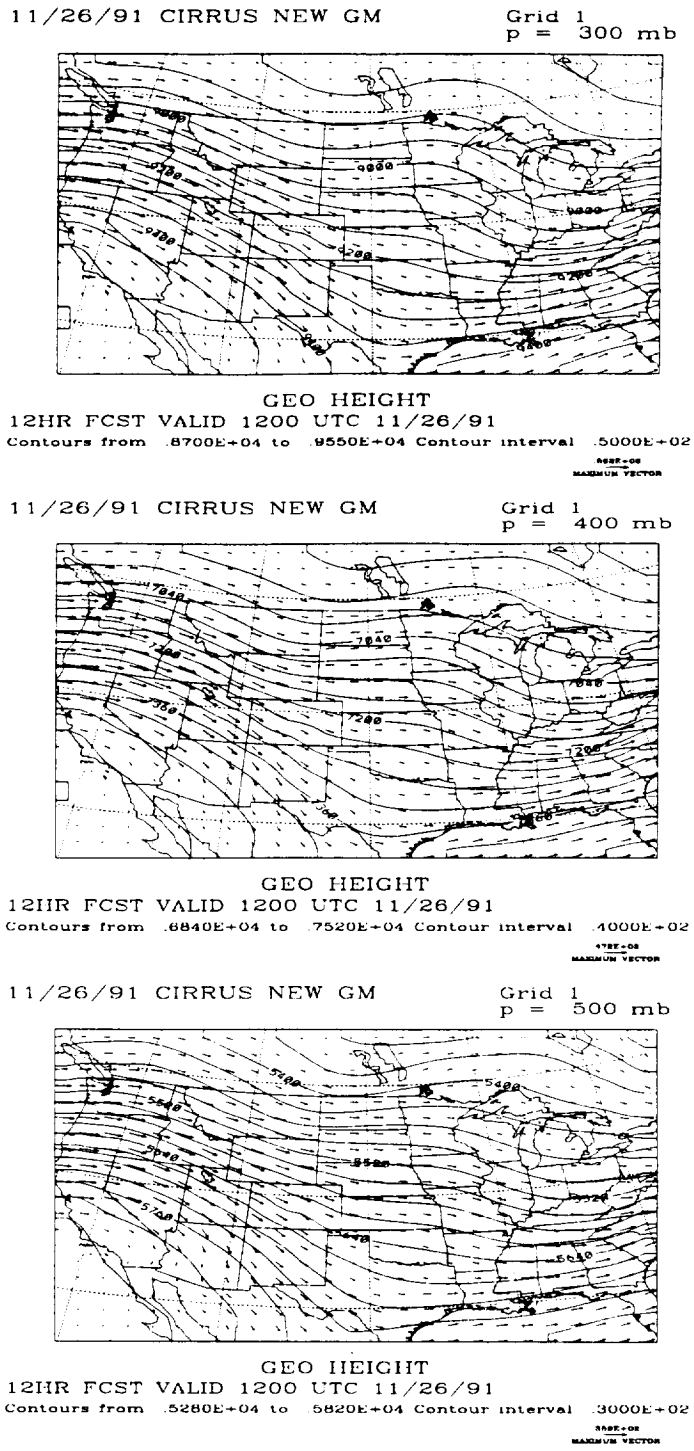

Figure 3.4: 12-hour model prediction of geopotential heights on Grid #1 at 300 mb, 400 mb, and 500 mb.

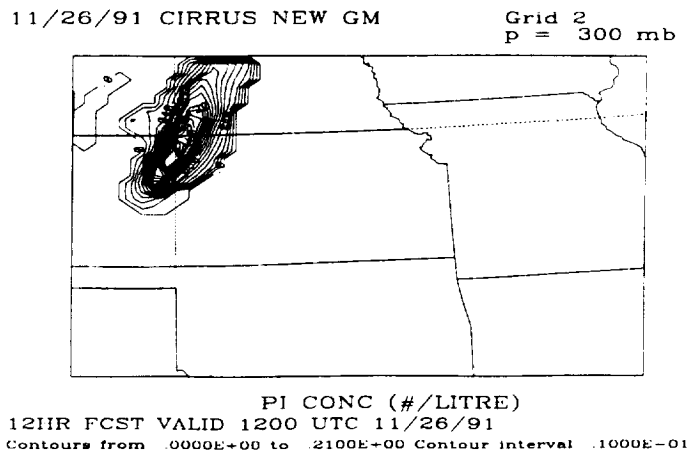

Figure 3.5: 12-hour model prediction of pristine-ice (PI) number concentration at 300 mb, 400 mb, and 500 mb.

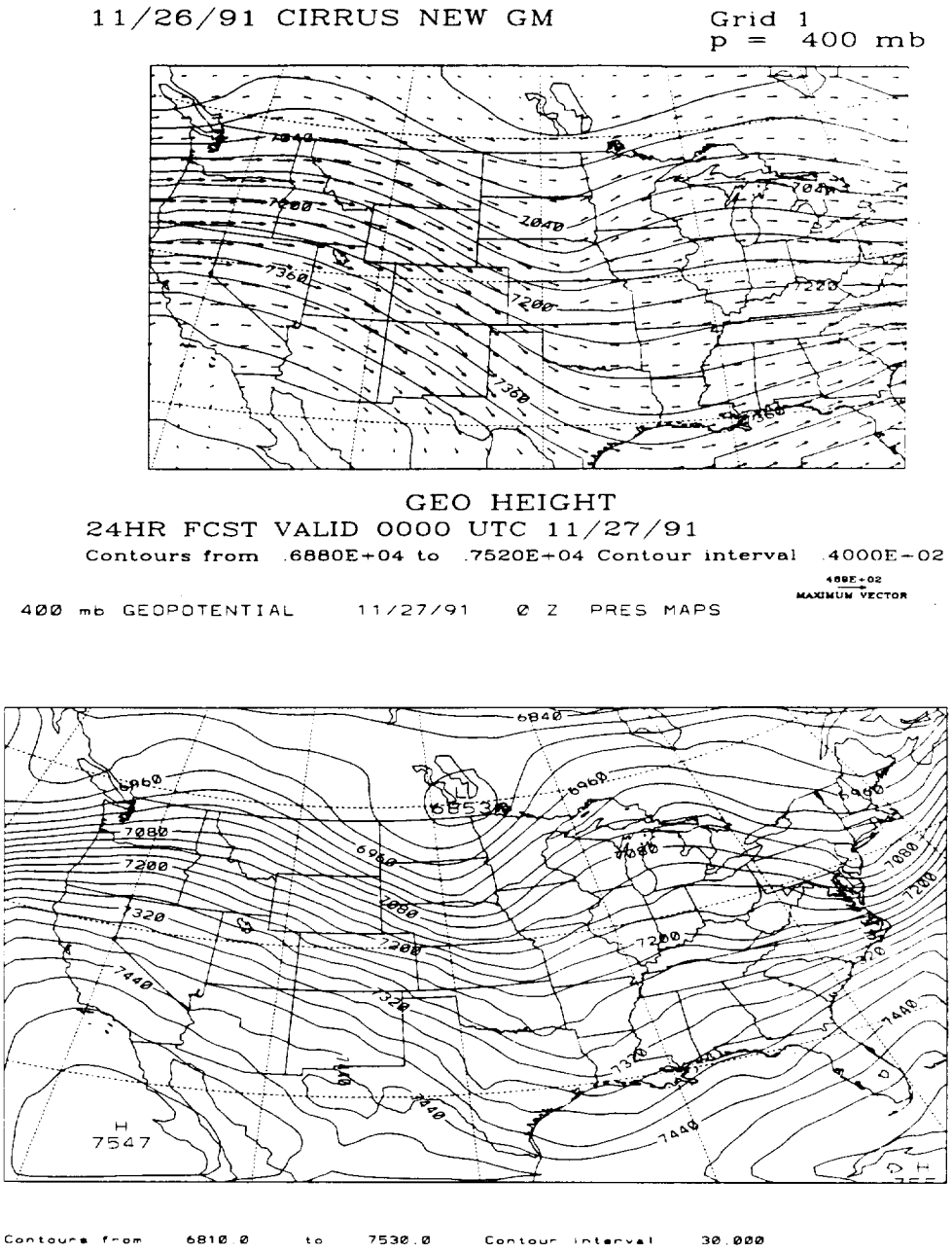

Figure 3.6: Model predicted 400 mb circulation at 0000 UTC of the November 27, 1991 (top) versus the MAPS analysis (bottom) at the same time.

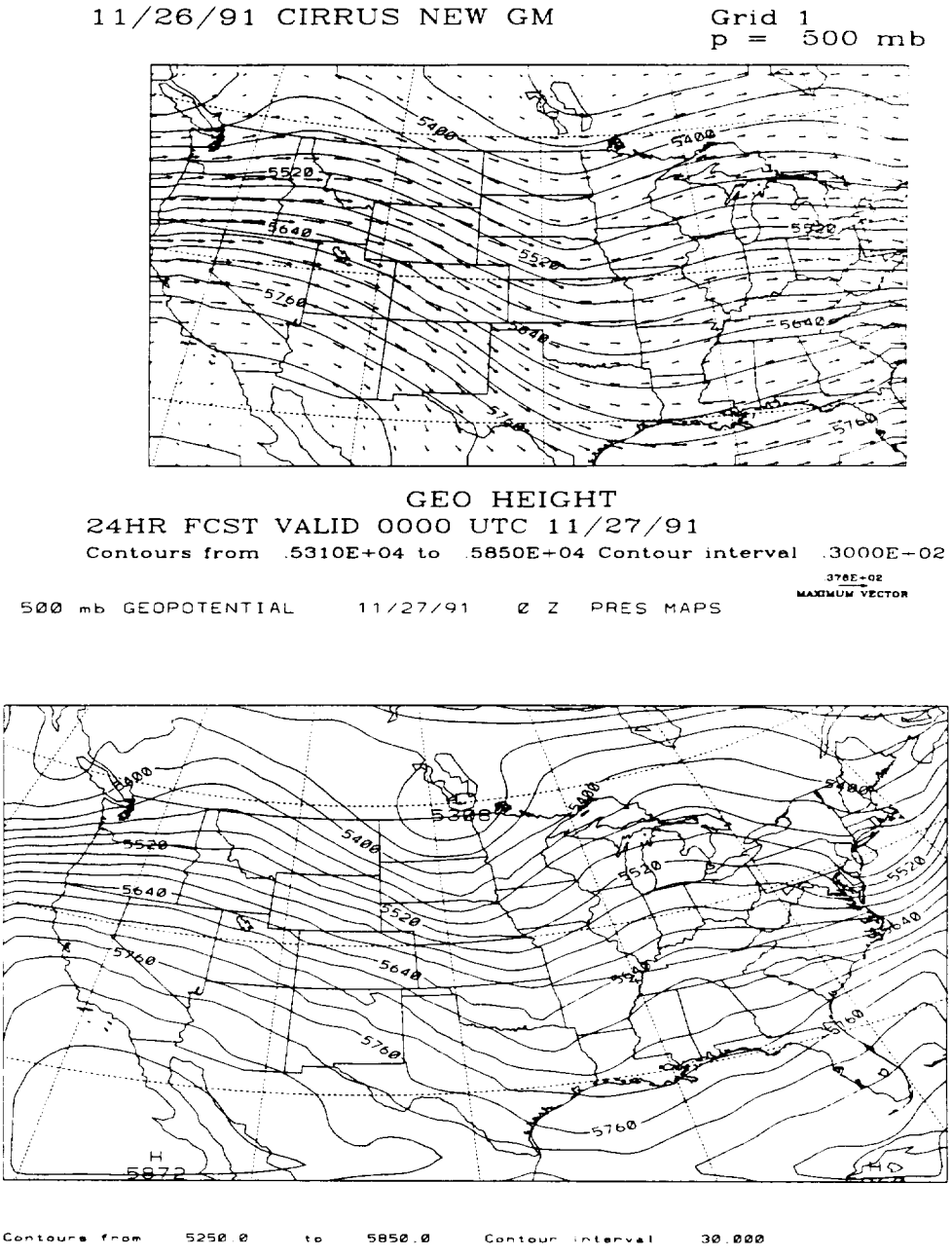

Figure 3.7: Model predicted 500 mb circulation at 0000 UTC of the November 27, 1991 (top) versus the MAPS analysis (bottom) at the same time.

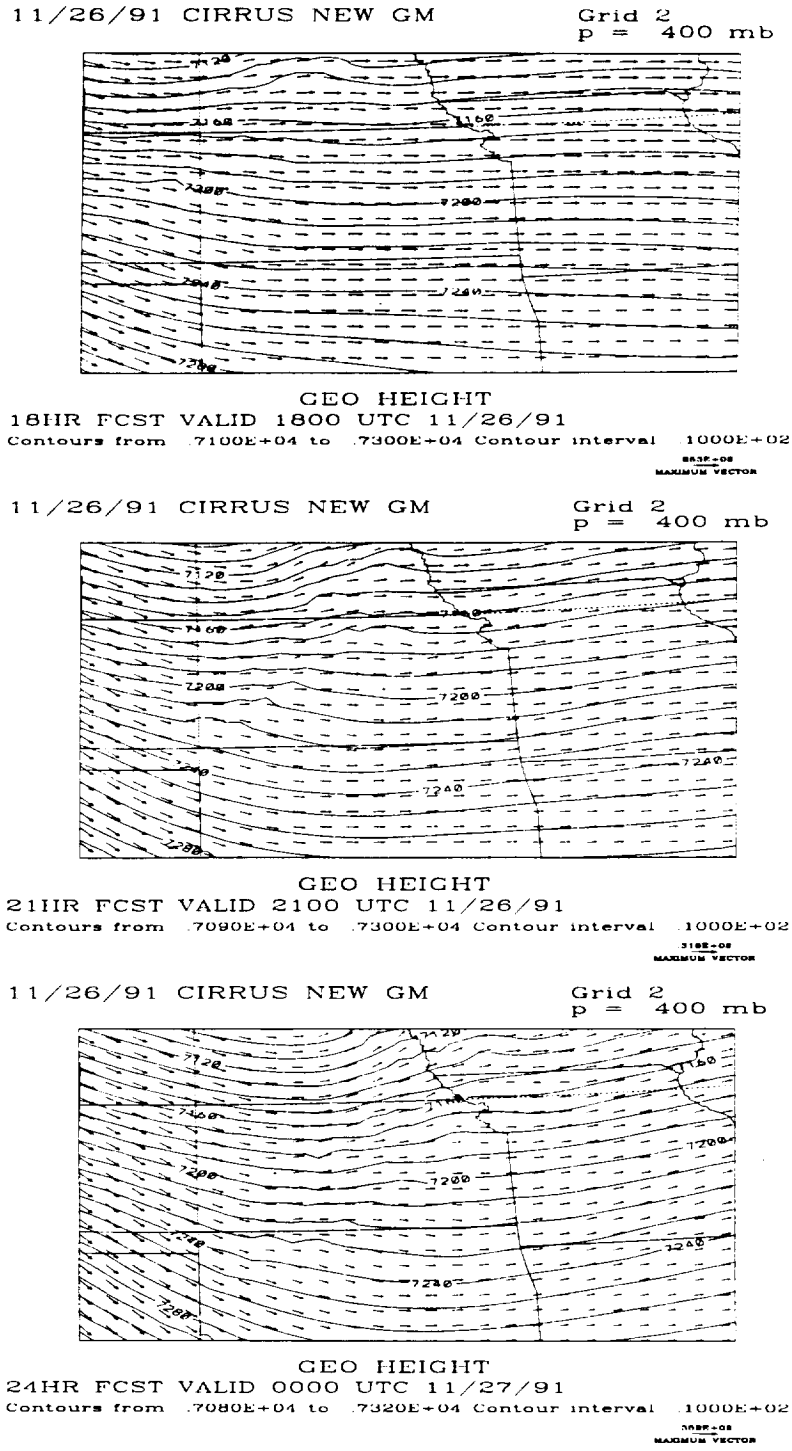

Figure 3.8: Model predicted 400 mb geopotential heights on Grid #2 at 1800 UTC, 2100 UTC of the November 26, and 0000 UTC of the November 27, 1991.

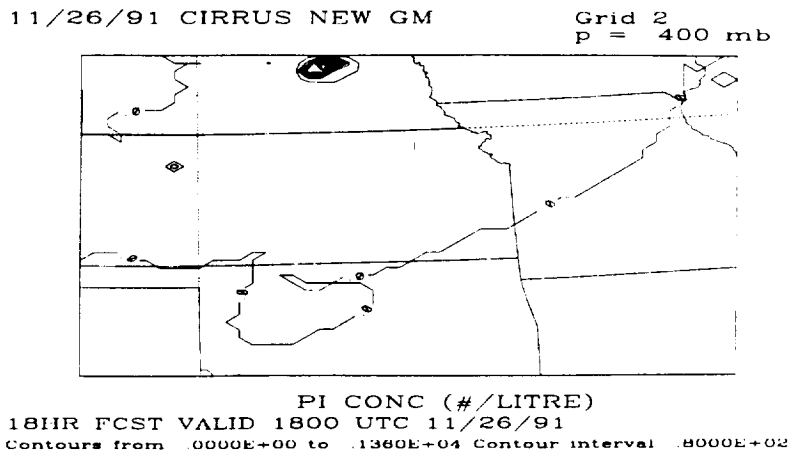

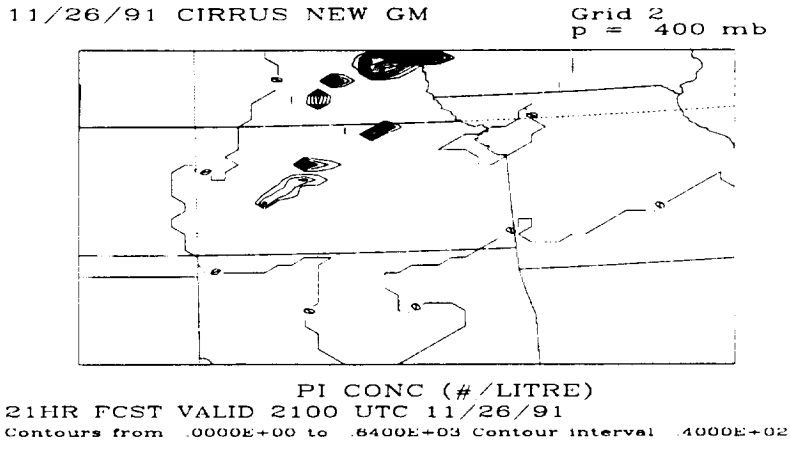

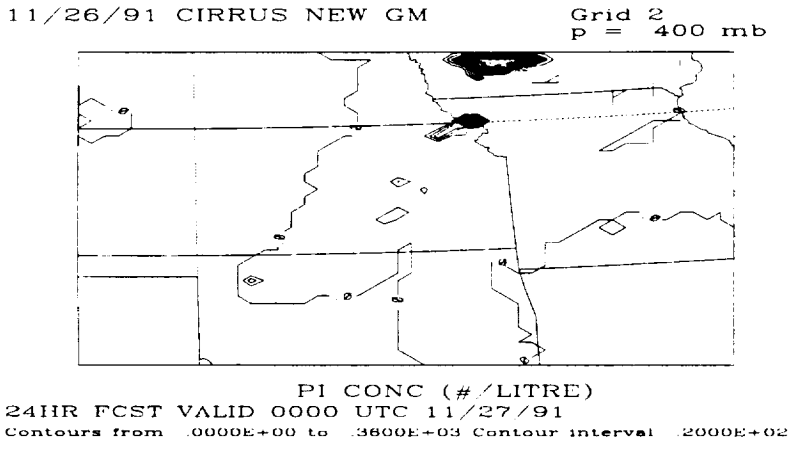

Figure 3.9: Model predicted 400 mb pristine ice number concentration on Grid #2 at 1800 UTC, 2100 UTC of the November 26, and 0000 UTC of the November 27, 1991.

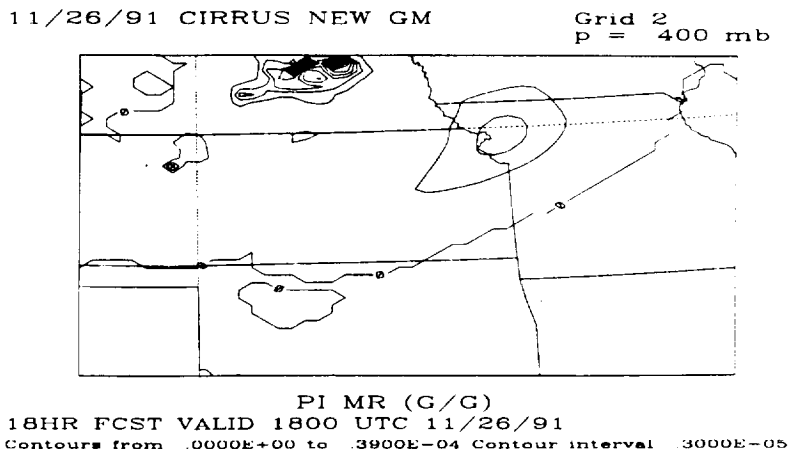

Figure 3.10: Model predicted 400 mb pristine ice mixing ratio on Grid #2 at 1800 UTC, 2100 UTC of the November 26, and 0000 UTC of the November 27, 1991.

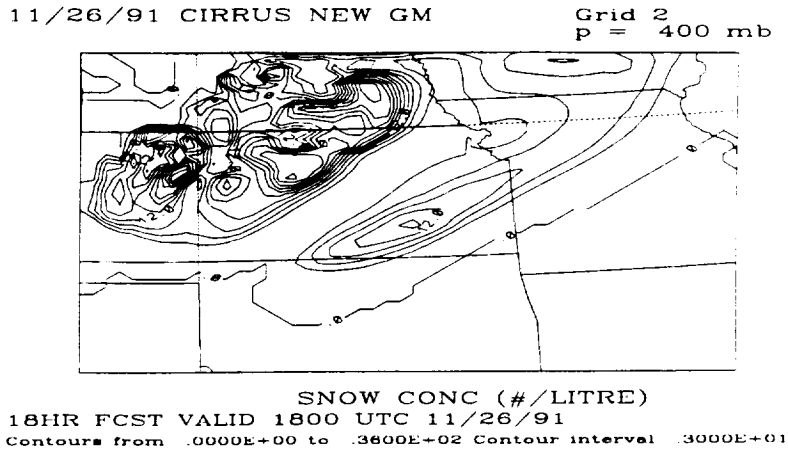

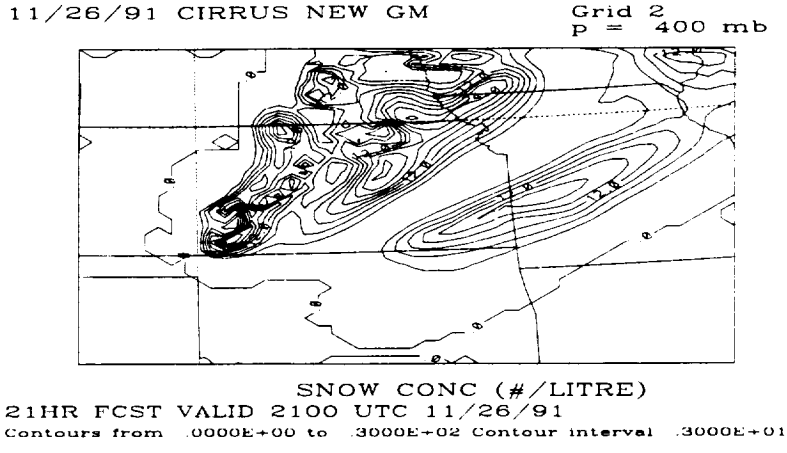

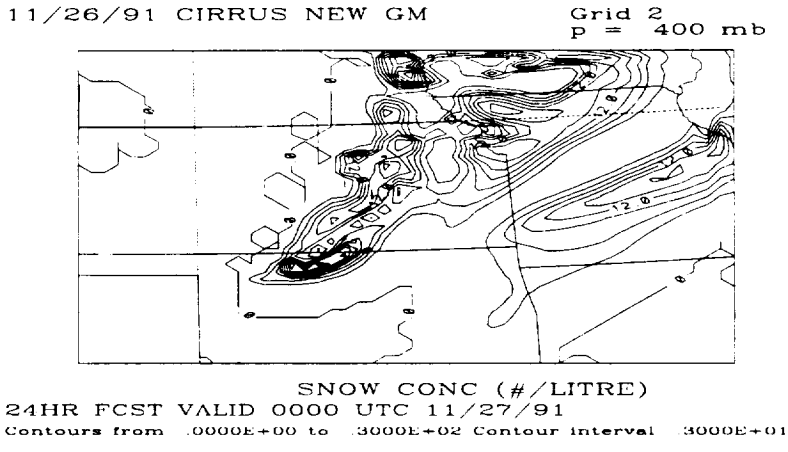

Figure 3.11: Model predicted 400 mb snow number concentration on Grid #2 at 1800 UTC, 2100 UTC of the November 26, and 0000 UTC of the November 27, 1991.

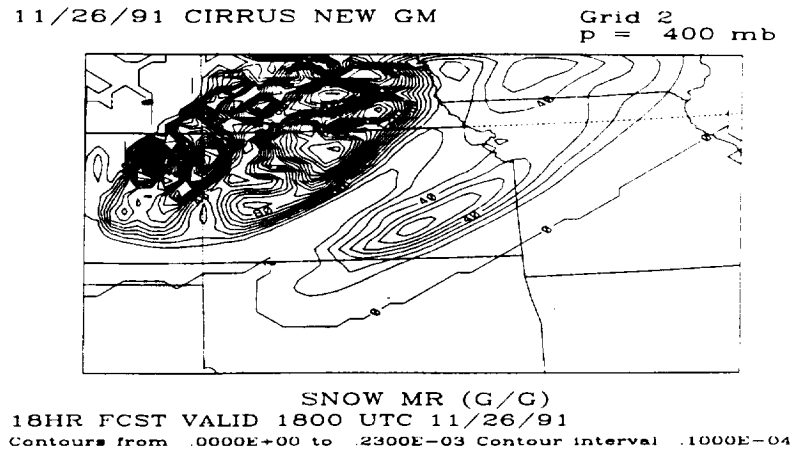

Figure 3.12: Model predicted 400 mb snow mixing ratio on Grid #2 at 1800 UTC, 2100 UTC of the November 26, and 0000 UTC of the November 27, 1991.

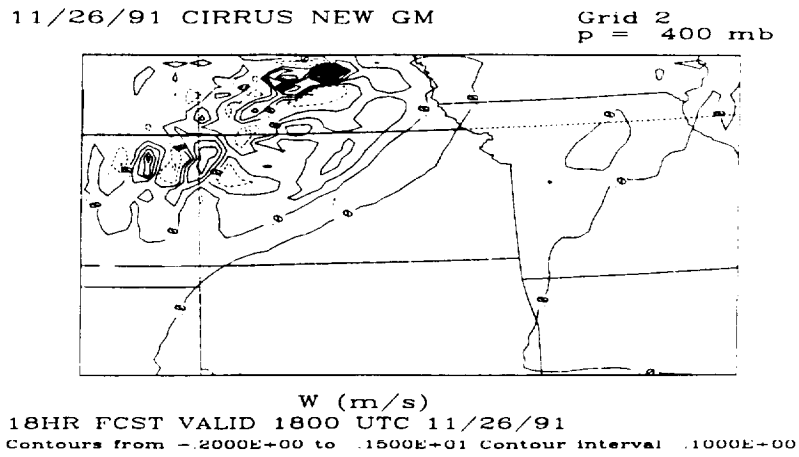

Figure 3.13: Model predicted 400 mb vertical velocity fields on Grid #2 at 1800 UTC, 2100 UTC of the November 26, and 0000 UTC of the November 27, 1991.

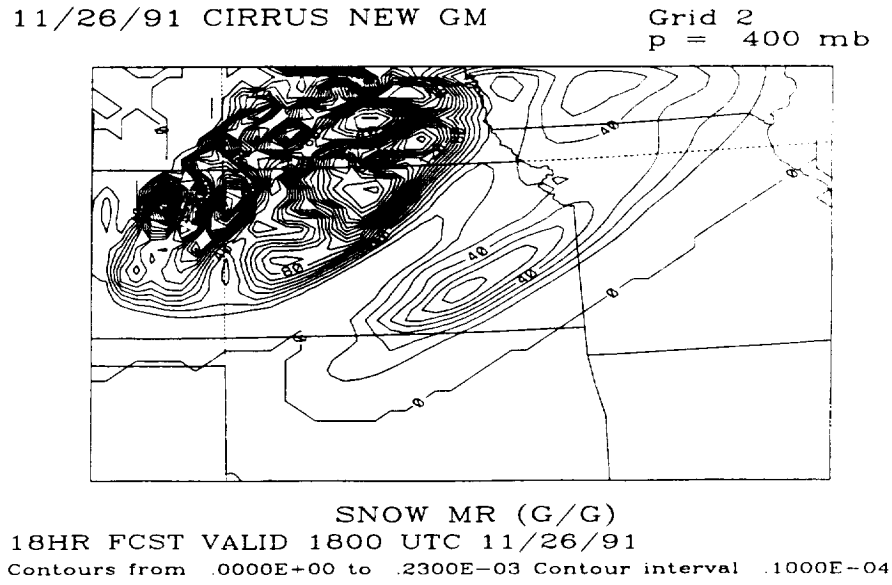

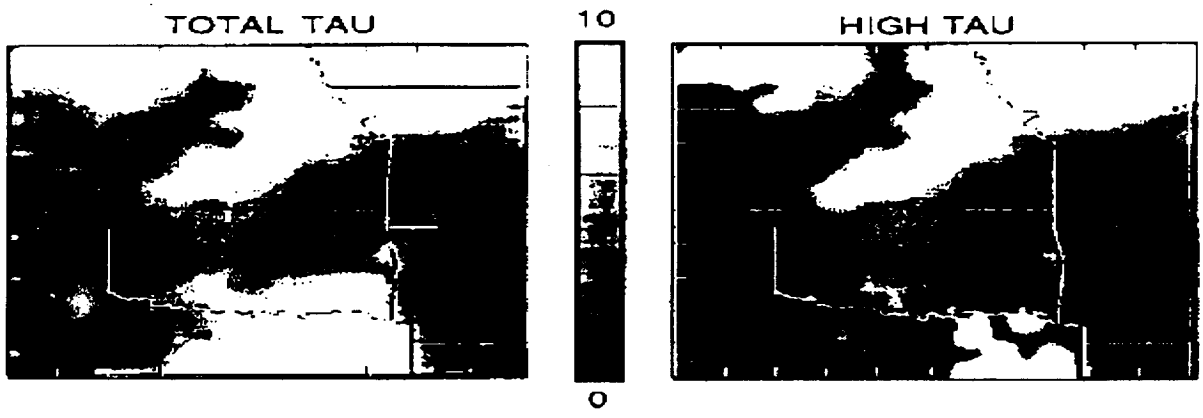

Figure 3.14: Model predicted snow mixing ratio (top) at 1800 UTC versus the retrieved total and high-cloud optical depths (bottom).

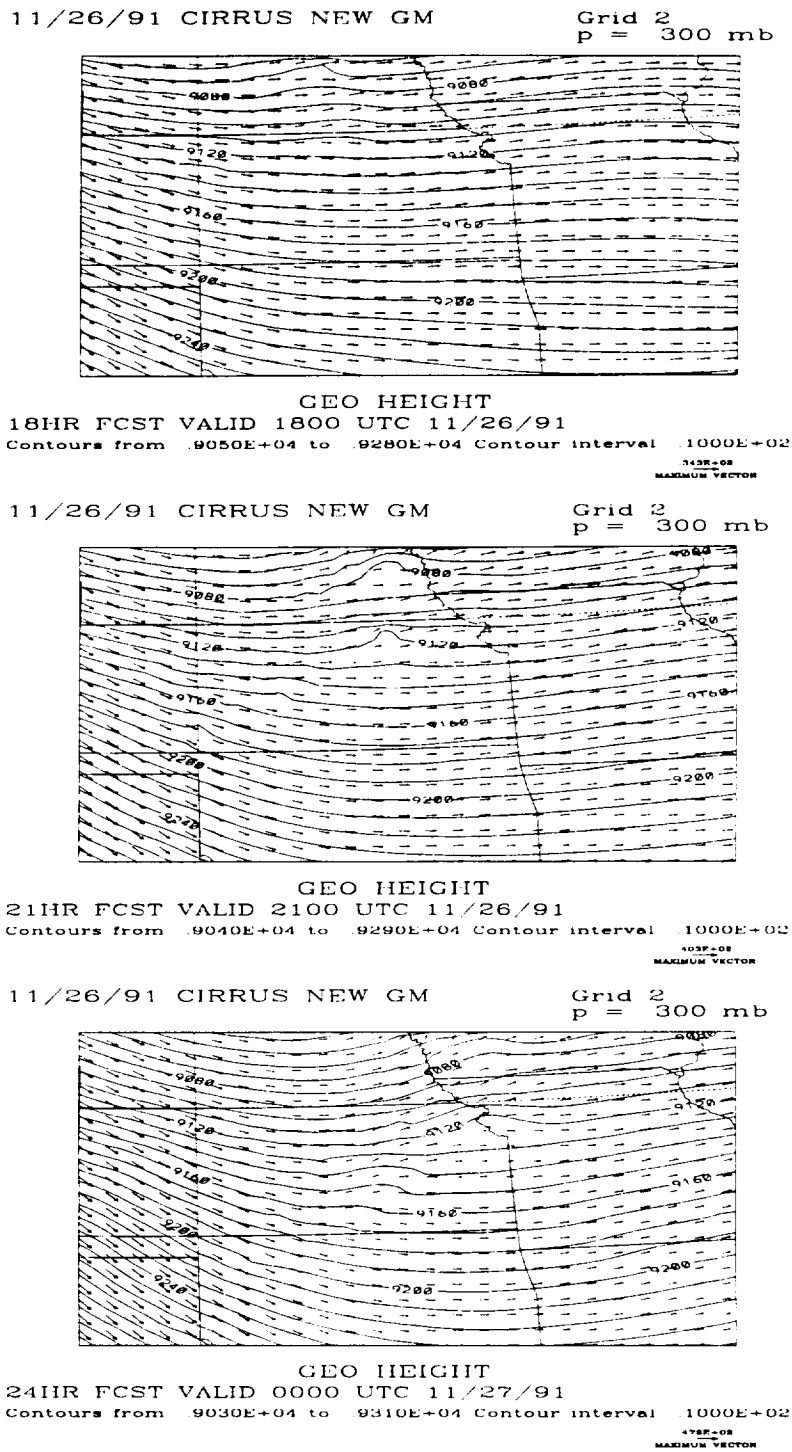

Figure 3.15: Model predicted 300 mb geopotential heights at 1800 UTC, 2100 UTC of the November 26, and 0000 UTC of the November 27, 1991.

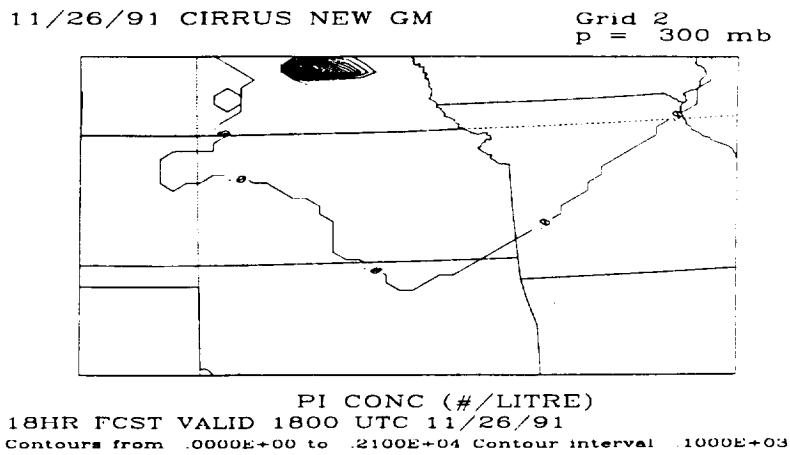

Figure 3.16: Model predicted 300 mb pristine ice number concentration at 1800 UTC, 2100 UTC of the November 26, and 0000 UTC of the November 27, 1991.

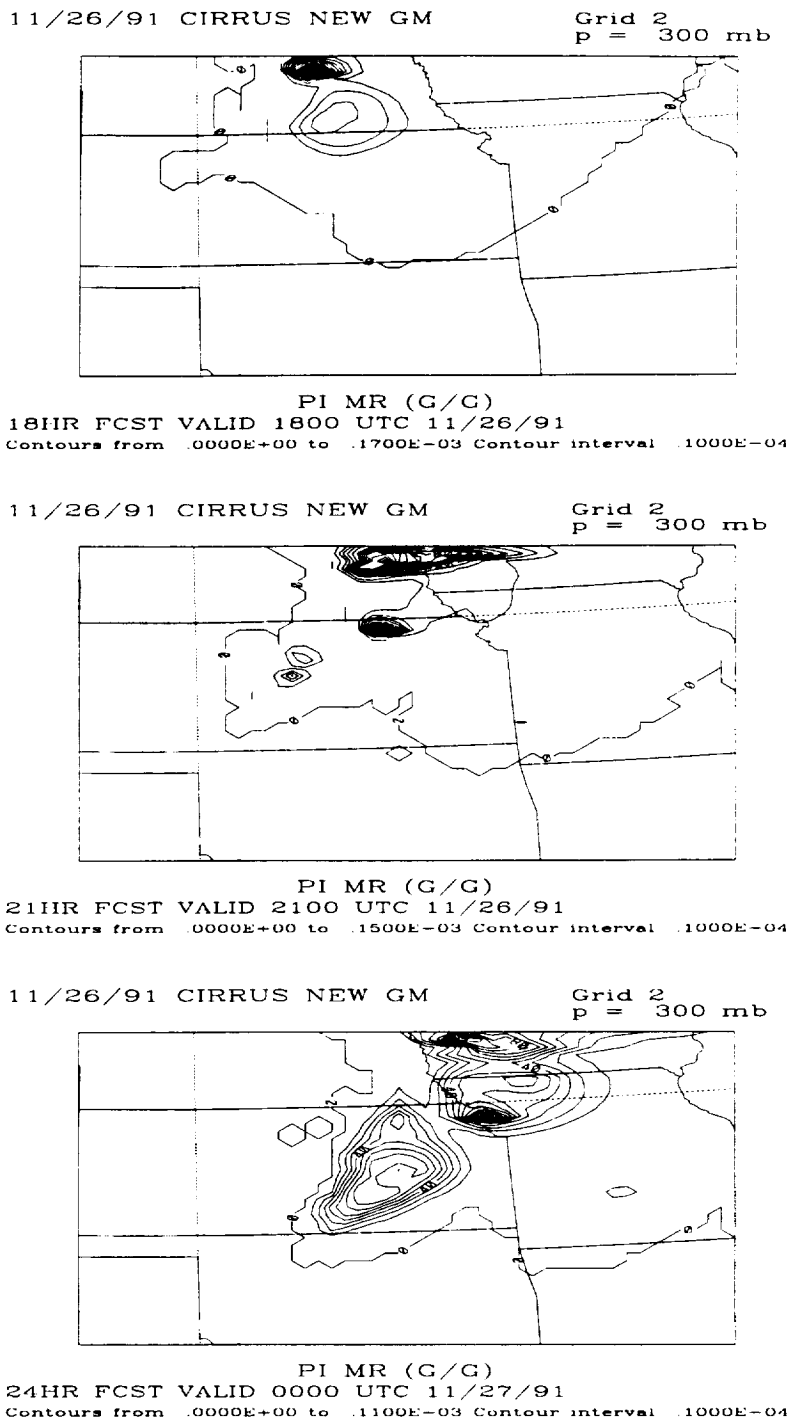

Figure 3.17: Model predicted 300 mb pristine ice mixing ratio at 1800 UTC, 2100 UTC of the November 26, and 0000 UTC of the November 27, 1991.

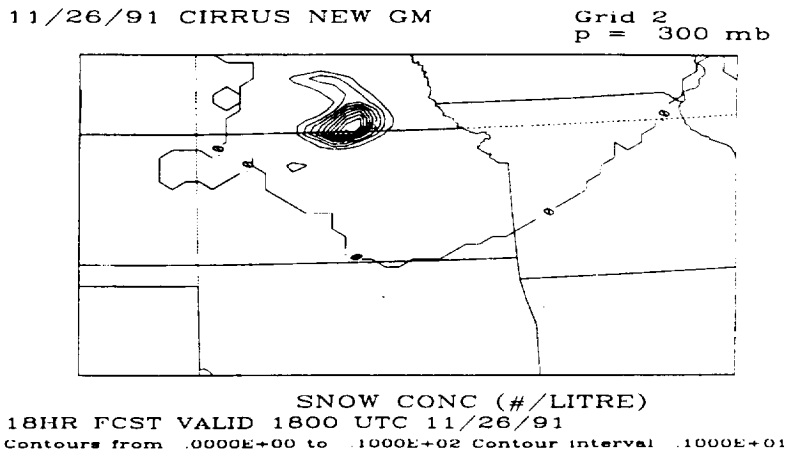

Figure 3.18: Model predicted 300 mb snow number concentration at 1800 UTC, 2100 UTC of the November 26, and 0000 UTC of the November 27, 1991.

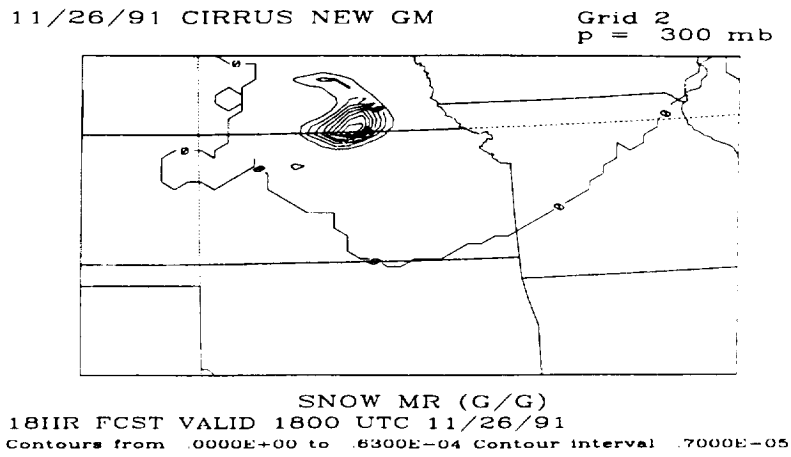

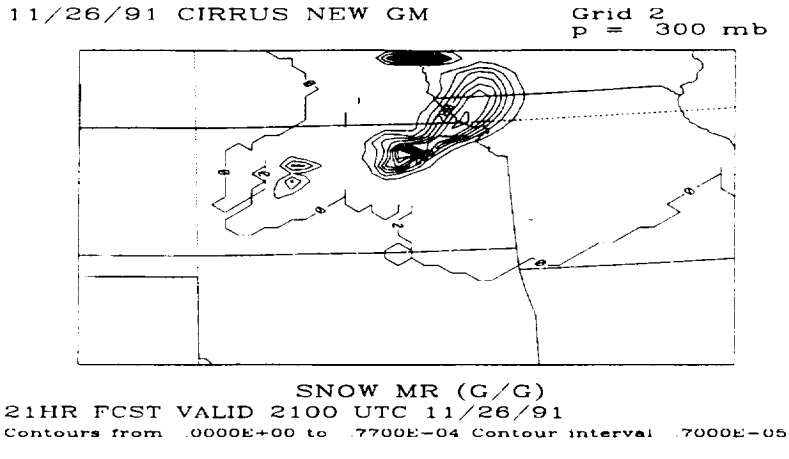

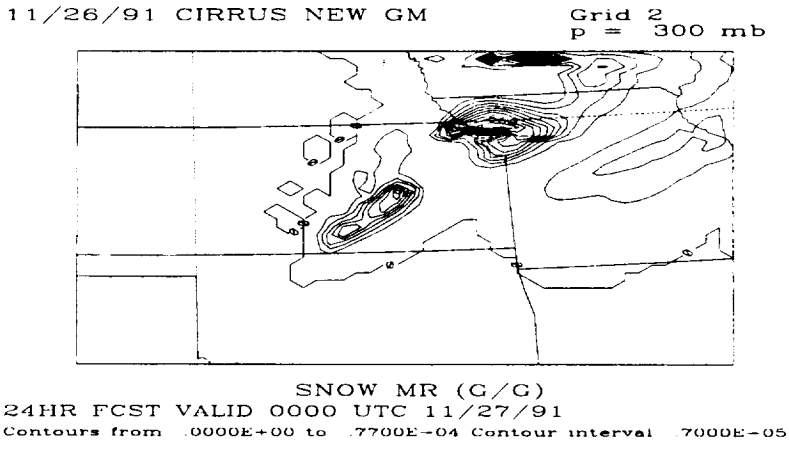

Figure 3.19: Model predicted 300 mb snow mixing ratio at 1800 UTC, 2100 UTC of the November 26, and 0000 UTC of the November 27, 1991.

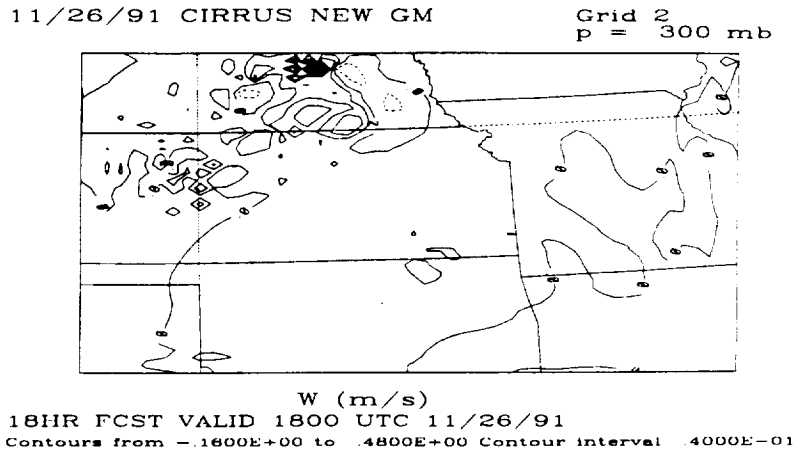

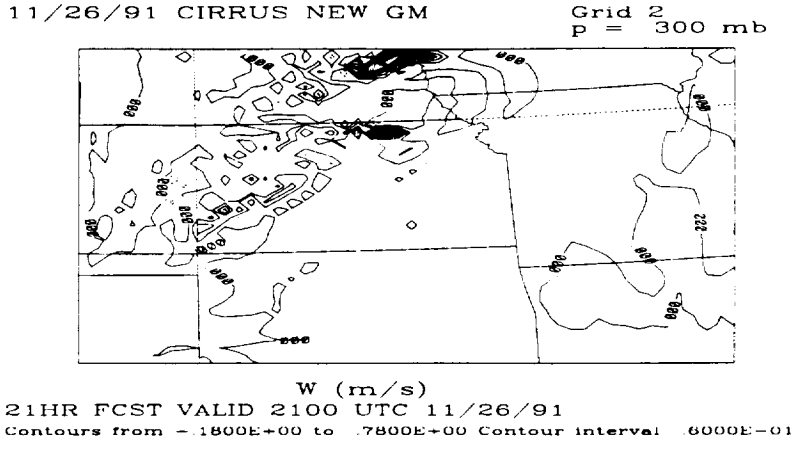

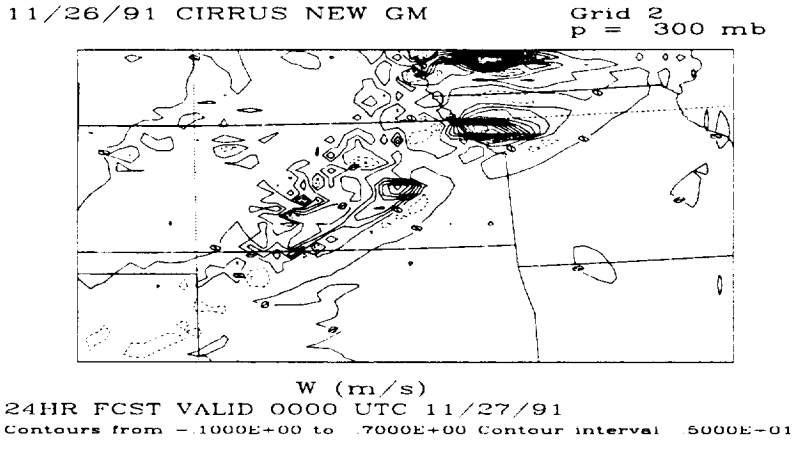

Figure 3.20: Model predicted 300 mb vertical velocity fields at 1800 UTC, 2100 UTC of the November 26, and 0000 UTC of the November 27, 1991.

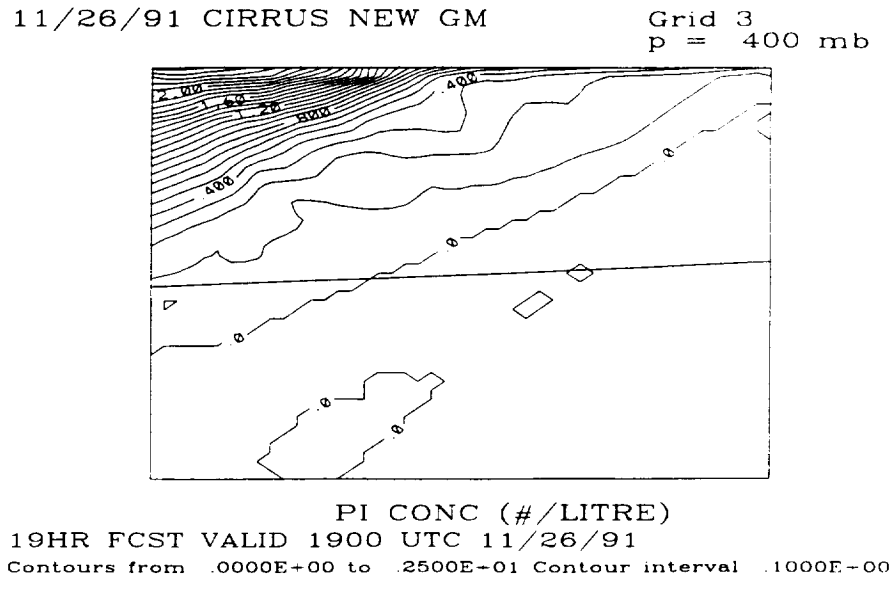

Figure 3.21: Model predicted 400 mb pristine ice number concentration at 1900 UTC on Grid #3 for Case a (top) and Case b (bottom).

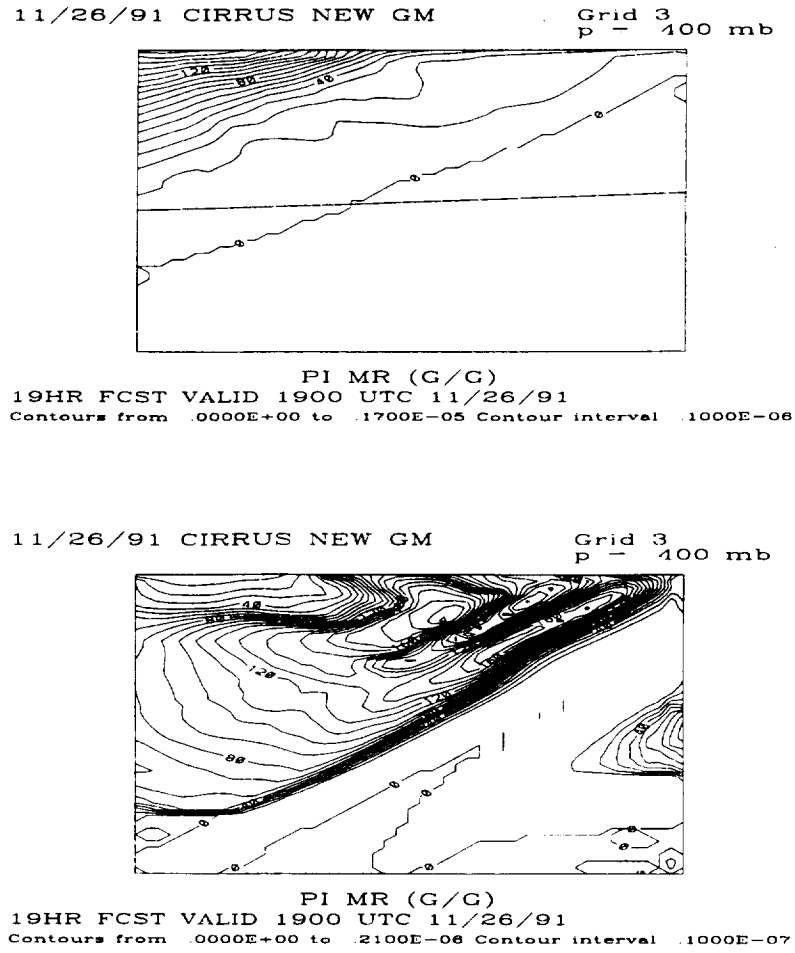

Figure 3.22: Model predicted 400 mb pristine ice mixing ratio at 1900 UTC on Grid #3 for Case a (top) and Case b (bottom).

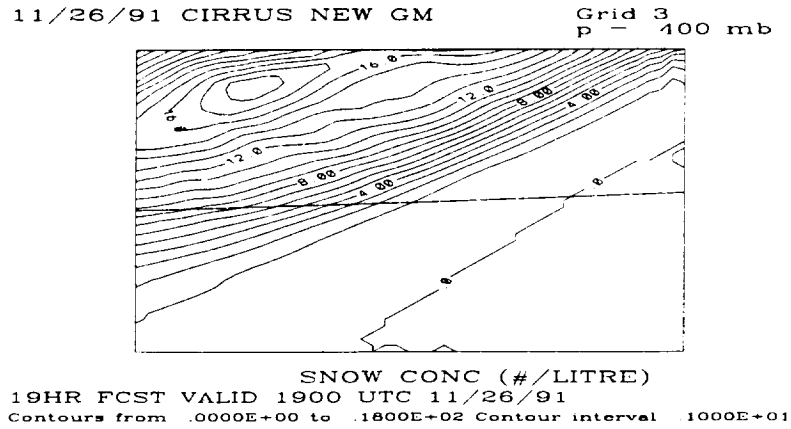

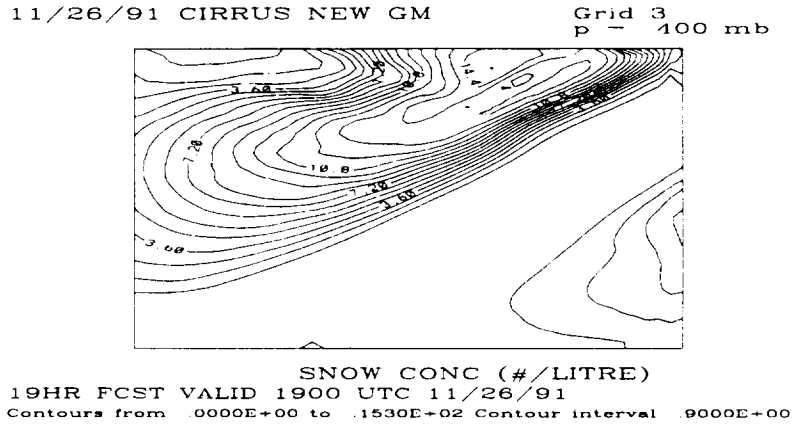

Figure 3.23: Model predicted 400 mb snow number concentration at 1900 UTC on Grid #3 for Case a (top) and Case b (bottom).

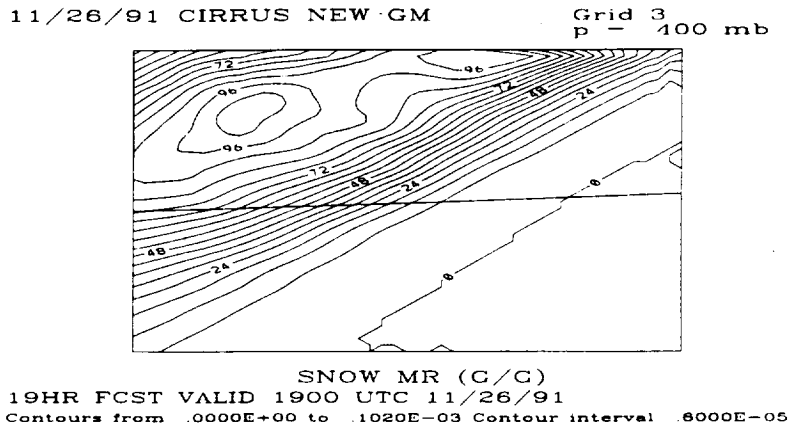

Figure 3.24: Model predicted 400 mb snow mixing ratio at 1900 UTC on Grid #3 for Case a (top) and Case b (bottom).

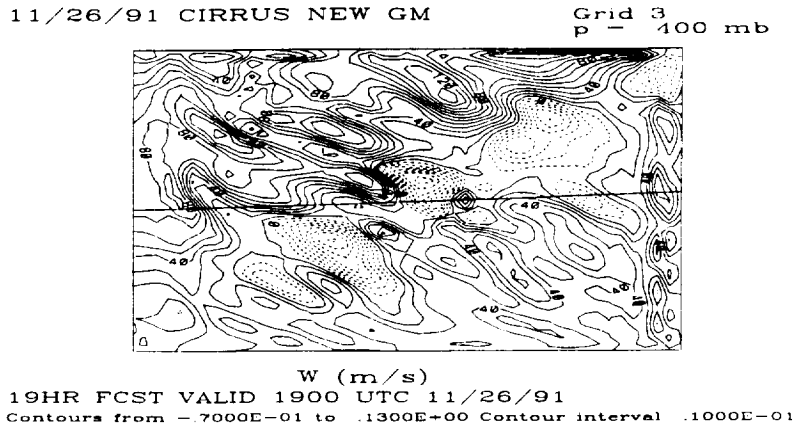

Figure 3.25: Model predicted 400 mb vertical velocity fields at 1900 UTC on Grid #3 for Case a (top) and Case b (bottom).

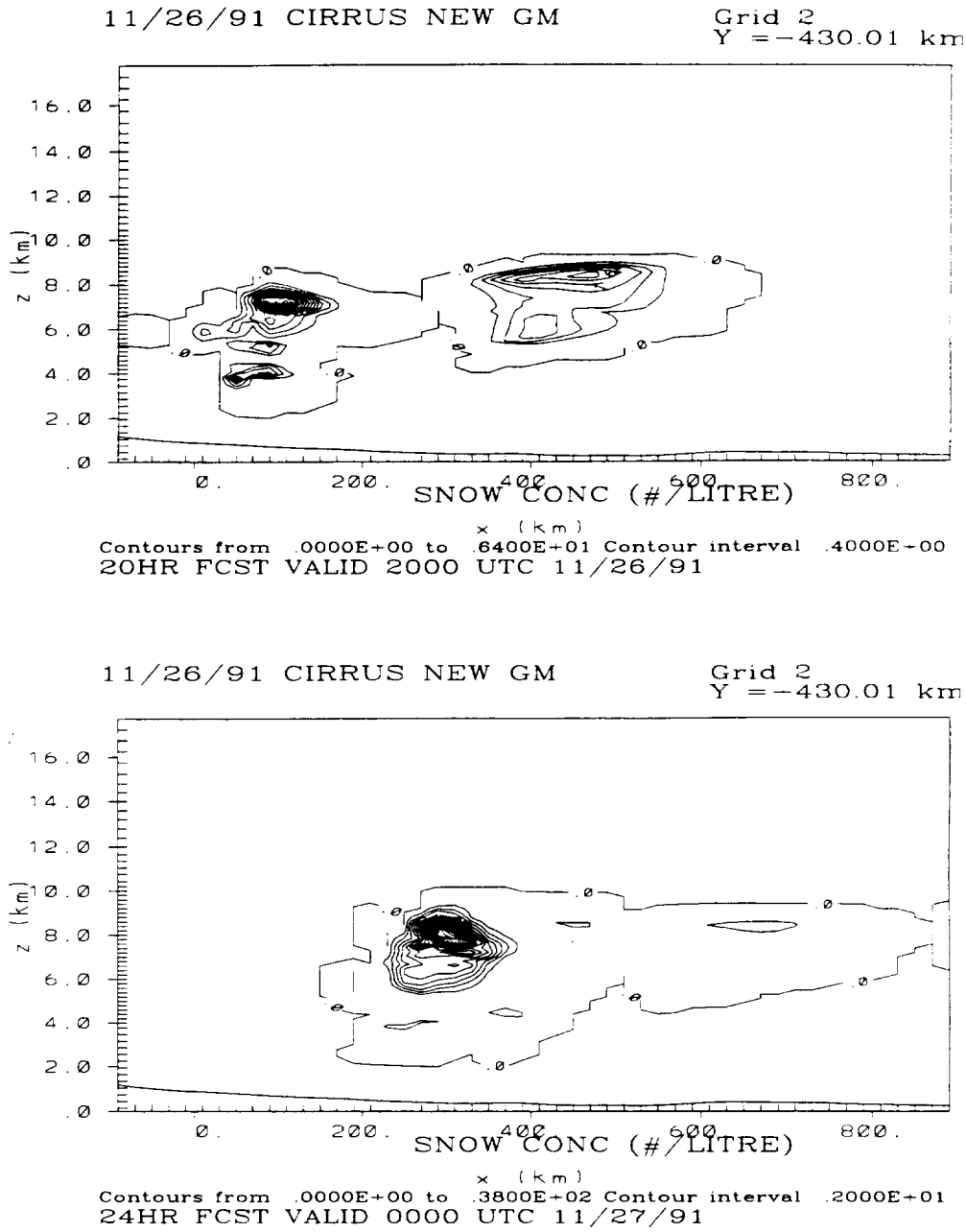

Figure 3.26: Model predicted snow concentrations at 2000 UTC (top) of the November 26 and 0000 UTC of the November 27, 1991. Coffeyville, Kansas is located at about 500 km along the horizontal coordinate.

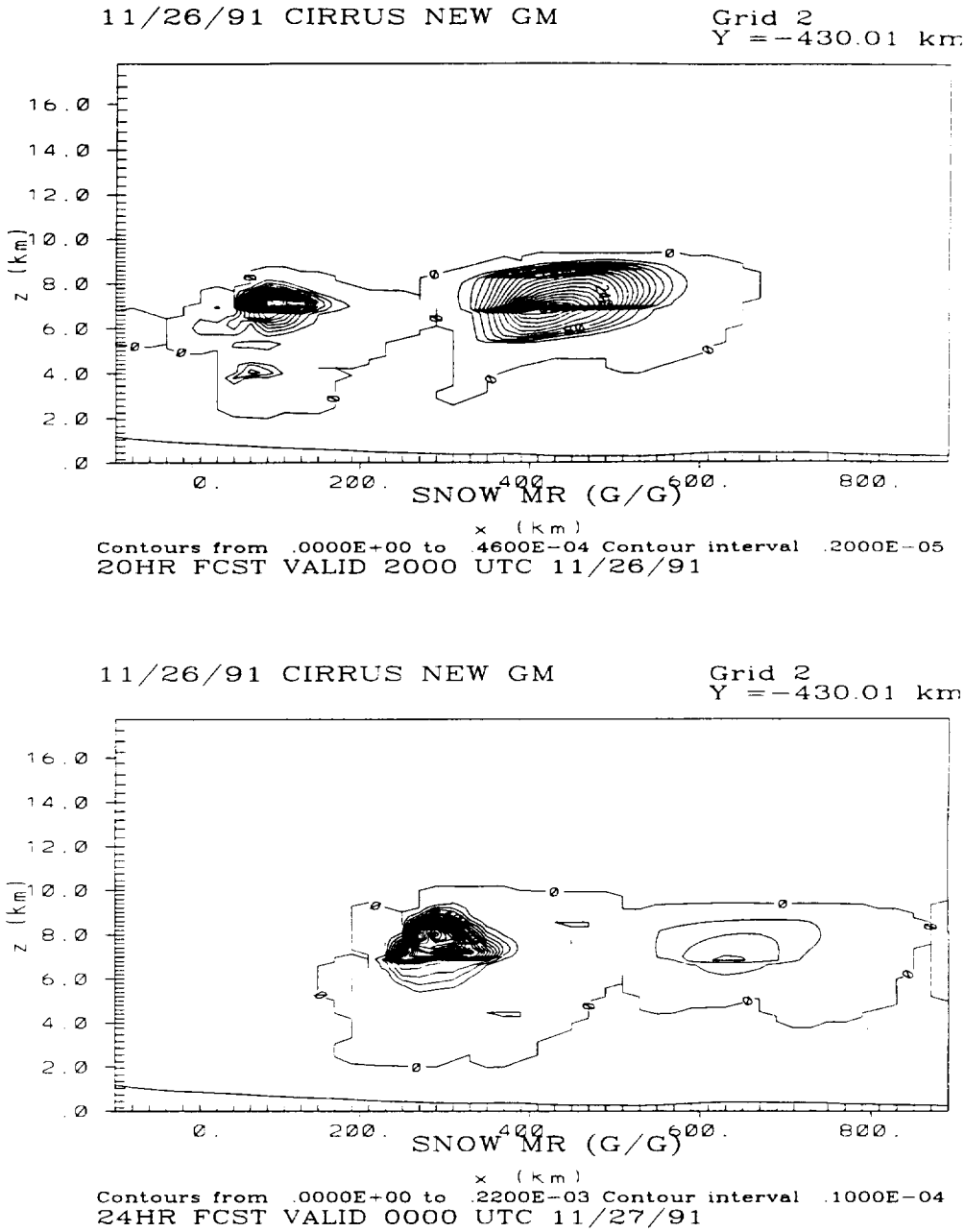

Figure 3.27: Model predicted snow mixing ratios at 2000 UTC (top) of the November 26 and 0000 UTC of the November 27, 1991. Coffeyville, Kansas is located at about 500 km along the horizontal coordinate.

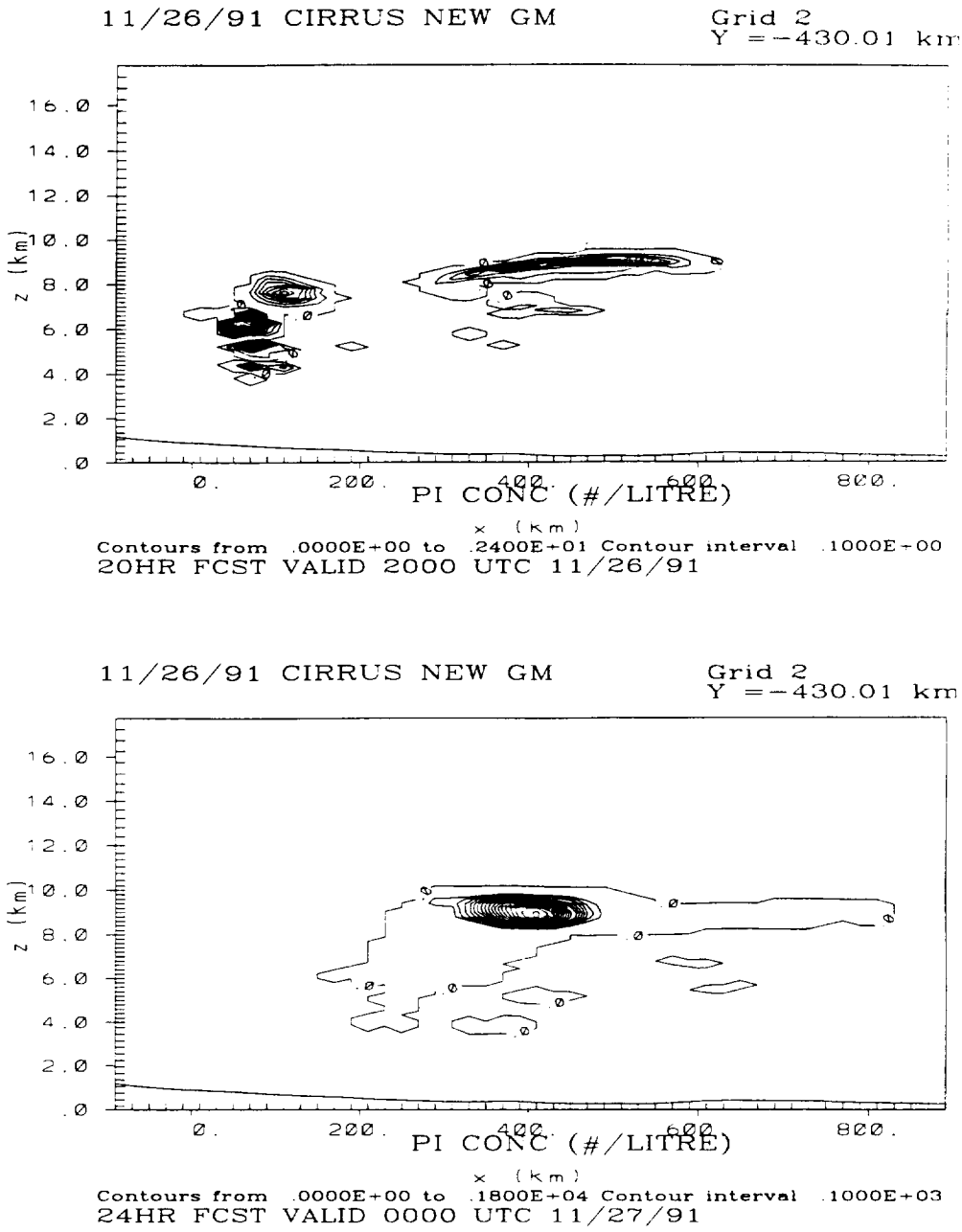

Figure 3.28: Model predicted pristine ice concentrations at 2000 UTC (top) of the November 26 and 0000 UTC of the November 27, 1991. Coffeyville, Kansas is located at about 500 km along the horizontal coordinate.

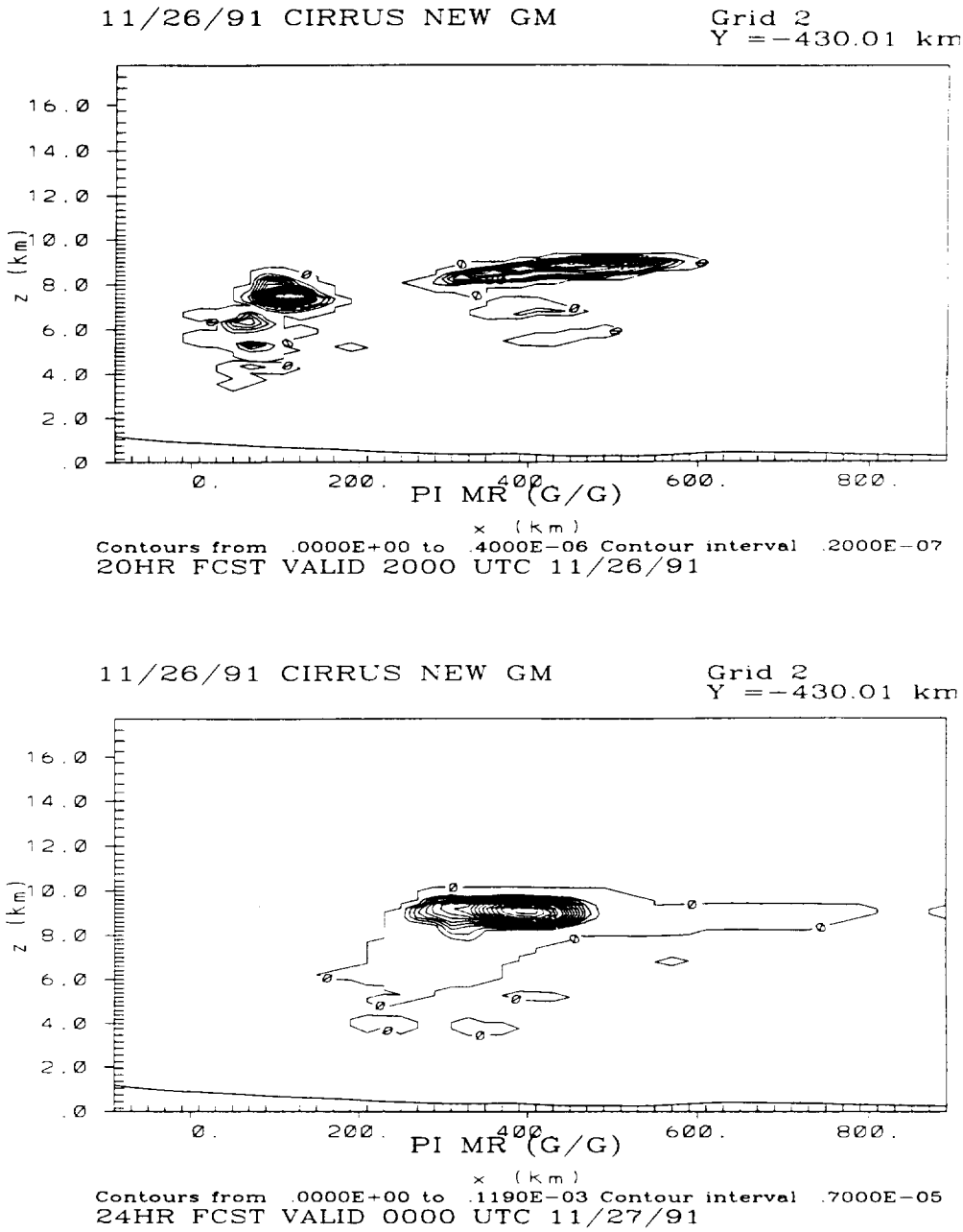

Figure 3.29: Model predicted pristine ice mixing ratios at 2000 UTC (top) of the November 26 and 0000 UTC of the November 27, 1991. Coffeyville, Kansas is located at about 500 km along the horizontal coordinate.

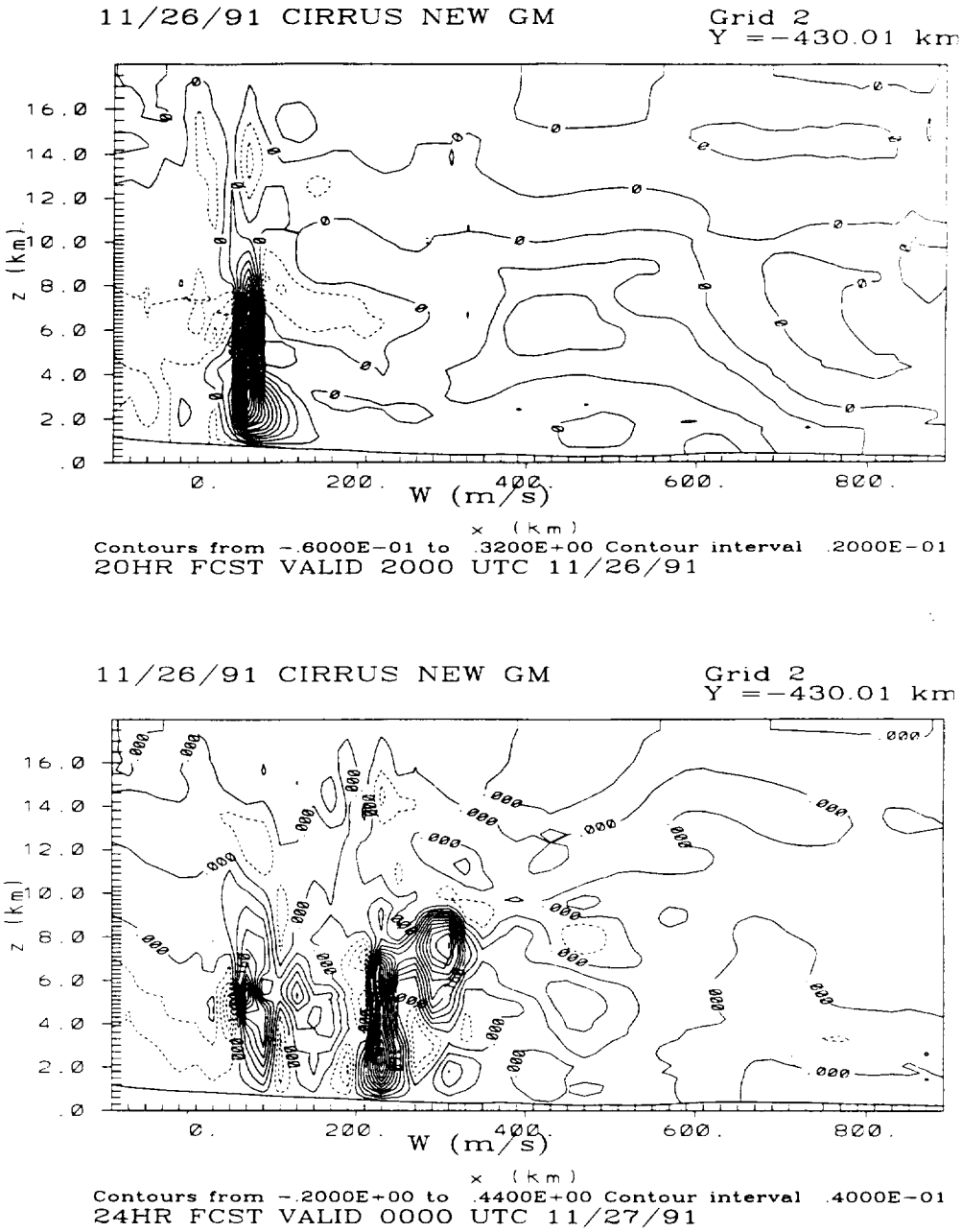

Figure 3.30: East-west cross sectional plots of the model predicted vertical velocity at 2000 UTC (top) of the November 26 and 0000 UTC of the November 27, 1991. Coffeyville, Kansas is located at about 500 km along the horizontal coordinate.

Chapter 4

LARGE- EDDY SIMULATIONS (LES) OF THE 26 NOVEMBER 1991 FIRE II CIRRUS CASE

The mesoscale modeling study of the November 26, 1991 cirrus event discussed in Chapter 3 is encouraging. LES studies of this event is a necessary continuition of this research towards the goal of understanding the dynamic, microphysical, and radiative processes occurring within midlatitude cirrus clouds. This chapter is dedicated to LES studies of this cirrus event. The LES model will be described in the first part of this chapter, while the last part of this chapter will be devoted to the discussion of two LES simulations.

4.1 The subgrid-scale (SGS) model

The LES model inherits the framework of RAMS version 3b. However, it includes a new radiation scheme developed by Harrington (1997). It also includes a new subgrid scale model developed by Branko (1996) at the University of Colorado.

The subgrid-scale (SGS) model needs to be addressed because the subgrid-scale parameterization represents a critical component of a successful large-eddy simulation. The commonly used linear SGS models result in erroneous mean velocity profiles in simulations of neutrally and stably stratified atmospheric boundary layers (Branko, 1996). In addition, linear models are absolutely dissipative resulting in relaminarization of the flows subjected to strong stable stratification (Branko, 1996). Since cirrus clouds in midlatitudes are generally associated with a stably stratified and strongly sheared atmospheric environment, we feel that Branko's SGS model, which is capable of reproducing the backscatter of energy as well as the effects of SGS anisotropy characteristics for shear-driven flows, is more suitable for this study.

According to Branko (1996)'s nonlinear model, the SGS stress is defined as

$$M_{ij} = -(C_s\Delta)^2\{2(2S_{mn}S_{mn})^{0.5}S_{ij} + C_1(S_{ik}S_{kj} - \frac{1}{3}S_{mn}S_{mn}\delta_{ij}) + C_2(S_{ik}\Omega_{kj} - \Omega_{ik}S_{kj})\} \tag{4.1}$$

where C_s is the traditional Smagorinsky constant which is defined as

$$C_s = (\frac{8(1+C_B)}{27\pi^2})^{0.5} \tag{4.2}$$

δ_{ij} is the Kronecker Delta (a scalar quantity which is equal to 1 when $i = j$ and 0 otherwise), and Δ is the length scale which is related to the grid-cell size (Moeng, 1984) and is defined as

$$\Delta = (\Delta x * \Delta y * \Delta z)^{\frac{1}{3}} \tag{4.3}$$

where Δx, Δy, and Δz are the grid sizes in x, y, and z directions, respectively.

Branko suggested that

$$C_B = 0.36 \tag{4.4}$$

In equation (4.1), S_{ij} and Ω_{ij} are strain rate tensors which are defined as

$$S_{ij} = \frac{1}{2}(\frac{\partial u_i}{\partial x_j} + \frac{\partial u_j}{\partial x_i}) \tag{4.5}$$

$$\Omega_{ij} = \frac{1}{2}(\frac{\partial u_i}{\partial x_j} - \frac{\partial u_j}{\partial x_i}) \tag{4.6}$$

where u_i and u_j are the model resolved wind components.

The nonlinear model parameters C_1 and C_2 are determined so that the model provides correct energy transfer and captures the normal stress effects observed in sheared flows. The following values for C_1 and C_2 are suggested by Branko (1996)

$$C_1 = \frac{31C_B}{7(1+C_B)S(k_c)} \tag{4.7}$$

$$S(k_c) = 0.5, C1 = C2 \tag{4.8}$$

This SGS model is implemented into RAMS. However, simulation tests show that the above suggested values for C_1 and C_2 are not appropriate because they can cause computational instability, even if smaller time steps are used. In stead, smaller values are used throughout this research.

4.2 Nudging LES model

Generally, horizontally homogeneous initialization is used in large-eddy simulation because of the small horizontal model domain. For this research, since the LES study is an extension of the mesoscale modeling studies, information from the mesoscale simulations is communicated with the LES grid domain as much as possible. Nudging the LES model is implemented into RAMS.

Nudging in this study takes the following form

$$u(k,i,j,t) = u(k,i,j,t-1) + (model - forcing - terms) + G * (u_{obs}(k) - \bar{u}(k,t-1)) \tag{4.9}$$

where $u(k,i,j,t)$ is the model predicted u value at the end of the current timestep, $u(k,i,j,t-1)$ is the model u value at the end of the previous timestep, model- forcing terms include advection, diffusion, buoyancy, etc., u_{obs} is the wind field being nudged to and is a function of the vertical index k, $\bar{u}(k,t-1)$ is the horizontal average of u at the end of the previous timestep, and G is the nudging factor which is related to nudging time scale. Because the nudging contribution is artificial, it must not be a dominant term in the governing equations and should be scaled by the slowest physical adjustment process in the model. By the way, using $\bar{u}$ instead of u avoids nudging out the fine scale features developed in the LES.

To do nudging, u_{obs} is calculated from the mesoscale simulation outputs by using a linear interpolation method. In this study, nudging is done for the three-dimensional wind components (u, v, and w), perturbation Exner function (π'), perturbation ice- liquid-water

potential temperature (θ'_{il}), and total water mixing ratio (r_t). Also, nudging is only done to the model boundaries with the boundary grid points used in nudging being user specified. For this study, a value of 5 is specified. This means that nudging is applied to the 5 outer grid points of the model domain.

4.3 Initialization and boundary conditions

The LES model is initialized using a sounding taken from the mesoscale simulations discussed in Chapter 3. The sounding profiles used in the LES studies are shown in Figure 4.1. One of these two soundings is taken from the shallow cloud band near the leading edge of the mesoscale simulated cirrus cloud system, while the other sounding is taken from a deep cloud layer in the northwest of the mesoscale simulated cloud. As discussed in the previous chapters, observations have shown that the leading edge of the observed cloud system was composed of a shallow, high cloud layer and the cloud layer to the northwest of the leading edge was deep with middle-level cloud underneath the highest cirrus cloud. The two LES runs to be discussed in this chapter are designed to simulate the dynamic, microphysical, and radiative processes in both shallow and deep ice cloud systems in order to obtain greater insight into the dynamics and physics of the observed cirrus cloud event.

A much finer grid mesh is used: $\Delta x = \Delta y = 150m$. Δz is used as a variable ranging from 50 (within the cloud layer from 6 to 10 km) to 400 m (near the surface). The model has a horizontal domain of $6 \times 6km^2$ and a vertical domain of 11.4 km (115 vertical levels, see Table 4.1). The horizontal boundary conditions are cyclic. The model top is a rigid lid with a Rayleigh friction layer applied to prevent gravity- wave reflection from the upper boundary. The lower surface, which is not as important for cirrus clouds as it is for convective storms, is a material surface across which fluxes of heat, moisture, and momentum are solved following a theory proposed by Louis (1979).

4.4 LES results: Case 1-A Shallow Cloud System

0.0	400.0	800.0	1200.0	1600.0	2000.0
2400.0	2800.0	3200.0	3500.0	3800.0	4100.0
4400.0	4600.0	4800.0	5000.0	5100.0	5200.0
5300.0	5400.0	5500.0	5600.0	5700.0	5800.0
5900.0	6000.0	6050.0	6100.0	6150.0	6200.0
6250.0	6300.0	6350.0	6400.0	6450.0	6500.0
6550.0	6600.0	6650.0	6700.0	6750.0	6800.0
6850.0	6900.0	6950.0	7000.0	7050.0	7100.0
7150.0	7200.0	7250.0	7300.0	7350.0	7400.0
7450.0	7500.0	7550.0	7600.0	7650.0	7700.0
7750.0	7800.0	7850.0	7900.0	7950.0	8000.0
8050.0	8100.0	8150.0	8200.0	8250.0	8300.0
8350.0	8400.0	8450.0	8500.0	8550.0	8600.0
8650.0	8700.0	8750.0	8800.0	8850.0	8900.0
8950.0	9000.0	9050.0	9100.0	9150.0	9200.0
9250.0	9300.0	9350.0	9400.0	9450.0	9500.0
9550.0	9600.0	9650.0	9700.0	9750.0	9800.0
9850.0	9900.0	9950.0	10000.0	10100.0	10200.0
10300.0	10400.0	10600.0	10800.0	11000.0	11200.0
11400.0					

Table 4.1: Vertical levels used in the LES (in m).

4.4.1 Simulation Overview

This 3D LES (Case 1) covered a two-hour simulation period which is initialized with a sounding taken at 1700 UTC of the November 26, 1991 (top panel, Figure 4.1). Snapshots of the vertical cross sections (at $X = -0.08km$) of PI number concentration, snow number concentration, and vertical velocity at 1730, 1800, and 1900 UTC are shown in Figures 4.2 through 4.4. The predicted cloud system has an apparent single cloud layer, even though some secondary peaks in both PI and snow fields are discernible. Both particle number concentration and mixing ratio are higher near the cloud top levels than in the levels below. The maximum PI concentration, PI mixing ratio, snow concentration, and snow mixing ratio are about $0.6litre^{-1}$, $2.1 \times 10^{-4}g/kg$, $0.12litre^{-1}$, and $8.0 \times 10^{-4}g/kg$, respectively.

As can be seen from the plots of vertical velocity (Figure 4.4), the cloud system is quite turbulent with cells of upward and downward activity. The horizontal sizes of the cells are found to be ranging from less than 1 km to as large as 3.5 km. Vertical sizes of the cells are generally less than 1 km. The larger horizontal widths for these cloud cells (shown as cloud bands in the horizontal cross sections) may imply that the cloud system is modulated dominantly by both shear-driven turbulence and by gravity-wave dynamics. These sizes of embedded cells are similar to those found in observational studies (Gultepe et al., 1995).

Horizontally averaged total water mixing ratio (r_t), ice- water mixing ratio (r_{ice}), ice-liquid-water potential temperature (θ_{il}), and potential temperature (θ) at 30 and 60 minutes into the simulation are shown in Figures 4.5 and 4.6. It is seen that, as simulation time goes on from 30 to 60 minutes, the profiles of r_t, θ_{il}, and θ stay nearly the same because the cloud system is inactive and sedimentation which can modify the profiles of r_t as well as θ_{il} is not a significant factor. A single layer of high ice water mixing ratio is predicted just below 9000 m level, with a depth of slightly more than 500 m. The maximum horizontally- averaged ice water mixing ratio is on the order of $1.0 \times 10^{-4}g/kg$ throughout the simulation. Corresponding to the single cloud layer, the profiles of θ_{il} and θ indicate a near neutral layer of about 1 km deep between 7 and 8 km levels.

4.4.2 Statistical Analyses

Vertical profiles of horizontally averaged turbulent kinetic energy (TKE) at 30, 60, and 120 minutes of the simulation time are shown in Figure 4.7. Associated with cloud development, the cloud layer is more turbulent in the early stage with a peak TKE of slightly less than $0.003m^2s^{-2}$. The TKE decreases as the cloud evolves into its mature stage. By the end of the simulation, the maximum horizontally averaged TKE within the cloud layer is only about $0.0012m^2s^{-2}$.

Profiles of momentum, ice-liquid water potential temperature (θ_{il}), and total water mixing ratio (r_t) fluxes are shown in Figures 4.8 through 4.11. As can be expected, fluxes of these quantities assume complex profiles because cirrus clouds have generally complicated internal structure, also because of the complicated processes involved in the exchanges of these quantities near the top and the bottom boundaries of the cirrus cloud system. There are varieties of peaks and local minimums of fluxes within the cloud layer, indicating decoupling, gravity-wave activities (to be discussed later), and intermittent turbulence possibly generated by local shear. Since the environmental atmosphere for Case 1 is stable, turbulence in this environment is generally intermittent and only indirectly related to the fluxes occurring near the top and bottom boundaries of the cloud system (Mahrt, 1985). It is worth pointing out that fluxes of these quantities near the top (about $9km$) and bottom (at about $5.5km$) of the cloud system can be larger or smaller than that within the cloud layer, indicating that the complicated entrainment and detrainment processes involved are of great significance in this case. The W momentum flux, $< W'W' >$, which is considered a measure of eddy strength, is strongly related to turbulent activities. The strong radiative cooling near cloud top can be responsible for the development of a stronger downdraft which is seen by comparing the central and bottom panels of Figure 4.4. The radiative effect combined with the gravity wave dynamics results in vigorous cloud scale circulations deep in the cloud layer which can be observed in the vertical profiles of $< W'W' >$ as is indicated by the peak near $7.5km$ above the ground.

Infrared radiative cooling throughout the whole cloud layer is largely compensated by solar warming effect, resulting in a maximum cooling of only about $1.2Kday^{-1}$ near the

cloud top (Figures 4.12 and 4.13). The fine ripple structure in the radiative heating rate profiles corresponds to the non-uniform cloud development. The bottom panels of these two figures also show that both solar and infrared optical depths peak at about $8.5km$ where the maximum number concentration of ice particles is predicted. Below this level, τ is much smaller because of the smaller ice particle number concentration and mixing ratio.

In Figure 4.14, vertical profiles of the horizontally averaged heating rates due to total radiative processes and latent heat release associated with phase change of water are shown for Case 1. The latent heating rates are peaked at mainly three different levels, implying development of layered cloud structure commonly observed within cirrus clouds, especially *forced passive cirrus* (to be discussed below). The overall latent heating rate in the cloud system is much smaller in absolute magnitude than that of radiative cooling effect. No obvious net evaporation at any level is seen in this case during the first 2-hour simulation time. The net radiative heating is much stronger throughout most part of the cloud system than latent heating, indicating that this cirrus case is dominantly driven by radiation. Strong radiative cooling is found through most of the cloud layer with a shallow radiative warming layer centered at about $5.2km$.

4.4.3 Probability Density Function (PDF) of w

Since the vertical velocity distribution is critical in the parameterization of cloud-scale physics for large-scale models, such as a general circulation model (GCM), the LES study is used to determine the PDF of w. According to mathematical definition, if $P(w)dw$ is the probability of w in the interval from w to $w + dw$, then for continuous w spectrum, the following integration must be satisfied

$$\int_0^\infty P(w)dw = 1 \tag{4.10}$$

Since the LES model domain contains discrete grid boxes, the following definition of $P(w)$ (PDF of w) can be used to evaluate the model- predicted distribution of vertical velocities (Mitrescu, 1998)

$$P(w) = \frac{dN(w)}{dV\,dw} \tag{4.11}$$

where $dN(w)$ represents the number of grid cells which have vertical velocities in the interval between w and $w + dw$, dV is the total number of grid cells within the model domain, and dw is the sampling threshold. In this study, dw has a value of $0.05ms^{-1}$.

Figures 4.15 and 4.16 show the PDFs at 5400, 7700, and 9100 m AGL at 30 and 60 minutes into the simulation. It is apparent that the PDFs for this simulation are quite consistent throughout the cloud layer with most of the model- predicted vertical velocities falling into a narrow w band between $-0.1ms^{-1}$ and $0.05ms^{-1}$. This is because the TKE level for this cloud system is very low, vertical variation of TKE has no significant impact on the variation of PDFs. Also, it is clearly seen in these Figures that the PDFs follow an approximate normal distribution throughout the cloud system.

4.5 LES results: Case 2-A Deep Cloud System

4.5.1 Simulation Overview

The two-hour 3D LES for Case 2 is initialized with a sounding taken at 1930 UTC. As stated above, the sounding used in this simulation is taken from a deep and active cloud layer predicted from the mesoscale simulation.

Active cells are seen in the vertical cross sectional plots along $X = -0.08km$ (Figures 4.17 through 4.19). Generally, the cells which, in fact, are horizontal bands as are seen in the horizontal cross sections (not shown), have widths less than 2 km in the horizontal and less than 1.5 km in the vertical. This range of the cell sizes is comparable to the results reported in Gultepe et al. (1995). The comparable horizontal widths and vertical sizes for the bands may indicate that the eddies are more buoyancy- driven than shear driven. Also, the horizontal banded structures may indicate that gravity wave dynamics is involved in the formation and evolution of the cloud system. A deep cloud system extending from 3.9 to about 9 km is simulated at 2130 UTC. A two-layer vertical cloud structure is identified at the later stage of the simulation. This compares nicely with the observations which indicated that this cloud system was composed of high cirrus with middle-level cloud underneath the highest cirrus layer. The top cloud layer which centered at about 8 km has larger amounts of PI particles (both in number and mass), while larger snow particle

number and mass are associated with the lower cloud layer which has its bottom boundary at as low as 3.5 km above the ground.

The maximum PI particles nucleated at the early stage of the simulation is $500 litre^{-1}$. The PI mixing ratio over the course of the simulation is $1.8 \times 10^{-2} g/kg$. Snow particle number concentrations are generally less than $20 litre^{-1}$ and snow mixing ratios are as large as $1.08 \times 10^{-1} g/kg$. The predicted vertical air velocities along this cross section range from $-2.0 ms^{-1}$ to $1.1 ms^{-1}$. This also compares very well with the available observations.

Shown in Figures 4.20 and 4.21 are the vertical profiles of r_t, r_{ice}, θ_{il}, and θ at 30 and 60 minutes into the simulation. As expected, r_t generally decreases with height, even though its profile is slightly modified due to the existence of condensate in the cloud. r_{ice} profiles display two distinct cloud layers with the top cirrus layer containing less total ice than in the layer below. The two-layer cloud structure indicates that the model performs very well in predicting the desired cloud system because as stated above, this case is designed to simulate the observed deep cloud system which had a middle-level cloud layer underneath the highest cirrus. The maximum total ice for the middle-level cloud layer is slightly less than $0.1 g/kg$ at 60 minutes into the simulation. An unstable layer can be identified in the θ profile. This unstable layer must be responsible for the active turbulent eddies predicted in this case.

4.5.2 Statistical Analyses

The TKE profiles in Figure 4.22 show that turbulent eddies are more active in Case 2 than in Case 1. The maximum TKE at one hour into the simulation is about $0.55 m^2 s^{-2}$ which is nearly 200 times of the maximum value predicted in Case 1. As simulation time goes on, transport of TKE both upward and downward can be clearly identified.

As can be deduced from Figures 4.23 and 4.24, eddies in this case are more active than in Case 1. $< W'W' >$ has a peak value of slightly more than $0.1 m^2/s^2$ at 60 minutes into the simulation. This may be compared to the corresponding $< W'W' >$ for Case 1 shown in Figure 4.8. Except for the significant difference in the absolute peak values in the fluxes between Case 1 and Case 2, the very small (near zero) momentum fluxes near the top and bottom boundaries of the cirrus cloud system may indicate that

contributions from entrainment and detrainment processes are not comparable to the eddy transport and mixing within the cloud system for this case. The fine structures at the later stage of the simulation demonstrate that the eddy transport and mixing are decoupled in the vertical after the cloud is well developed. This may also be a good indication of the development of layered cloud structure as discussed above. Consistent with the momentum flux profiles, total water mixing ratio (r_t) flux near the cloud top is close to zero. The very small downward flux of r_t near the cloud bottom boundary may be related to the weak precipitation process (see Figures 4.25 and 4.26).

Similar to what is seen in Case 1, infrared cooling dominates over solar warming, resulting in net radiative cooling in most part of the cloud system (Figures 4.27 and 4.28). The maximum net cooling near the cloud top is about three times as large as what is found in Case 1. However, below $8km$, net radiative cooling or warming is very small. Because a large number of small ice particles are suspended near the cloud top, both τ_{solar} and $\tau_{infrared}$ are peaked at $8.5km$ above the surface.

Vertical profiles of the total radiative and latent heating rates are shown in Figure 4.29. These profiles may be compared to the corresponding profiles for Case 1 shown in Figure 4.14. The change in scale of the horizontal axis between these two figures demonstrates that latent heating release plays a much more significant role in Case 2 than in Case 1. The maximum latent heating rate of about $0.85K/hr$ in the early stage of the cloud development is more than two orders larger than that for Case 1 (only about $0.05K/hr$). Two regions of net diffusional growth match nicely to the two cloud layers described above. A patch of net evaporation can be found between the two cloud layers after about one hour into the simulation. After all, net latent heating overwhelms the net radiative effect in the cloud development. Latent heat release can destablize the cloud layer, resulting in formation of convective cells which are very effective in transporting momentum, heat, and moisture. By the end of the simulation, net radiative cooling dominates the cloud top region at a maximum rate of about $3.36Kday^{-1}$ and the bottom levels of the cloud are dominated by net evaporation, even though strong latent heating is still present in the top cloud layer.

4.5.3 PDFs of w

LES- predicted PDFs of w for this case demonstrate distinct features which are not found in Case 1. It is shown in Figures 4.30 and 4.31 that in the middle-cloud level (at 7700 m), corresponding to active turbulent motions deep in the cloud system PDF demonstrates a wider distribution than both below and above. Even though the PDFs near cloud base and top follow an approximate normal distribution with a single peak near $w = 0$, multiple peaks are found in the PDF at the middle cloud levels. It should be pointed out that the wide PDF distribution deep in the cloud system must be modulated by buoyancy driven turbulent activities because the cloud layer between 7200 and 8500 m levels is unstable, especially in the early stage of the simulation. At the early stage of the simulation, the PDF at the middle cloud level covers an even wider w spectrum in the downward motion regime than that calculated in the later simulation stage. Although the PDF spectrum at the middle cloud levels narrows down later into the simulation, the multiple peaks and fine structures indicate that turbulent eddies are very active deep in the cloud system because both upward and downward motions are of nearly equal importance as can be seen in Figure 4.31.

4.6 Discussion and Summary

The LES model successfully simulates a single cloud layer for Case 1 and a two-layer cloud structure for Case 2. The simulated cirrus clouds display properties similar to that of the *forced boundary-Layer clouds* (Stull, 1985) because of the similarity in their dynamics, even though cirrus clouds generally have a much larger horizontal coverage than the *forced boundary-Layer clouds*. Mid-latitude cirrus clouds usually form in an stably- stratified environment with large scale forcing. In spite of the latent heat release during phase change, there is generally insufficient heating for cirrus clouds (such as the cloud predicted in Case 1) to become positively buoyant. Also, the strong inversion at the tropopause provides a lid to prevent cirrus clouds from development. As a result, the clouds behave as quasi-passive tracers of the top of the troposphere. This kind of cirrus cloud can be named *forced passive cirrus* in order to show its similarities to its boundary layer counterpart.

However, in some special cases such Case 2 discussed above, positively buoyant cells can be embedded in the cirrus layers. These cells are so active that the rising updraft induces its own pressure perturbations that affect the cloud evolution. This kind of cirrus can be classified as *forced active cirrus.*

The simulated Case 1 and Case 2 demonstrate that the cirrus cloud system can be modulated, to some extent, by gravity wave dynamics. Gravity waves can be the triggering mechanism for organized upward and downward motions. After the cloud formation, the evolution of the cloud system can be dominated by gravity wave dynamics, shear- driven turbulence which is common in cirrus level, and latent heat release associated with cloud formation and development.

The gravity waves are believed to be an important mechanism for transporting energy and momentum. The property of the gravity waves can be estimated based on pure internal gravity wave dynamics. As it is shown in dynamic meteorology (Holton, 1992), pure gravity waves are described according to the following relationships:

$$\hat{\nu} \equiv \nu - \bar{u}k = \pm Nk/(k^2 + m^2)^{1/2} \tag{4.12}$$

$$\hat{\nu} = \pm N cos\alpha, cos\alpha = \pm k/((k^2 + m^2)^{1/2} \tag{4.13}$$

where $\hat{\nu}$, the *intrinsic frequency*, is the frequency relative to the mean wind (ν is the wave frequency relative to the ground), N is the *buoyancy frequency* (or Brunt-Vaisala frequency), u is the horizontal mean wind, k and m are horizontal and vertical wave numbers, α is the angle of the phase lines to the local vertical, and the plus (minus) sign is to be taken for eastward (westward) phase propagation relative to the mean wind. The above relationships state that gravity wave frequencies must be less than the buoyancy frequency and that the tilt of phase lines for internal gravity waves depends only on the ratio of the wave frequency (Holton, 1992).

The above relationships can be used to estimate the wavelength and *intrinsic frequency* predicted in the simulations. As it is shown in the simulations (Figures 4.4 and 4.19),

the horizontal wavelengths are much larger than the vertical ones ($k \ll m$), the above relationships can be approximated as:

$$\hat{\nu} \equiv \nu - \bar{v}k = \pm Nk/m \tag{4.14}$$

$$\hat{\nu} = \pm N cos\alpha, cos\alpha = \pm L_z/L_y \tag{4.15}$$

where $\bar{v}$ is used to replace $\bar{u}$ in equation (4.12) to indicate that the wave analyses are done in the plane perpendicular to the x-axis of the model domain, L_z and L_y are the vertical and horizontal wavelengths.

For both Case 1 and Case 2, $|cos\alpha|$ can be approximated as 0.06 (the angle of the phase lines to the local vertical is approximately 86 to 87 degrees), meaning that the vertical wavelength is less than one tenth of the horizontal. For Case 1, $N \approx 0.010s^{-1}$ (model prediction at $z = 9000.0m$). According to the above relationships, the absolute value of the *intrinsic frequency* is only about $6.0 \times 10^{-4}s^{-1}$ for the gravity waves associated with Case 1. For Case 2, the absolute value of the *intrinsic frequency* is estimated to be $7.8 \times 10^{-4}s^{-1}$, corresponding to a slightly larger buoyancy frequency approximated at $0.013s^{-1}$ (also model prediction at $z = 9000.0m$).

Latent heat release can play a significant role in the formation and development of cirrus clouds (Figure 4.29). The release of latent heat can be an energy source for the development of upward motions which, in turn, can produce more supersaturation and cloud development. Vertical profiles of the total radiative and latent heating rates (Figures 4.14 and 4.29) indicate that for well developed, deep and active cirrus clouds radiative cooling and latent heating can be comparable on magnitude in the cloudy layer (see bottom panel, Figure 4.29). This implies that latent heating cannot be neglected in the construction of a cirrus cloud model, even though Lilly (1988) had reasonable success with his mixed-layer model in a study of anvil cirrus in which the latent heating effects were ignored. However, for shallow, optically- thin cirrus clouds, the latent heat release can be much smaller than the radiative cooling. In this case, the cloud development and evolution can be modulated dominantly by the radiative effects and the latent heat effects may be safely neglected in

cirrus cloud modeling. Generally, the LES studies in this research support Starr and Cox's model calculations (Starr and Cox, 1985) in which the authors showed that latent heating associated with depositional growth and sublimation of ice crystals can be a significant factor in modulating cirrus cloud evolution.

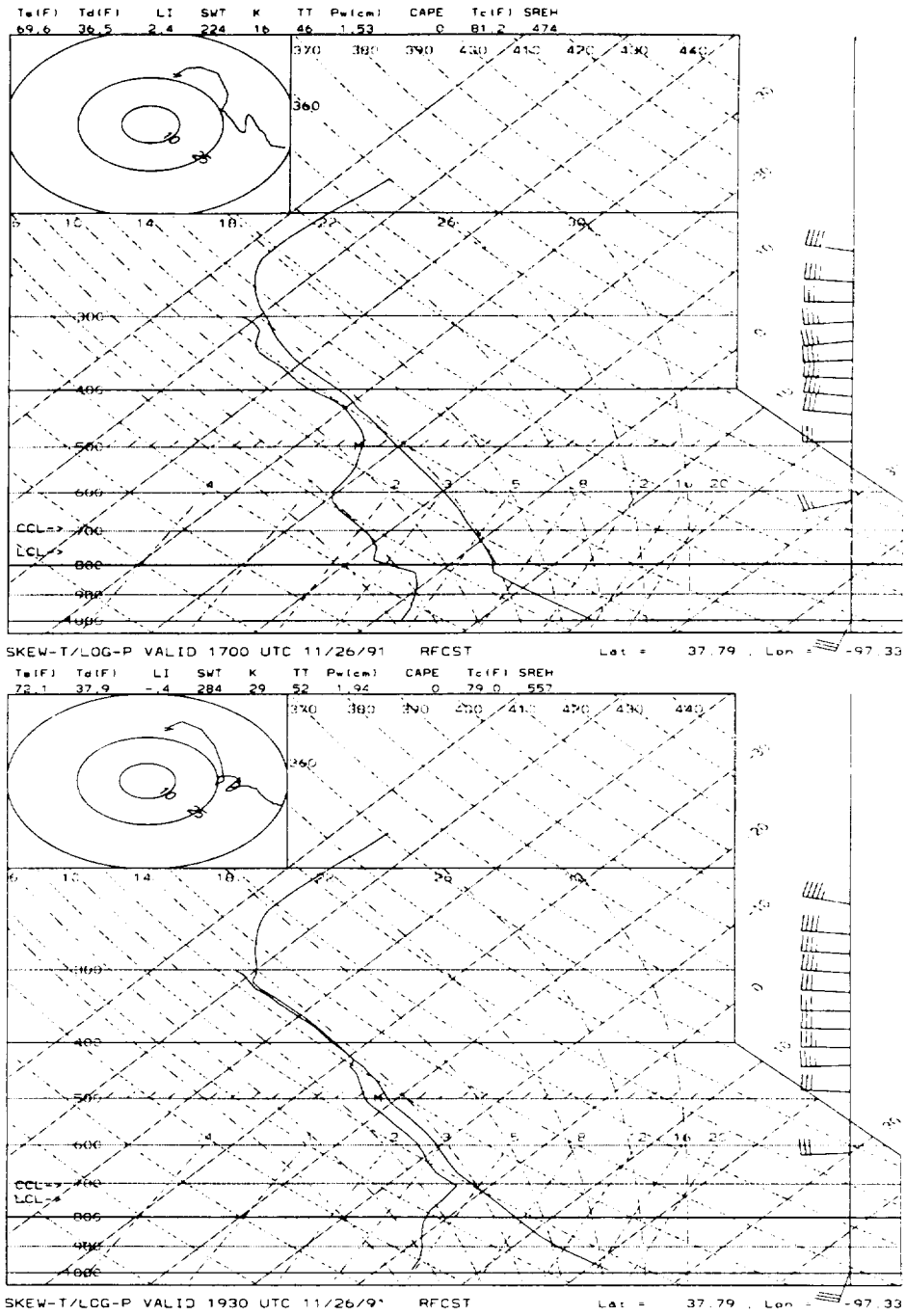

Figure 4.1: Soundings for the LES simulations. Top panel shows the sounding for Case 1, while bottom one shows that for Case 2.

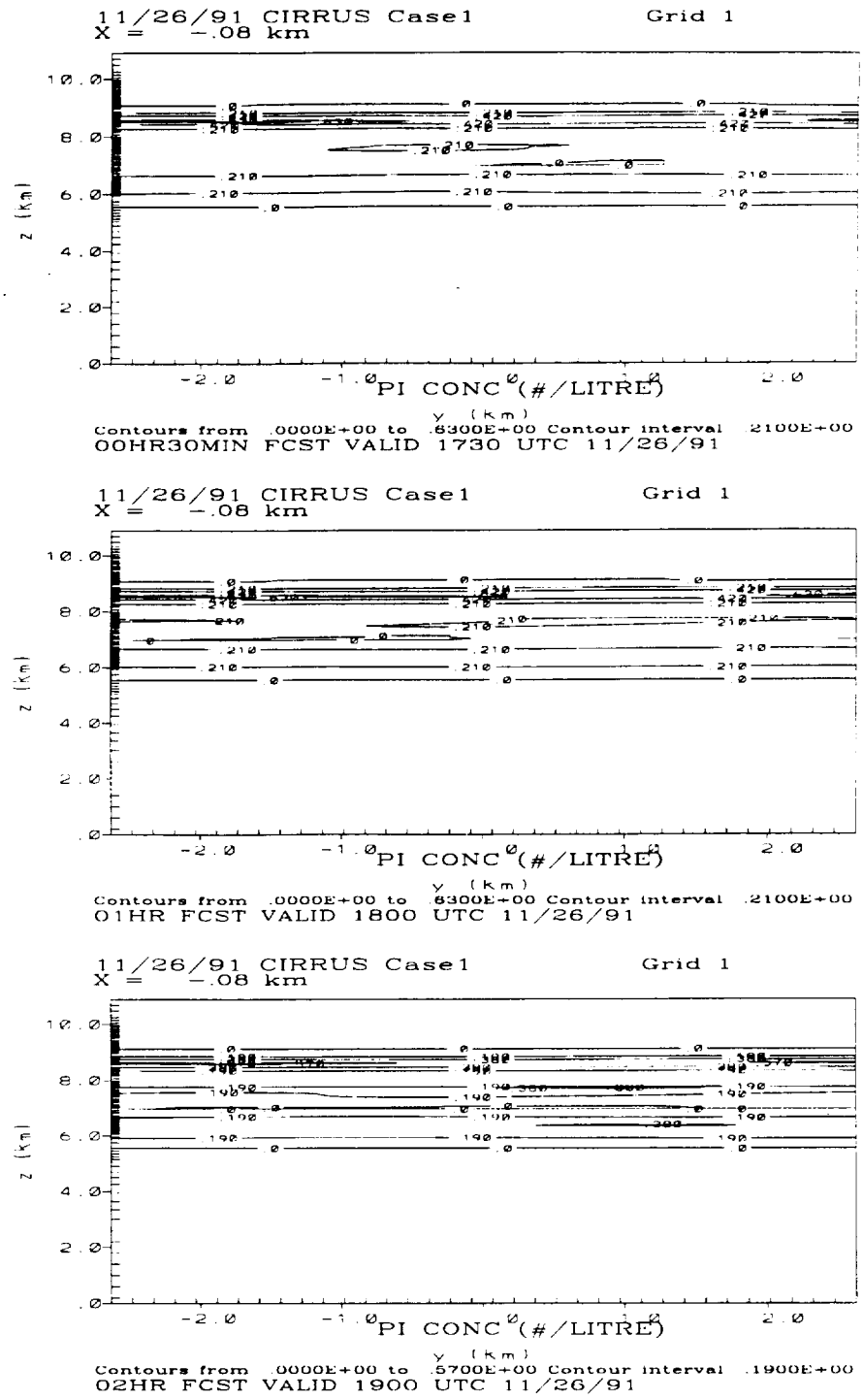

Figure 4.2: Vertical $y - z$ cross sections of pristine ice number concentration for Case1 at 1730, 1800, and 1900 UTC of the November 26, 1991.

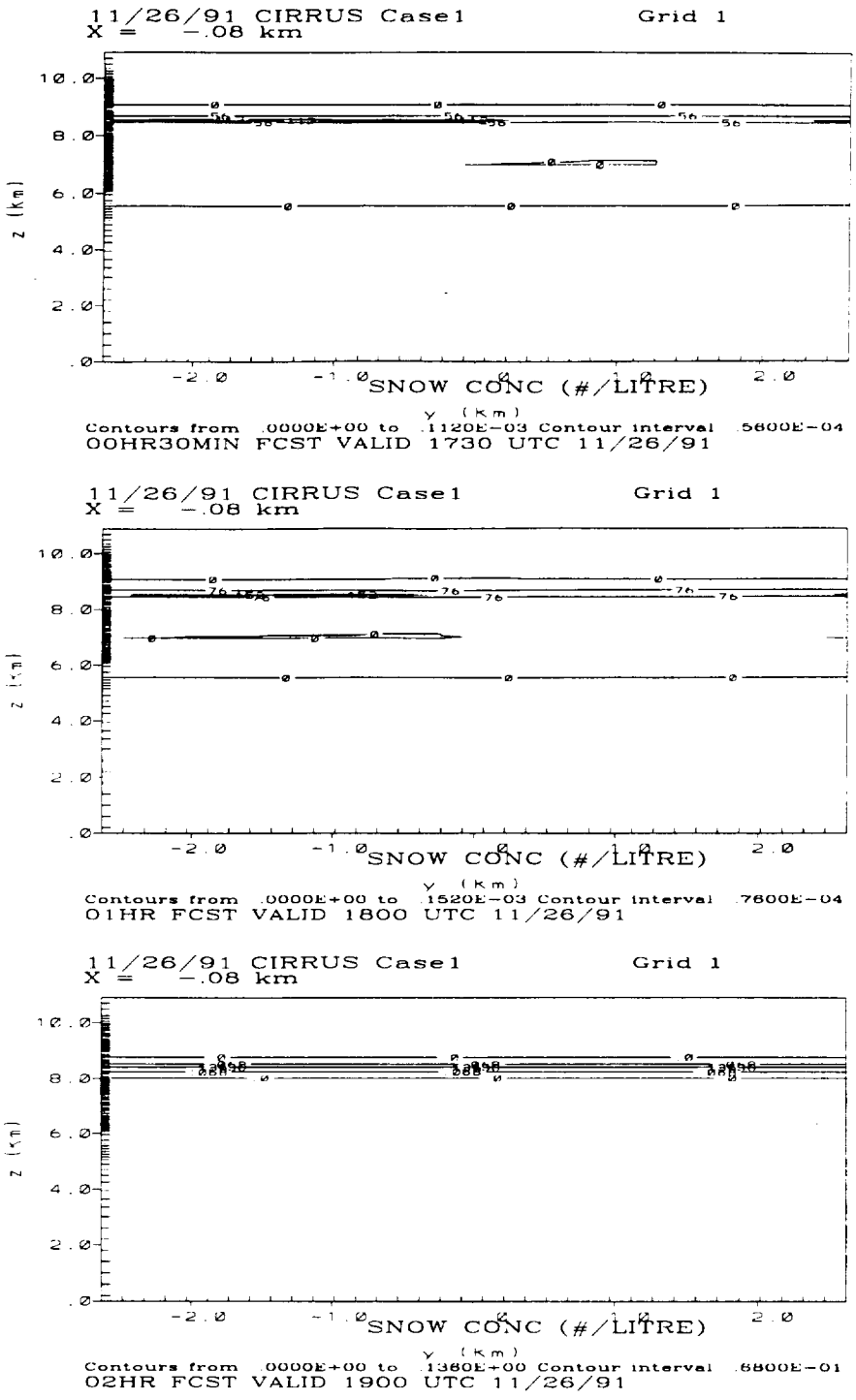

Figure 4.3: Vertical $y - z$ cross sections of snow particle number concentration for Case 1 at 1730, 1800, and 1900 UTC of the November 26, 1991.

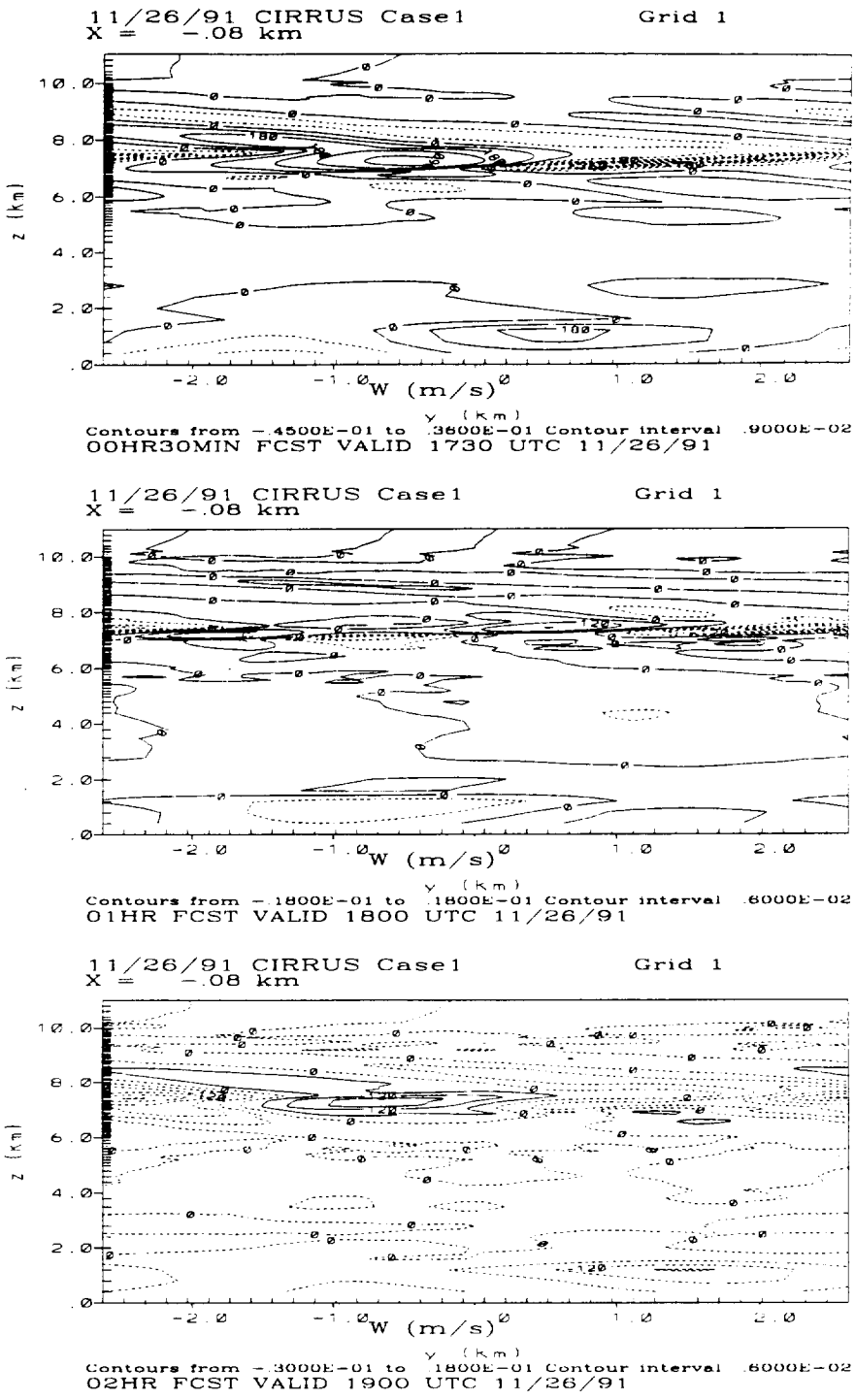

Figure 4.4: Vertical $y - z$ cross sections of vertical velocity for Case 1 at 1730, 1800, and 1900 UTC of the November 26, 1991.

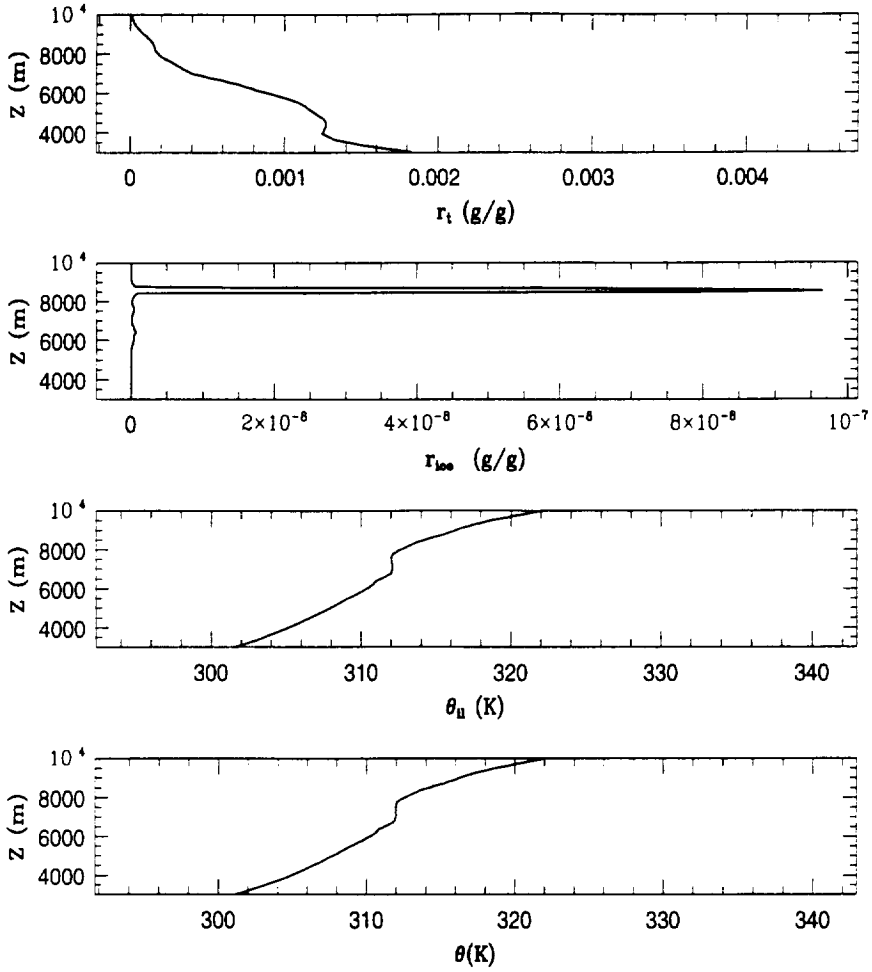

Figure 4.5: Profiles of horizontally- averaged r_t, r_{ice} (pristine ice + snow), θ_{il}, and θ at 30 minutes of simulation time for Case 1.

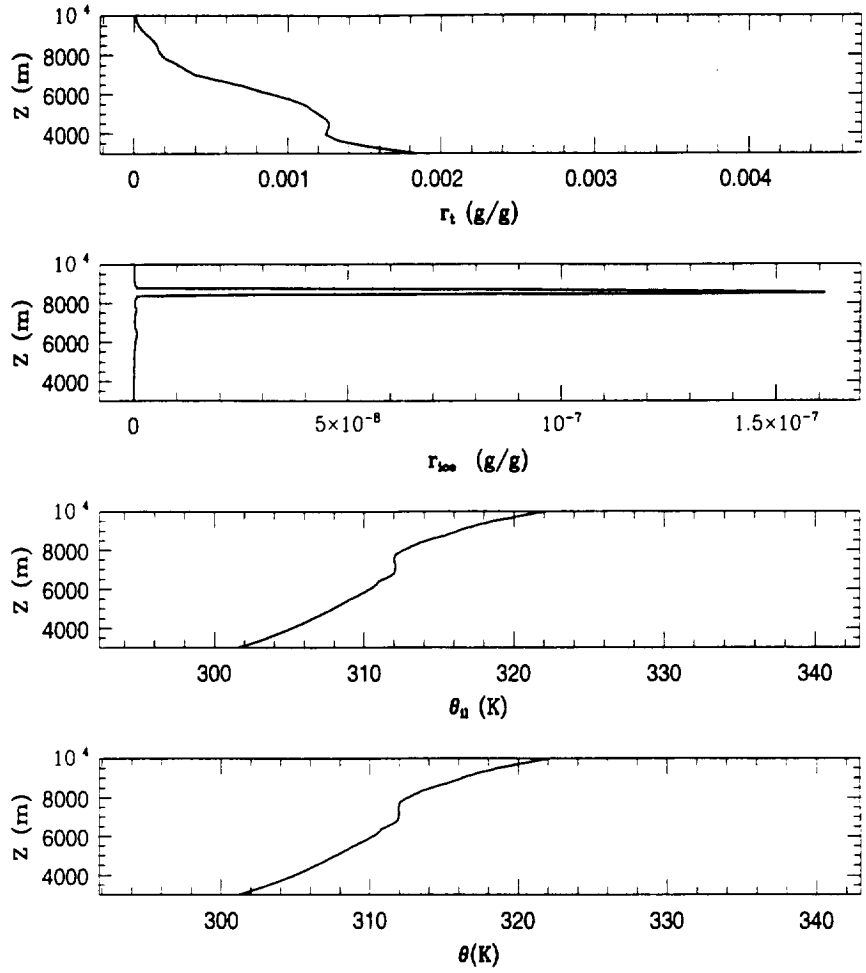

Figure 4.6: Profiles of horizontally- averaged r_t, r_{ice} (pristine ice +snow), θ_{il}, and θ at 60 minutes of simulation time for Case 1.

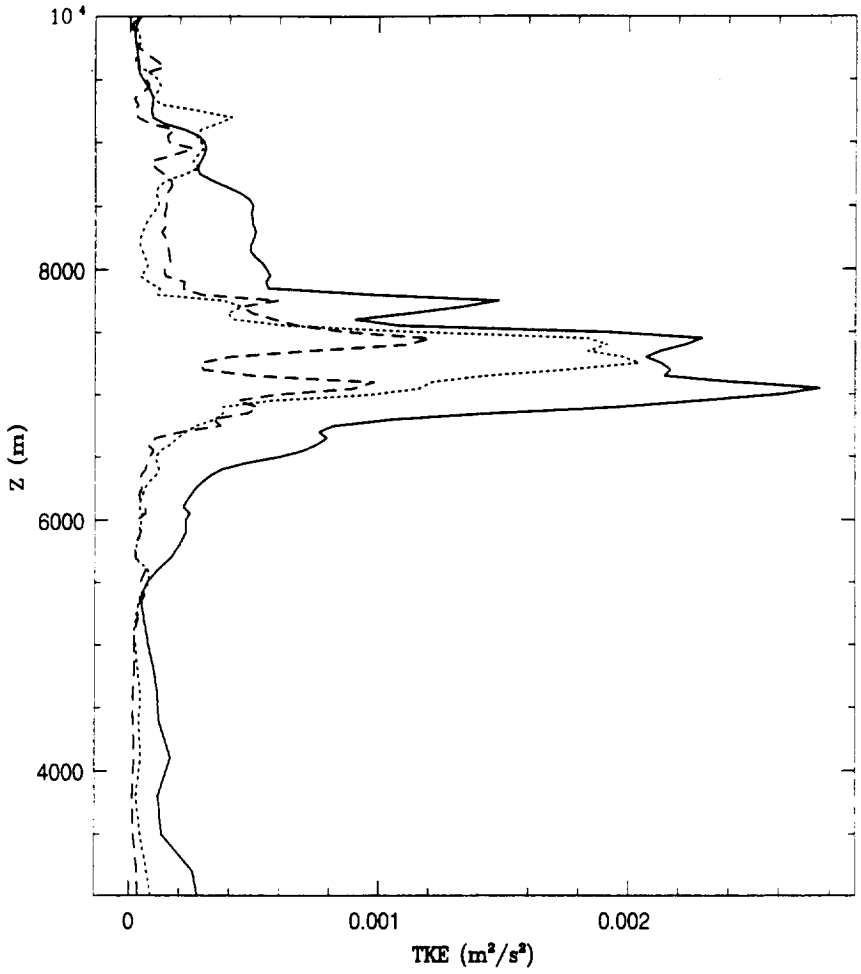

Figure 4.7: Profiles of horizontally averaged turbulent kinetic energy (TKE) at 30 (solid), 60 (dotted), and 120 minutes (dashed) into the simulation for Case 1.

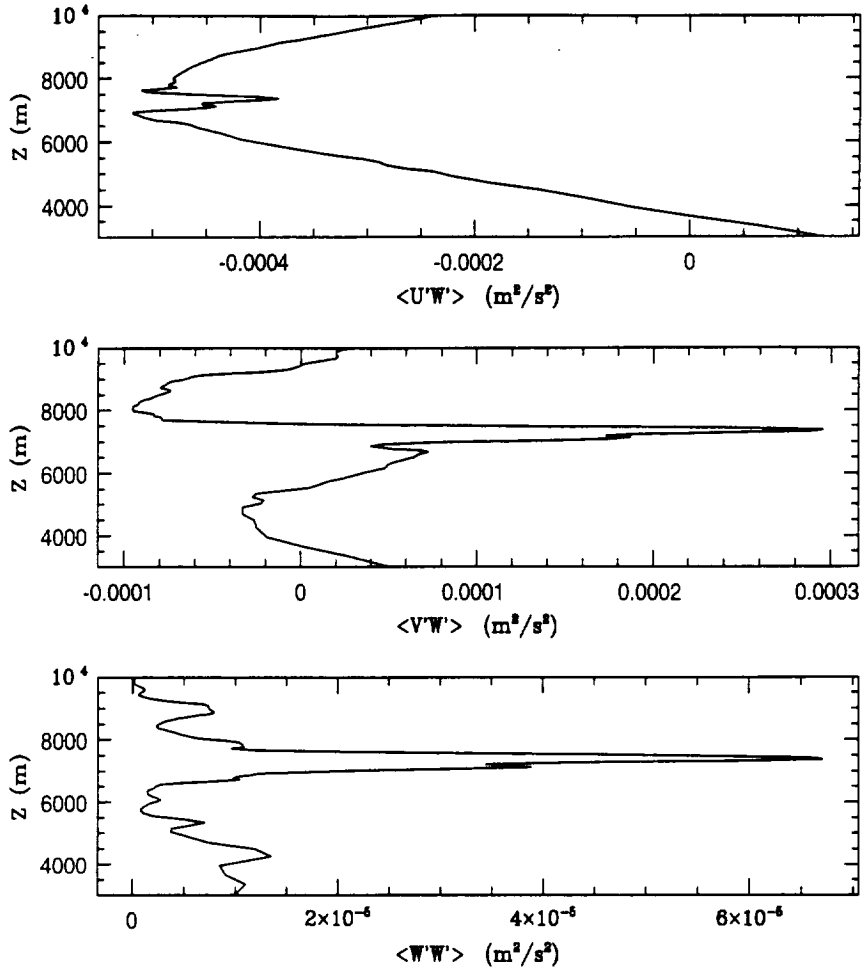

Figure 4.8: Momentum flux profiles at 60 minutes of simulation time for Case 1.

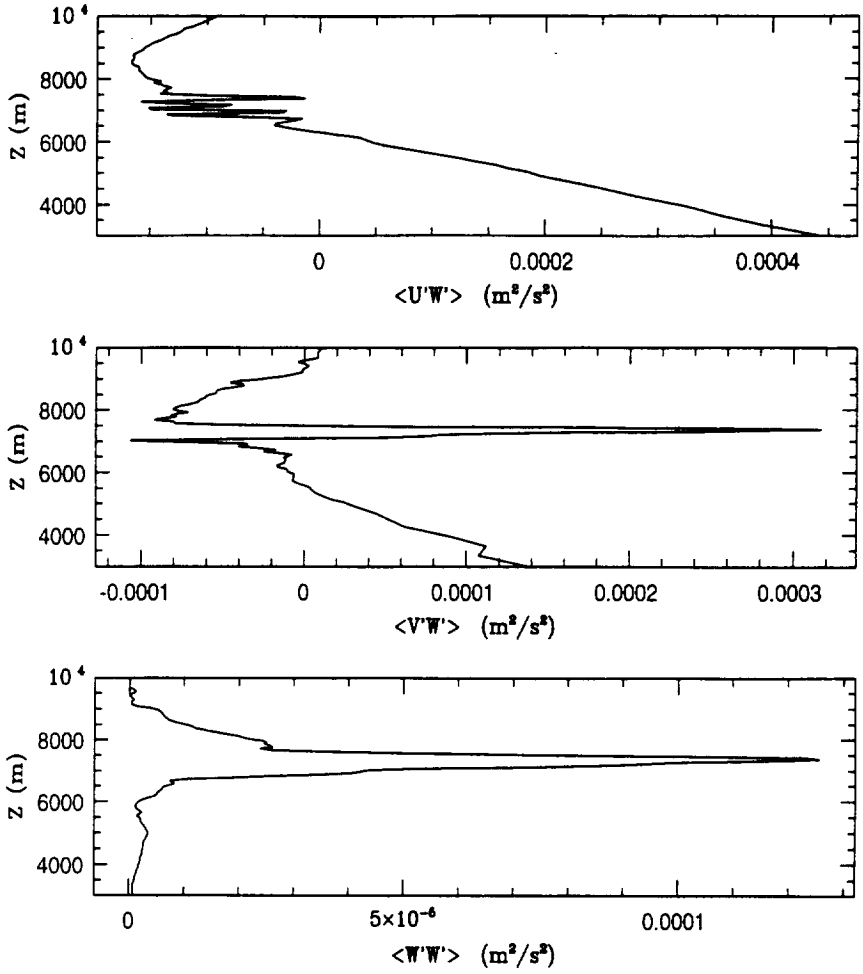

Figure 4.9: Momentum flux profiles at 2 hours of simulation time for Case 1.

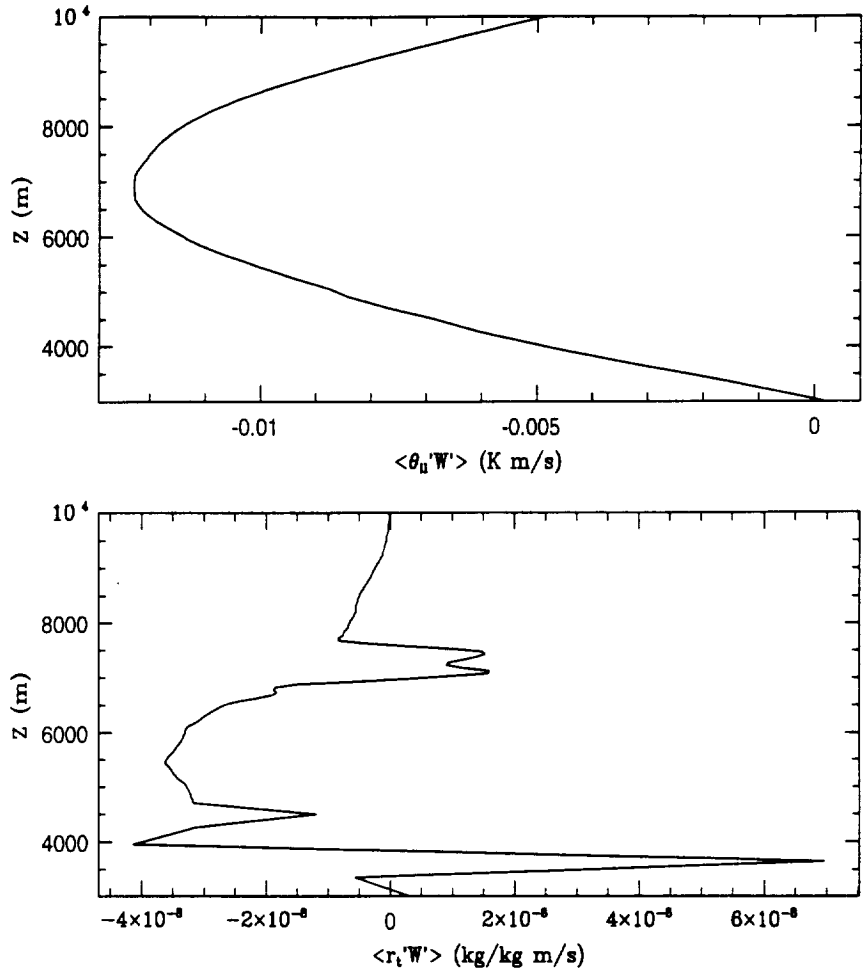

Figure 4.10: Profiles of $< \theta'_{il} W' >$ and $< r'_t W' >$ at 60 minutes of simulation time for Case 1.

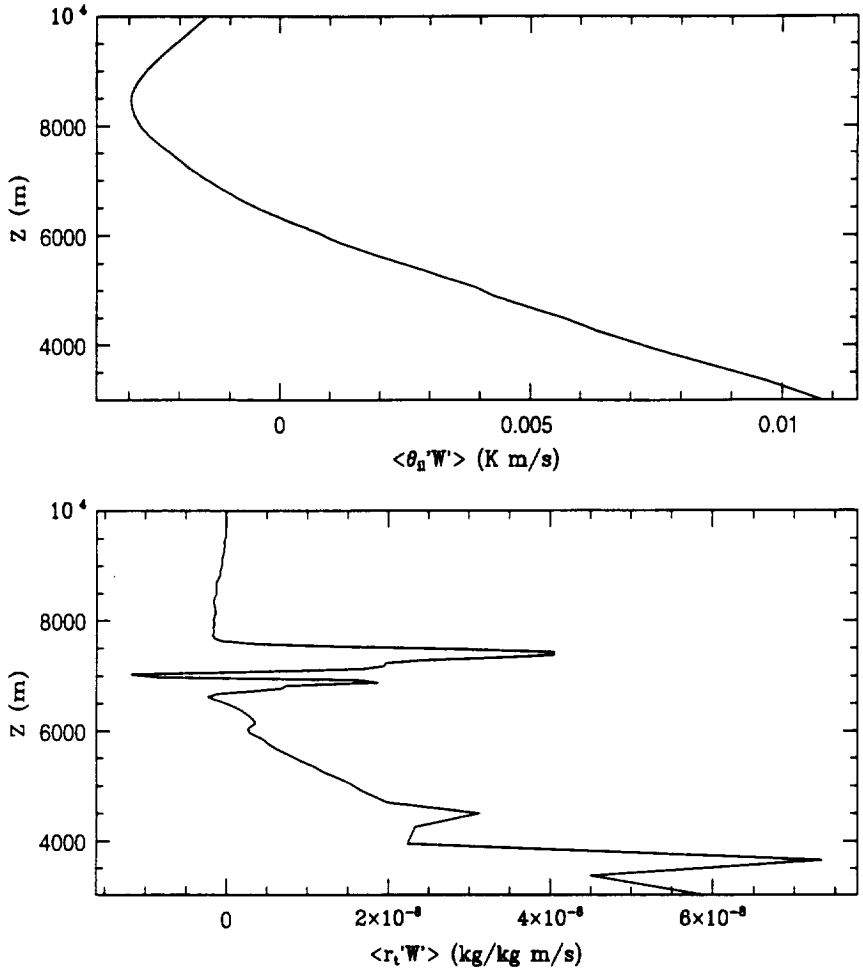

Figure 4.11: Profiles of $< \theta'_{il} W' >$ and $< r'_t W' >$ at 2 hours of simulation time for Case 1.

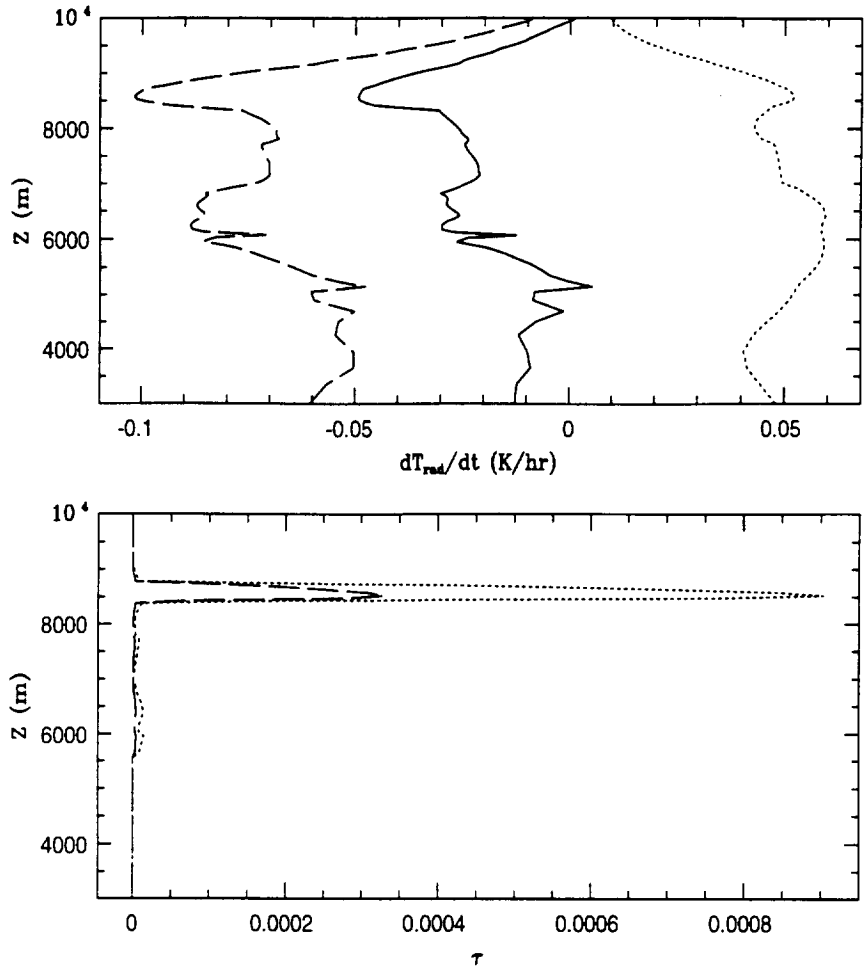

Figure 4.12: Profiles of radiative heating rate (top, solid line: total; dashed line: IR; dotted line: solar) and solar (τ_{solar}) and infrared ($\tau_{infrared}$) optical depths (bottom, dashed line: IR; dotted line: solar) at 60 minutes of simulation time for Case 1.

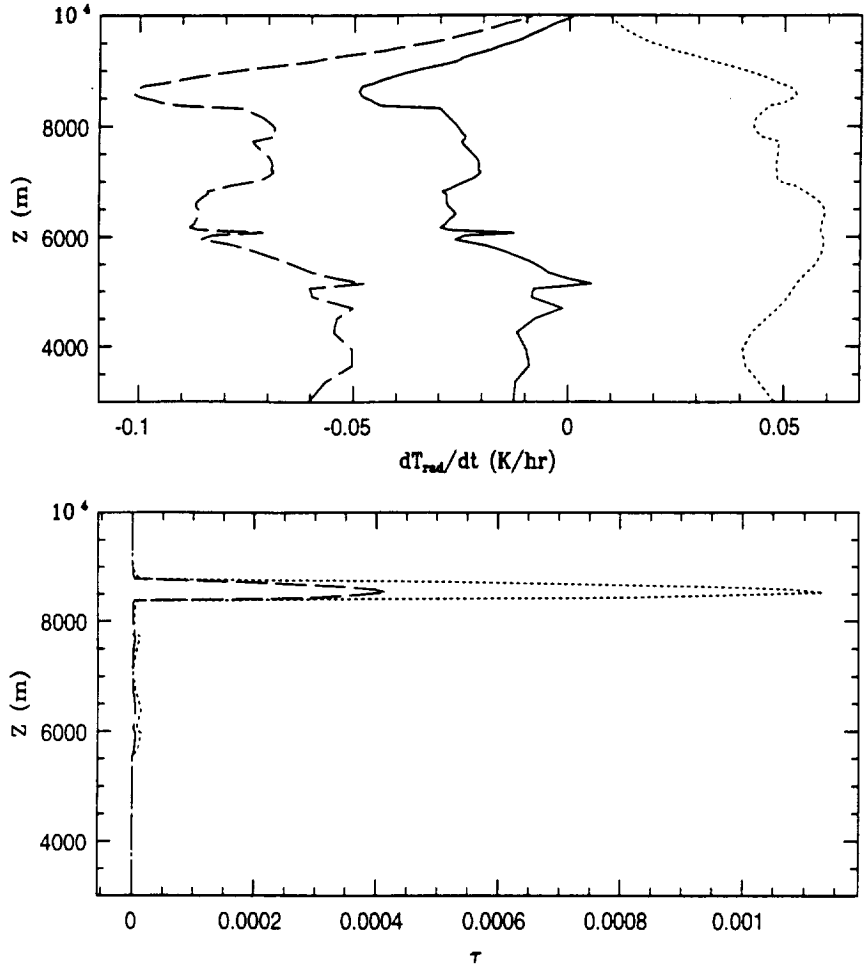

Figure 4.13: Profiles of radiative heating rate (top, solid line: total; dashed line: IR; dotted line: solar) and solar (τ_{solar}) and infrared ($\tau_{infrared}$) optical depths (bottom, dashed line: IR; dotted line: solar) at 2 hours of simulation time for Case 1.

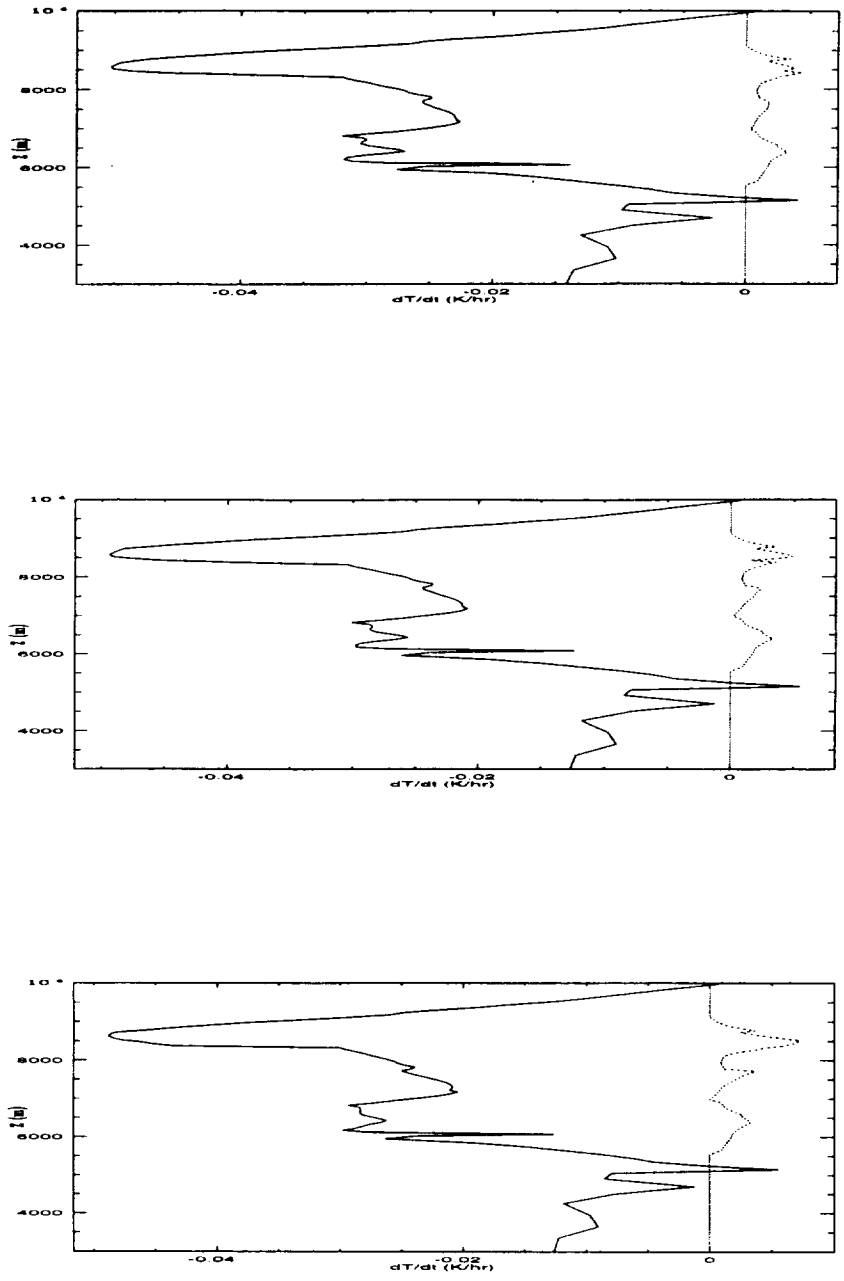

Figure 4.14: Profiles of total radiative (solid) and latent (dotted) heating rates at 30, 60, and 120 minutes of simulation time for Case 1.

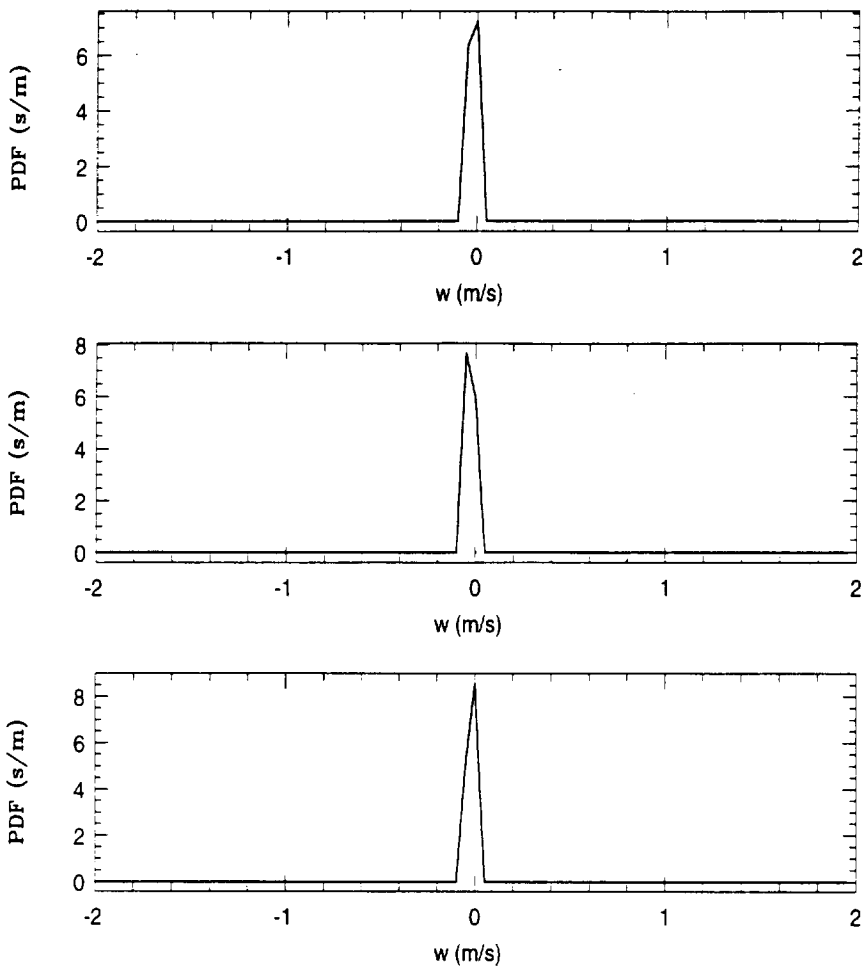

Figure 4.15: PDFs at 5400 (top), 7700 (middle), and 9100 m (bottom) above ground level (AGL) at 30 minutes of simulation time for Case 1.

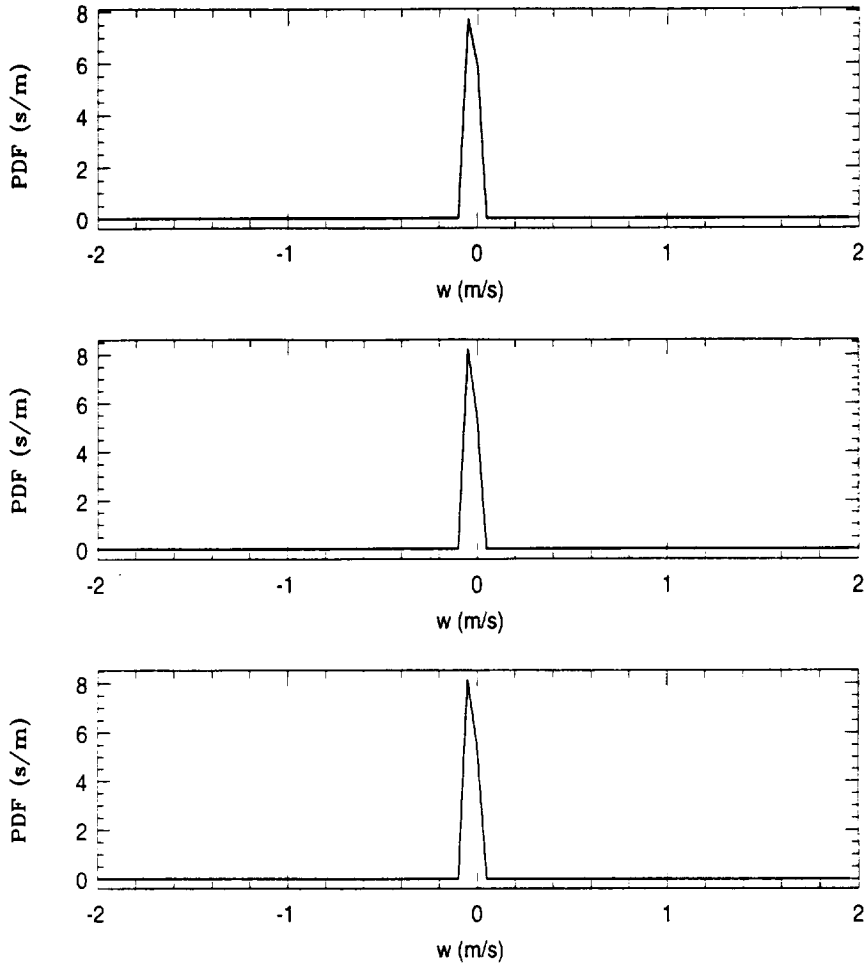

Figure 4.16: PDFs at 5400 (top), 7700 (middle), and 9100 m (bottom) AGL at 60 minutes of simulation time for Case 1.

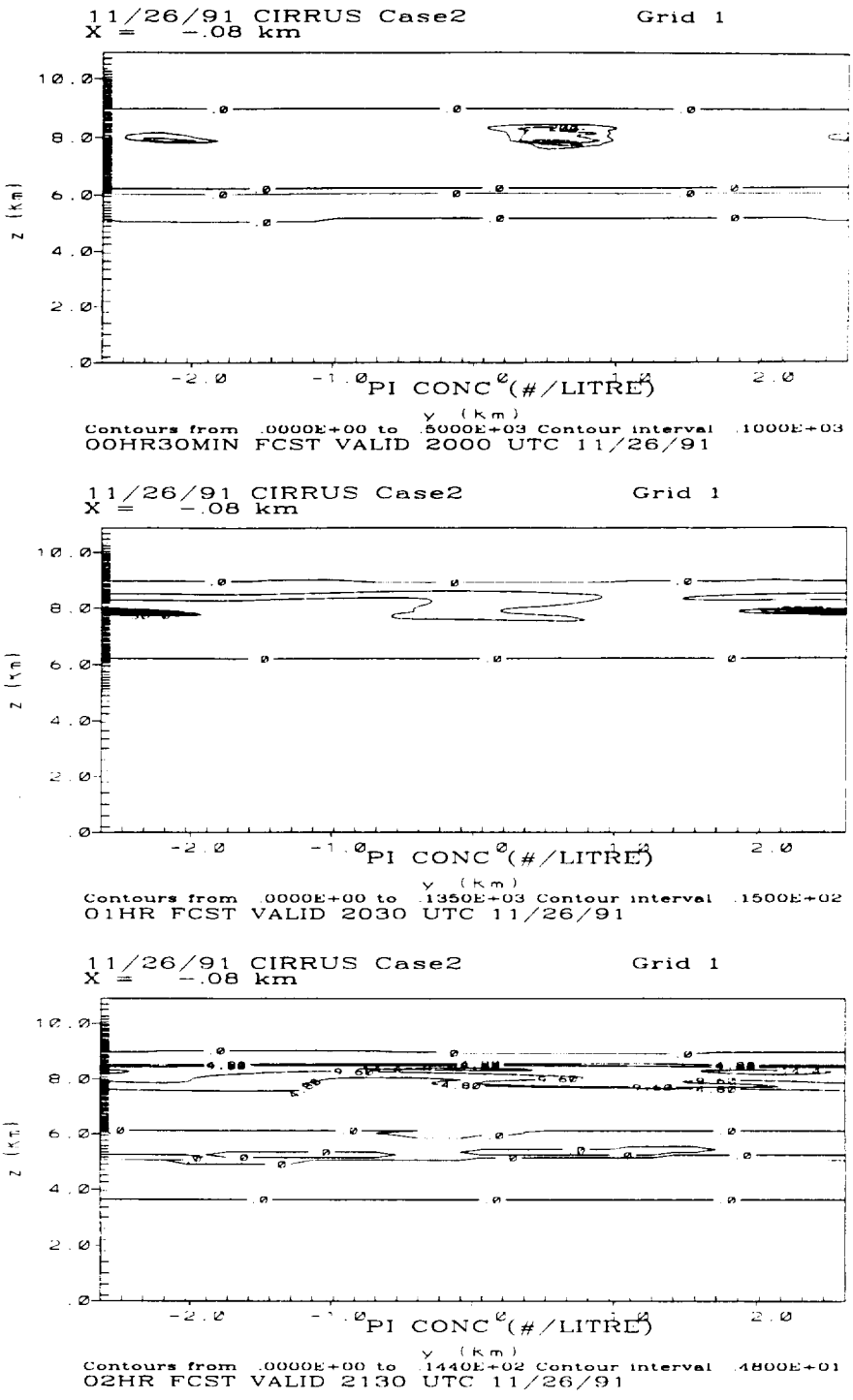

Figure 4.17: Vertical $y - z$ cross sections of pristine ice number concentration for Case 2 at 1730, 1800, and 1900 UTC of the November 26, 1991.

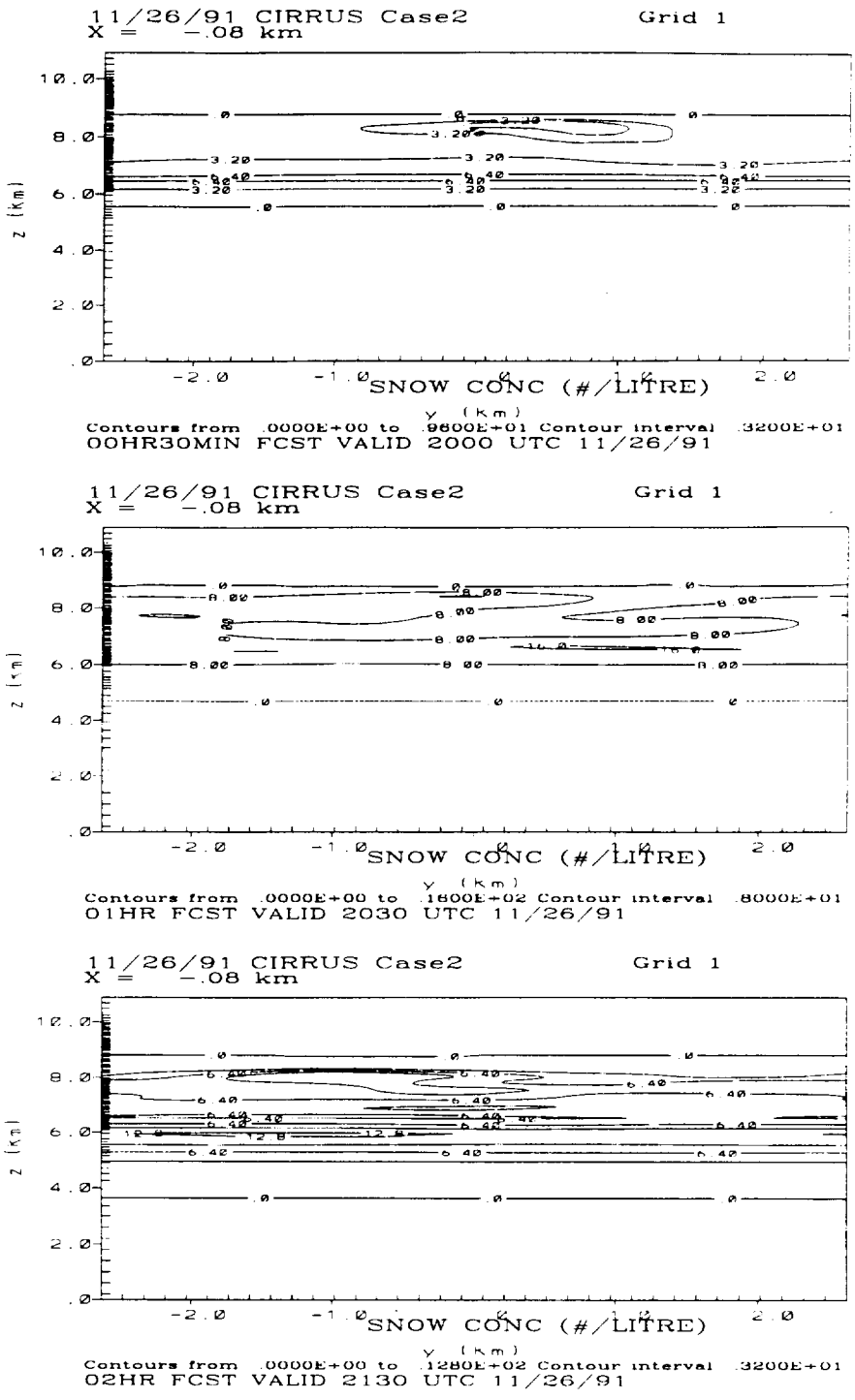

Figure 4.18: Vertical $y - z$ cross sections of snow particle number concentration for Case 2 at 1730, 1800, and 1900 UTC of the November 26, 1991.

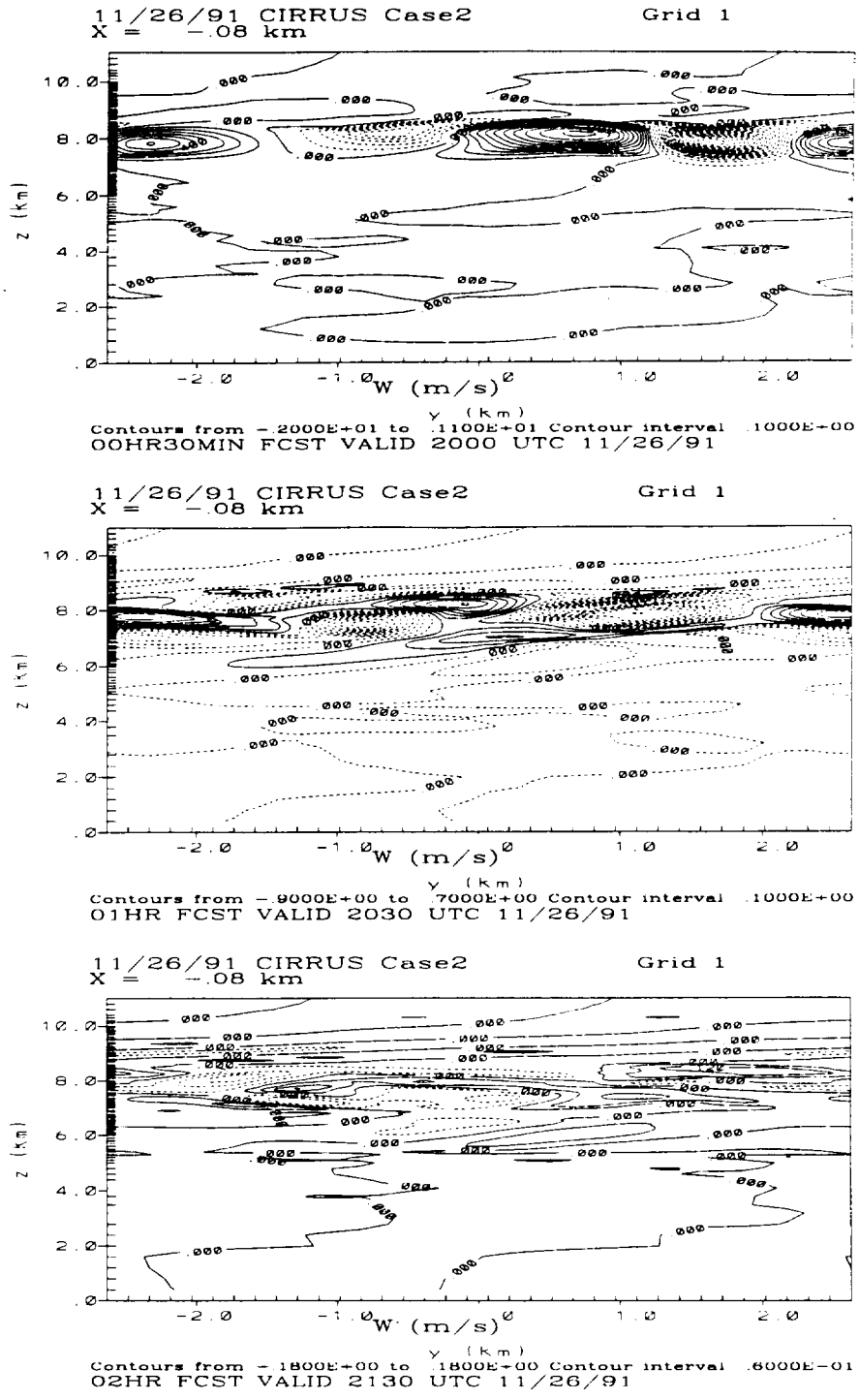

Figure 4.19: Vertical $y - z$ cross sections of vertical velocity for Case 2 at 1730, 1800, and 1900 UTC of the November 26, 1991.

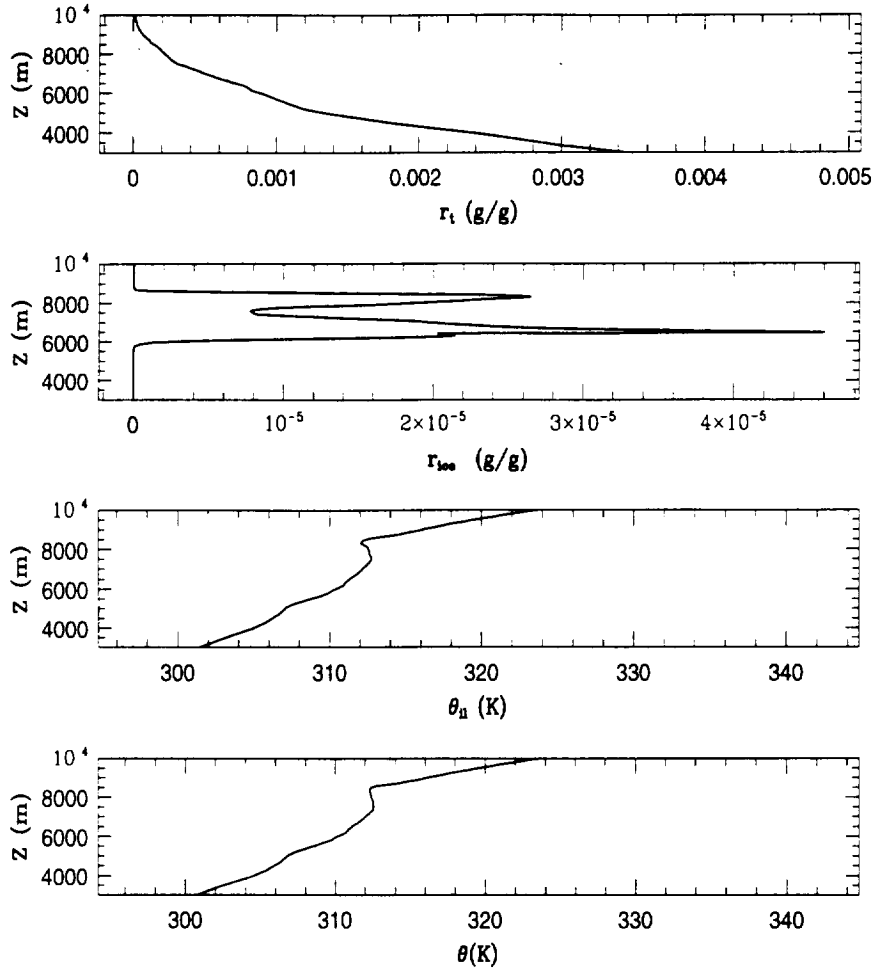

Figure 4.20: Profiles of horizontally- averaged r_t, r_{ice} (pristine ice + snow), θ_{il}, and θ at 30 minutes of simulation time for Case 2.

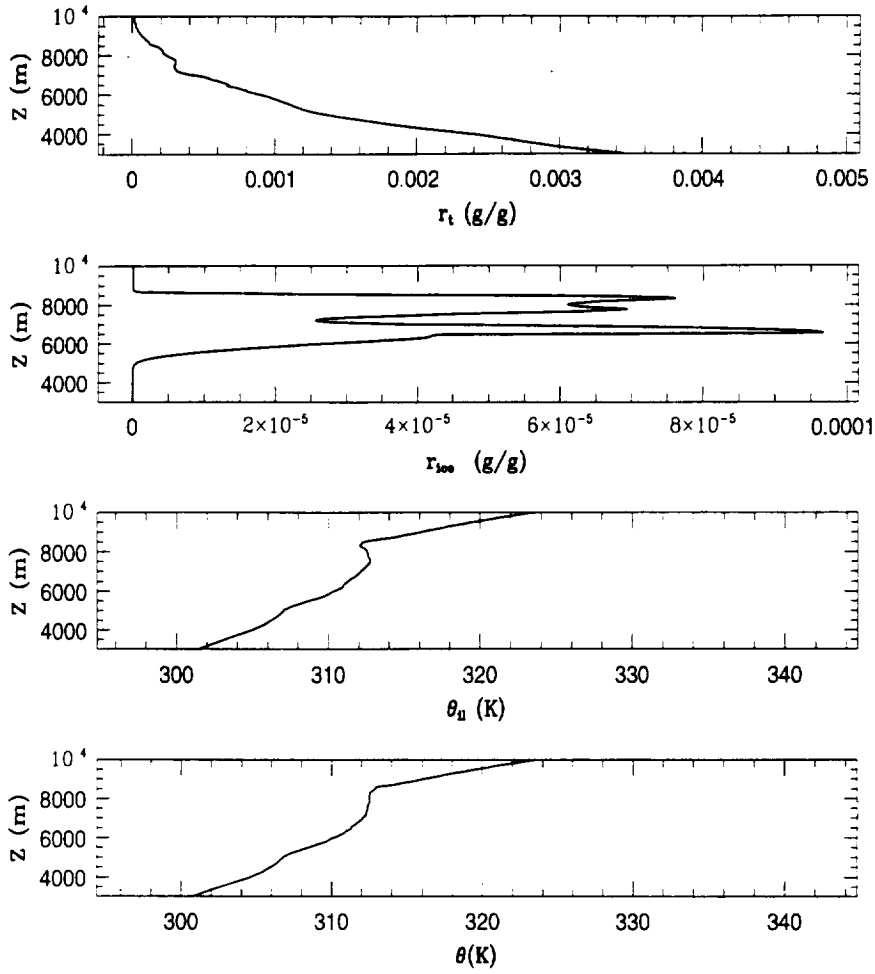

Figure 4.21: Profiles of horizontally- averaged r_t, r_{ice} (pristine ice + snow), θ_{il}, and θ at 60 minutes of simulation time for Case 2.

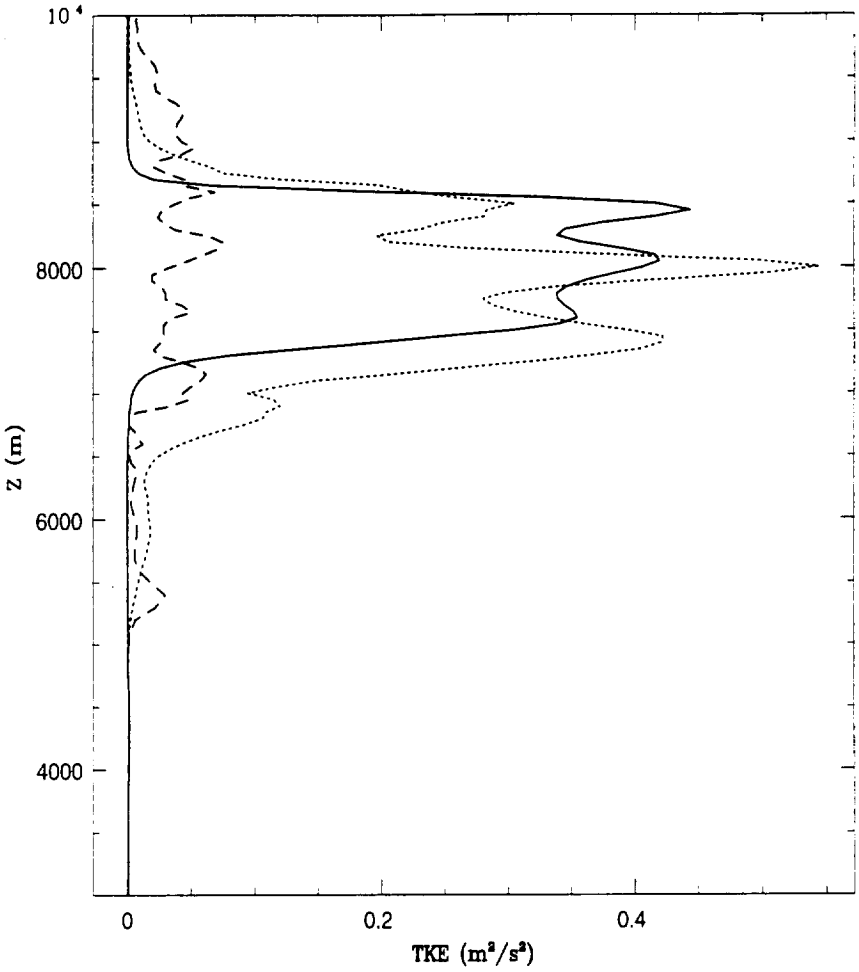

Figure 4.22: Profiles of horizontally averaged TKE at 30 (solid), 60 (dotted), and 120 minutes (dashed) into the simulation for Case 2.

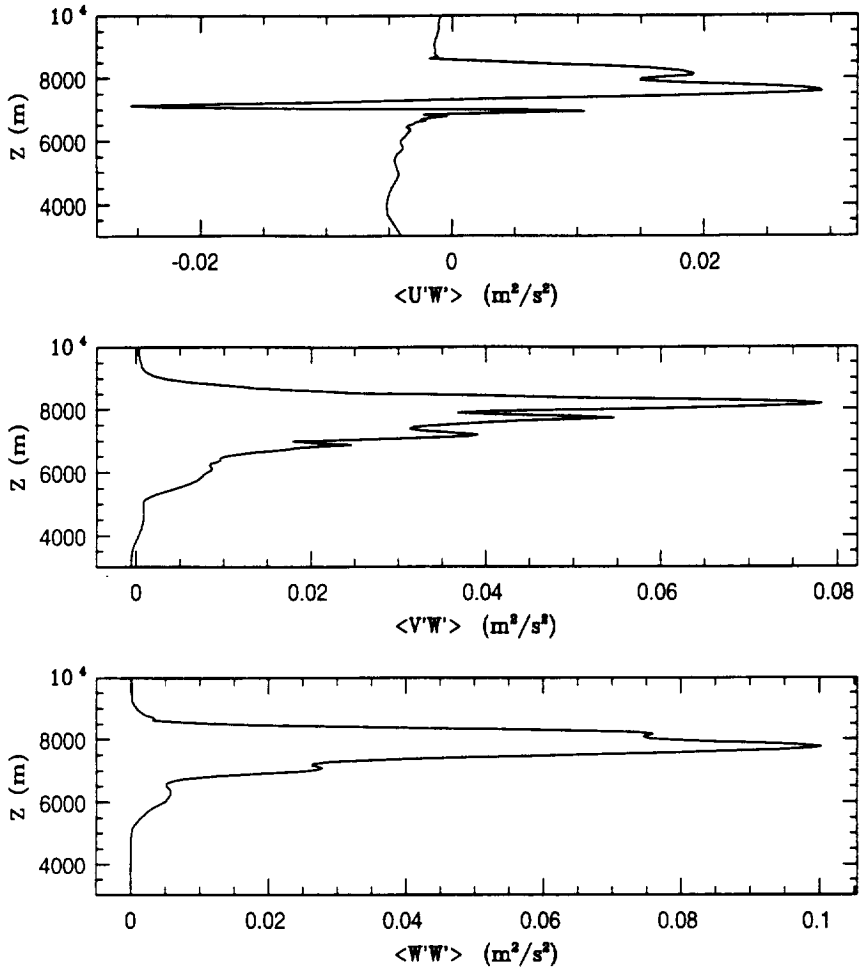

Figure 4.23: Momentum flux profiles at 60 minutes of simulation time for Case 2.

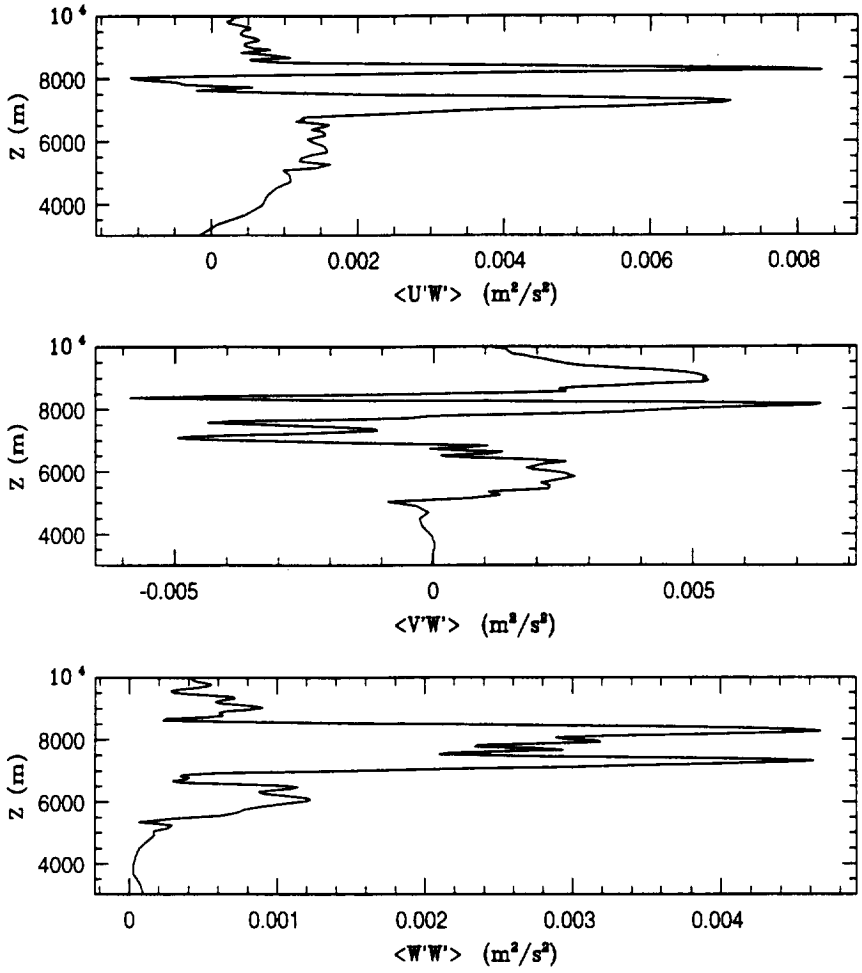

Figure 4.24: Momentum flux profiles at 2 hours of simulation time for Case 2.

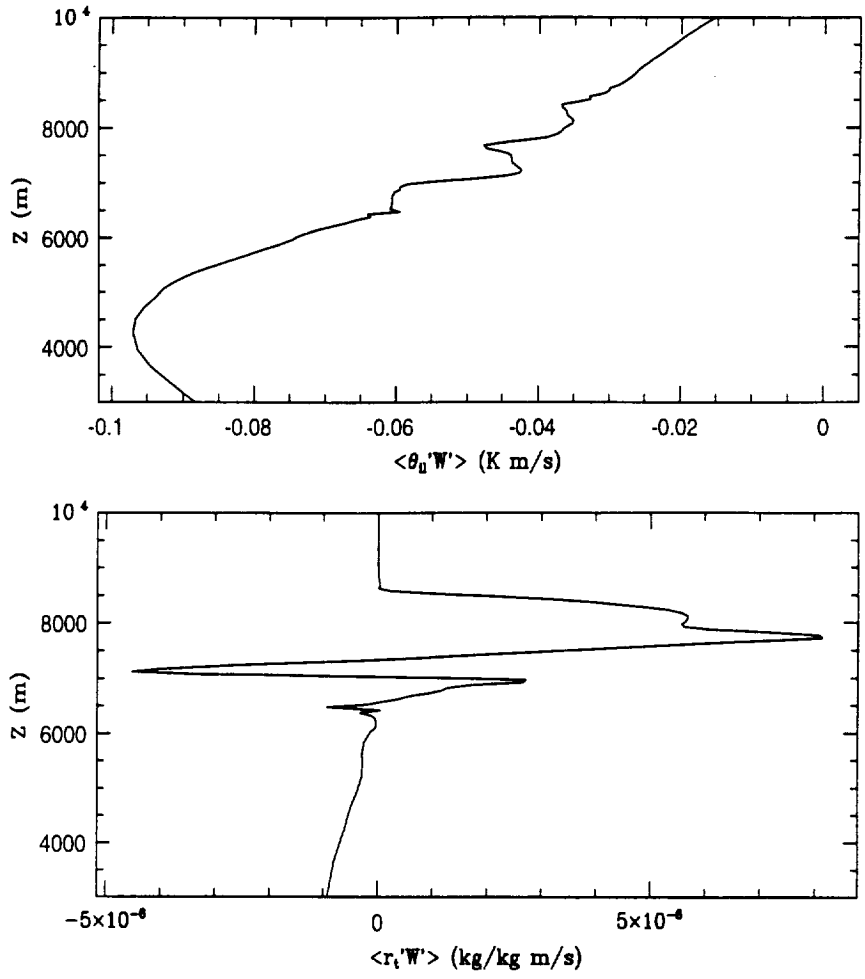

Figure 4.25: Profiles of $< \theta'_{il} W' >$ and $< r'_t W' >$ at 60 minutes of simulation time for Case 2.

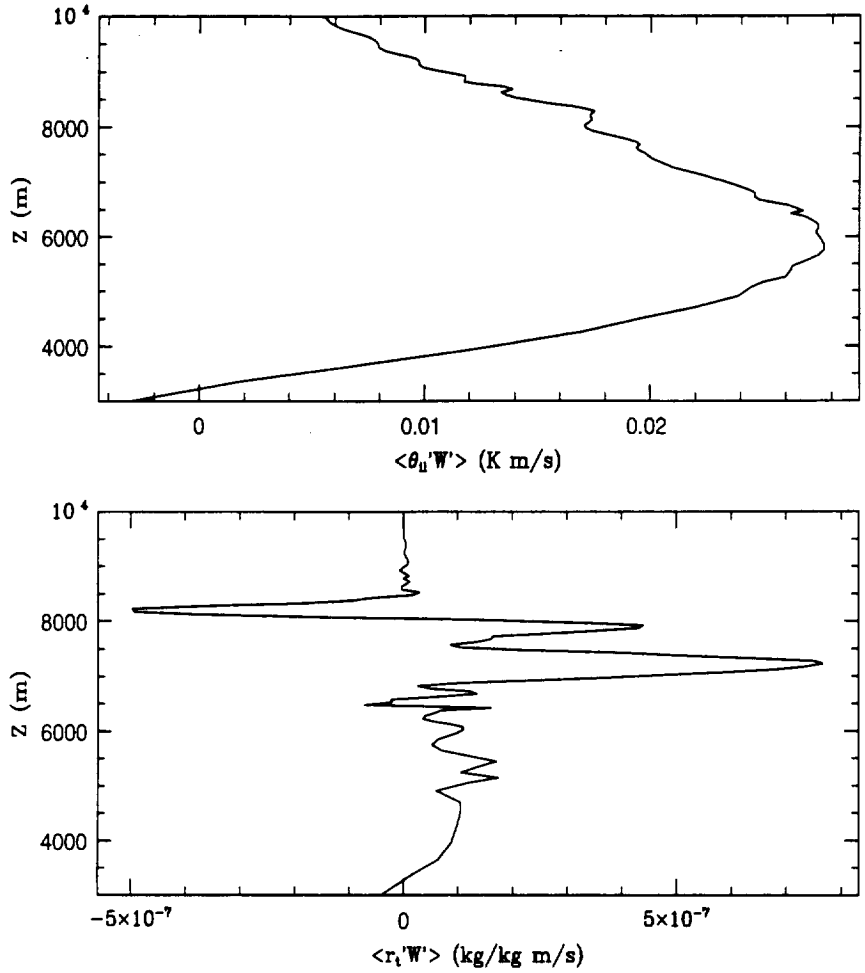

Figure 4.26: Profiles of $< \theta'_{il} W' >$ and $< r'_t W' >$ at 2 hours of simulation time for Case 2.

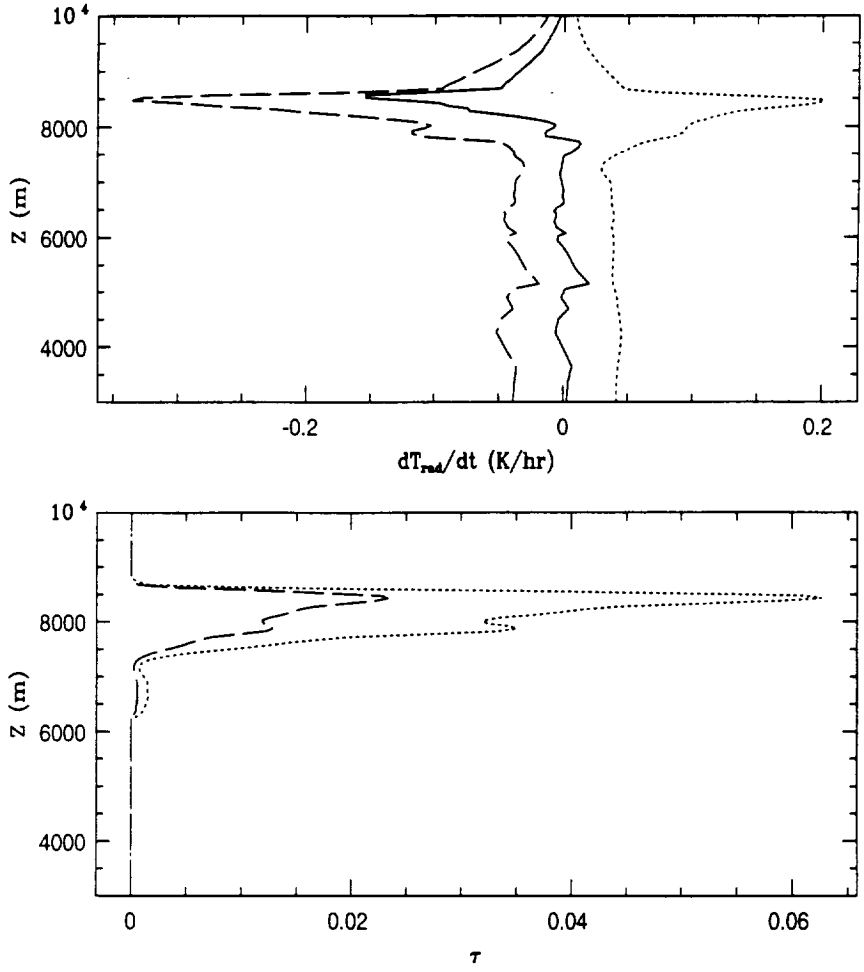

Figure 4.27: Profiles of radiative heating rate (top, solid line: total; dashed line: IR; dotted line: solar) and solar (τ_{solar}) and infrared ($\tau_{infrared}$) optical depths (bottom, dashed line: IR; dotted line: solar) at 60 minutes of simulation time for Case 2.

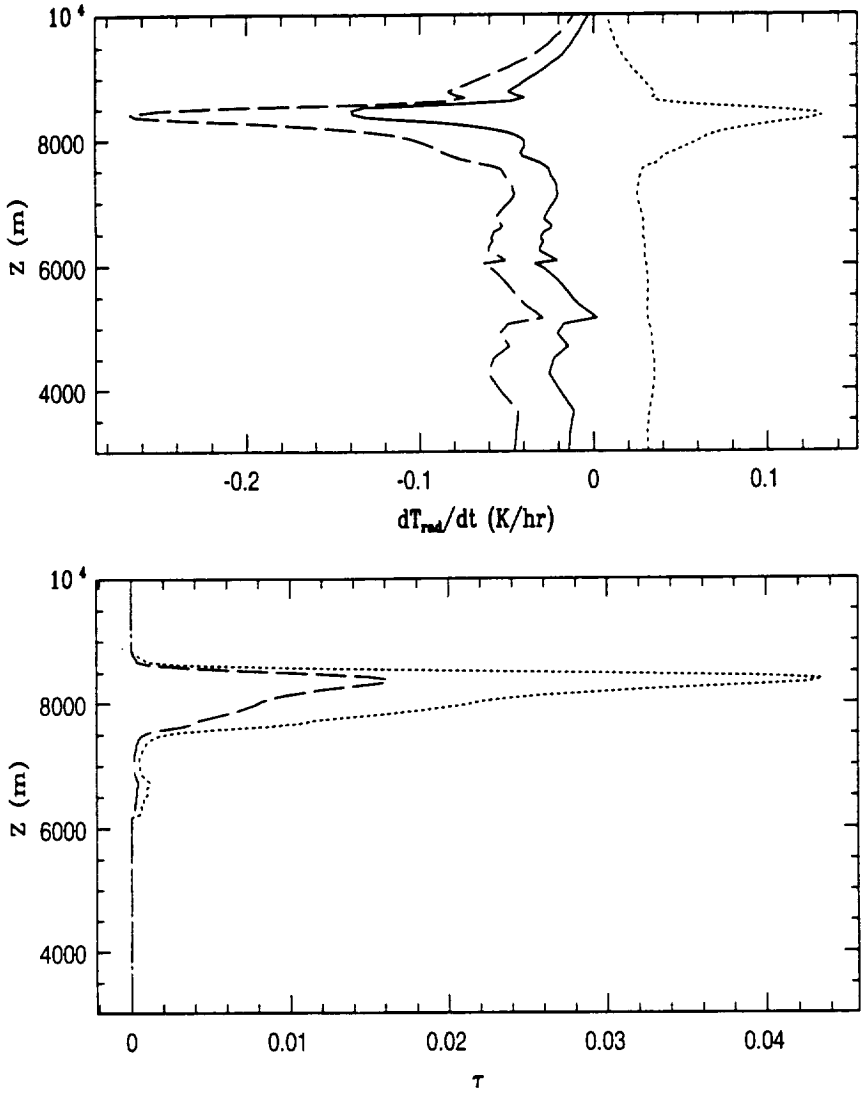

Figure 4.28: Profiles of radiative heating rate (top, solid line: total; dashed line: IR; dotted line: solar) and solar (τ_{solar}) and infrared ($\tau_{infrared}$) optical depths (bottom, dashed line: IR; dotted line: solar) at 2 hours of simulation time for Case 2.

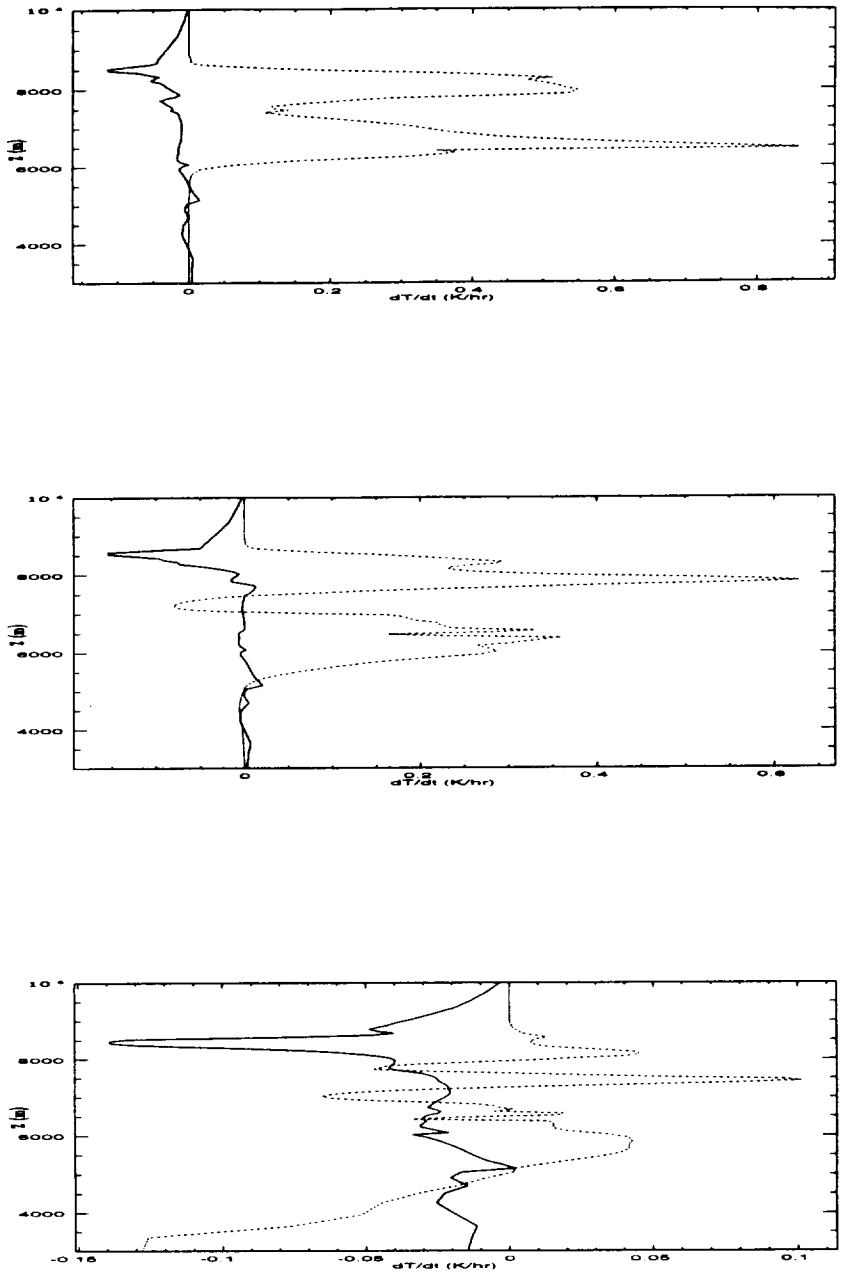

Figure 4.29: Profiles of total radiative (solid) and latent (dotted) heating rates at 30, 60, and 120 minutes of simulation time for Case 2.

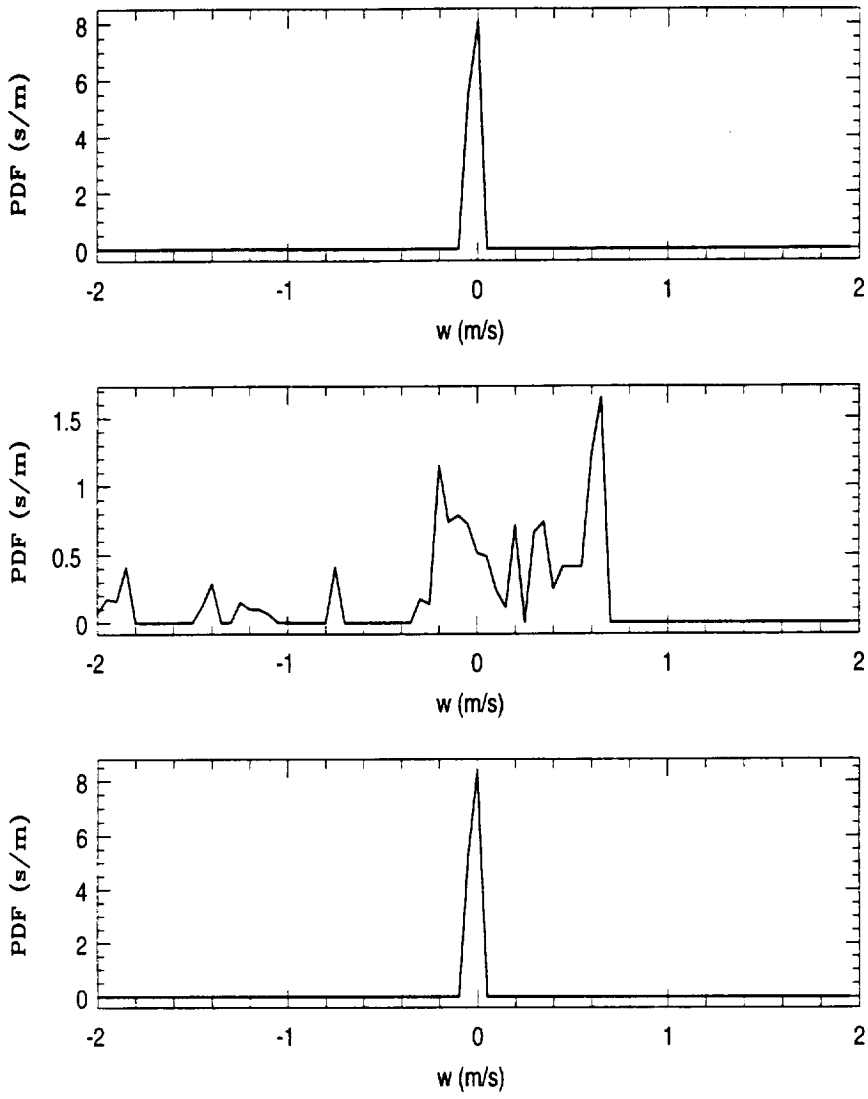

Figure 4.30: PDFs at 5400 (top), 7700 (middle), and 9100 m (bottom) above ground level (AGL) at 30 minutes of simulation time for Case 2.

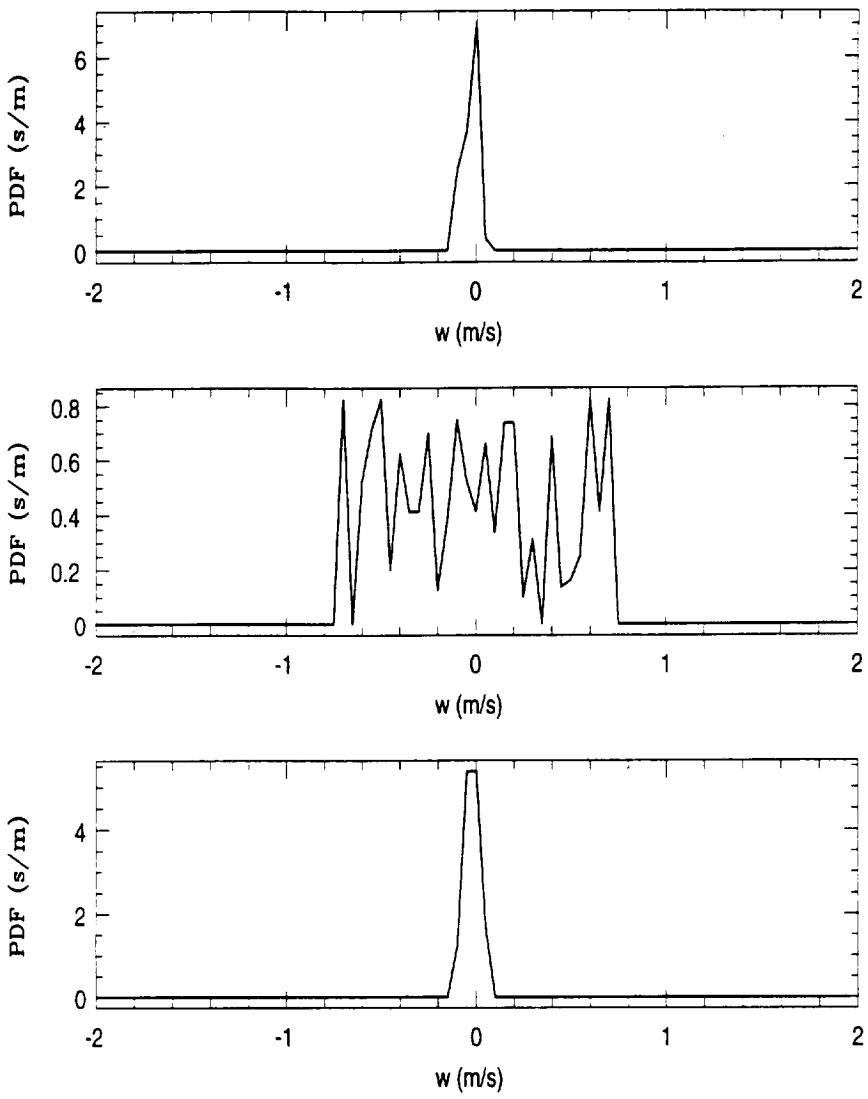

Figure 4.31: PDFs at 5400 (top), 7700 (middle), and 9100 m (bottom) AGL at 60 minutes of simulation time for Case 2.

Chapter 5

RADIATIVE EFFECTS ON THE DIFFUSIONAL GROWTH OF ICE PARTICLES

In this Chapter, the radiative effect on the diffusional growth of ice particles is investigated using a two-dimensional cloud resolving model (CRM) which includes a detailed bin-microphysics. The radiative effects are shown to have a significant impact on the supersaturation as well as total ice production.

5.1 Background

Once ice crystals are nucleated by some of the primary or secondary nucleation mechanisms, they can then grow by vapor deposition if the environment is supersaturated with respect to ice. The depositional (or diffusional) growth of ice particles is closely related to the saturation ratio relative to ice which can be written as:

$$S_i = \frac{e}{e_i} = \frac{e}{e_s}\frac{e_s}{e_i} = S(\frac{e_s}{e_i}) \tag{5.1}$$

where S denotes the saturation ratio with respect to water; S_i is the saturation ratio with respect to ice; e, e_i, and e_s denote the environmental vapor pressure, saturation vapor pressure with respect to ice, and saturation vapor pressure with respect to water, respectively.

Since the saturation vapor pressure with respect to water is always greater than that with respect to ice at the same temperature as long as the temperature is below 0^oC, a water saturated ($S = 1$) cloud is always supersaturated with respect to ice ($S_i > 1$) and is a favorable environment for rapid growth of ice crystals by vapor deposition or diffusion. The environment will remain favorable for ice crystal growth as long as liquid drops are

available to evaporate and maintain the saturation vapor pressure relative to water. This is commonly known as the *Bergeron-Findeisen mechanism.*

Traditionally, the diffusional growth of ice crystals follows the *Fickian diffusion* theory (Rogers and Yau, 1989). If the radiative effects are not considered, the diffusional growth equation can be written as (symbols in this equation are defined in Appendix (A)):

$$\frac{dm_i}{dt} = \frac{4\pi C f_1 f_2 (S_i - 1)}{\frac{R_v T}{D e_{si}(T)} + \frac{L_s}{KT}(\frac{L_s}{R_v T} - 1)} \tag{5.2}$$

However, radiative transfer has shown to have a significant effect on the mass and heat budgets of both ice crystals and cloud droplets (Roach, 1976; Stephens, 1983). In a theoretical study to investigate the effect of radiative heating and cooling on the mass and heat budgets of an ice crystal, Stephens (1983) showed that the effects of radiation on the growth and evaporation rates of ice crystals can be significant. Particle growth (evaporation) is enhanced (suppressed) in a radiatively cooled (heated) environment. It was further demonstrated by Stephens (1983) that the effects of radiative cooling in the upper regions of a cloud greatly enhances the particle fall distances. It was also demonstrated that radiation is the principal component in the diabatic heating of the cloud environment especially when the ice particle dimensions are large.

As shown above, the diffusional growth rate of an ice particle is determined by a steady state balance between heat released due to deposition and the conduction of heat away from the particle's surface when the radiative transfer that occurs between the ice particle and its environment is ignored. If the steady state requires that the heat release due to sublimation and the energy transferred to the particle by radiation are balanced by the conduction of heat away from the particle, then the diffusional growth equation can be written as (see Appendix (B)):

$$L_s \frac{dm_i}{dt} - R = 4\pi C K f_1^* f_2^* (T_r - T_\infty) \tag{5.3}$$

The total radiative energy absorbed by an ice particle of some characteristic dimension l_R for radiation received over all solid angles ω can be determined by (Stephens, 1983)

$$R = \int_0^{\infty} \int_0^{4\pi} G(l_R, \omega) Q_{abs}(\lambda, l_R, \omega)(J(T_\Sigma, \lambda, \omega) - B(T_s, \lambda, \omega)) d\omega d\lambda \qquad (5.4)$$

In (5.4), Q_{abs} is the particle absorption efficiency which is a function of the wavelength (λ), the refractive index of ice at that wavelength and the particle orientation with respect to the incident radiation. $G(l_R, \omega)$ is the geometric cross section of the particle normal to the flow of radiation. $J(T_\Sigma, \lambda, \omega)$ is the incoming radiation incident on the particle from the surrounding environment at some source temperature T_Σ. This temperature is the same as the environmental temperature T_∞ only for a particle immersed within a blackbody. $B(T_s, \lambda, \omega)$ is the Planck blackbody function and represents the emission by the particle of temperature T_s at the wavelength λ. The definition of radiative power absorbed by an ice particle as given in (5.4) involves the integral over all possible directions of incidence (ω) and over all wavelengths (λ).

Utilizing the two-stream approximation in the above integral one gets R for a spherical particle of radius r as (Harrington, 1997)

$$R = \int_0^{\infty} 4\pi r^2 Q_{abs}(r, \lambda)[\pi B(T_s, \lambda) - \frac{1}{2}(F^+ + F^-)] d\lambda \qquad (5.5)$$

where F^+ and F^- are the values of upward and downward fluxes at wavelength λ. For consistency with the two-stream model, an average value of Q_{abs} for a given spectral band, i, is used and the above equation becomes

$$\begin{aligned} R_i &= 4\pi r^2 \bar{Q}_{abs,i}(\bar{r}_k) E_{d,i} \\ E_{d,i} &= [\pi B_i(T_s) - \frac{1}{2}(F_i^+ + F_i^-)] \end{aligned} \qquad (5.6)$$

where $\bar{Q}_{abs,i}(\bar{r}_k)$ is the absorption coefficient averaged over spectral band i and computed at the mean size of microphysical bin number k as to be discussed later in this Chapter; F_i^+ and F_i^- are the values of fluxes for band i; $B_i(T_s)$ is the band integrated Planck function evaluated at the particle's surface temperature. The total radiative effect R can be obtained by summing up R_i over the total number of microphysical bins.

Now, it is straightforward to get the total radiative energy absorbed by a particle of size $\bar{r}_k$ as

$$R = 4\pi\bar{r}_k^2 \sum_{i=1}^{Nbands} \bar{Q}_{abs,i}(\bar{r}_k) E_{d,i} \tag{5.7}$$

where Nbands is the total number of radiation bands used in the radiation model. In order to evaluate the radiative effects on particle's diffusional growth in the explicit microphysical model, the radiative term shown above must be included in the model equations for supersaturation and for the growth of particle. These equations must be solved together in a manner that ensures self-consistency.

5.2 Cloud Resolving Model (CRM) Simulations of the November 26 ,1991 Cirrus

5.2.1 The Cloud Resolving Model

The model used to test the radiative effects on ice particle diffusional growth is a coupling of the RAMS with the bin-resolving microphysics model developed at the University of TelAviv (Tvivion et al., 1987; Tvivion et al., 1989; Reisen, 1995; Reisen et al., 1996). It is a two-dimensional version of the large eddy simulation model described in detail in Stevens et al. (1996a) and Feingold et al. (1996a). The strength of this model lies in its emphasis on both dynamics and microphysics through the coupling of the bin-resolving microphysical model with a dynamical model that resolves the large eddies. A detailed description of the coupled code for the liquid phase microphysics can be seen in Stevens et al. (1996a,b). Reisin (1995; Reisen et al., 1996) provides a detailed description of the model when both liquid and ice phases are included.

Although the two-dimensional (2D) CRM model does not represent the eddy structure as well as its three-dimensional (3D) large eddy simulation counterpart, it does include the essential interactions between large eddies and cloud microphysical properties and provides a valuable framework for testing hypotheses without enormous computational expense (Stevens et al., 1997). To accommodate the inclusion of radiative effects, the current version of the model couples the optical properties of the droplets and ice particles to an 8-band radiative transfer model discussed in Harrington (1997).

In this study, both water and ice phases are included in the bin-resolving microphysics which is referred to as Level_5. The Level_5 bin-microphysical representation of this model requires that equations for droplet activation, condensational/evaporational growth, collision-coalescence of drops, ice nucleation, deposition and sublimation of ice crystals, collision-coalescence of ice particles, and sedimentation all be explicitly solved. The decision on which processes are to be included in the model is based upon a number of factors (Reisin 1995):

- the importance of the process to the relevant problem studied,
- the availability of relevant data like collision efficiencies, terminal velocities, shape factors, etc.,
- limitations on computational resources.

Currently, three ice species named pristine ice, snow (aggregate), and graupel are included in the bin-microphysics representation of the model. Ice crystals in the model are created by nucleation of ice nuclei (IN) or by freezing of drops smaller that 100 μm in radius. The specific shape of the ice particles is assumed to be spherical in this study, even though some other shapes may be specified. Snow particles are formed by aggregation of ice crystals and are considered to have the minimum density ($0.2gcm^{-3}$) compared with pristine ice crystals ($0.7gcm^{-3}$) and graupel ($0.5gcm^{-3}$). Graupel particles are formed by freezing of drops with radii larger than $100\mu m$ and /or by different processes of particle coagulation.

The particle spectra for any category is divided into 25 bins ($x_k, k = 1, ..., 25$) with mass doubled in the next larger bin:

$$x_{k+1} = 2x_k \tag{5.8}$$

The initial mass is $x_1 = 1.598 \times 10^{-11}g$ for any category which corresponding to a diameter of $3.125\mu m$ for drops, $3.520\mu m$ for pristine ice crystals, $3.937\mu m$ for graupel particles, and $5.344\mu m$ for aggregate particles. The size of each category at bin #25 is

bin #	rain	pristine ice	graupel	aggregate
1	.31250E-03	.35195E-03	.39373E-03	.53437E-03
2	.39373E-03	.44343E-03	.49606E-03	.67326E-03
3	.49606E-03	.55869E-03	.62500E-03	.84826E-03
4	.62500E-03	.70390E-03	.78745E-03	.10687E-02
5	.78745E-03	.88686E-03	.99213E-03	.13465E-02
6	.99213E-03	.11174E-02	.12500E-02	.16965E-02
7	.12500E-02	.14078E-02	.15749E-02	.21375E-02
8	.15749E-02	.17737E-02	.19843E-02	.26930E-02
9	.19843E-02	.22348E-02	.25000E-02	.33930E-02
10	.25000E-02	.28156E-02	.31498E-02	.42749E-02
11	.31498E-02	.35475E-02	.39685E-02	.53861E-02
12	.39685E-02	.44695E-02	.50000E-02	.67860E-02
13	.50000E-02	.56312E-02	.62996E-02	.85499E-02
14	.62996E-02	.70949E-02	.79370E-02	.10772E-01
15	.79370E-02	.89390E-02	.10000E-01	.13572E-01
16	.10000E-01	.11262E-01	.12599E-01	.17100E-01
17	.12599E-01	.14190E-01	.15874E-01	.21544E-01
18	.15874E-01	.17878E-01	.20000E-01	.27144E-01
19	.20000E-01	.22525E-01	.25198E-01	.34200E-01
20	.25198E-01	.28380E-01	.31748E-01	.43089E-01
21	.31748E-01	.35756E-01	.40000E-01	.54288E-01
22	.40000E-01	.45050E-01	.50397E-01	.68399E-01
23	.50397E-01	.56759E-01	.63496E-01	.86177E-01
24	.63496E-01	.71512E-01	.80000E-01	.10858E+00
25	.80000E-01	.90100E-01	.10079E+00	.13680E+00

Table 5.1: Bin number and particle size relation for the first 25 bins. The particle sizes are in cm.

$800\mu m$ for drops, $901\mu m$ for pristine ice crystals, $1008\mu m$ for graupel, and $1368\mu m$ for aggregate particles. Table 5.1 shows the size-bin information for bins from 1 to 25. The number of total bins can be larger or smaller than 25, depending upon the specific cases. These spectra shown in the table are believed to be adequate to mid-latitude cirrus clouds.

The evolution of the supersaturaion with respect to both water and ice is prognosed according to the equations described in Appendix (B). Radiative effect on the diffusional growth (or evaporation) of drops and ice particles can be turned on and /or off in order to test its importance.

5.2.2 CRM Simulation Results

The CRM simulations to be discussed in this chapter have close relations to the LES studies discussed in Chapter 4 because the soundings used in the CRM simulations are the same as what were used in the LES studies. In Chapter 4, a shallow and a deep cloud system were simulated in the framework of two- moment microphysics, while in this Chapter, the two corresponding systems will be simulated under the framework of ice-phase bin-microphysics. Since the bin-microphysics has the advantage of predicting particle size-dependent supersaturation with respect water as well as ice, it is ideal (at present) to study the radiative effects on ice crystal's depositional growth (which is a function of supersaturation) in cirrus clouds.

In order to test the radiative effects on a particle's diffusional growth two simulations are done for each case. In one of the two simulations, the radiative effect is added to the particle's diffusional growth equation as well as the supersaturation equation, while in the other simulation, radiative feedback is turned off.

CRM Results: Case 1-A Shallow Cloud System

Figures 5.1 through 5.5 compare the CRM simulated supersaturation with respect to ice (SSI), water vapor mixing ratio, PI number concentration, snow (aggregate) number concentration, and total ice mass. It is seen in Figure 5.1 that a maximum SSI of more than 23% is produced in the simulation with radiative feedback being added to the relevant equations, while in the simulation without radiative feedback the maximum SSI predicted is generally less than 3%. Also, it is apparent that the largest jump in SSI production occurs in the lower levels of the cloud. In response to greater SSI production, a maximum PI concentration of nearly $1300/L$ is predicted near the cloud top at 30 minutes into the simulation with radiative feedback. This compares to the maximum PI concentration of about less than $100/L$ in the simulation without radiative feedback (Figure 5.3) at the same time. In contrast to the massive production of PI in the simulation with radiative feedback, Figure 5.4 shows that maximum aggregate number concentration produced in this simulation has dropped significantly from about $8.0 \times 10^{-5}/L$ (in the simulation without

radiative feedback) to slightly more than $2.0 \times 10^{-5}/L$. As the simulation proceeds from 30 to 60 minutes, the number concentration of PI has reduced dramatically while the maximum snow particle number concentration has increased by a factor of about 6. This is because the interaction of PI particles results in production of snow. Also evident is that most aggregate particles in the simulation without radiative feedback reside near the cloud base (below 6 km level) while in the simulation with radiative feedback, most of the aggregate particles are deep in the cloud layer between 5.2 km to 8 km levels.

Even though much more PI crystals are produced in the simulation with radiative feedback than in the simulation without radiative feedback, the maximum PI mixing ratio ($0.24g/kg$) predicted in the simulation with radiative feedback is only about half of the value ($0.42g/kg$) produced in the other simulation. Following a similar trend as to the PI mixing ratio prediction, maximum aggregate mixing ratio predicted in the simulation with radiative feedback ($3 \times 10^{-7}g/kg$) has reduced by more than one order of magnitude compared with the prediction in the simulation without radiative feedback (1.5×10^{-5} g/kg) at 30 minutes of simulation time. Figure 5.5 compares the total ice prediction for the two simulations at 30 and 60 minutes of the simulation time. It is clearly seen that with the radiative feedback, the model is unable to produce as much ice as in the simulation without radiative feedback.

The model prediction of ice production seems to be intriguing to some extent because one would expect to see not only a significant change in the ice production, but also enhanced ice production when the radiative effect is added to ice particle's diffusional growth. Explanations to the model performance can be assisted by referring to Figures 5.6 and 5.7. Figure 5.6 shows the particle size- dependent radiative flux toward a particle at 100 time steps for a parcel which has its origin at 4038.0 m, while Figure 5.7 displays the radiative flux for another parcel whose origin is deep in the cloud layer at 7013.47 m above the ground. The results shown in these two Figures tell us that radiative warming of ice particles (see bottom panels of the two Figures) are dominant in the cloud layer. Also it is clearly shown in these Figures that smaller ice particles tend to experience less radiative warming than larger particles. It should be noted that radiative warming or cooling for an

ice particle is different from the warming or cooling of the atmospheric environment because one depends on the balance described by equation (5.4) (for a particle) while the other depends on the divergence of the net radiative fluxes (upwelling plus downwelling). So, when the model predicts that the atmosphere experience radiative cooling, it is not implied that each particle sees the same effect because as these two Figures display, radiative warming or cooling for a particle is size- dependent.

Based upon Figures 5.6 and 5.7, one can explain the lack of ice production in the simulation with radiative feedback easily. Production of SSI or haze particles activates the ice nucleation processes in the bin-microphysics model. The ice particles produced through nucleation processes are added to the relevant bins (always very small bins) of the PI category. After the formation of these ice particles, they experience diffusional growth in an environment of positive SSI. The newly nucleated ice crystals are so small that the radiative effect is not a significant factor in the early stage of ice particle's diffusional growth.

As more and more PI crystals are produced, interactions among the ice particles results in the formation of aggregates. Both aggregates and PI crystals can experience significant growth through diffusion of water vapor as long as $-R$ in Equation (5.3) is not enough to balance the right-hand side (note that R is negative for radiative warming). On attaining a certain size (for example, r_{limit}), an ice particles finds itself in a situation in which the radiation it absorbs is balanced by the diffusion of heat away and from there on no mass increase through diffusional growth is allowed because the mass added to the particle through diffusional growth would break the balance described in Equation (5.3). However, particles larger than r_{limit} can be produced through some other processes such as collision and aggregation, but these larger particles can not survive for very long because the radiation they absorb is more than what the diffusion of heat is able to take away. Eventually, particles larger than r_{limit} will warm and experience evaporation which adds water vapor to the free air, resulting in higher water mixing ratio, especially in the region between 4 and 6 km levels (Figure 5.2) in the simulation with radiative feedback than in the simulation without radiative feedback. Since water vapor can be continuously provided

through evaporation of large ice particles, high SSI can be maintained in the simulation with radiative feedback. It is worth pointing out that the largest water vapor surplus between 4 and 6 km levels matches nicely the maximum SSI production excess (Figures 5.1 and 5.2) between the two simulations. The persistent high SSI is the reason for the large number of PI production and the radiative warming results in a reduction of ice mass in the simulation with radiative feedback relative to the one without radiative feedback. It should also be pointed out that large ice particles in the simulation without radiative feedback are not restricted in their growth by the processes stated above. This is the key reason why greater ice mass production in the simulation without radiative feedback than in the simulation with radiative feedback.

Fluxes of momentum, θ_{il}, and r_t are also compared between the simulation with radiative feedback and that without radiative feedback at 30 minutes and 60 minutes of simulation time (see Figures 5.8 through 5.11). The two simulations have generally similar vertical profiles for these fluxes, except that $< V'W' >$ displays significant difference below 6 km level. The larger absolute magnitude in $< V'W' >$ associated with the simulation without radiative feedback may indicate that more active entrainment and detrainment processes are involved. This conclusion may also be supported by the larger $< r_t'W' >$ near the cloud base for the simulation without radiative feedback.

Figure 5.12 and the top panels of Figures 5.15 and 5.16 compare the total turbulent kinetic energy (TKE) and TKE production between the two simulations. The total TKE profile indicates that the simulation without radiative feedback tends to be more turbulent than the simulation with radiative feedback, especially in the upper levels of the cloud system. Generally, the upper levels of the cloud system tend to be negatively buoyant, while below $7700m$, positive buoyancy dominates for the simulation without radiative feedback. Also, shear production which is not a significant factor compared with buoyancy production is confined to a very shallow region between 7500 to $7700m$ for this simulation. However, for the simulation with radiative feedback, shear production is comparable to buoyancy, even though it is still limited to a very shallow region similar to that in the other simulation. The appearance of dominant fine structures in the total as well as

the buoyancy TKE profiles may indicate that the cloud system is more decoupled in the vertical for the simulation with radiative feedback than for the simulation without radiative feedback.

Consistent with the difference in ice mass production, the optical depthes (both solar as well as infrared) predicted in the simulation without radiative feedback are dominant over that predicted in the simulation with radiative feedback (Figures 5.13 and 5.14). The two peaks near 5 km and 6 km in the optical depth profiles correspond very well to the peaks in aggregate and PI production, respectively. Since the model-predicted cloud system without radiative feedback is optically thick and consists of more larger ice particles than the cloud predicted in the simulation with radiative feedback, it is seen that a pattern of upper level cooling and lower level warming dominates in the simulation without radiative feedback because the cloud system is able to absorb more long-wave radiation from below (resulting in warming near cloud base) and emits more long-wave radiation near cloud top which results in more radiative cooling above than in the simulation with radiative feedback (Figures 5.15 and 5.18). Also it is clearly seen in these Figures that, in the simulation with radiative feedback, since the model- predicted cloud system is optically thinner, solar radiation can penetrate deeper in the cloud layer than in the simulation without radiative feedback, resulting in a peak of solar warming just below 6000 m level. Both cooling and warming in the simulation without radiative feedback are more significant than in the other simulation just because of the significant difference in the optical properties of the model-predicted clouds.

CRM Results: Case 2-A Deep Cloud System

Following a similar format to Case 1, model predictions for Case 2 are shown in Figures 5.19 through 5.34.

Similar to Case 1, by 30 minutes into the simulation, the model has predicted significant differences in SSI between the simulation with radiative feedback and that without radiative feedback. High SSI predicted in the simulation with radiative feedback is confined to a region near cloud base (which corresponds to a region of larger water vapor mixing ratio surplus for the simulation with radiative feedback (Figure 5.20)) with a maximum

domain- averaged value as large as nearly 24%. This is compared with the maximum SSI production of only 1.2% at 30 minutes into the simulation without radiative feedback (Figure 5.19). Also, it is noticed that higher SSI regions predicted in the simulation without radiative feedback are quite disperse. Since the SSI production in the simulation with radiative feedback is much higher than that in the other simulation, it is not surprising that a lot more PI crystals are produced through ice nucleation which is highly dependent upon the available SSI in simulation (Figure 5.21). Also, as expected, most PI crystals remain suspended near the cloud top because of their very small terminal velocities. In the simulation with radiative feedback, the maximum aggregate number concentration predicted is only about one third (or even less) of the corresponding value predicted in the other simulation (Figure 5.22). Most of the aggregate particles produced are located close to the cloud base. Both PI and aggregate mixing ratios predicted in the simulation with radiative feedback are smaller than in the other simulation because, as it is discussed in Case 1, production of large particles are also prohibited in this Case. The maximum aggregate mixing ratio predicted in the simulation with radiative feedback is more than 20 times less than that produced in the other simulation, a good indication of suppressed vapor deposition of larger ice particles when radiative effects are included (discussed above). For the total ice mixing ratio, the predicted maximum value in the simulation with radiative feedback is only about one-half of the maximum value predicted in the other simulation (Figure 5.23).

Statistical profiles (Figures 5.24 through 5.27) display quite similar features for the two simulations with respect to the fluxes of $< U'W' >$, $< V'W' >$, $< W'W' >$, $< \theta'_{il}W' >$, and $< r'_t W' >$. These similar profiles may imply that the two simulations involve similar dynamic and microphysical processes. TKE profiles at 60 minutes into the simulation also indicate quite similar TKE intensity with maximum TKE predicted at about 6500 m above the ground for both simulations (Figure 5.28. For both simulations, shear production of TKE is not a factor in TKE generation compared with buoyancy production. The cloud top region predicted in the simulation with radiative feedback is not as turbulent as that predicted in the other simulation.

Profiles of both solar and infrared optical depths at 30 and 60 minutes of the simulation time are compared and shown in Figures 5.29 and 5.30. Also, as expected, the larger ice

mass production in the simulation without radiative feedback results in larger optical depths than in the simulation with radiative feedback. The peaks in the optical depth profiles correspond very well to the peaks in PI and aggregate mixing ratios.

Similar to the model prediction for Case 1, radiative cooling is predicted almost throughout the cloud system for the simulation with radiative feedback, while for the simulation without radiative feedback, radiative warming dominates the cloud system from the cloud base to the middle cloud levels and cooling dominates from the middle cloud level to the cloud top (Figures 5.31 through 5.34).

5.3 Brief summary

CRM simulations of the November 26, 1991 cirrus event demonstrate that the radiative effects on ice particle's diffusional growth (or sublimation) can be significant on the evolution as well as ice mass production of cirrus clouds. Even in a radiatively cooling atmospheric environment, an ice particle may experience radiative warming because the total radiation which a particle experiences depends upon a three-way balance among its total emission and the local upwelling and downwelling radiative fluxes.

Radiative impact on the evolution and properties of cirrus clouds can be very complex. Radiative warming for an ice particle will restrict the particle's diffusional growth. In the case of radiative warming, ice particles larger than a certain size at which the radiative warming is balanced by the diffusion of heat away will have to undergo evaporation, resulting in inefficient production of large ice particles and total ice mass. However, ice mass production can be enhanced in the case of radiative cooling for an ice particle. In this case, the latent heat has to balance the diffusion of heat away as well as the outgoing radiation, speeding up the diffusional growth of the ice particle and theoretically putting no cap on the particle size which can be attained.

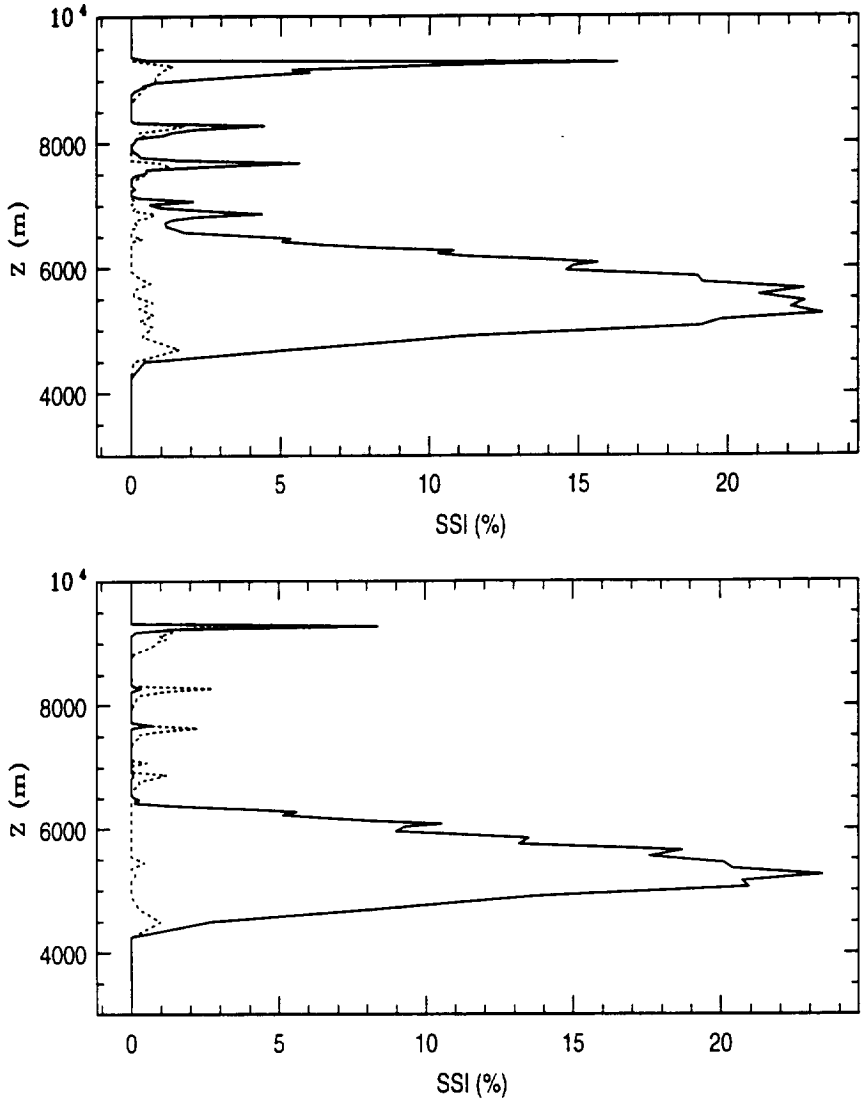

Figure 5.1: Profiles of domain averaged supersaturation with respect to ice at 30 (top) and 60 minutes (bottom) into the simulations for Case 1 (solid line: with radiative feedback; dotted line: without radiative feedback).

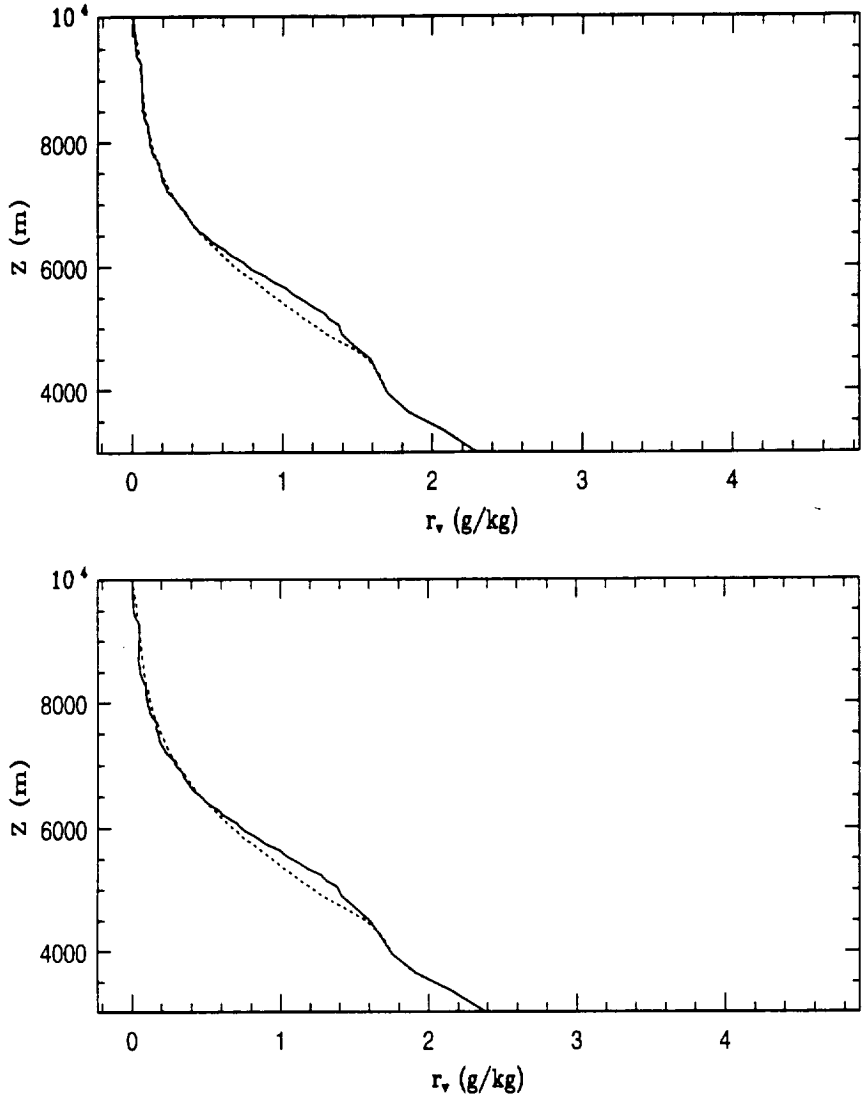

Figure 5.2: Profiles of domain averaged water vapor mixing ratio at 30 (top) and 60 minutes (bottom) into the simulations for Case 1 (solid line: with radiative feedback; dotted line: without radiative feedback).

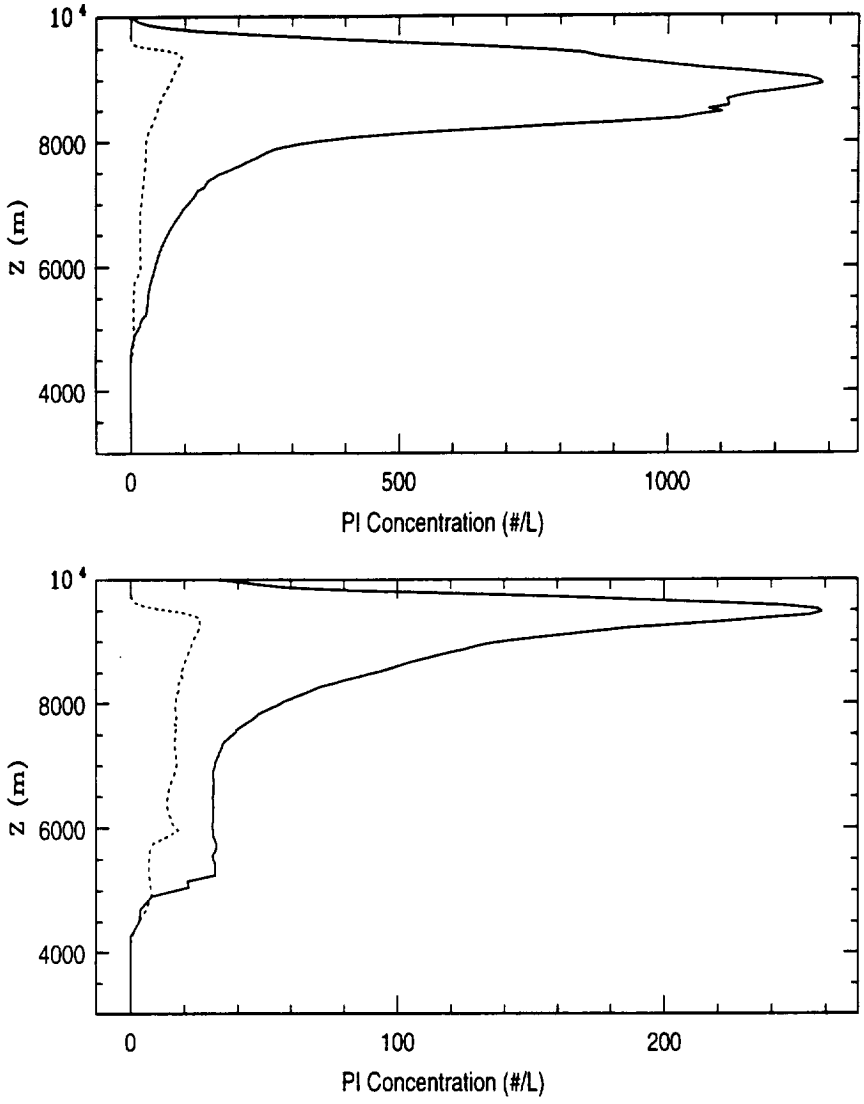

Figure 5.3: Profiles of domain averaged PI number concentration at 30 (top) and 60 minutes (bottom) into the simulations for Case 1 (solid line: with radiative feedback; dotted line: without radiative feedback).

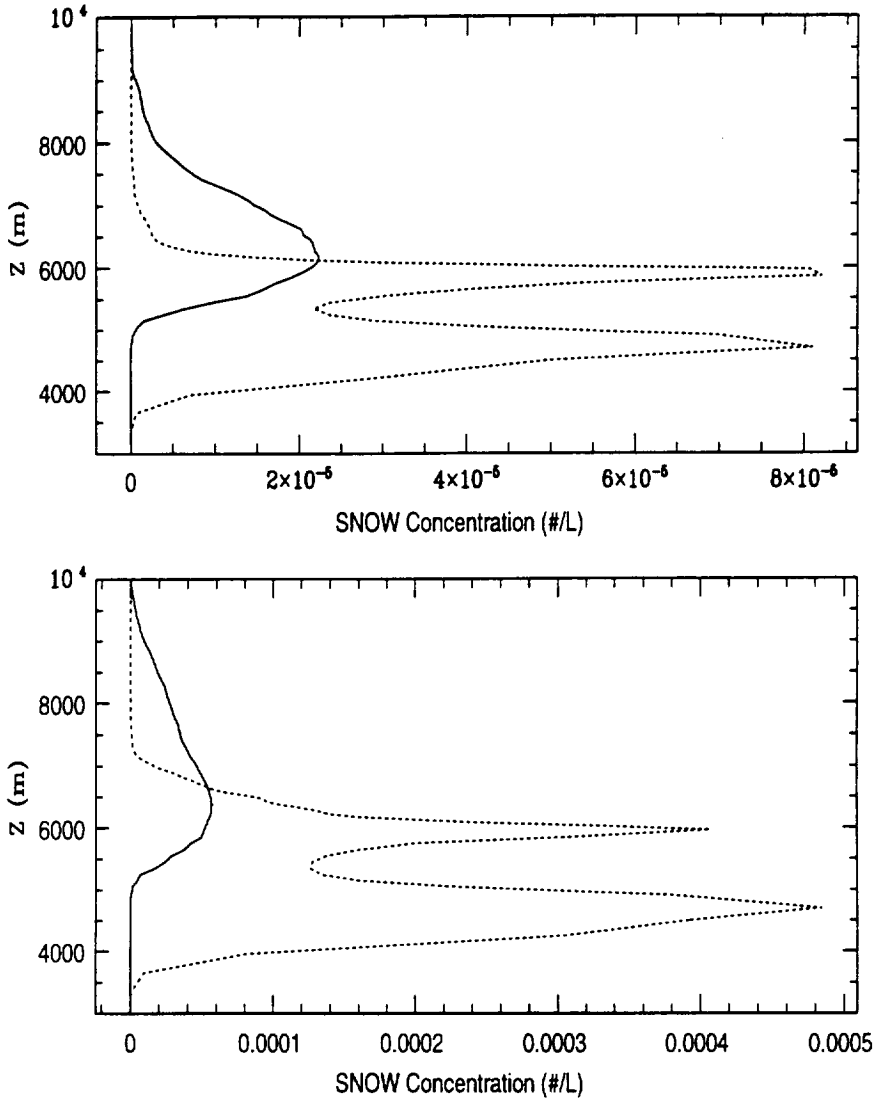

Figure 5.4: Profiles of domain averaged SNOW number concentration at 30 (top) and60 minutes (bottom) into the simulations for Case 1 (solid line: with radiative feedback; dotted line: without radiative feedback).

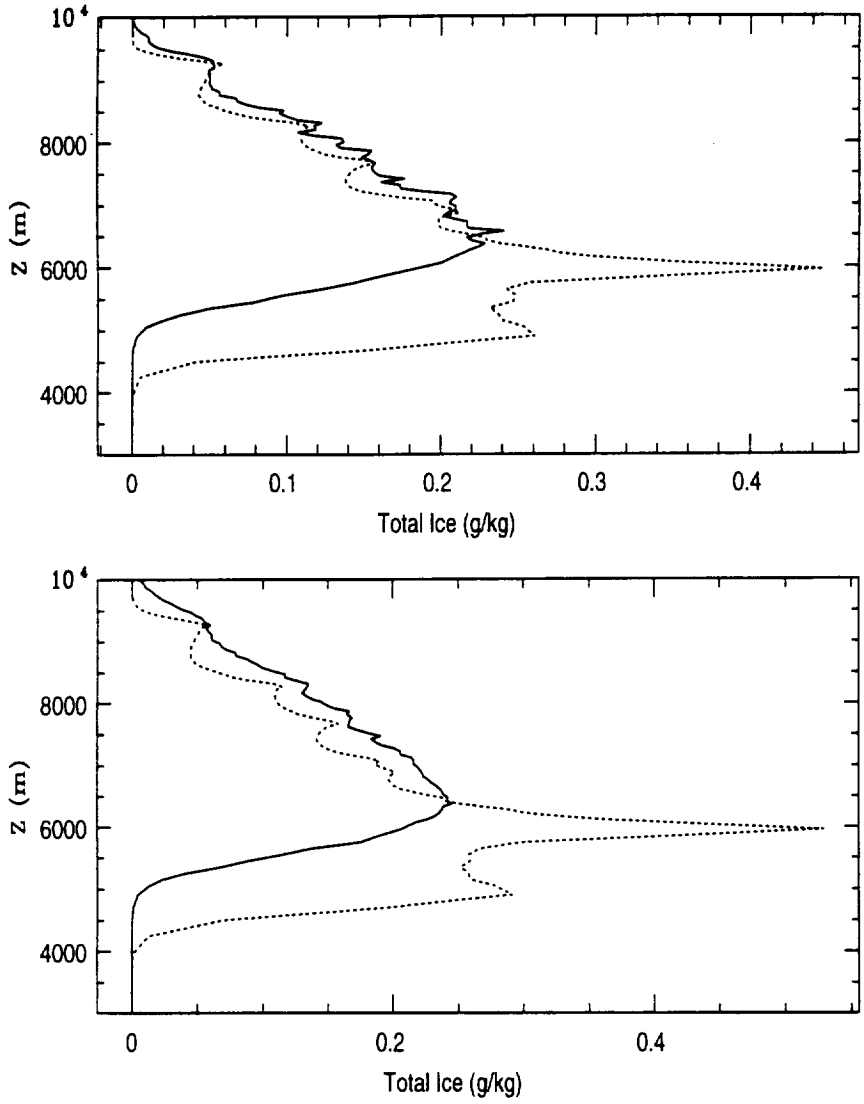

Figure 5.5: Profiles of domain averaged total ice at 30 (top) and 60 minutes (bottom) into the simulations for Case 1 (solid line: with radiative feedback; dotted line: without radiative feedback).

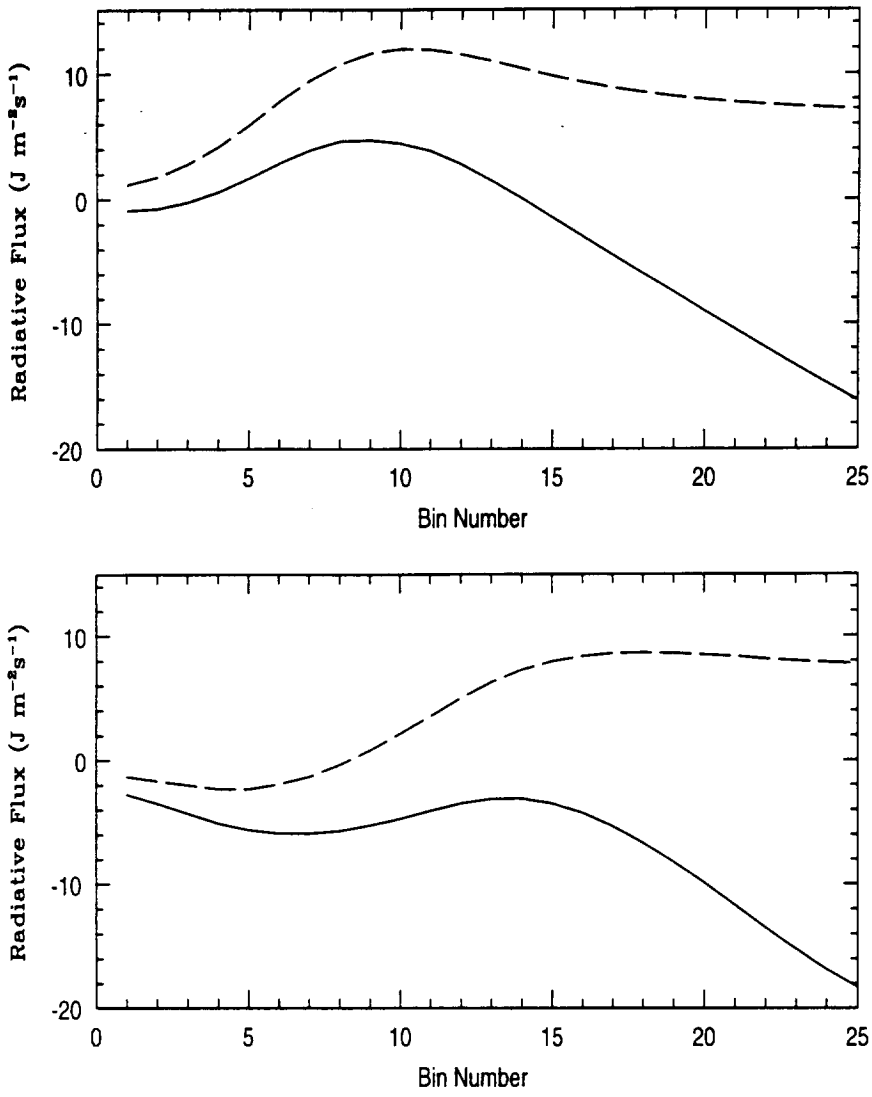

Figure 5.6: Examples of bin dependent radiative flux toward water (top) and ice (bottom) particles at 100 timestep (δt = 2 seconds) for a parcel originated near the cloud base for Case 2. Positive flux denotes radiative cooling, while negative denotes radiative warming effect.

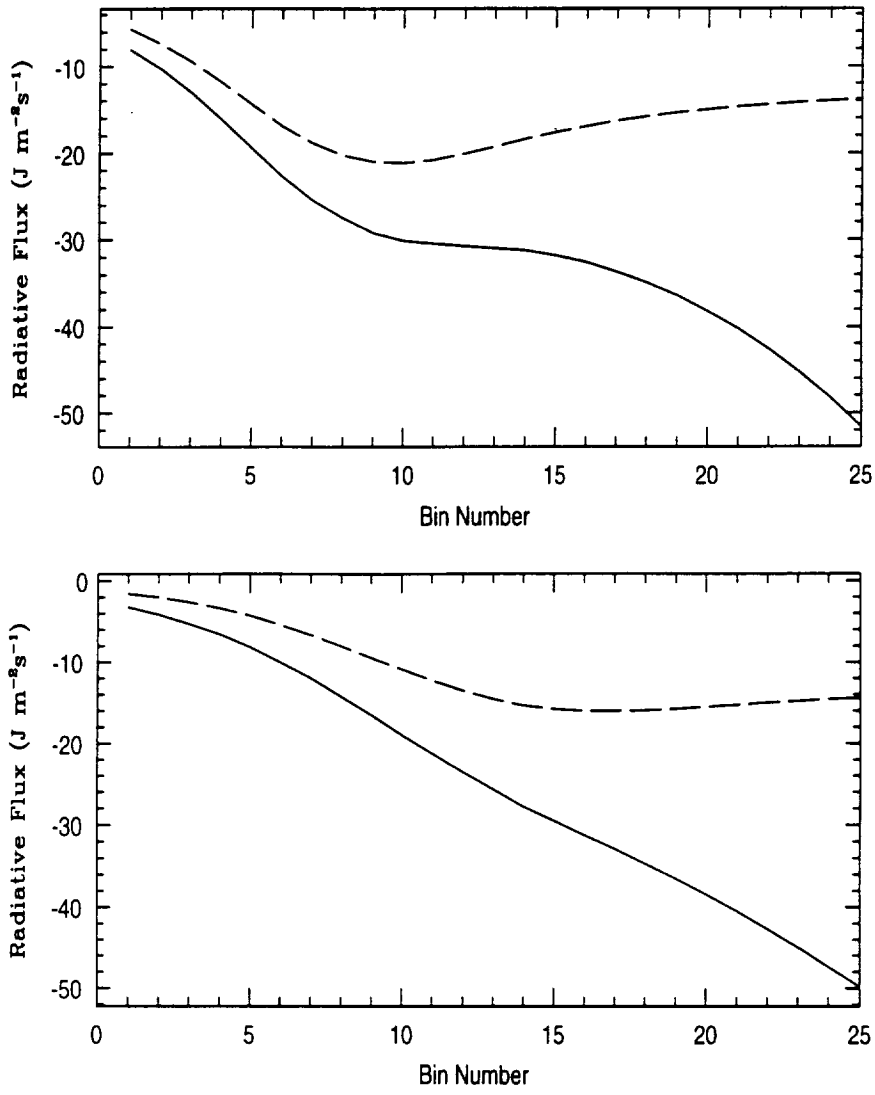

Figure 5.7: Examples of bin dependent radiative flux toward water (top) and ice (bottom) particles at 100 timestep ($\delta t = 2$ seconds) for a parcel originated deep in the cloud layer for Case 2. Positive flux denotes radiative cooling, while negative denotes radiative warming effect.

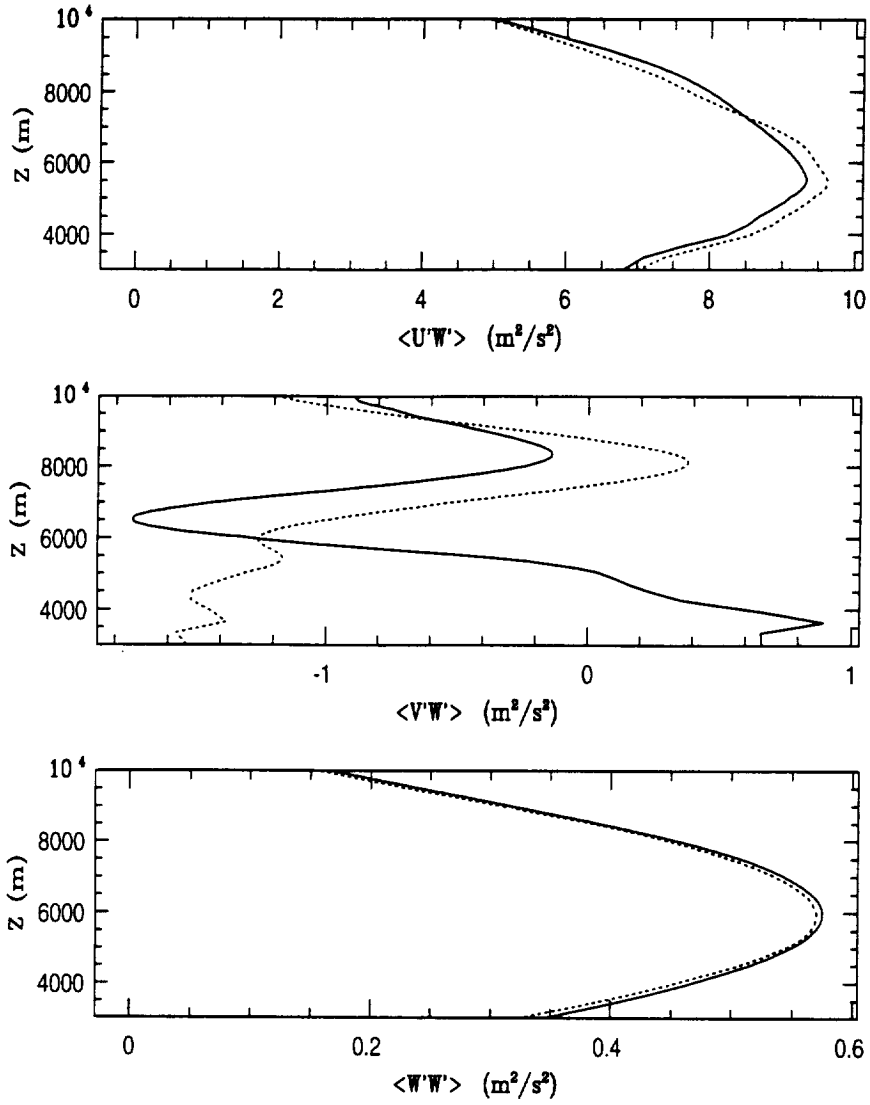

Figure 5.8: Profiles of momentum fluxes at 30 minutes of the simulation time for Case 1. The solid line and dotted line are for runs with and without radiative feedback, respectively.

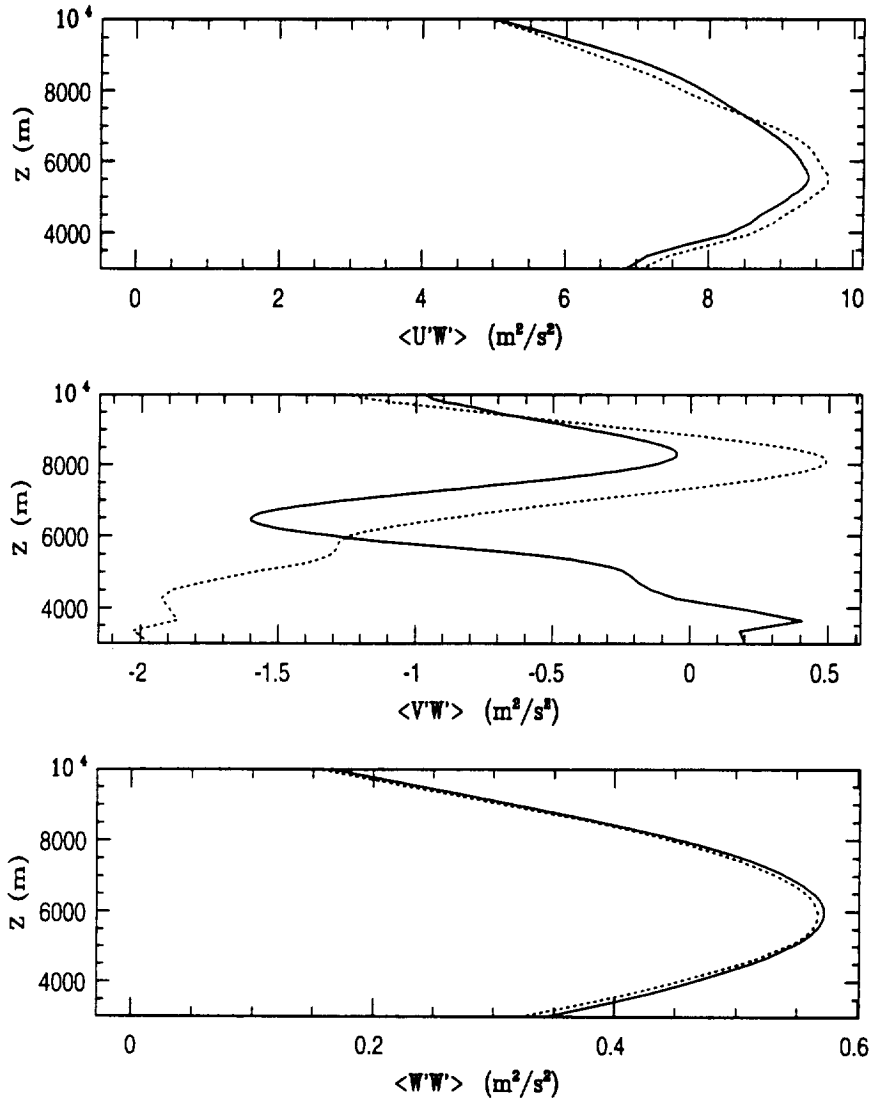

Figure 5.9: Momentum flux profiles at 60 minutes of simulation time for Case 1.

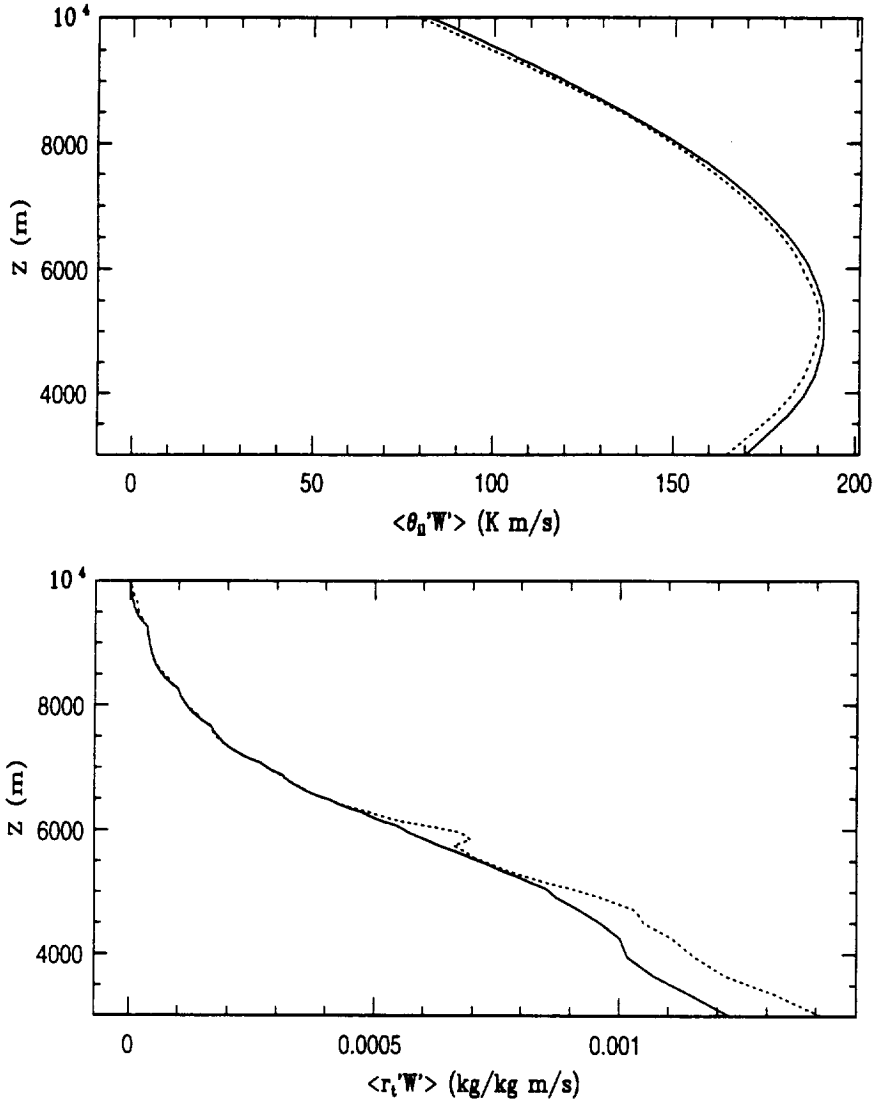

Figure 5.10: Profiles of $< \theta'_{il} W' >$ and $< r'_t W' >$ at 30 minutes of simulation time for Case 1. The solid line and dotted line are for runs with and without radiative feedback, respectively.

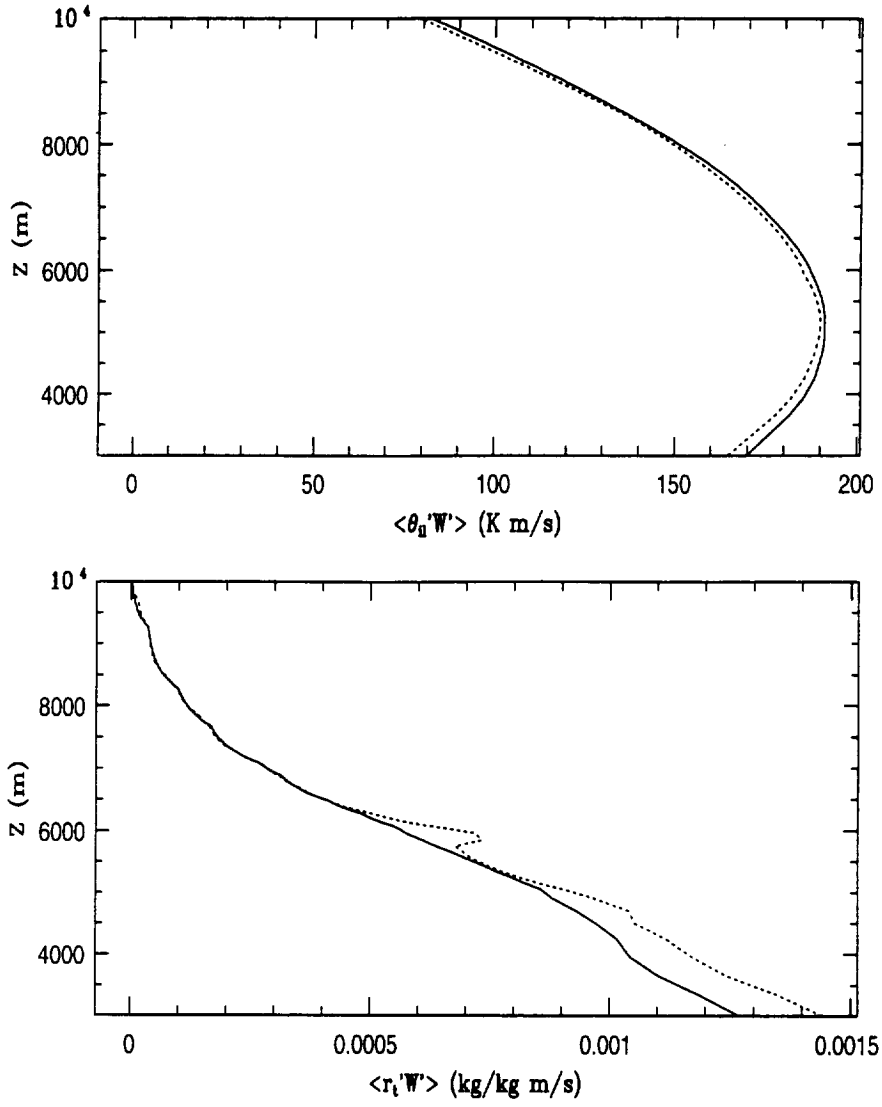

Figure 5.11: Profiles of $< \theta'_{il} W' >$ and $< r'_t W' >$ at 60 minutes of simulation time for Case 1. The solid line and dotted line are for runs with and without radiative feedback, respectively.

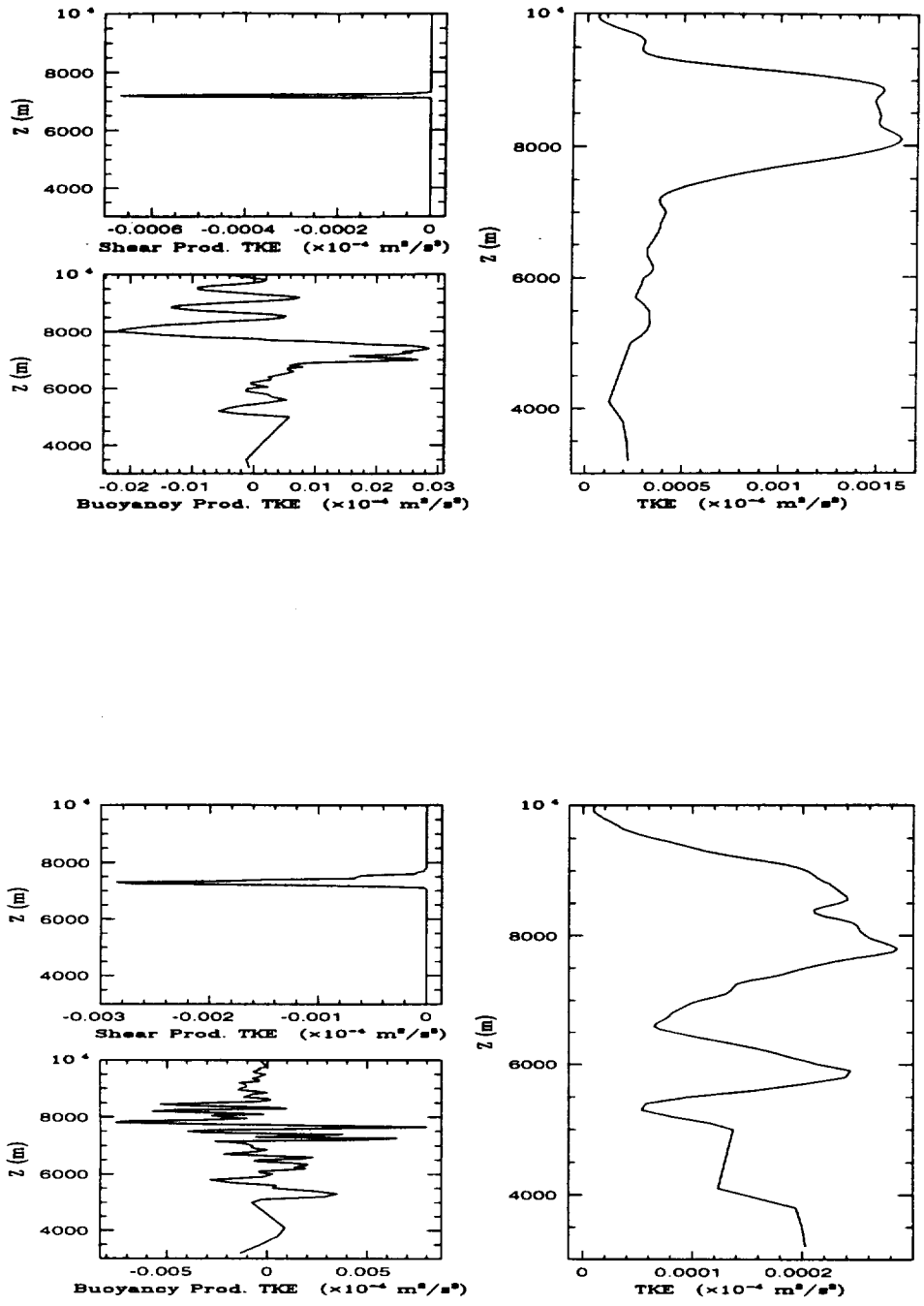

Figure 5.12: Profiles of total TKE and TKE production terms for the simulations without (top) and with (bottom) radiative feedback on particle's diffusional growth at 60 minutes of the simulation time for Case1.

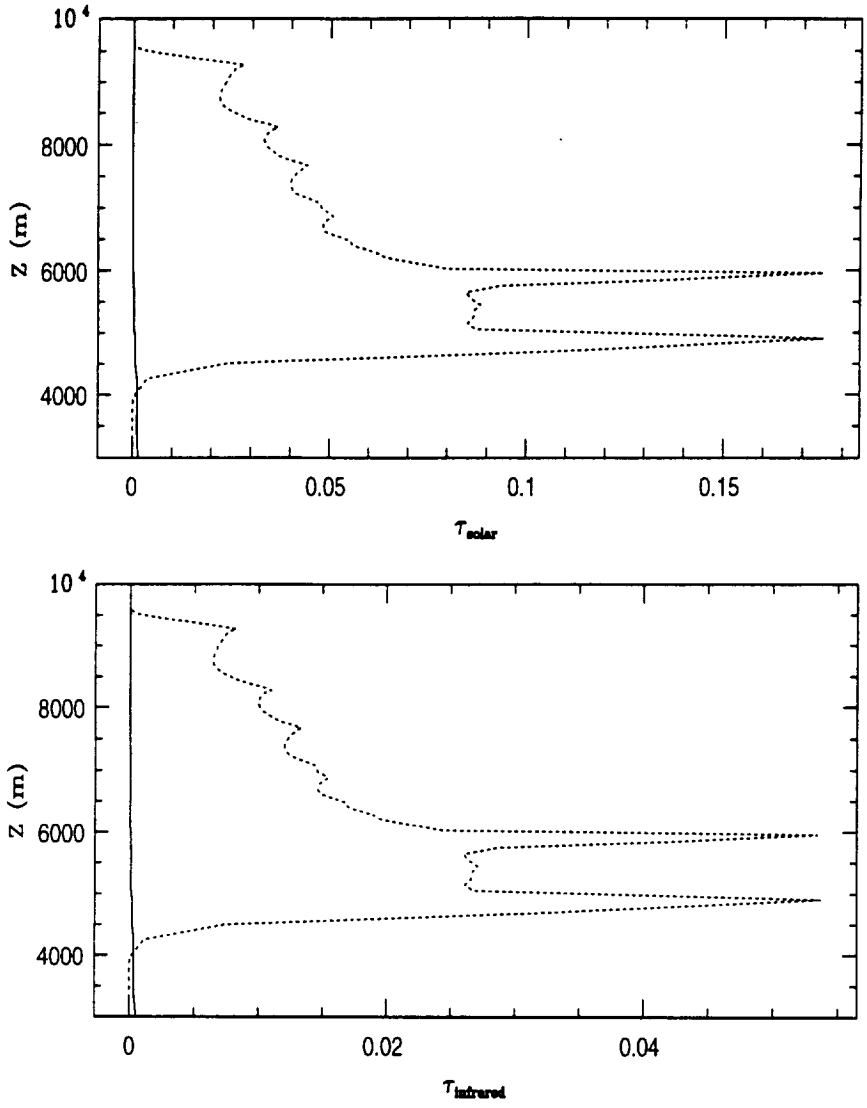

Figure 5.13: Profiles of solar (τ_{solar}) and infrared ($\tau_{infrared}$) optical depths at 30 minutes of simulation time for Case 1. The solid line and dotted line are for runs with and without radiative feedback, respectively.

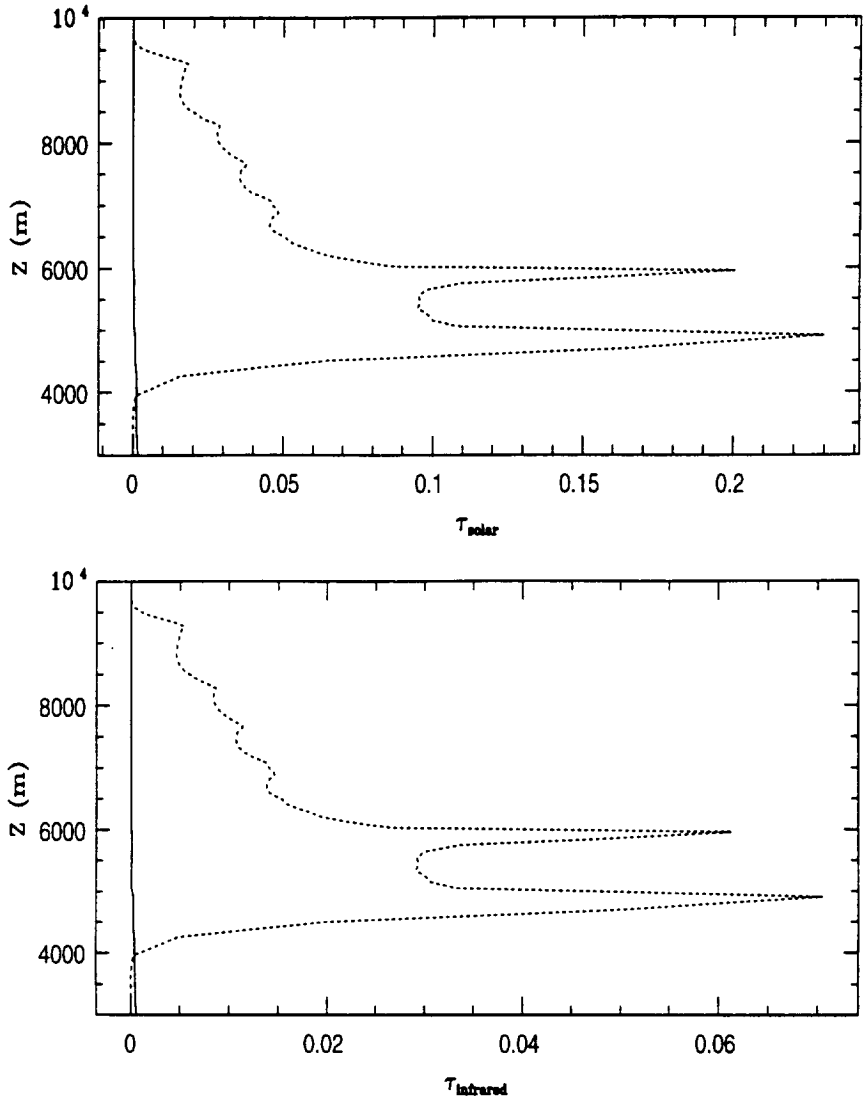

Figure 5.14: Profiles of solar (τ_{solar}) and infrared ($\tau_{infrared}$) optical depths at 60 minutes of simulation time for Case 1. The solid line and dotted line are for runs with and without radiative feedback, respectively.

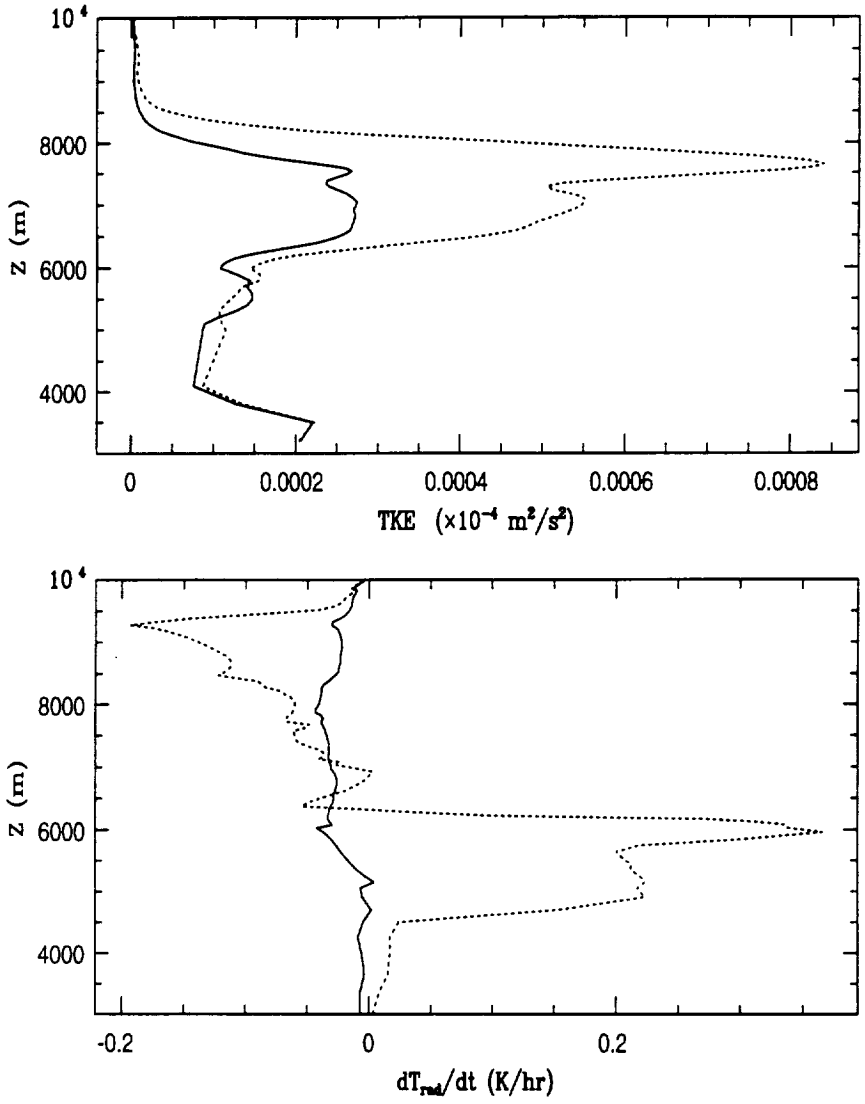

Figure 5.15: Profiles of turbulent kinetic energy (TKE) and radiative heating rate (dT_{rad}/dt) at 30 minutes of simulation time for Case 1. The solid line and dotted line are for runs with and without radiative feedback, respectively.

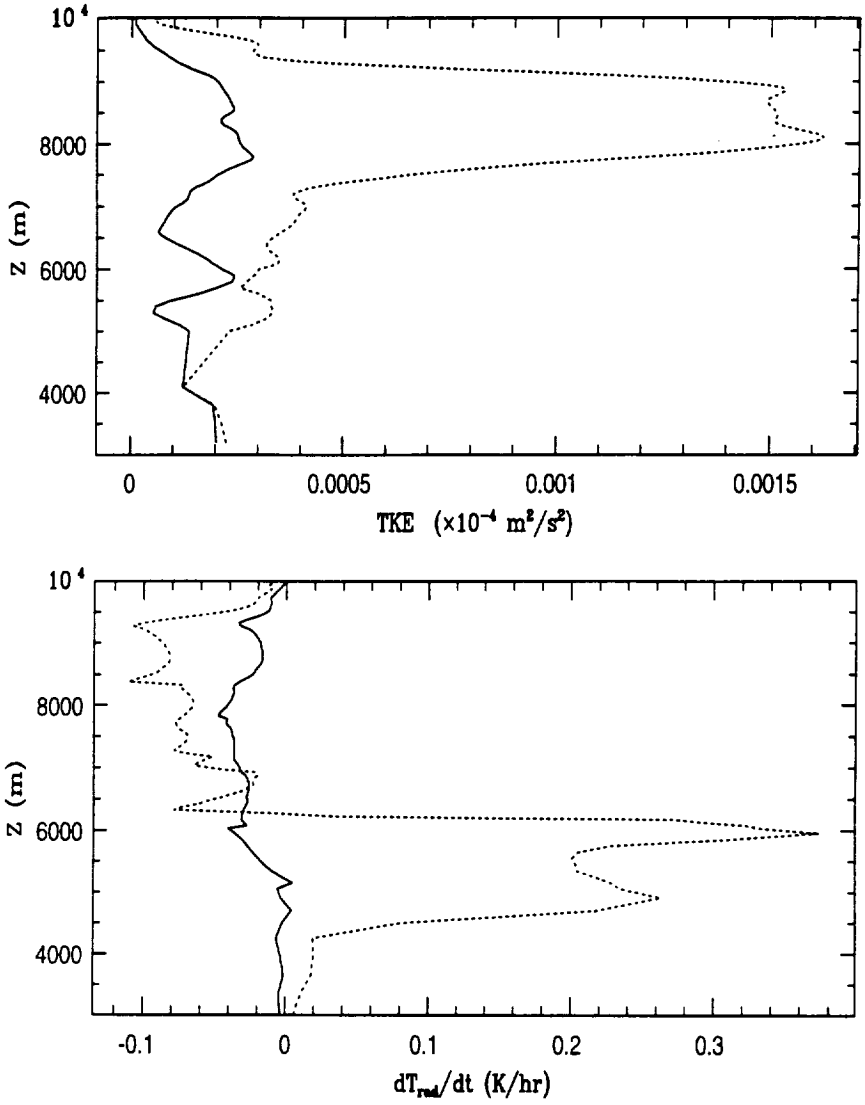

Figure 5.16: Profiles of turbulent kinetic energy (TKE) and radiative heating rate (dT_{rad}/dt) at 60 minutes of simulation time for Case 1. The solid line and dotted line are for runs with and without radiative feedback, respectively.

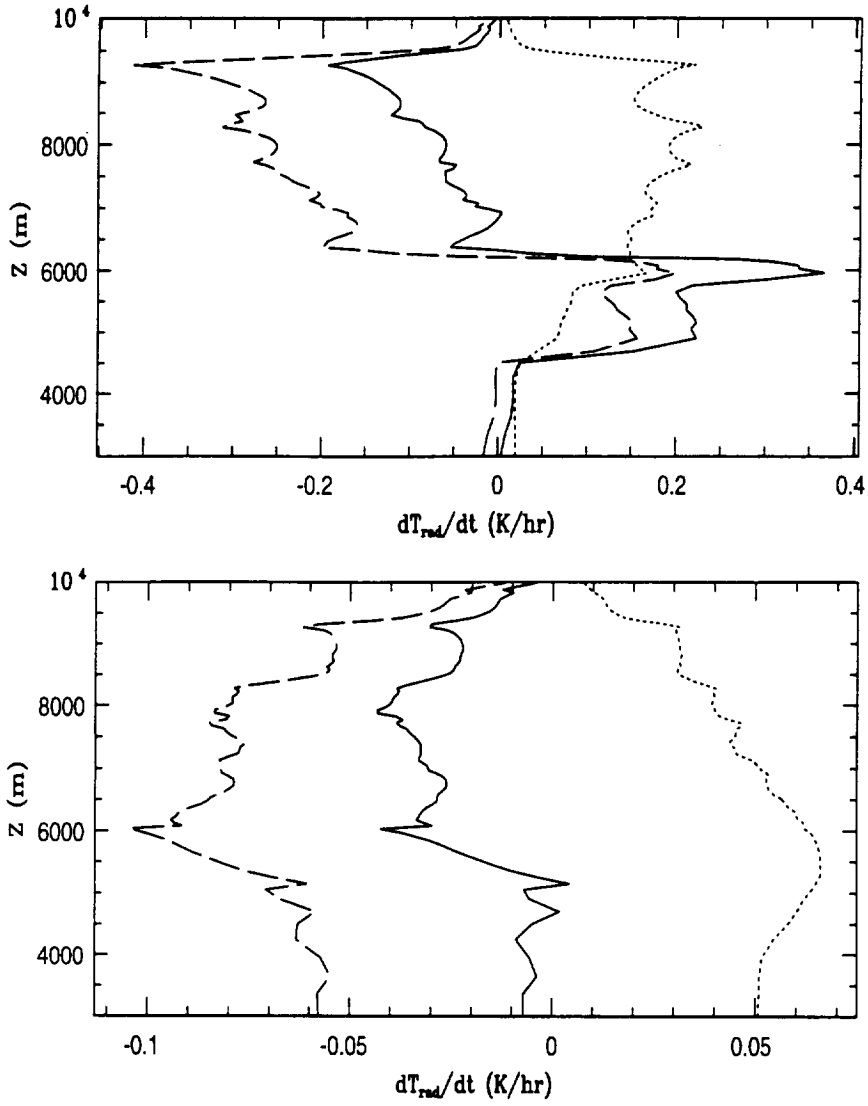

Figure 5.17: Profiles of total (solid), infrared (dashed), and solar (dotted) radiative heating rates at 30 minutes of simulation time for Case 1. Top: without radiative feedback on particles' diffusional growth; bottom: with radiative feedback.

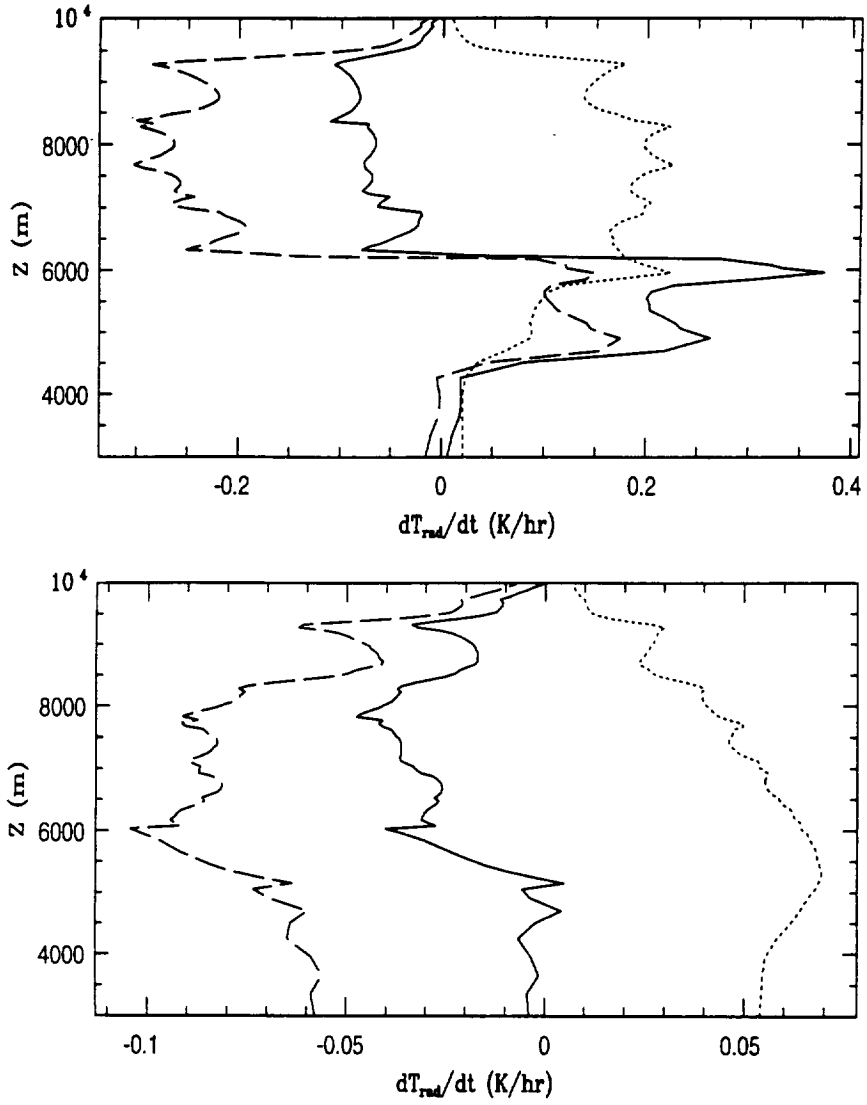

Figure 5.18: Profiles of total (solid), infrared (dashed), and solar (dotted) radiative heating rates at 60 minutes of simulation time for Case 1. Top: without radiative feedback on particles' diffusional growth; bottom: with radiative feedback.

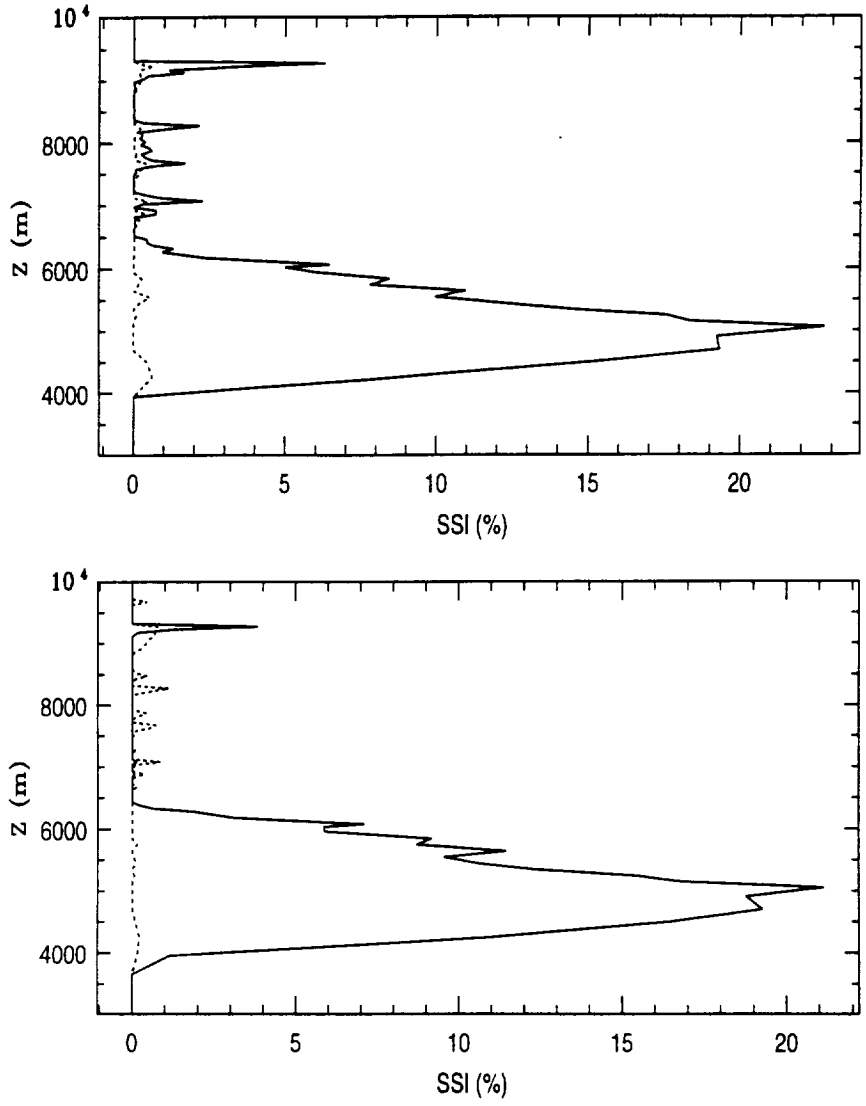

Figure 5.19: Profiles of domain averaged supersaturation with respect to ice at 30 (top) and 60 minutes (bottom) into the simulations for Case 2 (solid line: with radiative feedback; dotted line: without radiative feedback).

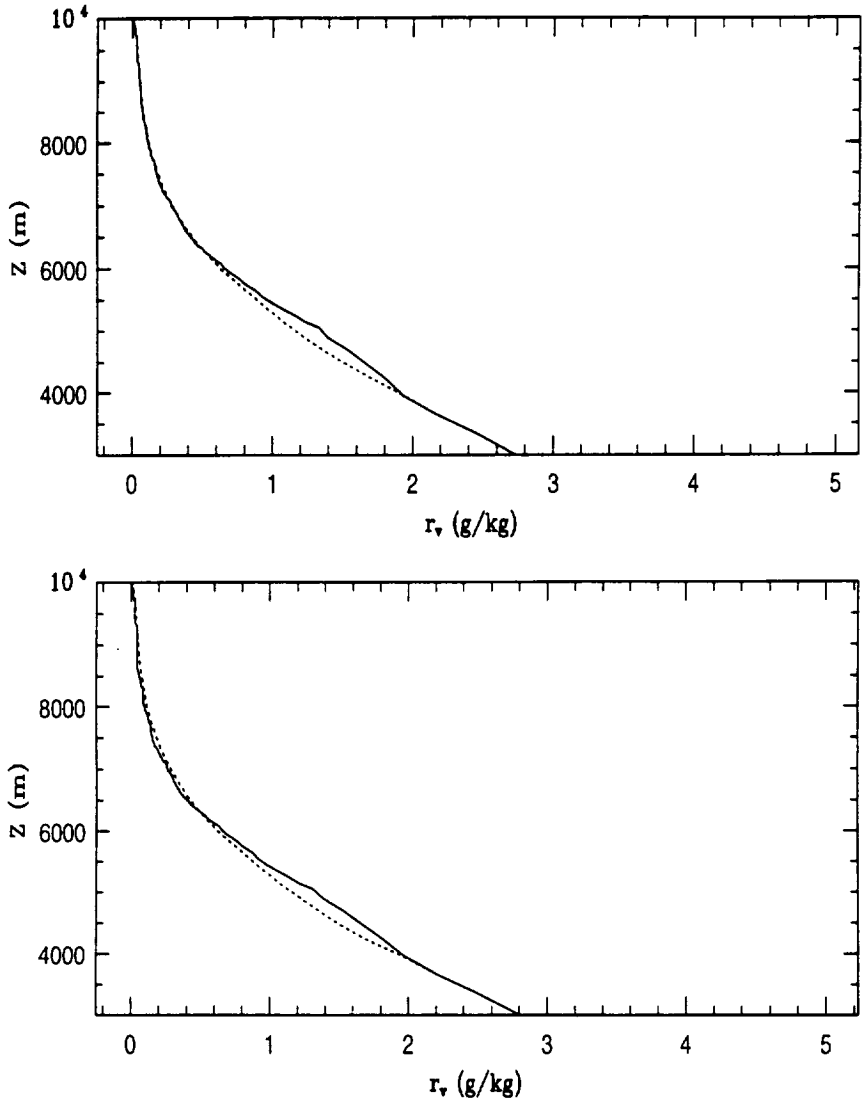

Figure 5.20: Profiles of domain averaged water vapor mixing ratio at 30 (top) and 60 minutes (bottom) into the simulations for Case 2 (solid line: with radiative feedback; dotted line: without radiative feedback).

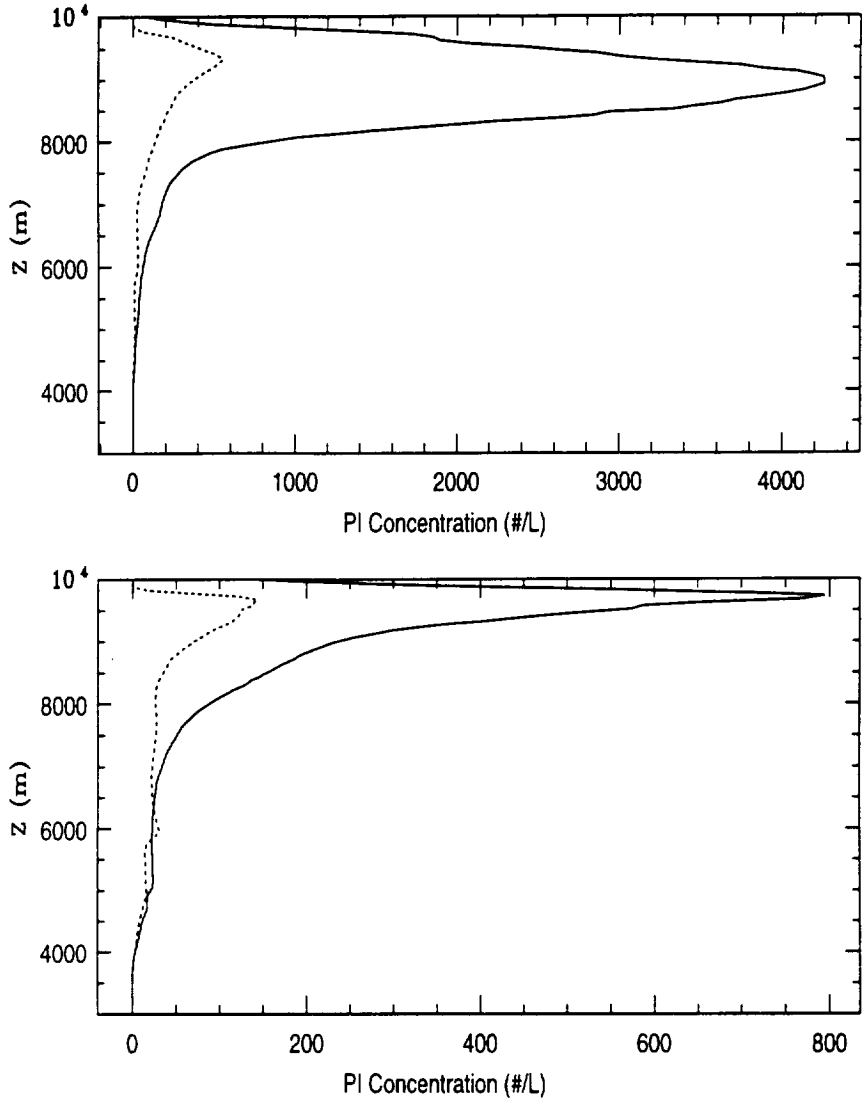

Figure 5.21: Profiles of domain averaged PI number concentration at 30 (top) and 60 minutes (bottom) into the simulations for Case 2 (solid line: with radiative feedback; dotted line: without radiative feedback).

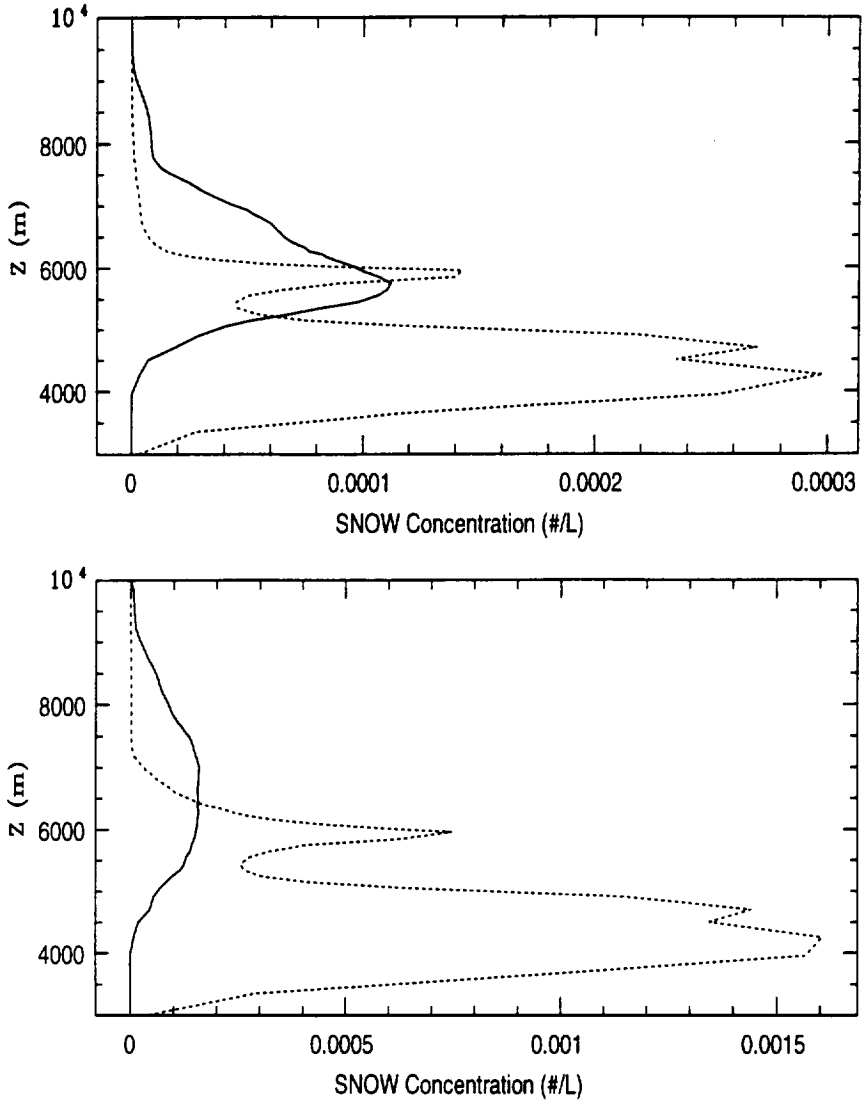

Figure 5.22: Profiles of domain averaged SNOW number concentration at 30 (top) and 60 minutes (bottom) into the simulations for Case 2 (solid line: with radiative feedback; dotted line: without radiative feedback).

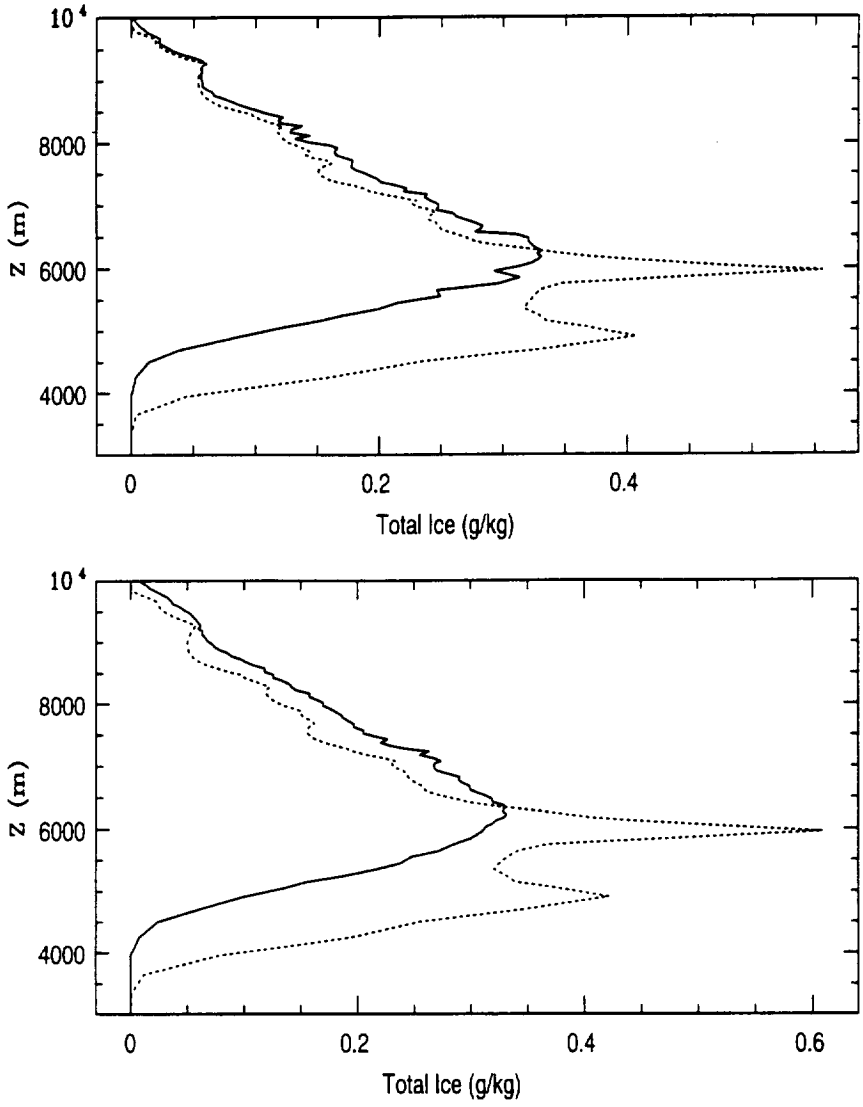

Figure 5.23: Profiles of domain averaged total ice at 30 (top) and 60 minutes (bottom) into the simulations for Case 2 (solid line: with radiative feedback; dotted line: without radiative feedback).

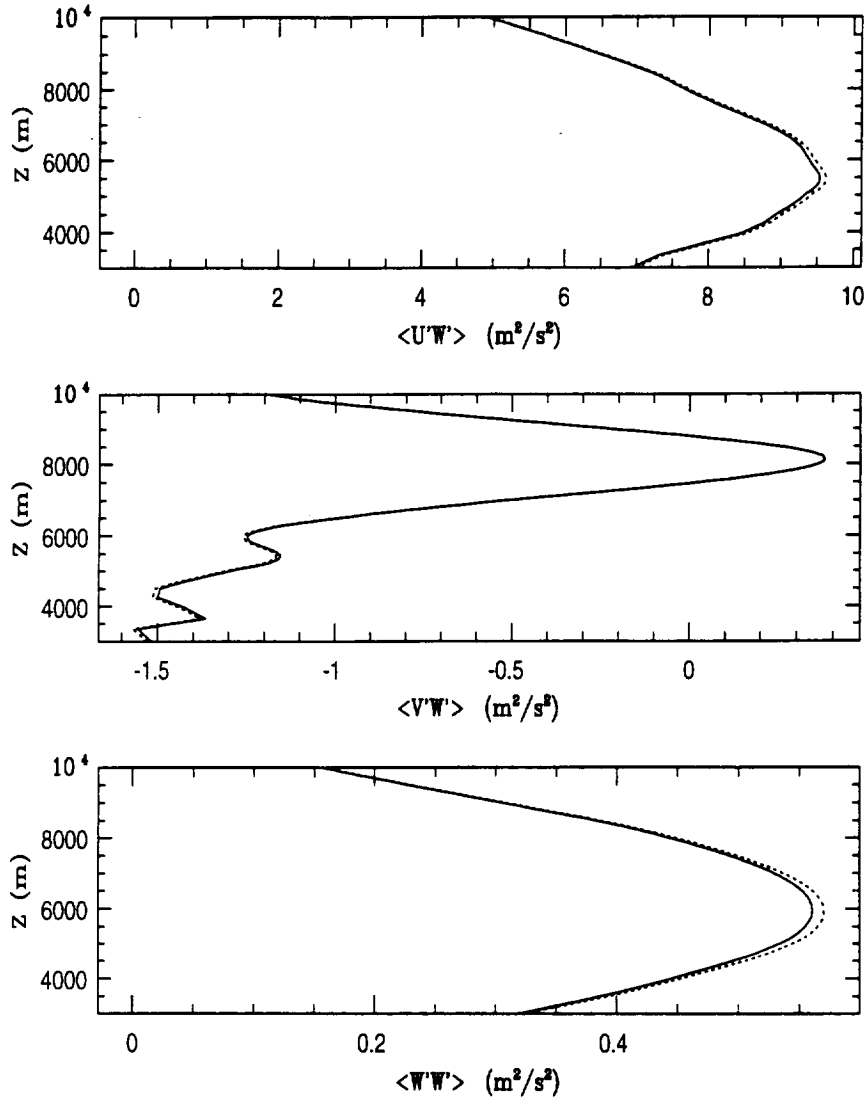

Figure 5.24: Profiles of momentum fluxes at 30 minutes of the simulation time for Case 2. The solid line and dotted line are for runs with and without radiative feedback, respectively.

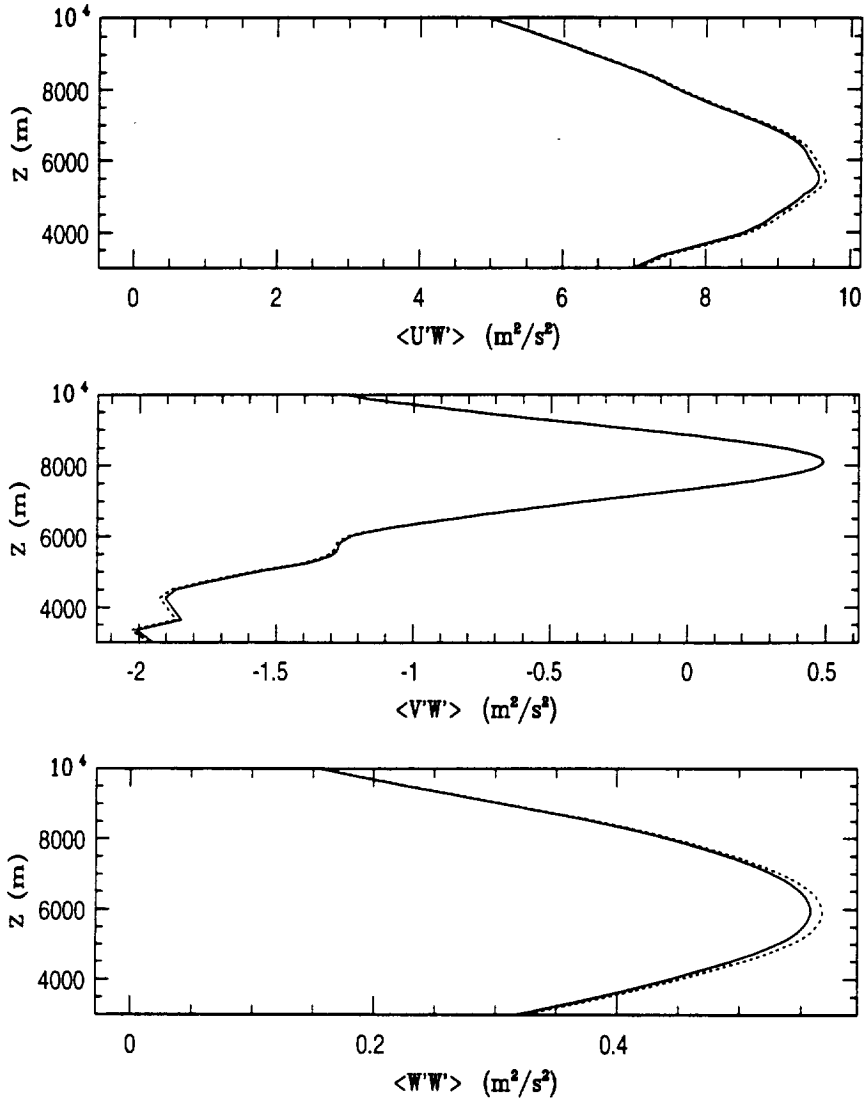

Figure 5.25: Momentum flux profiles at 60 minutes of simulation time for Case 2. The solid line and dotted line are for runs with and without radiative feedback, respectively.

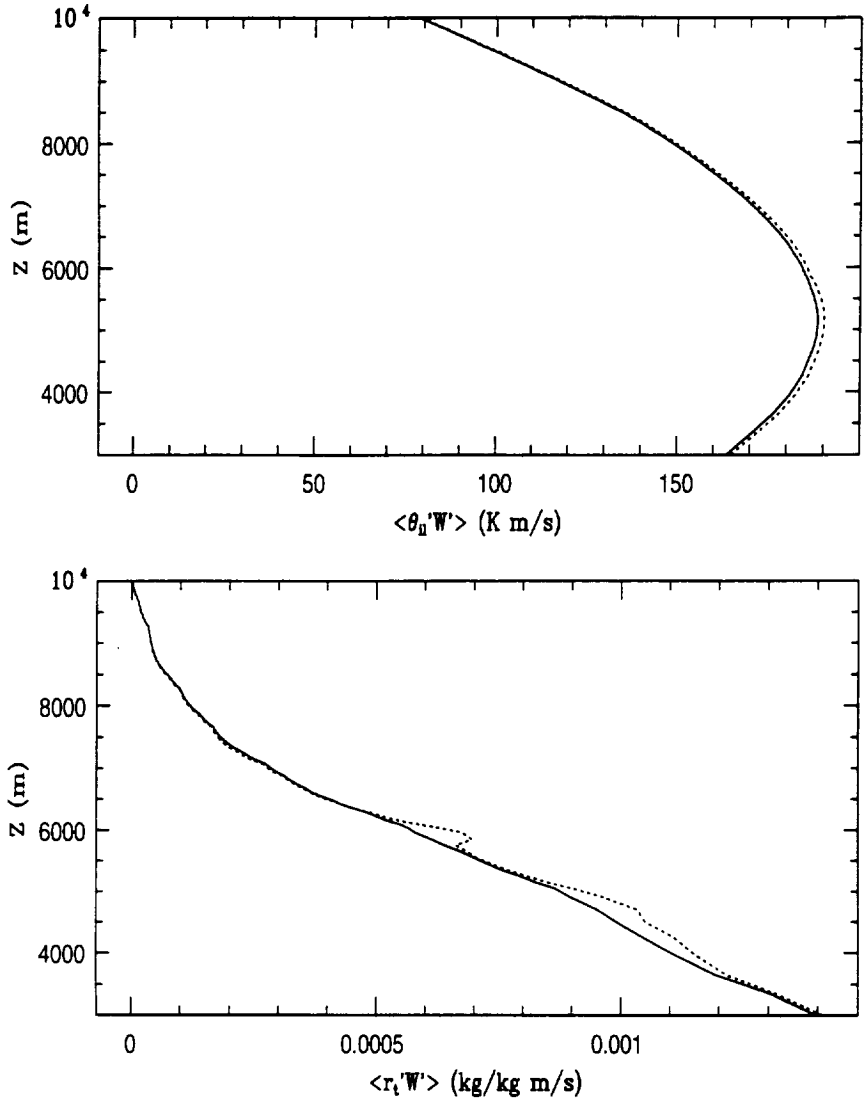

Figure 5.26: Profiles of $< \theta'_{il} W' >$ and $< r'_t W' >$ at 30 minutes of simulation time for Case 2. The solid line and dotted line are for runs with and without radiative feedback, respectively.

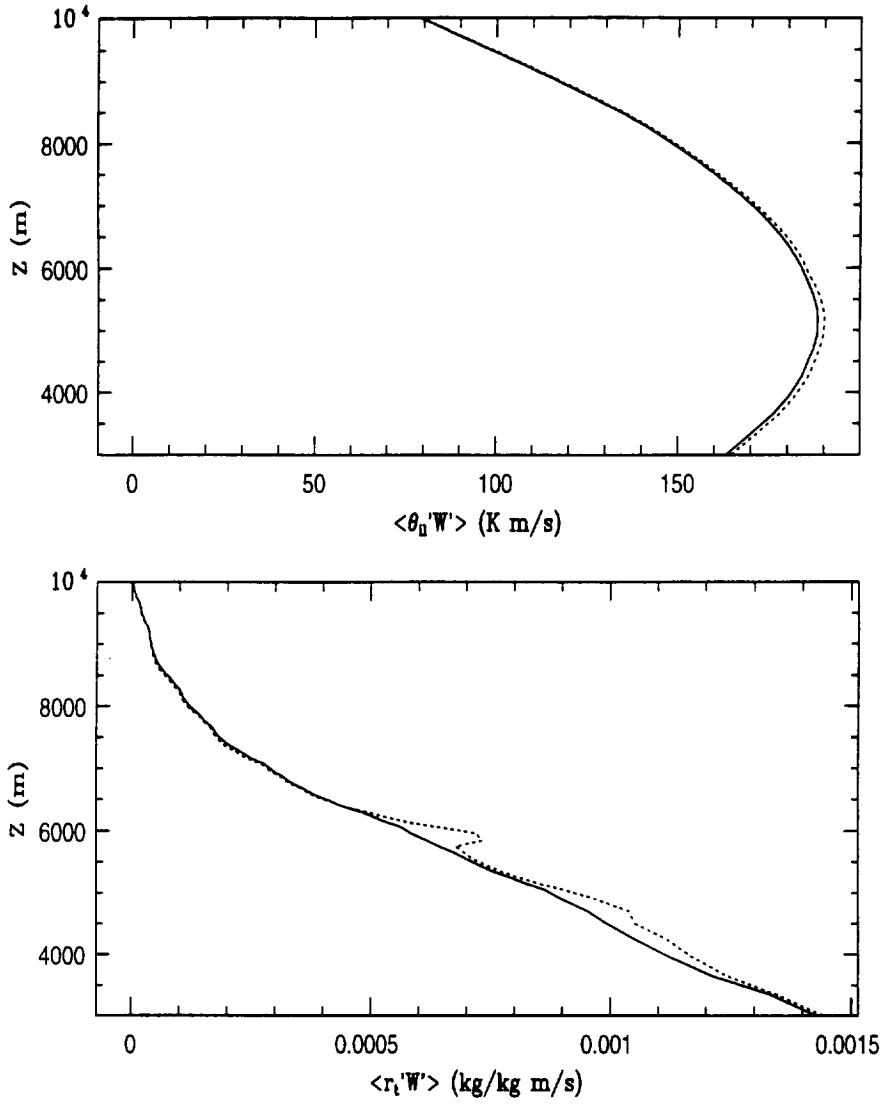

Figure 5.27: Profiles of $< \theta'_{il} W' >$ and $< r'_t W' >$ at 60 minutes of simulation time for Case 2. The solid line and dotted line are for runs with and without radiative feedback, respectively.

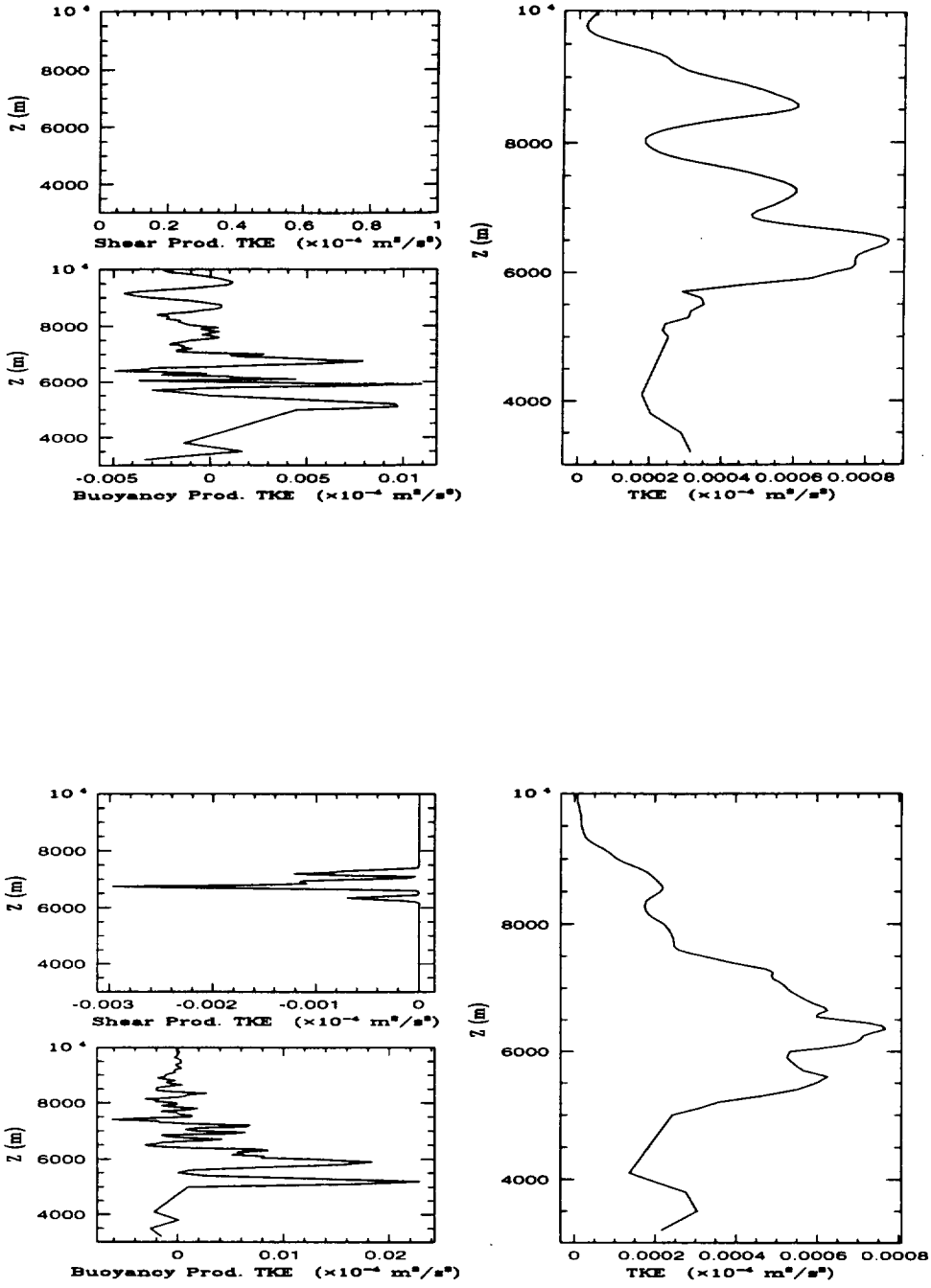

Figure 5.28: Profiles of total TKE and TKE production terms for the simulations without (top) and with (bottom) radiative feedback on particle's diffusional growth at 60 minutes of the simulation time for Case2.

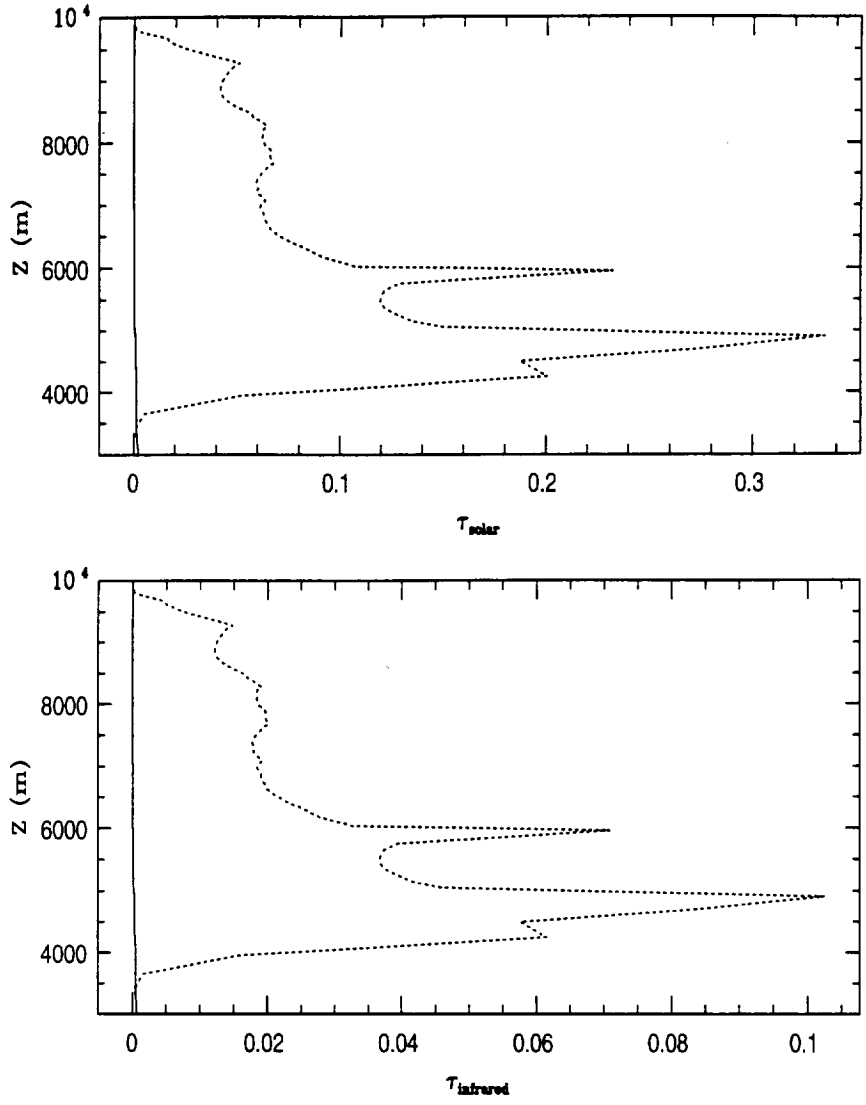

Figure 5.29: Profiles of solar (τ_{solar}) and infrared ($\tau_{infrared}$) optical depths at 30 minutes of simulation time for Case 2. The solid line and dotted line are for runs with and without radiative feedback, respectively.

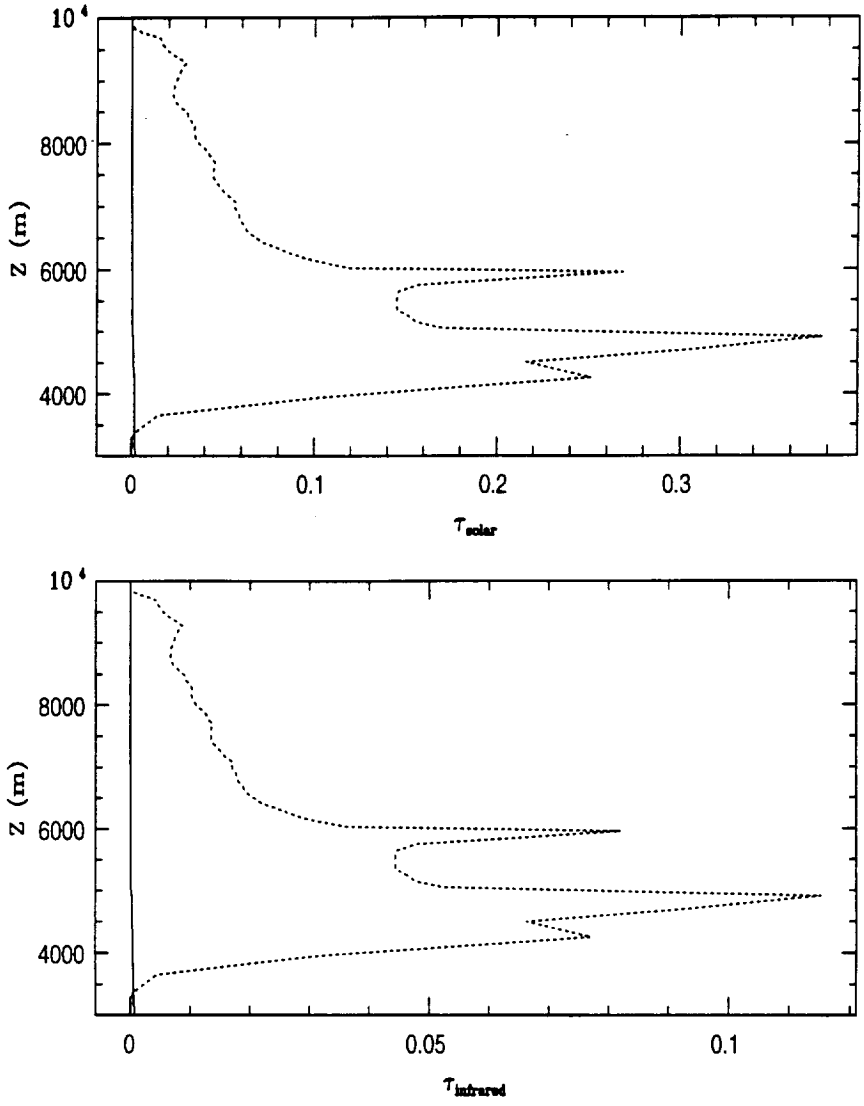

Figure 5.30: Profiles of solar (τ_{solar}) and infrared ($\tau_{infrared}$) optical depths at 60 minutes of simulation time for Case 2. The solid line and dotted line are for runs with and without radiative feedback, respectively.

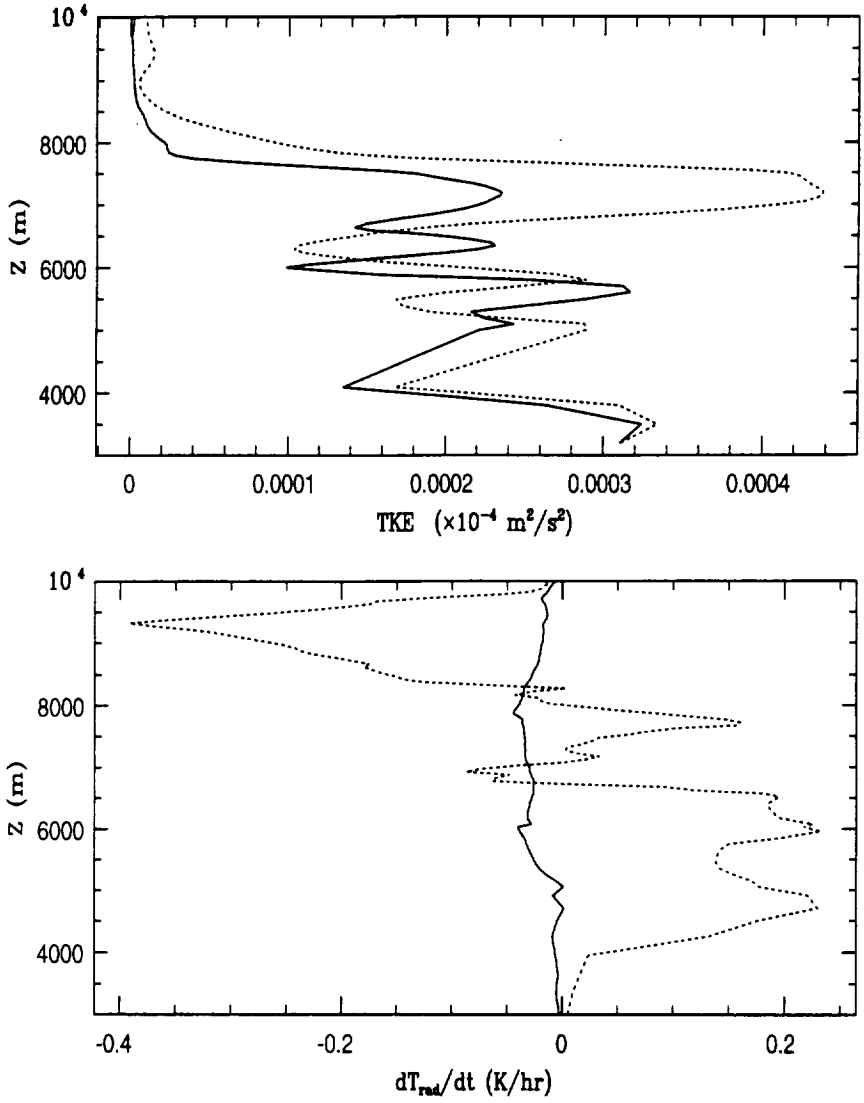

Figure 5.31: Profiles of turbulent kinetic energy (TKE) and total radiative heating rate (dT_{rad}/dt) at 30 minutes of simulation time for Case 2. The solid line and dotted line are for runs with and without radiative feedback, respectively.

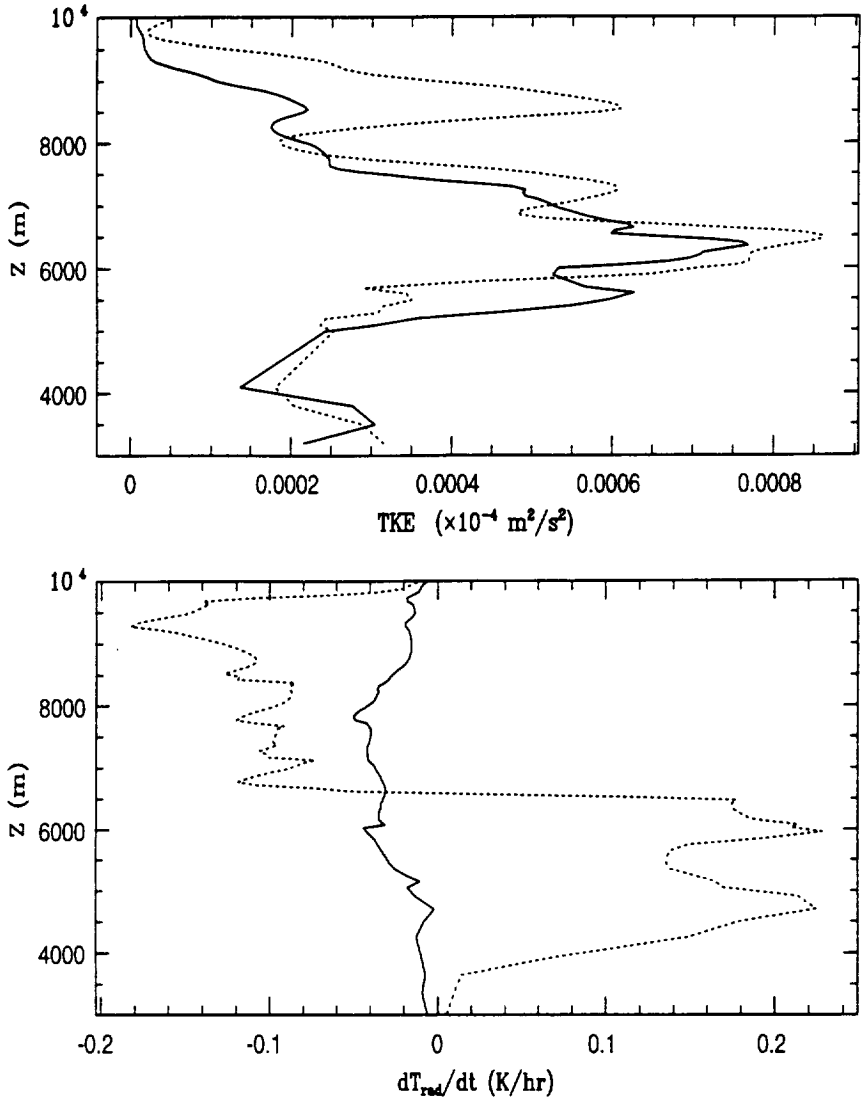

Figure 5.32: Profiles of turbulent kinetic energy (TKE) and total radiative heating rate (dT_{rad}/dt) at 60 minutes of simulation time for Case 2. The solid line and dotted line are for runs with and without radiative feedback, respectively.

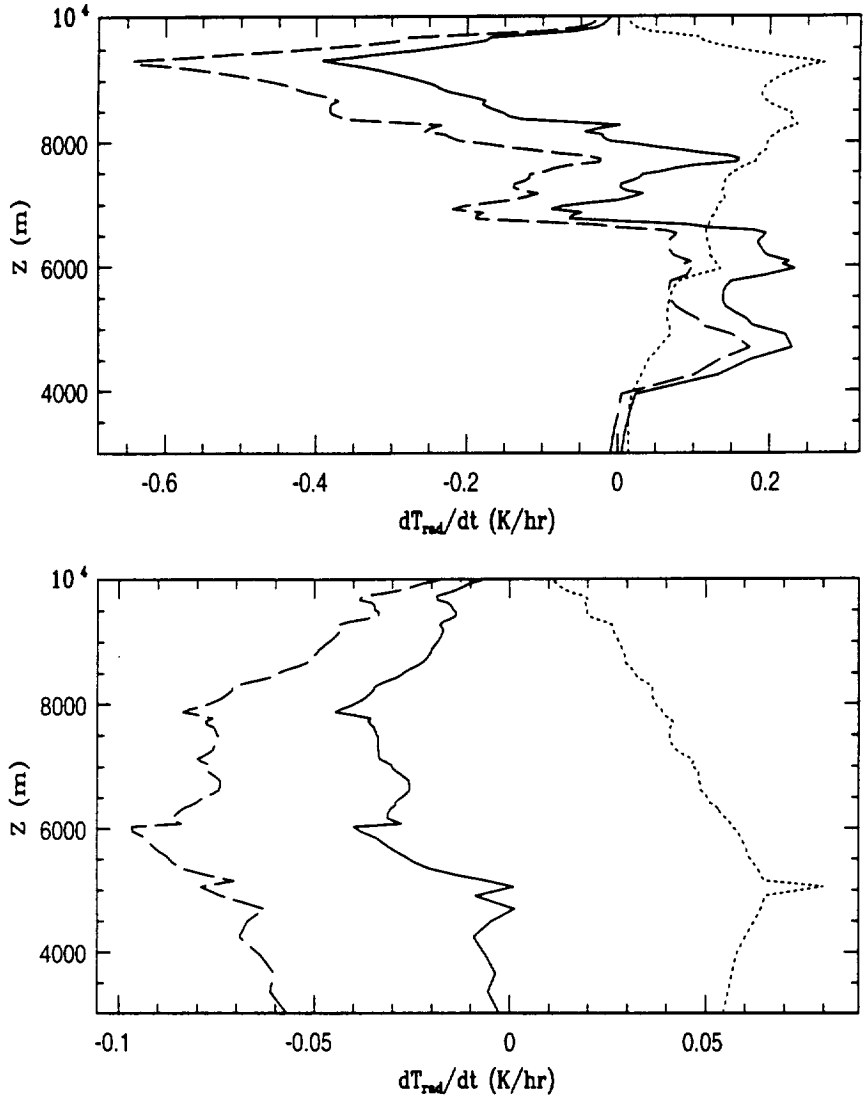

Figure 5.33: Profiles of total (solid), infrared (dashed), and solar (dotted) radiative heating rates at 30 minutes of simulation time for Case 2. Top: without radiative feedback on particles' diffusional growth; bottom: with radiative feedback.

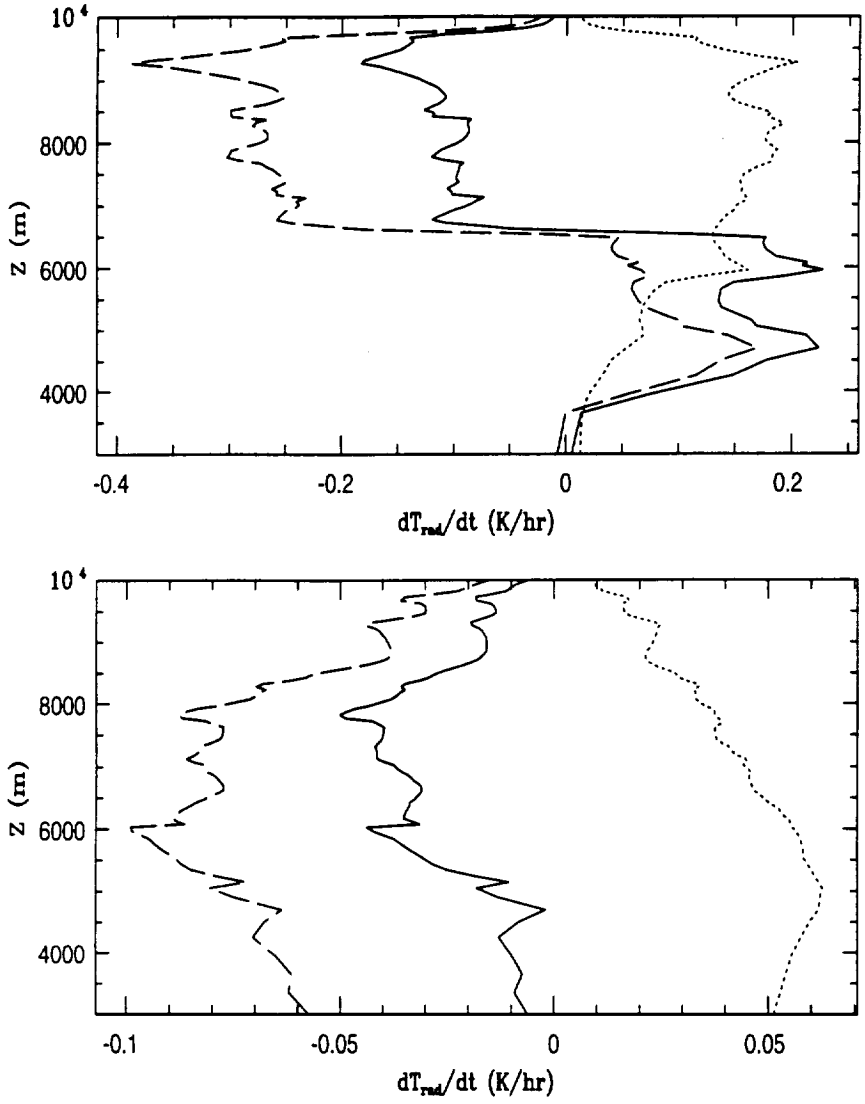

Figure 5.34: Profiles of total (solid), infrared (dashed), and solar (dotted) radiative heating rates at 60 minutes of simulation time for Case 2. Top: without radiative feedback on particles' diffusional growth; bottom: with radiative feedback.

Chapter 6

SUMMARY AND FUTURE WORK

6.1 Summary

The November 26, 1991 cirrus event is investigated. The cloud system is simulated using RAMS mesoscale nested grids, LES grid, and CRM framework. RAMS mesoscale nested grids (65 vertical levels) and LES grid (115 vertical levels), coupled to two-moment microphysics are the most sophisticated numerical models with the highest vertical resolutions (to our knowledge) for any three-dimensional simulations attempted to study the dynamic, microphysical, and radiative processes in cirrus clouds. Radiative effects on ice particle's diffusional growth are first investigated under the CRM framework which is coupled to a detailed bin-microphysical model and a new two-stream radiative transfer code.

Results from the RAMS nested grid simulations display considerable agreement with the observations. The strong agreement between the large scale circulation as well as cloud bands from RAMS mesoscale nested grid prediction and the observations provides confidence and lays credible foundation for the LES and CRM studies of this cirrus event. Listed below is a summary of the significant findings from this research work.

- The ageostrophic circulation associated with the exit region of an upper-level jet stream provides large scale forcing for the cloud development under favorable moisture conditions.

- The simulated cirrus clouds display properties similar to *forced boundary-layer clouds* because of the similarity in their dynamics. In spite of the latent heat release during phase change, there is insufficient heating for cirrus clouds to become positively buoyant, especially for the shallow cirrus case. As a result, the LES simulated shallow

cirrus cloud system behaves as a quasi-passive tracer at the top of the troposphere. However, in some cases, such as the LES simulated deep cloud system, positively buoyant cells are quite actively embedded in cirrus layers. These active cells significantly affect the cloud evolution.

- Latent heating cannot be simply neglected in cirrus cloud models. In fact, it can be a key factor in the development of layered structures in cirrus clouds. Corresponding to active cloud development, the maximum latent heating rate can be as large as $0.85K/hr$ in the early stage of simulation. For thin and passive cirrus clouds, latent heating can be very small compared with radiative heating (or cooling). However, latent heating can be as important as radiative heating (or cooling) when clouds are active and deep.

- The fluxes of momentum, θ_{il}, and r_t show strong variation for the LES simulations. Generally, momentum fluxes have magnitudes less than $0.1m^2s^{-2}$, θ_{il} fluxes less than $0.1Kms^{-1}$, and r_t fluxes less than $10^{-5}kg/kgms^{-1}$. Corresponding to layered cloud structures which are commonly seen in mid-latitude cirrus clouds, LES studies also show that eddy transport and mixing can be decoupled in the vertical after the clouds are well developed.

- LES simulations also display a feature that fluxes of quantities near cloud top can be quite small compared with the in-cloud fluxes and near cloud base they can be as large as or even larger than the corresponding in-cloud fluxes. The small magnitude of fluxes near cloud top may be because of the strong stability there which prevents active transport, mixing, and entrainment while the large ones near cloud base may indicate that processes occurring near and beneath cloud base (entrainment, detrainment, and mixing) can have significant influence on the cloud evolution.

- Gravity-waves which are common in a stably stratified atmosphere play an important role in the cloud evolution. The spectrum of gravity waves which are of interest for cirrus clouds ranges from several to several hundred kilometers. LES simulations with very high vertical resolutions also shows that the vertical wavelength for gravity waves can be less than one tenth of the horizontal one.

- PDF analyses of vertical velocity show that for the shallow cloud layer, an approximate normal distribution of w can be obtained throughout the cloud layer. However, for the deep cloud layer, the PDF structure can be complex, especially deep in the cloud layer.

- Radiative effects on ice particle's diffusional growth can be of significance on the microphysical, radiative, and dynamic properties of cirrus clouds. Computations with the CRM show that with the radiative effects, supersaturation with respect to ice (SSI) produced in the early stage of simulation can be more than ten times of that predicted without radiative effects. The high SSI produced in simulations with radiative effects results in the nucleation of large numbers (on the order of 2000 for Case 2) of ice crystals.

- Ice particles, especially large ones, tend to experience radiative warming (note that this is different from radiative cooling or warming of the cloudy environment) which results in the evaporation of large ice particles, leading to less ice mass production in the simulations with radiative effects.

6.2 Future Work

Through extensive simulations of the well observed November 26, 1991 cirrus event, we obtain some insights into middle-latitude cirrus. One should keep in mind that this study consists of only one cirrus case, even though multiple simulations are performed. In order to generalize the findings and to obtain general knowledge about mid-latitude as well as tropical cirrus, this research can be only regarded as the necessary foundation and the first step towards the long-term goal which is to develop a successful cirrus cloud parameterization scheme for large scale models. The following extensions in this research are needed in the future.

- Simulation of other well observed cirrus events, such as the FIRE II December 3-5, 1991 cirrus case. This simulation should be really challenging because this cirrus event was strongly affected by stratospheric aerosols (Sassen et al., 1995). However,

the detailed response of cirrus clouds to aerosol concentrations in the lower stratosphere is still not clear. This implies that successful simulation of the December 3-5, 1991 cirrus event will rely on knowledge about the cloud-aerosol interactions which, in turn, must be properly taken into account in the numerical model.

- Simulation of well observed tropical cirrus events is desired. The December 22, 1992 Tropical Ocean Global Atmosphere Coupled Ocean-Atmosphere Response Experiment (TOGA COARE) cirrus case simulated by Mitrescu (1998) did not have detailed measurements of cirrus structure. Since generally observational data are not as easily obtained in tropical regions as in mid-latitude, correct representation of the large scale environment for cirrus cloud development and evolution may be very hard to generate. For this reason, model initialization can be very difficult and involve many uncertainties. Even if a model is reasonably initialized, time-dependent model boundaries can be very hard to provide. Until more extensive observations of tropical cirrus are available, the difficulties mentioned above will hamper numerical modeling of tropical cirrus clouds.

- Further sensitivity tests of the radiative effects on ice particle's diffusional growth should be done under the CRM and LES frameworks. Even though the CRM simulations of this study have shown significant difference between the simulations with radiative feedback and that without radiative feedback, it should be born in mind that the simulation results only apply to a specific case. Using the same CRM framework without ice phase microphysics, Harrington (1997) studied the radiative effects on droplet condensational growth for Arctic stratus clouds (ASC). He found that drizzle production could occur as much as one hour earlier (because of predicted spectral broadening) with the radiative effects and that the character of the simulated clouds was not greatly altered. Apparently, the CRM results (for cirrus clouds) in this study which do not support spectral broadening at all (in fact, production of large ice particles is suppressed) are not consistent with his results for ASC with respect to the radiative effects on cloud properties. This inconsistency can be explained only through more extensive sensitivity studies.

- The trajectory parcel model (TPM) which has some advantages over the CRM in studying radiative effects (Harrington, 1997) should be used as an extension of this research. It may also be necessary that time-dependent parcel information which is used to drive TPM be extracted from a 3D simulation because, as shown in previous chapters, 3D LES simulations can produce active eddies which are likely to generate more realistic trajectories.

Appendix A

DEFINITIONS OF SOME SYMBOLS

C	capacity
c_p	specific heat at constant pressure
D	molecular diffusion coefficient
e_{si}	saturation vapor pressure with respect to ice
e_{sw}	saturation vapor pressure with respect to water
f_1	ventilation factor
f_2	gas kinetic factor
K	thermal conductivity of air
L_c	latent heat of condensation
L_s	latent heat of sublimation
M_i	total ice mass due to depositional growth
M_w	total liquid mass due to condensational growth
m_i	mass of a single ice particle
m_w	mass of a single water droplet
q_v	specific humidity (water vapor mixing ratio)
q_{si}	saturation water vapor mixing ratio with respect to ice
q_{sw}	saturation water vapor mixing ratio with respect to water
R	longwave radiative energy
R_v	gas constant for water vapor
r	radius of a particle
S_i	saturation ratio with respect to ice
ΔS_i	specific humidity surplus with respect to ice

S_w	saturation ratio with respect to water
ΔS_w	specific humidity surplus with respect to water
T	air temperature
T_r	temperature at the surface of a particle
T_∞	environmental temperature (is equal to T)
$\rho_{s,r}$	saturation (to water) vapor density at the surface of a particle
$\rho_{si,r}$	saturation (to ice) vapor density at the surface of a particle
ρ_∞	environmental vapor density

Appendix B

DERIVATION OF THE DIFFUSIONAL MASS GROWTH AND SUPERSATURATION EQUATIONS

B.1 The diffusional mass growth equations for water and ice

The basic equation for diffusional growth of either cloud drops or ice crystals has been presented by numerous authors. When radiative effects on the diffusional growth of a particle are added to the mass growth equation, the equation becomes complicated. In this chapter, we derive the diffusional mass growth equation for a particle with the infrared radiative effects included.

The basic equations for diffusional growth of a particle are given by

for water drops:

$$L_c \frac{dm_w}{dt} - R = 4\pi r K f_1^* f_2^* (T_r - T_\infty) \tag{B.1}$$

$$\frac{dm_w}{dt} = 4\pi r D f_1 f_2 (\rho_\infty - \rho_{s,r}) \tag{B.2}$$

and for ice particles:

$$L_s \frac{dm_i}{dt} - R_{ice} = 4\pi C K f_1^* f_2^* (T_r - T_\infty) \tag{B.3}$$

$$\frac{dm_i}{dt} = 4\pi C D f_1 f_2 (\rho_\infty - \rho_{si,r}) \tag{B.4}$$

It should be noted that, generally, coefficient f needs not be the same for heat and for vapor transfer. However, for simplicity and as a convenient approximation, we assume that $f_1 = f_1^*$ and $f_2 = f_2^*$ in the following derivations.

B.1.1 The depositional growth equation for ice particles

Since the surface of the ice particle is assumed to be saturated, the vapor density at the particle surface is

$$\rho_{si,r}(T_r) = \frac{e_{si}(T_r)}{R_v T_r} \tag{B.5}$$

From (B.5), we can get that

$$\frac{d\rho_{si,r}}{\rho_{si,r}} = \frac{de_{si}}{e_{si}} - \frac{dT_r}{T_r} \tag{B.6}$$

By using Clausius-Clapeyron equation, (B.6) can be rewritten as

$$\frac{d\rho_{si,r}}{\rho_{si,r}} = \frac{L_s}{R_v} \cdot \frac{dT_r}{T_r^2} - \frac{dT_r}{T_r} \tag{B.7}$$

Integrate (B.7) from T_r to T_∞ and assume that $\frac{T_\infty}{T_r} \approx 1$. Also, since $\frac{\rho_{si,r}(T_\infty)}{\rho_{si,r}(T_r)}$ and $\frac{T_\infty}{T_r}$ are close to unity, $ln\frac{\rho_{si,r}(T_\infty)}{\rho_{si,r}(T_r)}$ and $ln\frac{T_\infty}{T_r}$ can be expanded according to Taylor series with respect to 1 to get the following approximations

$$ln\frac{\rho_{si,r}(T_\infty)}{\rho_{si,r}(T_r)} \approx \frac{\rho_{si,r}(T_\infty) - \rho_{si,r}(T_r)}{\rho_{si,r}(T_r)} \tag{B.8}$$

$$ln\frac{T_\infty}{T_r} \approx \frac{T_\infty - T_r}{T_r} \tag{B.9}$$

Then, we can get

$$\frac{\rho_{si,r}(T_\infty) - \rho_{si,r}(T_r)}{\rho_{si,r}(T_r)} \approx \frac{L_s(T_\infty - T_r)}{R_v T_r T_\infty} - \frac{T_\infty - T_r}{T_r} \approx \frac{T_\infty - T_r}{T_\infty} \cdot (\frac{L_s}{R_v T_\infty} - 1) \tag{B.10}$$

Combining (B.10) and (B.3),

$$\frac{\rho_{si,r}(T_\infty) - \rho_{si,r}(T_r)}{\rho_{si,r}(T_r)} = (1 - \frac{L_s}{R_v T_\infty}) \frac{1}{4\pi C K T_\infty f_1 f_2} (L_s \frac{dm_i}{dt} - R_{ice}) \tag{B.11}$$

From mass growth equation $\frac{dm_i}{dt} = 4\pi C D f_1 f_2 (\rho_\infty - \rho_{si,r}(T_r))$, we know that

$$\frac{\rho_\infty - \rho_{si,r}(T_r)}{\rho_{si,r}(T_r)} = \frac{dm_i}{dt}\frac{1}{4\pi C D f_1 f_2 \rho_{si,r}(T_r)} \tag{B.12}$$

Subtracting (B.11) from (B.12) to get

$$\frac{\rho_\infty - \rho_{si,r}(T_\infty)}{\rho_{si,r}(T_r)} = \frac{1}{4\pi C f_1 f_2}\{[\frac{1}{D\rho_{s,r}(T_r)} + \frac{L_s}{KT_\infty}(\frac{L_s}{R_v T_\infty} - 1)]\frac{dm_i}{dt} - \frac{R_{ice}}{KT_\infty}(\frac{L_s}{R_v T_\infty} - 1)\} \tag{B.13}$$

Since $T_\infty \approx T_r = T$ and $\rho_{si,r}(T_r) \approx \rho_{si,r}(T_\infty) = \frac{e_{si}(T)}{R_v T}$, also note that $\frac{\rho_\infty}{\rho_{si,r}(T)} = S_i$, the supersaturation ratio with respect to ice, then we get

$$4\pi C f_1 f_2 (S_i - 1) + \frac{R_{ice}}{KT}(\frac{L_s}{R_v T} - 1) = \frac{dm_i}{dt}[\frac{R_v T}{De_{si}(T)} + \frac{L_s}{KT}(\frac{L_s}{R_v T} - 1)] \tag{B.14}$$

Following Tzivion et al. (1989), let $\Delta S_i = q_v - q_{si}$ and $C_i(P,T,m_i) = f_1 q_{si}^{-1}[\frac{R_v T}{De_{si}(T)} + \frac{L_s}{KT}(\frac{L_s}{R_v T} - 1)]^{-1}$ (note that f_1, the ventilation factor, is a function of the Reynolds number which is related to the particle mass). Also, note that $S_i - 1 = \frac{\Delta S_i}{q_{si}}$, where ΔS_i is called the specific humidity surplus. Then (B.14) can be rewritten as

$$\frac{dm_i}{dt} = f_2 C_i(P,T,m_i)[4\pi C \Delta S_i + \frac{R_{ice} q_{si}}{K f_1 f_2 T}(\frac{L_s}{R_v T} - 1)] \tag{B.15}$$

Equation (B.15) approximates the depositional growth of an ice particle with the radiative effects included.

B.1.2 The diffusional growth equation for water drops

Following similar procedure, the diffusional growth equation for a water drop can be derived as

$$\frac{dm_w}{dt} = f_2 C_w(P,T,m_w)[4\pi r \Delta S_w + \frac{R q_{sw}}{K f_1 f_2 T}(\frac{L_c}{R_v T} - 1)] \tag{B.16}$$

where $C_w(P,T,m_w)$ is defined as

$$C_w(P,T,m_w) = f_1 q_{sw}^{-1}[\frac{R_v T}{De_{sw}(T)} + \frac{L_c}{KT}(\frac{L_c}{R_v T} - 1)]^{-1} \tag{B.17}$$

B.2 Solutions to the diffusional mass growth equations

B.2.1 Solution to the diffusional mass growth equation for water drops

For water drops, the mass growth equation (B.16) can be rewritten as (similar to Harrington (1997))

$$\frac{dm_w}{dt} = C_{w,new}(P,T,m_w)\frac{m_w^{2/3}}{m_w^{1/3}+l_0}[\Delta S_w + \frac{Rq_{sw}m_w^{-1/3}}{Kf_1f_2TB_w}(\frac{L_c}{R_vT}-1)] \tag{B.18}$$

where B_w is a constant equal to $4\pi(\frac{3}{4\pi\rho_w})^{1/3}$ and $C_{w,new}(P,T,m_w)$ is defined in Tzivion et al. (1989) and equal to $C_w(P,T,m_w)B_w$. In deriving (B.18), the gas kinetic effect, f_2, is represented by (Clarke 1974a)

$$f_2 = \frac{m_w^{1/3}}{m_w^{1/3}+l_0} \tag{B.19}$$

where l_0 is a length-scale representing the gas kinetic effects. The radius of a drop is related to the mass as

$$r = (\frac{3}{4\pi\rho_l}m_w)^{1/3} \tag{B.20}$$

Replacing the radiative effect R in the above equation according to Harrington (1997), we get

$$\frac{dm_w}{dt} = C_{w,new}(P,T,m_w)\frac{m_w^{2/3}}{m_w^{1/3}+l_0}\left[\Delta S_w + \frac{q_{sw}m_w^{1/3}B_w^{\star}E_d(m_w)}{Kf_1f_2T}\left(\frac{L_c}{R_vT}-1\right)\right] \tag{B.21}$$

here $B_w^{\star} = \left(\frac{3}{4\pi\rho_w}\right)^{1/3}$ and $E_d(m_w)$ is the radiative effect that includes all of the flux terms (the definition of $E_d(m_w)$ can be found in Harrington (1997)).

Equation (B.21) must be integrated in order to deduce how a water drop grows over a time step in numerical model. To solve for the analytic solution to (B.21) without the radiation term, integration is taken for a single time increment Δt, during which the effect of changes in $C_{w,new}(P,T,m_w)$ is assumed to be negligible (Tzivion et al., 1989). Stevens

et al. (1996) showed the analytic solution to (B.21) without the radiative term on the right-hand side as

$$m_w(t+\delta t) = [((m_w(t)^{1/3} + l_0)^2 + \frac{2}{3}\tau)^{1/2} - l_0]^3 \tag{B.22}$$

where $\tau = \int_t^{t+\delta t} C_{w,new}(P,T,m_w)\Delta S_w dt$.

With the radiative effects, analytic solution to (B.21) can not be obtained easily because a mass related term which multiplies the radiative effect R appears on the right-hand side. So, the equation must be solved iteratively. Harrington (1997) discussed simplification to solving the equation (B.21). By using a mean value of the radiative term for each bin (for the bin microphysics model), Harrington (1997) showed that acceptable accuracy (the largest errors never exceed 1.5% under reasonable atmospheric conditions) can be obtained by comparing the approximations with the solutions obtained using iterative method. By applying the mean value of the radiative term for each bin and integrating over a single time step $\Delta t(= t_2 - t_1)$, equation (B.21) becomes

$$\begin{aligned}
&\int_{m_w(t)}^{m_w(t+\Delta t)} \frac{m_w^{1/3} + l_0}{m_w^{2/3}} dm_w = \\
&\quad C_{w,new}(P,T,\bar{m}_{w,k}) \int_t^{t+\Delta t} \Delta S_w dt \\
&\quad + C_{w,new}(P,T,\bar{m}_{w,k}) \frac{q_{sw}\bar{m}_{w,k}^{1/3} B_w^* E_d(\bar{m}_{w,k})}{K f_1(\bar{m}_{w,k}) f_2(\bar{m}_{w,k}) T} \left(\frac{L_c}{R_v T} - 1\right) \Delta t \\
&\quad = \tau_r = \tau + \tau_k
\end{aligned} \tag{B.23}$$

which has the solution

$$m_w(t+\Delta t) = \left\{ \left[\left(m_w(t)^{1/3} + l_0 \right)^2 + \frac{2}{3}\tau_r \right]^{1/2} - l_0 \right\}^3 \tag{B.24}$$

where $m_w(t)$ and $m_w(t+\Delta t)$ stand for the initial and final masses of a droplet; $E_d(\bar{m}_{w,k})$ and $\bar{m}_{w,k}$ stand for the mean radiative effects and the mean mass for bin number k, respectively; τ_k is the bin- dependent radiative forcing term and τ_r the total forcing on the mass for bin number k.

Detailed discussion about the calculation of the radiative term is available in Harrington (1997).

B.2.2 Solution to the diffusional mass growth equation for ice particle

The solution to (B.15) is not as easily obtained as that to the diffusional mass growth equation for water drops because of the electrical capacitance C which can be a complicated function of the particle dimensions.

For spherical ice particle, equation (B.15) can be written similarly as (B.21) when the radiative effect R is replaced according to Harrington (1997) and the approximate solution to (B.15) has the same form as (B.24) except that τ_r is now replaced by $\tau_{r,i}$ which is defined with respect to ice and can be written as

$$\begin{aligned}\tau_{ri} &= \tau_i + \tau_{ki} = \int_{m_i(t)}^{m_i(t+\Delta t)} \frac{m_i^{1/3} + l_0}{m_i^{2/3}} dm_i \\ &= C_{i,new}(P,T,\bar{m}_{i,k}) \int_t^{t+\Delta t} \Delta S_i dt \\ &\quad + C_{i,new}(P,T,\bar{m}_{i,k}) \frac{q_{si}\bar{m}_{i,k}^{1/3} B_i^\star E_d(\bar{m}_{i,k})}{K f_1(\bar{m}_{i,k}) f_2(\bar{m}_{i,k}) T} \left(\frac{L_s}{R_v T} - 1\right) \Delta t \end{aligned} \tag{B.25}$$

where $C_{i,new}(P,T,m_i)$ is defined as $C_i(P,T,m_i)B_i$ and B_i is equal to $4\pi(\frac{3}{4\pi\rho_i})^{1/3}$; $B_i^\star$ is equal to $\left(\frac{3}{4\pi\rho_i}\right)^{1/3}$.

For other ice particle habits, the solution should be modified according to the mass-particle size relation used.

B.3 Supersaturation (specific humidity surplus) equations

Following Tzivion et al. (1989), using equations

$$q_{sw}(T) = 0.622 \frac{e_{sw}(T)}{P} \tag{B.26}$$

$$\frac{de_{sw}}{dT} = \frac{L_c e_{sw}(T)}{R_v T^2} \tag{B.27}$$

$$\frac{\partial q_{sw}(T)}{\partial t} = \frac{0.622}{P} \frac{L_c e_{sw}(T)}{R_v T^2} \frac{\partial T}{\partial t} \tag{B.28}$$

$$\frac{\partial q_v}{\partial t} = -\left(\frac{\partial M_w}{\partial t} + \frac{\partial M_i}{\partial t}\right)_{condensation,evaporation} \tag{B.29}$$

$$\frac{\partial T}{\partial t} = \frac{L_c}{c_p}\frac{\partial M_w}{\partial t} + \frac{L_s}{c_p}\frac{\partial M_i}{\partial t} \tag{B.30}$$

we get

$$\begin{aligned}
\frac{\partial \Delta S_w}{\partial t} &= \frac{\partial (q_v - q_{sw})}{\partial t} = -\frac{\partial M_w}{\partial t} - \frac{\partial M_i}{\partial t} - \frac{0.622 L_c e_{sw}(T)}{R_v T^2 P c_p}[L_f \frac{\partial M_w}{\partial t} + L_s \frac{\partial M_i}{\partial t}] \\
&= -(1 + \frac{0.622 L_c^2 e_{sw}(T)}{R_v T^2 P c_p})\frac{\partial M_w}{\partial t} - (1 + \frac{0.622 L_c L_s e_{sw}(T)}{R_v T^2 P c_p})\frac{\partial M_i}{\partial t} \\
&= -A(P,T)\frac{\partial M_w}{\partial t} - A_1(P,T)\frac{\partial M_i}{\partial t}
\end{aligned} \tag{B.31}$$

Similarly, the time dependence of ΔS_i can be derived as

$$\frac{\partial \Delta S_i}{\partial t} = -A_2(P,T)\frac{\partial M_w}{\partial t} - A_3(P,T)\frac{\partial M_i}{\partial t} \tag{B.32}$$

where

$$A_2(P,T) = (1 + 0.622\frac{L_s L_c e_{si}(T)}{R_v P c_p T^2}) \tag{B.33}$$

$$A_3(P,T) = (1 + 0.622\frac{L_s^2 e_{si}(T)}{R_v P c_p T^2}) \tag{B.34}$$

Since

$$\frac{\partial M_w}{\partial t} = \int \frac{dm_w}{dt} n(m_w) dm_w \tag{B.35}$$

$$\frac{\partial M_i}{\partial t} = \int \frac{dm_i}{dt} n(m_i) dm_i \tag{B.36}$$

where $n(m)$ is the distribution function with respect to mass and the right-hand side of each equation is integrated over the whole spectrum, then we get (assuming spherical ice particles)

$$
\begin{aligned}
\frac{\partial \Delta S_w}{\partial t} &= -A(P,T)\int \frac{dm_w}{dt} n(m_w)dm_w - A_1(P,T)\sum_{ice\ species}\int \frac{dm_i}{dt} n(m_i)dm_i \\
&= -A(P,T)\Delta S_w \int C_{w,new}(P,T,m_w)\frac{m_w^{2/3}}{m_w^{1/3}+l_0} n(m_w)dm_w \\
&\quad -A(P,T)\frac{q_{sw}B_w^\star}{KT}\left(\frac{L_c}{R_vT}-1\right)\int \frac{C_{w,new}(P,T,m_w)}{f_1(m_w)} m_w^{2/3}E_d(m_w)n(m_w)dm_w \\
&\quad -A_1(P,T)\Delta S_i \sum_{ice\ species}\int C_{i,new}(P,T,m_i)\frac{m_i^{2/3}}{m_i^{1/3}+l_0} n(m_i)dm_i \\
&\quad -A_1(P,T)\frac{q_{si}}{KT}\left(\frac{L_s}{R_vT}-1\right)\sum_{ice\ species} B_i^\star \int \frac{C_{i,new}(P,T,m_i)}{f_1(m_i)} m_i^{2/3}E_d(m_i)n(m_i)dm_i \\
&= G_1\Delta S_w + G_2\Delta S_i + D_1
\end{aligned}
\tag{B.37}
$$

$$
\begin{aligned}
\frac{\partial \Delta S_i}{\partial t} &= -A_2(P,T)\int \frac{dm_w}{dt} n(m_w)dm_w - A_3(P,T)\sum_{ice\ species}\int \frac{dm_i}{dt} n(m_i)dm_i \\
&= -A_2(P,T)\Delta S_w \int C_{w,new}(P,T,m_w)\frac{m_w^{2/3}}{m_w^{1/3}+l_0} n(m_w)dm_w \\
&\quad -A_2(P,T)\frac{q_{sw}B_w^\star}{KT}\left(\frac{L_c}{R_vT}-1\right)\int \frac{C_{w,new}(P,T,m_w)}{f_1(m_w)} m_w^{2/3}E_d(m_w)n(m_w)dm_w \\
&\quad -A_3(P,T)\Delta S_i \sum_{ice\ species}\int C_{i,new}(P,T,m_i)\frac{m_i^{2/3}}{m_i^{1/3}+l_0} n(m_i)dm_i \\
&\quad -A_3(P,T)\frac{q_{si}}{KT}\left(\frac{L_s}{R_vT}-1\right)\sum_{ice\ species} B_i^\star \int \frac{C_{i,new}(P,T,m_i)}{f_1(m_i)} m_i^{2/3}E_d(m_i)n(m_i)dm_i \\
&= G_3\Delta S_w + G_4\Delta S_i + D_2
\end{aligned}
\tag{B.38}
$$

where D_1 and D_2 represent the longwave radiative effects on the specific humidity surplus. Also, the dynamic term (the term representing increase/decrease in specific humidity surplus due to vertical motions) can be easily combined with D_1 and D_2.

B.4 Solution to the supersaturation equations

Equations (B.37) and (B.38) can be solved analytically if G_1, G_2, G_3, G_4, D_1, and D_2 are assumed constants within a timestep. For the bin-microphysics model, the changes of these variables with time are neglected within a time increment $\Delta t = t - t_0$. Thus Δt

should be small enough so as to justify this assumption. A detailed discussion about this assumption is available in Tzivion et al. (1989).

In order to solve equations (B.37) and (B.38), we first solve for the eigenvalues of the following coefficient matrix

$$\begin{bmatrix} G_1 & G_2 \\ G_3 & G_4 \end{bmatrix} \tag{B.39}$$

This eigenvalue problem can be easily solved and the eigenvalues are

$$\lambda_1 = \frac{(G_1 + G_4) + \sqrt{(G_1 + G_4)^2 - 4(G_1 G_4 - G_2 G_3)}}{2} \tag{B.40}$$

$$\lambda_2 = \frac{(G_1 + G_4) - \sqrt{(G_1 + G_4)^2 - 4(G_1 G_4 - G_2 G_3)}}{2} \tag{B.41}$$

Then, general solutions to the homogeneous forms of (B.37) and (B.38) can be easily obtained and written as

$$\Delta S_w = a e^{\lambda_1 t} + b e^{\lambda_2 t} \tag{B.42}$$

$$\Delta S_i = \frac{\lambda_1 - G_1}{G_2} a e^{\lambda_1 t} + \frac{\lambda_2 - G_1}{G_2} b e^{\lambda_2 t} \tag{B.43}$$

where a and b are any constants.

Now, we need to find particular solutions to (B.37) and (B.38) in order to completely solve these two equations. The particular solutions can be obtained by considering a and b as functions of t and solving the following two equations

$$e^{\lambda_1 t} \frac{da}{dt} + e^{\lambda_2 t} \frac{db}{dt} = D_1 \tag{B.44}$$

$$\frac{\lambda_1 - G_1}{G_2} e^{\lambda_1 t} \frac{da}{dt} + \frac{\lambda_2 - G_1}{G_2} e^{\lambda_2 t} \frac{db}{dt} = D_2 \tag{B.45}$$

These two equations can be easily solved. A solution for a and b can be written as

$$a_1 = -\frac{(\lambda_2 - G_1)D_1 - G_2D_2}{\lambda_1(\lambda_2 - \lambda_1)}e^{-\lambda_1 t} \tag{B.46}$$

$$b_1 = -\frac{1}{\lambda_2}[D_1 - \frac{(\lambda_2 - G_1)D_1 - G_2D_2}{\lambda_2 - \lambda_1}]e^{-\lambda_2 t} \tag{B.47}$$

Substituting a_1 and b_1 into (B.42) and (B.43) for a and b, we can get the particular solutions to these two equations. The particular solutions can be written as

$$\Delta S_w^* = -\frac{(\lambda_2 - G_1)D_1 - G_2D_2}{\lambda_1(\lambda_2 - \lambda_1)} - \frac{1}{\lambda_2}[D_1 - \frac{(\lambda_2 - G_1)D_1 - G_2D_2}{\lambda_2 - \lambda_1}] \tag{B.48}$$

$$\Delta S_i^* = -\frac{\lambda_1 - G_1}{G_2}\frac{(\lambda_2 - G_1)D_1 - G_2D_2}{\lambda_1(\lambda_2 - \lambda_1)} - \frac{\lambda_2 - G_1}{G_2}\frac{1}{\lambda_2}[D_1 - \frac{(\lambda_2 - G_1)D_1 - G_2D_2}{\lambda_2 - \lambda_1}] \tag{B.49}$$

The final solutions to (B.37) and (B.38) can be obtained by adding these particular solutions to (B.42) and (B.43) to get

$$\Delta S_w = ae^{\lambda_1 t} + be^{\lambda_2 t} + \Delta S_w^* \tag{B.50}$$

$$\Delta S_i = \frac{\lambda_1 - G_1}{G_2}ae^{\lambda_1 t} + \frac{\lambda_2 - G_1}{G_2}be^{\lambda_2 t} + \Delta S_i^* \tag{B.51}$$

Constants a and b in the above equations can be determined from the initial conditions at the start of each time step.

REFERENCES

Ackerman, S. A., W. L. Smith, J. D. Spinhirne, and H. E. Revercomb, 1990: The 27-28 October 1986 FIRE IFO cirrus case study: Spectral properties of cirrus clouds in the 8-12 μm window. *Mon. Wea. Rev.*, **118**, 2377-2388.

Alexander, M. J., J. R. Holton, and D. R. Durran, 1995: The gravity wave response above deep convection in a squall line simulation. *J. Atmos. Sci.*, **52**, 2212-2226.

Atlas, D., S. Y. Matrosov, A. J. Heymsfield, M.-D. Chou, and D. B. Wolff, 1995: Radar and radiation properties of ice clouds. *J. of Applied Meteorology*, **34**, 2329-2345.

Benjamin, S. G., K. A. Brewster, R. Brummer, B. F. Jewett, T. W. Schlatter, T. L. Smith, and P. A. Stamus, 1991: An isentropic three-hourly data assimilation system using ACARS aircraft observations. *Mon. Wea. Rev.*, **119**, 888- 906.

Brown, P. R. A., 1990: In-situ measurements of the ice water content in cirrus clouds. *Preprint Volume, Conf. on Cloud Physics*, San Fransisco, Amer. Meteor. Soc., 193-195.

Cotton, W. R., M. A. Stephens, T. Nehrkorn, and G. J. Tripoli, 1982: The Colorado State University three-dimensional cloud/mesoscale model. Part II: An ice parameterization. *J. de Rech. Atmos.*, **16**, 295-320.

Cotton, W. R. and R. A. Anthes, 1989: Storm and cloud dynamics. *Academic Press, Inc.*, 883 pp.

Cram, J. M., R. A. Pielke, and W. R. Cotton, 1992a: Numerical simulation and analysis of a prefrontal squall line. Part I: Observations and basic simulation results. *J. Atmos. Sci.*, , **49**, 189-208.

Cram, J. M., R. A. Pielke, and W. R. Cotton, 1992b: Numerical simulation and analysis of a prefrontal squall line. Part II: Propagation of the squall line as an internal gravity wave. *J. Atmos. Sci.*, , **49**, 209-228.

Davies, H. C., 1983: Limitations of some common lateral boundary schemes used in regional NWP models. *Mon. Wea. Rev.*, **111**, 1002-1012.

Deardorff, J. W., 1980: Stratocumulus-capped mixed layers derived from a three-dimensional model. *Boundary-Layer Meteorol.*, **18**, 495-527.

DeMott, P. J., M. P. Meyers, and W. R. Cotton, 1994: Parameterization and impact of ice initiation processes relevant to numerical model simulations of cirrus clouds. *J. Atmos. Sci.*, , **51**, 77-90.

Dmitriyev, V. K., T. P. Kapitanova, V. D. Litvinova, N. Z. Pinus, G. A. Potertikova, and G. N. Shur, 1986: Experimental investigations of turbulence in tropospheric upper-level clouds. *Atmospheric and Oceanic Physics*, **22**, 108-113.

Feingold, G., B. Stevens, W. R. Cotton, and A. S. Frisch, 1996a: The relationship between drop in-cloud residence time and drizzle production in numerically simulated stratocumulus clouds. *J. Atmos. Sci.*, , **53**, 1108-1122.

Flatau, P. J., G. A. Dalu, W. R. Cotton, G. L. Stephens, and A. J. Heymsfield, 1989: Mixed layer model of cirrus clouds: Growth and dissipation mechanisms. *Symposium on the role of clouds in atmospheric chemistry and global climate, Anaheim, California*, 151-156.

Flatau, P. J., I. Gultepe, G. Nastrom, W. R. Cotton, and A. J. Heymsfield, 1990: Cirrus cloud spectra and layers observed during the FIRE and GASP projects. *Preprint Volume, Conf. on Cloud Physics*, San Fransisco, Amer. Meteor. Soc., 200-207.

Francis, P. N., A. Jones, R. W. Saunders, K. P. Shine, A. Slingo, and Z. Sun, 1994: An observational and theoretical study of the radiative properties of cirrus: Some results from ICE'89. *Q. J. R. Meteorol. Soc.*, **120**, 809-848.

Gayet, J. F., G. Febvre, J. Brogniez, H. Chepfer, W. Renger, and P. Wendling, 1996: Microphysical and optical properties of cirrus and contrails: Cloud field study on 13 October 1989. *J. Atmos. Sci.*, **53**, 126-138.

Gierens, K. M., 1996: Numerical simulations of persistent contrails. *J. Atmos. Sci.*, **53**, 3333-3348.

Grund, C. J. and E. W. Eloranta, 1990: The 27-28 October 1986 FIRE IFO cirrus case study: Cloud optical properties determined by high spectral resolution lidar. *Mon. Wea. Rev.*, **118**, 2344-2355.

Gultepe, I., A. J. Heymsfield, and G. V. Rao, 1990: Moisture and heat budgets of a cirrus cloud from aircraft measurements during FIRE-October 31 case study. *Preprint Volume, Conf. on Cloud Physics*, San Fransisco, Amer. Meteor. Soc., 196-199.

Gultepe, I. and D. O'C. Starr, 1995: Dynamical structure and turbulence in cirrus clouds: Aircraft observations during FIRE. *J. Atmos. Sci.*, **52**, 4159-4182.

Gultepe, I., D. O'C. Starr, A. J. Heymsfield, T. Uttal, T. P. Ackerman, and D. L. Westphal, 1995: Dynamical characteristics of cirrus clouds from aircraft and radar observations in micro and meso-γ scales. *J. Atmos. Sci.*, **52**, 4060-4078.

Harimaya, T., 1968: On the shape of cirrus uncinus clouds: A numerical computation-Studies of cirrus clouds: Part III. *J. Meteor. Soc. Japan*, **46**, 272-279.

Harrington, J. Y., 1997: The Effects of Radiative and Microphysical Processes on Simulated Warm and Transition-Season Arctic Stratus. Ph.D. dissertation, Colorado State University, Fort Collins, Colorado, 270pp.

Harrington, J. Y., 1994: Parameterization of ice crystal conversion processes in cirrus clouds using double-moment basis functions. M.S. thesis, Department of Atmospheric Science, Colorado State University, Fort Collins, CO, 135 pp.

Heckman, S. T. and W. R. Cotton, 1993: Mesoscale numerical simulation of cirrus clouds-FIRE case study and sensitivity analysis. *Mon. Wea. Rev.*, **121**, 2264-2284.

Heymsfield, A. J. and R. G. Knollenberg, 1972: Properties of cirrus generating cells. *J. Atmos. Sci.*, **29**, 1358-1366.

Heymsfield, A. J., 1975a: Cirrus uncinus generating cells and the evolution of cirroform clouds. Part I: Aircraft observations of the growth of the ice phase. *J. Atmos. Sci.*, **32**, 798-808.

Heymsfield, A. J., 1975b: Cirrus uncinus generating cells and the evolution of cirroform clouds. Part II: The structure and circulations of the cirrus uncinus generating head. *J. Atmos. Sci.*, **32**, 809-819.

Heymsfield, A. J., 1975c: Cirrus uncinus generating cells and the evolution of cirroform clouds. Part III: Numerical computations of the growth of the ice phase. *J. Atmos. Sci.*, **32**, 820-830.

Heymsfield, A. J., 1977: Precipitation development in stratiform ice clouds: A microphysical and dynamical study. *J. Atmos. Sci.*, **34**, 367-381.

Heymsfield, A. J. and C. M. R. Platt, 1984: A parameterization of the particle size spectrum of ice clouds in terms of the ambient temperature and the ice water content. *J. Atmos. Sci.*, **41**, 846-855.

Heymsfield, A. J. and L. J. Donner, 1990: A scheme for parameterizing ice-cloud water content in general circulation models. *J. Atmos. Sci.*, **47**, 1865-1877.

Heymsfield, A. J., K. M. Miller, and J. D. Spinhirne, 1990: The 27-28 October 1986 FIRE IFO cirrus case study: Cloud microstructure. *Mon. Wea. Rev.*, **118**, 2313-2328.

Holton, J. R., 1992: An introduction to dynamic meteorology. Third edition, Acedemic Press, 511pp.

Intrieri, J. M. and G. Feingold, 1993: Lidar and radar derived cirrus microphysical properties for the 26 November 1991 case study. Preprints, *FIRE Cirrus Science Conf.*, June 14-17, 1993, Breckenridge, Colorado, 48-51.

Intrieri, J. M., W. L. Eberhard, T. Uttal, J. A. Shaw, J. B. Snider, Y. Han, B. W. Orr, and S. Y. Matrosov, 1995: Multiwavelength observations of a developing cloud system: The FIRE II 26 November 1991 case study. *J. Atmos. Sci.*, **52**, 4079-4093.

Jensen, E. J., O. B. Toon, D. L. Westphal, S. Kinne, and A. J. Heymsfield, 1994: Microphysical modeling of cirrus. 1. Comparison with 1986 FIRE IFO measurements. *J. of Geophysical Research*, **99**, 10421-10442.

Jensen, E. J., O. B. Toon, D. L. Westphal, S. Kinne, and A. J. Heymsfield, 1994: Microphysical modeling of cirrus. 2. Sensitivity studies. *J. of Geophysical Research*, **99**, 10443-10454.

Kosovic, B., 1996: Subgrid-scale modeling for the large-eddy simulation of stably stratified boundary layers. Ph.D. thesis, Department of Aerospace Engineering Sciences, University of Colorado, Boulder, CO, 253 pp.

Lilly, D. K., 1968: Models of cloud-topped mixed layer under a strong inversion. *Q. J. R. Meteorol. Soc.*, **94**, 292-309.

Lilly, D. K., 1983: Stratified turbulence and the mesoscale variability of the atmosphere. *J. Atmos. Sci.*, **40**, 749-761.

Lilly, D. K., 1988: Cirrus outflow dynamics. *J. Atmos. Sci.*, **45**, 1594-1605.

Lilly, D. K., 1989: Two-dimensional turbulence generated by energy sources at two scales. *J. Atmos. Sci.*, **46**, 2026-2030.

Liou, K.-N., 1986: Influence of cirrus clouds on weather and climate processes: A global perspective. *Mon. Wea. Rev.*, **114**, 1167-1199.

Louis, J. F., 1979: A parametric model of vertical eddy fluxes in the atmosphere. *Boundary Layer Meteorology*, **17**, 187-202.

Mace, G. G., D. O'C. Starr, T. P. Ackerman, and P. Minnis, 1995: Examination of coupling between an upper-tropospheric cloud system and synoptic-scale dynamics diagnosed from wind profiler and radiosonde data. *J. Atmos. Sci.*, **52**, 4094-4127.

Mahrt, L., 1985: Vertical structure and turbulence in the very stable boundary layer. *J. Atmos. Sci.*, **42**, 2333-2349.

Mahrt, L., 1991: Eddy asymmetry in the sheared heated boundary layer. *J. Atmos. Sci.*, **48**, 472-492.

Mahrt, L., J. I. MacPherson, and R. Desjardins, 1994: Observations of fluxes over heterogeneous surfaces. *Bound.-Layer Meteor.*, **67**, 345-367.

Matrosov, S. Y., R. A. Kropfli, B. W. Orr, and J. B. Snider, 1993: Microphysical properties of the November 26 cirrus cloud retrieved by Doppler radar/IR radiometer technique. Preprints, *FIRE cirrus Science Conf.*, June 14-17, 1993, Breckenridge, Colorado, 44-47.

Matrosov, S. Y., A. J. Heymsfield, J. M. Intrieri, B. W. Orr, and J. B. Snider, 1995: Ground-based remote sensing of cloud particle sizes during the 26 November 1991 FIRE II cirrus case: Comparisons with in situ data. *J. Atmos. Sci.*, **52**, 4128-4142.

Meyers, M. P., P. J. DeMott, and W. R. Cotton, 1992: New primary ice nucleation parameterizations in an explicit cloud model. *J. Appl. Meteor.*, **31**, 708-721.

Meyers, M. P., 1995: The impact of a two-moment cloud model on the microphysical structure of two precipitation events. Ph.D. thesis, Department of Atmospheric Science, Colorado State University, Fort Collins, CO, 165 pp.

Meyers, M. P. and W. R. Cotton, 1995: Numerical investigation of two diverse precipitation events with the new two-moment microphysical scheme in RAMS. *Preprints, Conf. on Cloud Physics*, 15-20 January, 1995, Dallas, Texas.

Minnis, P., D. F. Young, K. Sassen, J. M. Alvarez, and C. J. Grund, 1990: Cirrus parameter relationships derived from satellite and lidar data. *Mon. Wea. Rev.*, **118**, 2402-2425.

Minnis, P., Smith, W. L., Jr., D. F. Young, and P. W. Heck, 1993: Cloud fields derived from satellite and surface data during FIRE cirrus phase II. Preprints, *FIRE cirrus Science Conf.*, June 14-17, 1993, Breckenridge, Colorado, 36-39.

Mitchell, D. L., S. K. Chai, Y. Liu, A. J. Heymsfield, and Y. Dong, 1996: Modeling cirrus clouds. Part I: Treatment of bimodal size spectra and case study analysis. *J. Atmos. Sci.*, **53**, 2952-2966.

Mitchell, D. L., A. Macke, and Y. Liu, 1996: Modeling cirrus clouds. Part II: Treatment of radiative properties. *J. Atmos. Sci.*, **53**, 2967-2987.

Mitrescu, C., 1998: Cloud-resolving simulations of tropical cirrus clouds. M.S. thesis, Department of Atmospheric Science, Colorado State University, Fort Collins, CO 80523, 85 pp.

Moeng, C-H, 1984: A large-eddy-simulation model for the study of planetary boundary-layer turbulence. *J. Atmos. Sci.*, **41**, 2052-2062.

Nakajima, T. Y. and T. Nakatima, 1995: Wide-area determination of cloud microphysical properties from NOAA AVHRR measurements for FIRE and ASTEX regions. *J. Atmos. Sci.*, **52**, 4043-4059.

Nebuda, S. E., 1995: Development of an upper-level cloud parameterization for large scale models. M.S. thesis, Department of Atmospheric Science, Colorado State University, Fort Collins, CO 80523, 125 pp.

Ou, S. C., K. N. Liou, Y. Takano, N. X. Rao, Q. Fu, A. J. Heymsfield, L. M. Miloshevich, B. Baum, and S. A. Kinne, 1995: Remote sounding of cirrus cloud optical depths and ice crystal sizes from AVHRR data: Verification using FIRE II IFO measurements. *J. Atmos. Sci.*, **52**, 4143-4158.

Pielke, R. A., W. R. Cotton, R. L. Walko, C. J. Tremback, W. A. Lyons, L. D. Grasso, M. E. Nicholls, M. D. Moran, D. A. Wesley, T. J. Lee, and J. H. Copeland, 1992: A comprehensive meteorological modeling system - RAMS. *Meteorol. Atmos. Phys.*, **49**, 69-91.

Platt, C. Martin R., 1997: Size spectra, extinction and ice/water content of frontal and capping cirrus clouds. Accepted to *J. Atmos. Sci.*.

Quante, M., P. Scheidgen, M. Laube, and E. Raschke, 1990: The structure of turbulence in cirrus clouds. *Preprint Volume, Conf. on Cloud Physics*, San Fransisco, Amer. Meteor. Soc., 211-218.

Reisin, T., 1995: A numerical study of cloud seeding in Israel using as axisymmetrical cloud model with detailed microphysics. Ph.D. dissertation, Department of Geophysics and Planetary Sciences, Tel Aviv University, 238pp.

Reisin, T., Z. Levin, and S. Tzivion, 1996: Rain production in convective clouds as simulated in an axisymmetric model with detailed microphysics. Part I: Description of the model. *J. Atmos. Sci.*, **53**, 497-519.

Roach, W. T., 1976: On the effect of radiative exchange on the growth by condensation of a cloud or fog droplet. *Quart. J. R. Met. Soc.*, 102, 361-372.

Rogers, R. R. and M. K. Yau, 1989: A short course in cloud physics. Third edition, *Pergamon Press*, 293 pp.

Sassen, K., D. O'C. Starr, and T. Uttal, 1989: Mesoscale and microscale structure of cirrus clouds: Three case studies. *J. Atmos. Sci.*, **46**, 371-396.

Sassen, K., 1990: Characterization of supercooled liquid water in cirrus clouds from FIRE ETO lidar observations. *Preprint Volume, Conf. on Cloud Physics*, San Fransisco, Amer. Meteor. Soc., 189-192.

Sassen, K., C. J. Grund, J. D. Spinhirne, M. M. Hardesty, and J. M. Alvarez. The 27-
28 October 1986 FIRE IFO cirrus case study: A five lidar overview of ructure
and evolution. *Mon. Wea. Rev.*, **118**, 2288-2312.

Sassen, K., D. O'C. Starr, G. G. Mace, M. R. Poellot, S. H. Melfi, W. L. E J. D.
Spinhirne, E. W. Eloranta, D. E. Hagen, and J. Hallett, 1995: The 5-6 I 1991
FIRE IFO II jet stream cirrus case study: Possible influences of volcan
Atmos. Sci., **52**, 97-123.

Schmidt, J. M., 1991: Numerical and observational investigations of long
induced, severe surface wind events: The derecho. Ph.D. Dissertation
of Atmospheric Science, Colorado State University, Fort Collins, CO 8(

Schmidt, J. M. and W. R. Cotton, 1990: Interactions between upper and lower
gravity waves on squall line structure and maintenance. *J. Atmos. Sci*
1222.

Skamorack, W. C. and J. B. Klemp, 1993: Adaptive grid refinement for two-
and three-dimensional nonhydrostatic atmospheric flow. *Mon. Wea.*
788-804.

Smith, W. L., Jr., P. F. Hein, and S. K. Cox, 1990: The 27-28 October 198(
cirrus case study: In situ observations of radiation and dynamic propertie
cloud layer. *Mon. Wea. Rev.*, **118**, 2389-2401.

Spinhirne, J. D. and W. D. Hart, 1990: Cirrus structure and radiative para
airborne lidar and spectral radiometer observations: The 28 October
study. *Mon. Wea. Rev.*, **118**, 2329-2343.

Starr, D. O'C. and S. K. Cox, 1985: Cirrus clouds. Part I: A cirrus cloud
Atmos. Sci., **42**, 2663-2681.

Starr, D. O'C. and S. K. Cox, 1985: Cirrus clouds. Part II: Numerical experim
formation and maintenance of cirrus. *J. Atmos. Sci.*, **42**, 2682-2694.

Starr, D. O'C. and D. P. Wylie, 1990: The 27-28 October 1986 FIRE cirrus
Meteorology and clouds. *Mon. Wea. Rev.*, **118**, 2259-2287.

Stephens, G. L., 1983: The influence of radiative transfer on the mass and heat budgets of ice crystals falling in the atmosphere. *J. Atmos. Sci.*, **40**, 1729-1739.

Stephens, G. L., P. J. Flatau, S.-C. Tsay, and P. Hein, 1989: Radiative diffusivity factors in cirrus and stratocumulus clouds - application to two- stream models. *FIRE Annual Scientific Meeting*, 10-14 July 1989, Monterrey, California.

Stevens, B., G. Feingold, W. R. Cotton, and R. L. Walko, 1996a: Elements of the microphysical structure of numerically simulated nonprecipitating stratocumulus. *J. Atmos. Sci.*, , **53**, 980-1007.

Stevens, B., R. L. Walko, W. R. Cotton, and G. Feingold, 1996b: The spurious production of cloud-edge supersaturation by Eulerian model. *Mon. Wea. Rev.*, , **124**, 1034-1041.

Stevens, B., W. R. Cotton, and G. Feingold, 1997: On a detailed representation of cloud-drop spectra in one- and two-dimensional models of boundary layer clouds: a critique. To be published in *Atmos, Res.*

Thompson, G, 1993: Prototype real-time mesoscale prediction during 1991-92 winter season and statistical verification of model data. M.S. thesis, Department of Atmospheric Science, Colorado State University, Fort Collins, CO, 105 pp.

Tremback, C. J., G. J. Tripoli, and W. R. Cotton, 1985: A regional scale atmospheric numerical model including explicit moist physics and a hydrostatic time-split scheme. *Preprint Volume of the Seventh Conference on Numerical Weather Prediction*, June 1985, AMS, Montreal, Canada, 355-358.

Tremback, C. J., 1990: Numerical simulation of a mesoscale convective complex: model development and numerical results. Ph.D. dissertation, Department of Atmospheric Science, Colorado State University, Fort Collins, CO, 274pp.

Tripoli, G. J. and W. R. Cotton, 1982: The Colorado State University three- dimensional cloud/mesoscale model. Part I: General theoretical framework and sensitivity experiments. *J. de Rech. Atmos.*, **16**, 185-220.

Tripoli, G. J., 1986: A numerical investigation of an orogenic mesoscale convective system. Ph.D. dissertation, Department of Atmospheric Science, Colorado State University, Fort Collins, CO, 290pp.

Tzivion, S., G. Feingold, and Z. Levin, 1987: An efficient numerical solution to the stochastic collection equation. *J. Atmos. Sci.*, , **44**, 3139-3149.

Tzivion, S., G. Feingold, and Z. Levin, 1989: The evolution of rain-drop spectra. Part II: Collisional collection/breakup and evaporation in a rain shaft. *J. Atmos. Sci.*, , **46**, 3312-3327.

Walko, R. L., C. J. Tremback, R. A. Pielke, and W. R. Cotton, 1995: An interactive nesting algorithm for stretched grids and variable nesting ratios. *J. of Applied Meteorology*, **34**, 994-999.

Weinstock, J., 1981: Energy dissipation rates of turbulence in the stable free atmosphere. *J. Atmos. Sci.*, **38**, 880-883.

Westphal, D. L., S. Kinne, J. M. Alvarez, S. G. Benjamin, W. L. Eberhard, A. J. Heymsfield, R. A. Kropfli, G. G. Mace, S. Y. Matrosov, S. H. Melfi, P. Minnis, P. Pilewskie, J. B. Snider, B. J. Soden, D. O'C. Starr, T. A. Uttal, and D. F. Young, 1996: Initialization and validation of a simulation of cirrus using FIRE II data. *J. Atmos. Sci.*, **53**, 3397-3429.

Wielicki, B. A., J. T. Suttles, A. J. Heymsfield, R. M. Welch, J. D. Spinhirne, M.-L. C. Wu, D. O'C Starr, L. Parker, and R. T. Arduini, 1990: The 27-28 October 1986 FIRE IFO cirrus case study: Comparison of radiative transfer theory woth observations by satellite and aircraft. *Mon. Wea. Rev.*, **118**, 2356-2376.

APPENDIX 2

Radiative Effects on the Diffusional Growth of Ice Particles in Cirrus Clouds

Ting Wu and William R. Cotton[1]

Department of Atmospheric Science

Colorado State University

Fort Collins, CO

Submitted to *J. Atmos. Sci.*

May 20, 1999

[1]Corresponding Author Address: William Cotton, Department of Atmospheric Science, Colorado State University, Fort Collins, CO 80523-1371 - e-mail: cotton@atmos.colostate.edu

Abstract

At Colorado State University the Regional Atmospheric Modeling System (RAMS) has been used to study the radiative effect on the diffusional growth of ice particles in cirrus clouds. Using soundings extracted from a mesoscale simulation of the November 26, 1991 cirrus event, the radiative effect was studied using a two-dimensional cloud-resolving model (CRM) version of RAMS, coupled to an explicit bin-resolving microphysics.

The CRM simulations of the November 26, 1991 cirrus event demonstrate that the radiative impact on the diffusional growth (or sublimation) of ice crystals is significant. Even in a radiatively-cooled atmospheric environment, ice particles may experience radiative warming because the net radiation received by an ice particle depends upon the emission from the particle, and the local upwelling and downwelling radiative fluxes.

Model results show that radiative feedbacks in the diffusional growth of ice particles can be very complex. Radiative warming of an ice particle will restrict the particle's diffusional growth. In the case of radiative warming, ice particles larger than a certain size will experience so much radiative warming that surface ice saturation vapor pressures become large enough to cause sublimation of the larger crystals, while smaller crystals are growing by vapor deposition. However, ice mass production can be enhanced in the case of radiative cooling of an ice particle. For the November 26, 1991 cirrus event, radiative feedback results in significant reduction in the total ice mass, especially in the production of large ice crystals, and consequently, both radiative and dynamic properties of the cirrus cloud are significantly affected.

1. Introduction

The climatic importance of cirrus clouds has been recognized for a long time. Cirrus clouds, which cover about 20% of the globe on average, are believed to have profound impacts upon the planetary energy budget due to their radiative effects. Even though during the past decades, the effect of ice clouds on the radiative budget of the earth - atmosphere system has gained considerable impetus in terms of its importance to the World Climate Research Program, studies of cloud evolution, which ultimately involve the physics of the growth of cloud particles and should hold a special place in cloud-climate research, have not made significant progress because of the complexity of cirrus clouds.

The growth of ice crystals in cirrus clouds has significant consequence because of its contribution to the total diabatic heating or cooling of the atmospheric environment. The microphysical representation of an ice particle's depositional/sublimational growth is usually based on solutions to a set of coupled differential equations that describe a balance between latent heat release associated with deposition of water vapor and heat diffusion; the radiative influence on the particle being ignored.

However, the effects of radiation on the growth of ice particles has been postulated to be potentially important. In a theoretical study, Stephens (1983) investigated the effect of radiative heating and cooling on the mass and heat budgets of an ice crystal. In his study, the radiation budget was solved in terms of upper limits of warming and cooling. His results showed that the effects of radiation on the growth and evaporation rates of ice crystals were significant. Particle growth (sublimation) was enhanced (suppressed) in a radiatively-cooled (heated) environment. It was further demonstrated in his study that the effects of radiative cooling in the upper regions of the cloud greatly enhanced the particle fall distances.

Using two modeling frameworks, a cloud-resolving model (CRM) and a trajectory parcel model (TPM), Harrington et al. (1999) studied the effects of radiative heating (cooling) on the heat budget, and therefore on the condensational growth, of a population of cloud droplets within an Arctic stratus cloud. His TPM model analysis showed that the radiative effect reduced the time required for the onset of drizzle by up to 30 minutes in some cases, depending on the cloud-top residence time of the parcels, cloud top cooling, and the size of the activated drops.

In this paper, we examine the influence of the radiative heating on the vapor- depositional growth (sublimation) of a population of ice crystals simulated in a CRM of cirrus clouds.

2. Background

Once ice crystals are nucleated by some of the primary or secondary nucleation mechanisms, they then grow by vapor deposition if the environment is supersaturated with respect to ice. The vapor-depositional (or diffusional) growth of ice particles is closely related to the saturation ratio relative to ice which can be written as:

$$S_i = \frac{e}{e_i} = \frac{e}{e_s}\frac{e_s}{e_i} = S(\frac{e_s}{e_i}) \tag{1}$$

where S denotes the saturation ratio with respect to water; S_i is the saturation ratio with respect to ice; e, e_i, and e_s denote the environmental vapor pressure, saturation vapor pressure with respect to ice, and saturation vapor pressure with respect to water, respectively.

Since the saturation vapor pressure with respect to water is always greater than that with respect to ice at the same temperature as long as the temperature is below 0^oC, a water saturated ($S = 1$) cloud is always supersaturated with respect to ice ($S_i > 1$) and is a favorable environment for rapid growth of ice crystals by vapor deposition or diffusion. The environment will remain favorable for ice crystal growth as long as liquid drops are

available to evaporate and maintain the saturation vapor pressure relative to water. This is commonly known as the *Bergeron-Findeisen mechanism.*

Traditionally, the diffusional growth of ice crystals follows the *Fickian diffusion* theory (Rogers and Yau, 1989). If the radiative effects are not considered, the diffusional growth equation can be written as (symbols in this equation are defined in Appendix A).

$$\frac{dm_i}{dt} = \frac{4\pi C f_1 f_2 (S_i - 1)}{\frac{R_v T}{De_{si}(T)} + \frac{L_s}{KT}(\frac{L_s}{R_v T} - 1)}. \tag{2}$$

However, it has been shown that radiative transfer can have a significant effect on the mass and heat budgets of both ice crystals and cloud droplets (Stephens, 1983). In deriving (2), the diffusional growth rate of an ice particle is determined by a steady state balance between heat released due to deposition and the conduction of heat away from the particle's surface. If it is assumed that the heat release due to sublimation and the energy transferred to the particle by radiation are balanced by the conduction of heat away from the particle, then the diffusional growth equation can be written as (see Appendix B).

$$L_s \frac{dm_i}{dt} - R = 4\pi C K f_1^* f_2^* (T_r - T_\infty). \tag{3}$$

The total radiative energy absorbed by an ice particle of some characteristic dimension l_R for radiation received over all solid angles ω can be determined by (Stephens, 1983)

$$R = \int_0^\infty \int_0^{4\pi} G(l_R, \omega) Q_{abs}(\lambda, l_R, \omega)(J(T_\Sigma, \lambda, \omega) - B(T_s, \lambda, \omega)) d\omega d\lambda. \tag{4}$$

In (4), Q_{abs} is the particle absorption efficiency which is a function of the wavelength (λ), the refractive index of ice at that wavelength and the particle orientation with respect to the incident radiation. $G(l_R, \omega)$ is the geometric cross section of the particle normal to the flow of radiation. $J(T_\Sigma, \lambda, \omega)$ is the incoming radiation incident on the particle from the surrounding environment at some source temperature T_Σ. This temperature is the same

as the environmental temperature T_∞ only for a particle immersed within a blackbody. $B(T_s, \lambda, \omega)$ is the Planck blackbody function and represents the emission by the particle of temperature T_s at the wavelength λ. The definition of radiative power absorbed by an ice particle as given in (4) involves the integral over all possible directions of incidence (ω) and over all wavelengths (λ).

Utilizing the two-stream approximation in the above integral one gets R for a spherical particle of radius r as (Harrington, 1997)

$$R = \int_0^\infty 4\pi r^2 Q_{abs}(r, \lambda)[\pi B(T_s, \lambda) - \frac{1}{2}(F^+ + F^-)]d\lambda \tag{5}$$

where F^+ and F^- are the values of upwelling and downwelling fluxes at wavelength λ. For consistency with the two-stream model, an average value of Q_{abs} for a given spectral band, i, is used and the above equation becomes

$$\begin{aligned} R_i &= 4\pi r^2 \bar{Q}_{abs,i}(\bar{r}_k) E_{d,i} \\ E_{d,i} &= [\pi B_i(T_s) - \frac{1}{2}(F_i^+ + F_i^-)] \end{aligned} \tag{6}$$

where $\bar{Q}_{abs,i}(\bar{r}_k)$ is the absorption coefficient averaged over spectral band i and computed at the mean size of microphysical bin number k as to be discussed; F_i^+ and F_i^- are the values of fluxes for band i; $B_i(T_s)$ is the band-integrated Planck function evaluated at the particle's surface temperature. The total radiative effect R can be obtained by summing up R_i over the total number of microphysical bins.

Now, it is straightforward to get the total radiative energy absorbed by a particle of size $\bar{r}_k$ as

$$R = 4\pi \bar{r}_k^2 \sum_{i=1}^{Nbands} \bar{Q}_{abs,i}(\bar{r}_k) E_{d,i} \tag{7}$$

where *Nbands* is the total number of radiation bands used in the radiation model. In order to evaluate the radiative effects on particle's diffusional growth in the explicit microphysical model, the radiative term shown above is included in the model equations for supersaturation and for the growth of particle. These equations are solved together in a manner that ensures self-consistency.

3. Model Description

The model used to examine the radiative effects on ice particle's diffusional growth is a coupling of the RAMS CRM with the bin-resolving microphysics model developed at the University of Tel Aviv (Tzivion et al., 1987; Tzivion et al., 1989; Reisin, 1995; Reisin et al., 1996; Feingold et al., 1996). It is a two-dimensional version of the large eddy simulation model described in detail in Stevens et al. (1996a) and Feingold et al. (1996). The strength of this model lies in its emphasis on both dynamics and microphysics through the coupling of the bin-resolving microphysical model with a dynamical model that resolves the large eddies. A detailed description of the coupled code for the liquid phase microphysics can be seen in Stevens et al. (1996a,b). Reisin (1995; Reisin et al., 1996) provide a detailed description of the mixed-phase microphysics model.

Although the two-dimensional (2D) CRM model does not represent the eddy structure as well as its three-dimensional (3D) large eddy simulation counterpart, it does include the essential interactions between large eddies and cloud microphysical processes and provides a valuable framework for testing hypotheses without enormous computational expense (Stevens et al., 1997). To accommodate the inclusion of radiative effects, the current version of the model couples the optical properties of the droplets and ice particles to an 8-band radiative transfer model developed by Harrington (1997; see also Olsson et al., 1998).

The Level-5 mixed-phase bin-microphysical representation of this model requires that equations for droplet activation, condensational/evaporational growth, collision-coalescence

of drops, ice nucleation, deposition and sublimation of ice crystals, collision-coalescence of ice particles, and sedimentation all be explicitly modeled. The decision on which processes are to be included in the model is based upon a number of factors (Reisin, 1995):

- The importance of the process to the relevant problem studied,
- the availability of relevant data such as collision efficiencies, terminal velocities, shape factors, etc., and
- limitations on computational resources.

Currently, three ice species named pristine ice, snow (aggregates), and graupel are included in the bin-microphysics representation of the model. Ice crystals in the model are created by nucleation of ice nuclei (IN) or by freezing of drops smaller that 100 μm in radius. The specific shape of the ice particles is assumed to be spherical in this study. Snow particles are formed by aggregation of ice crystals and are considered to have the minimum density ($0.2gcm^{-3}$) compared with pristine ice crystals ($0.7gcm^{-3}$) and graupel ($0.5gcm^{-3}$). Graupel particles are formed by freezing of drops with radii larger than $100\mu m$ and /or by different processes of particle coagulation.

The particle spectra for any category is divided into 25 bins ($x_k, k = 1, ..., 25$) with mass doubled in the next larger bin:

$$x_{k+1} = 2x_k. \tag{8}$$

The initial mass is $x_1 = 1.598 \times 10^{-11} g$ for any category which corresponds to a diameter of $3.125\mu m$ for drops, $3.520\mu m$ for pristine ice crystals, $3.937\mu m$ for graupel particles, and $5.344\mu m$ for aggregates. The size of each category at bin #25 is $800\mu m$ for drops, $901\mu m$ for pristine ice crystals, $1008\mu m$ for graupel, and $1368\mu m$ for aggregates. Table B.4 shows the size-bin information for bins from 1 to 25. The number of total bins can be larger or

smaller than 25, depending upon the specific cases. These spectra shown in the table are adequate for simulating mid-latitude cirrus clouds.

The evolution of the supersaturation with respect to both water and ice is prognosed according to the equations described in Appendix B. The radiative effect on the diffusional growth (or evaporation) of drops and ice particles can be turned on and /or off in order to test its importance.

4. CRM Simulation Results

The sounding used to drive the CRM simulations was extracted from a mesoscale simulation of the November 26, 1991 FIRE II cirrus event (Wu, 1999) and is shown in Figure 1. Since the bin-microphysics has the advantage of predicting particle size-dependent supersaturation with respect to water as well as ice, it is quite suitable for the study of the radiative effects on ice crystal vapor-depositional growth in cirrus clouds.

In order to examine radiative effects on ice particle diffusional growth, two simulations were performed. In one of the simulations, the radiative effect was added to the particle's diffusional growth equation as well as the supersaturation equation, while in the other simulation, radiative feedback was turned off.

Figures 2 through 6 compare the CRM simulated supersaturation with respect to ice (SSI), water vapor mixing ratio, PI number concentration, snow (aggregate) number concentration, and total ice mass. It is seen in Figure 2 that a maximum SSI of more than 23% is produced in the simulation with radiative feedback, while in the simulation without radiative feedback the maximum SSI predicted is generally less than 3%. Also, it is apparent that the largest jump in SSI production occurs in the lower levels of the cloud. In response to greater SSI production, a maximum PI concentration of nearly $1300/L$ is predicted near the cloud top at 30 minutes into the simulation with radiative feedback. This compares to the maximum PI concentration of less than $100/L$ in the simulation without radiative

feedback (Figure 4) at the same time. In contrast to the massive production of PI in the simulation with radiative feedback, Figure 5 shows that maximum aggregate number concentration produced in this simulation has dropped significantly from about $8.0 \times 10^{-5}/L$ (in the simulation without radiative feedback) to slightly more than $2.0 \times 10^{-5}/L$. As the simulation proceeds from 30 to 60 minutes, the number concentration of PI has reduced dramatically while the maximum snow particle number concentration has increased by a factor of about 6. This is because vapor deposition of PI particles results in production of snow. Also evident is that most aggregate particles in the simulation without radiative feedback reside near the cloud base (below 6 km level) while in the simulation with radiative feedback, most of the aggregate particles are deep in the cloud layer between 5.2 km to 8 km levels.

Even though much more PI crystals are produced in the simulation with radiative feedback than in the simulation without radiative feedback, the maximum PI mixing ratio ($0.24g/kg$) predicted in the simulation with radiative feedback is only about half of the value ($0.42g/kg$) produced in the other simulation. Following a similar trend as in the PI mixing ratio prediction, maximum aggregate mixing ratio predicted in the simulation with radiative feedback ($3 \times 10^{-7}g/kg$) is more than one order less than predicted in simulation without radiative feedback (1.5×10^{-5} g/kg) at 30 minutes of simulation time. Figure 6 compares the total ice prediction for the two simulations at 30 and 60 minutes of the simulation time. It is evident that much less ice mass is produced in the simulation with radiative feedback compared to the prediction without radiative feedback.

Figure 7 shows the particle size-dependent radiative flux toward a particle at 100 time steps for a parcel which has its origin at 4038.0 m, while Figure 8 displays the radiative flux for another parcel whose origin is deep in the cloud layer at 7013.47 m above the ground. The results show that radiative warming of ice particles (see bottom panels of the two Figures) is dominant in the cloud layer. Also smaller ice particles tend to experience

less radiative warming than larger particles in the simulation with radiative feedback. It should be noted that radiative warming or cooling for an ice particle is different from the warming or cooling of the atmospheric environment because one depends on the balance described by equation (4) (for a particle) while the other depends on the divergence of the net radiative fluxes (upwelling plus downwelling). So, when the model predicts that the atmosphere experiences radiative cooling, it does not necessarily imply that each particle sees the same effect because as these two Figures display, radiative warming or cooling for a particle is size-dependent.

Based upon Figures 7 and 8, one can explain the lack of ice production in the simulation with radiative feedback easily. High SSI activates the ice nucleation processes in the bin-microphysics model. The ice particles produced through nucleation processes are added to the relevant bins (always very small bins) of the PI category. After the formation of these ice particles, they experience diffusional growth in an environment of positive SSI. The newly nucleated ice crystals are so small that the radiative effect is not a significant factor in the early stage of an ice particle's diffusional growth.

As more and more PI crystals are produced, collision and coalescence among the ice particles results in the formation of aggregates. Both aggregates and PI crystals can experience significant growth through diffusion of water vapor as long as $-R$ in Equation (3) is not enough to balance the right-hand side (note that R is negative for radiative warming). On attaining a certain size (for example, r_{limit}), an ice particle finds itself in a situation in which the radiation it absorbs is balanced by the diffusion of heat away from the particle's surface and diffusional growth is substantially retarded because the saturation vapor pressure at the particle's surface is enhanced. However, particles larger than r_{limit} can be produced through aggregation, but these larger particles can not survive for very long because the radiation they absorb maintains high values of surface ice saturation vapor pressures. Eventually, particles larger than r_{limit} will warm sufficiently to experience

evaporation which adds water vapor to the free air, resulting in higher water mixing ratio (or supersaturation with respect to ice), especially in the region between 4 and 6 km levels. Large ice particles in the simulation without radiative feedback, however, are not restricted in their vapor depositional growth by the processes stated above. This is the reason why more ice mass production is predicted in the simulation without radiative feedback than in the simulation with radiative feedback.

Fluxes of momentum, θ_{il}, and r_t are also compared between the simulation with radiative feedback and that without radiative feedback (see Figures 9 through 10). The two simulations have generally similar vertical profiles for these fluxes, except that $< V'W' >$ displays significant difference below 6 km level. The larger absolute magnitude in $< V'W' >$ associated with the simulation without radiative feedback may indicate that more active entrainment and detrainment processes are involved. This conclusion is supported by the larger $< r_t'W' >$ near the cloud base for the simulation without radiative feedback.

Figure 11 compares the total turbulent kinetic energy (TKE) and TKE production between the two simulations. The total TKE profile indicates that the simulation without radiative feedback tends to be more turbulent than the simulation with radiative feedback, especially in the upper levels of the cloud system. Generally, the upper levels of the cloud system tend to be negatively buoyant, while below $7700m$, positive buoyancy dominates for the simulation without radiative feedback. Also, shear production which is not a significant factor compared with buoyancy production is confined to a very shallow region between 7500 to $7700m$ for this simulation. However, for the simulation with radiative feedback, shear production is comparable to buoyancy in the very shallow region similar to that in the other simulation. The appearance of layered structures in the total TKE profiles for the case with radiative feedback suggests that the cloud system is more decoupled in the vertical for the simulation with radiative feedback than for the simulation without radiative feedback.

Consistent with the difference in ice mass production, the optical depths (both solar as well as infrared) predicted in the simulation without radiative feedback are larger than that predicted in the simulation with radiative feedback (Figure 12). The two peaks near 5 km and 6 km in the optical depth profiles correspond very well to the peaks in aggregate and PI production, respectively. Since the model-predicted cloud system without radiative feedback is optically thick and consists of larger ice particles than the cloud predicted in the simulation with radiative feedback, Figure 13 shows that a well-defined pattern of upper level cooling and lower level warming dominates the simulation without radiative feedback because the cloud system is able to absorb more longwave radiation from below (resulting in warming near cloud base) and emits more longwave radiation near cloud top which results in more radiative cooling above than in the simulation with radiative feedback. In the simulation with radiative feedback, since the model-predicted cloud system is optically thinner, solar radiation can penetrate deeper into the cloud layer than in the simulation without radiative feedback, resulting in a peak of solar warming just below 6000 m level. Both cooling and warming in the simulation without radiative feedback are more significant than in the other simulation just because of the significant difference in the optical depth of the model-predicted clouds.

5. Summary

CRM simulations of the November 26, 1991 FIRE II cirrus event demonstrate that the radiative effects on ice particle's diffusional growth (or evaporation) can significantly affect the macro-structure and microstructure of cirrus clouds. However, the radiative impact on the evolution and properties of cirrus clouds can be very complex. Radiative warming for an ice particle will restrict the particle's diffusional growth. In the case of radiative warming, saturation vapor pressure on the surface of ice crystals can increase to

the point that vapor deposition growth is retarded or changed to sublimation. However, ice mass production can be enhanced in the case of net radiative cooling of an ice particle.

Further sensitivity tests of the radiative effects on ice particle's diffusional growth should be done for different cirrus cloud regimes using the CRM and LES frameworks. Even though the CRM simulations of this study have shown significant difference between the simulations with radiative feedback and that without radiative feedback, it should be remembered that the simulation results apply only to this specific case.

Acknowledgments

This work was supported by the National Aeronautics and Space Administration under contracts #NAG-1-1703 and #NAG-1-2045. Jerry Harrington and Tamir Reisin are acknowledged for their critique of the derivations in the text. The help of Brenda Thompson in preparing this manuscript is greatly appreciated.

APPENDIX A. Definition of Symbols

C	capacity
c_p	specific heat at constant pressure
D	molecular diffusion coefficient
e_{si}	saturation vapor pressure with respect to ice
e_{sw}	saturation vapor pressure with respect to water
f_1	ventilation factor
f_2	gas kinetic factor
K	thermal conductivity of air
L_c	latent heat of condensation
L_s	latent heat of sublimation
M_i	total ice mass due to depositional growth
M_w	total liquid mass due to condensational growth
m_i	mass of a single ice particle
m_w	mass of a single water droplet
q_v	specific humidity (water vapor mixing ratio)
q_{si}	saturation water vapor mixing ratio with respect to ice
q_{sw}	saturation water vapor mixing ratio with respect to water
R	longwave radiative energy
R_v	gas constant for water vapor
r	radius of a particle
S_i	saturation ratio with respect to ice
ΔS_i	specific humidity surplus with respect to ice
S_w	saturation ratio with respect to water
ΔS_w	specific humidity surplus with respect to water

T	air temperature
T_r	temperature at the surface of a particle
T_∞	environmental temperature (is equal to T)
$\rho_{s,r}$	saturation (to water) vapor density at the surface of a particle
$\rho_{si,r}$	saturation (to ice) vapor density at the surface of a particle
ρ_∞	environmental vapor density

APPENDIX B. Derivation of the Diffusional Mass Growth and Supersaturation Equations

B.1 The diffusional mass growth equations for water and ice

The basic equation for diffusional growth of either cloud drops or ice crystals has been presented by numerous authors. When radiative effects on the diffusional growth of a particle are added to the mass growth equation, the equation becomes complicated. In this chapter, we derive the diffusional mass growth equation for a particle with the infrared radiative effects included.

The basic equations for diffusional growth of a particle are given by

for water drops:

$$L_c \frac{dm_w}{dt} - R = 4\pi r K f_1^* f_2^* (T_r - T_\infty) \tag{B.1}$$

$$\frac{dm_w}{dt} = 4\pi r D f_1 f_2 (\rho_\infty - \rho_{s,r}) \tag{B.2}$$

and for ice particles:

$$L_s \frac{dm_i}{dt} - R_{ice} = 4\pi C K f_1^* f_2^* (T_r - T_\infty) \tag{B.3}$$

$$\frac{dm_i}{dt} = 4\pi C D f_1 f_2 (\rho_\infty - \rho_{si,r}). \tag{B.4}$$

It should be noted that, generally, coefficient f needs not be the same for heat and for vapor transfer. However, for simplicity and as a convenient approximation, we assume that $f_1 = f_1^*$ and $f_2 = f_2^*$ in the following derivations.

B.1.1 The depositional growth equation for ice particles

Since the surface of the ice particle is assumed to be saturated, the vapor density at the particle surface is

$$\rho_{si,r}(T_r) = \frac{e_{si}(T_r)}{R_v T_r}. \tag{B.5}$$

From B.5, we can get that

$$\frac{d\rho_{si,r}}{\rho_{si,r}} = \frac{de_{si}}{e_{si}} - \frac{dT_r}{T_r}. \tag{B.6}$$

By using Clausius-Clapeyron equation, B.6 can be rewritten as

$$\frac{d\rho_{si,r}}{\rho_{si,r}} = \frac{L_s}{R_v} \cdot \frac{dT_r}{T_r^2} - \frac{dT_r}{T_r}. \tag{B.7}$$

Integrate B.7 from T_r to T_∞ assuming that $\frac{T_\infty}{T_r} \approx 1$. Also, since $\frac{\rho_{si,r}(T_\infty)}{\rho_{si,r}(T_r)}$ and $\frac{T_\infty}{T_r}$ are close to unity, $ln\frac{\rho_{si,r}(T_\infty)}{\rho_{si,r}(T_r)}$ and $ln\frac{T_\infty}{T_r}$ can be expanded according to Taylor series with respect to 1 to get the following approximations

$$ln\frac{\rho_{si,r}(T_\infty)}{\rho_{si,r}(T_r)} \approx \frac{\rho_{si,r}(T_\infty) - \rho_{si,r}(T_r)}{\rho_{si,r}(T_r)} \tag{B.8}$$

$$ln\frac{T_\infty}{T_r} \approx \frac{T_\infty - T_r}{T_r}. \tag{B.9}$$

Then, we can get

$$\frac{\rho_{si,r}(T_\infty) - \rho_{si,r}(T_r)}{\rho_{si,r}(T_r)} \approx \frac{L_s(T_\infty - T_r)}{R_v T_r T_\infty} - \frac{T_\infty - T_r}{T_r} \approx \frac{T_\infty - T_r}{T_\infty} \cdot (\frac{L_s}{R_v T_\infty} - 1). \tag{B.10}$$

Combining B.10 and B.3,

$$\frac{\rho_{si,r}(T_\infty) - \rho_{si,r}(T_r)}{\rho_{si,r}(T_r)} = (1 - \frac{L_s}{R_v T_\infty}) \frac{1}{4\pi C K T_\infty f_1 f_2} (L_s \frac{dm_i}{dt} - R_{ice}). \tag{B.11}$$

From mass growth equation $\frac{dm_i}{dt} = 4\pi CDf_1f_2(\rho_\infty - \rho_{si,r}(T_r))$, we know that

$$\frac{\rho_\infty - \rho_{si,r}(T_r)}{\rho_{si,r}(T_r)} = \frac{dm_i}{dt}\frac{1}{4\pi CDf_1f_2\rho_{si,r}(T_r)}. \tag{B.12}$$

Subtracting B.11 from B.12 to get

$$\frac{\rho_\infty - \rho_{si,r}(T_\infty)}{\rho_{si,r}(T_r)} = \frac{1}{4\pi Cf_1f_2}\{[\frac{1}{D\rho_{s,r}(T_r)} + \frac{L_s}{KT_\infty}(\frac{L_s}{R_vT_\infty} - 1)]\frac{dm_i}{dt} - \frac{R_{ice}}{KT_\infty}(\frac{L_s}{R_vT_\infty} - 1)\}. \tag{B.13}$$

Since $T_\infty \approx T_r = T$ and $\rho_{si,r}(T_r) \approx \rho_{si,r}(T_\infty) = \frac{e_{si}(T)}{R_vT}$, also note that $\frac{\rho_\infty}{\rho_{si,r}(T)} = S_i$, the supersaturation ratio with respect to ice, then we get

$$4\pi Cf_1f_2(S_i - 1) + \frac{R_{ice}}{KT}(\frac{L_s}{R_vT} - 1) = \frac{dm_i}{dt}[\frac{R_vT}{De_{si}(T)} + \frac{L_s}{KT}(\frac{L_s}{R_vT} - 1)]. \tag{B.14}$$

Following Tzivion et al. (1989), let $\Delta S_i = q_v - q_{si}$ and $C_i(P,T,m_i) = f_1q_{si}^{-1}[\frac{R_vT}{De_{si}(T)} + \frac{L_s}{KT}(\frac{L_s}{R_vT} - 1)]^{-1}$ (note that f_1, the ventilation factor, is a function of the Reynolds number which is related to the particle mass). Also, note that $S_i - 1 = \frac{\Delta S_i}{q_{si}}$, where ΔS_i is called the specific humidity surplus. Then B.14 can be rewritten as

$$\frac{dm_i}{dt} = f_2C_i(P,T,m_i)[4\pi C\Delta S_i + \frac{R_{ice}q_{si}}{Kf_1f_2T}(\frac{L_s}{R_vT} - 1)]. \tag{B.15}$$

Equation B.15 approximates the depositional growth of an ice particle with the radiative effects included.

B.1.2 The diffusional growth equation for water drops

Following similar procedure, the diffusional growth equation for a water drop can be derived as

$$\frac{dm_w}{dt} = f_2C_w(P,T,m_w)[4\pi r\Delta S_w + \frac{Rq_{sw}}{Kf_1f_2T}(\frac{L_c}{R_vT} - 1)] \tag{B.16}$$

where $C_w(P,T,m_w)$ is defined as

$$C_w(P,T,m_w) = f_1 q_{sw}^{-1}[\frac{R_v T}{De_{sw}(T)} + \frac{L_c}{KT}(\frac{L_c}{R_v T} - 1)]^{-1}. \tag{B.17}$$

B.2 Solutions to the diffusional mass growth equations

B.2.1 Solution to the diffusional mass growth equation for water drops

For water drops, the mass growth equation (B.16) can be rewritten as (similar to Harrington et al., 1999)

$$\frac{dm_w}{dt} = C_{w,new}(P,T,m_w)\frac{m_w^{2/3}}{m_w^{1/3} + l_0}[\Delta S_w + \frac{R q_{sw} m_w^{-1/3}}{K f_1 f_2 T B_w}(\frac{L_c}{R_v T} - 1)] \tag{B.18}$$

where B_w is a constant equal to $4\pi(\frac{3}{4\pi\rho_w})^{1/3}$ and $C_{w,new}(P,T,m_w)$ is defined in Tzivion et al. (1989) and equal to $C_w(P,T,m_w)B_w$. In deriving B.18, the gas kinetic effect, f_2, is represented by (Clark, 1973)

$$f_2 = \frac{m_w^{1/3}}{m_w^{1/3} + l_0} \tag{B.19}$$

where l_0 is a length-scale representing the gas kinetic effects. The radius of a drop is related to the mass as

$$r = (\frac{3}{4\pi\rho_l} m_w)^{1/3}. \tag{B.20}$$

Replacing the radiative effect R in the above equation according to Harrington et al. (1999), we get

$$\frac{dm_w}{dt} = C_{w,new}(P,T,m_w)\frac{m_w^{2/3}}{m_w^{1/3} + l_0}\left[\Delta S_w + \frac{q_{sw} m_w^{1/3} B_w^{\star} E_d(m_w)}{K f_1 f_2 T}\left(\frac{L_c}{R_v T} - 1\right)\right] \tag{B.21}$$

here $B_w^{\star} = \left(\frac{3}{4\pi\rho_w}\right)^{1/3}$ and $E_d(m_w)$ is the radiative effect that includes all of the flux terms (the definition of $E_d(m_w)$ as found in Harrington et al., 1999).

Equation B.21 must be integrated in order to deduce how a water drop grows over a time step in numerical model. To solve for the analytic solution to B.21 without the radiation term, integration is taken for a single time increment Δt, during which the effect of changes in $C_{w,new}(P,T,m_w)$ is assumed to be negligible (Tzivion et al., 1989). Stevens et al. (1996a) showed the analytic solution to B.21 without the radiative term on the right-hand side as

$$m_w(t+\delta t) = [((m_w(t)^{1/3} + l_0)^2 + \frac{2}{3}\tau)^{1/2} - l_0]^3 \tag{B.22}$$

where $\tau = \int_t^{t+\delta t} C_{w,new}(P,T,m_w)\Delta S_w dt$.

With the radiative effects, analytic solution to B.21 can not be obtained easily because a mass related term which multiplies the radiative effect R appears on the right-hand side. So, the equation must be solved iteratively. Harrington et al. (1999) discussed simplifications to solving the equation B.21. By using a mean value of the radiative term for each bin (for the bin microphysics model), Harrington et al. (1999) showed that acceptable accuracy (the largest errors never exceed 1.5% under reasonable atmospheric conditions) can be obtained by comparing the approximations with the solutions obtained using iterative method. By applying the mean value of the radiative term for each bin and integrating over a single time step $\Delta t(= t_2 - t_1)$, equation B.21 becomes

$$\begin{aligned}
&\int_{m_w(t)}^{m_w(t+\Delta t)} \frac{m_w^{1/3} + l_0}{m_w^{2/3}} dm_w = \\
&\quad C_{w,new}(P,T,\bar{m}_{w,k}) \int_t^{t+\Delta t} \Delta S_w dt \\
&\quad + C_{w,new}(P,T,\bar{m}_{w,k}) \frac{q_{sw}\bar{m}_{w,k}^{1/3} B_w^{\star} E_d(\bar{m}_{w,k})}{K f_1(\bar{m}_{w,k}) f_2(\bar{m}_{w,k}) T} \left(\frac{L_c}{R_v T} - 1\right) \Delta t \\
&\quad = \tau_r = \tau + \tau_k
\end{aligned} \tag{B.23}$$

which has the solution

$$m_w(t+\Delta t) = \left\{ \left[\left(m_w(t)^{1/3} + l_0 \right)^2 + \frac{2}{3}\tau_r \right]^{1/2} - l_0 \right\}^3 \tag{B.24}$$

where $m_w(t)$ and $m_w(t+\Delta t)$ stand for the initial and final masses of a droplet; $E_d(\bar{m}_{w,k})$ and $\bar{m}_{w,k}$ stand for the mean radiative effects and the mean mass for bin number k, respectively; τ_k is the bin- dependent radiative forcing term and τ_r the total forcing on the mass for bin number k.

Detailed discussion about the calculation of the radiative term is available in Harrington et al. (1999).

B.2.2 Solution to the diffusional mass growth equation for ice particles

The solution to B.15 is not as easily obtained as that to the diffusional mass growth equation for water drops because of the electrical capacitance C which can be a complicated function of the particle dimensions.

For a spherical ice particle, equation B.15 can be written similarly as B.21 when the radiative effect R is replaced according to Harrington et al. (1999) and the approximate solution to B.15 has the same form as B.24 except that τ_r is now replaced by $\tau_{r,i}$ which is defined with respect to ice and can be written as

$$\begin{aligned} \tau_{ri} &= \tau_i + \tau_{ki} = \int_{m_i(t)}^{m_i(t+\Delta t)} \frac{m_i^{1/3} + l_0}{m_i^{2/3}} dm_i \\ &= C_{i,new}(P,T,\bar{m}_{i,k}) \int_t^{t+\Delta t} \Delta S_i dt \\ &\quad + C_{i,new}(P,T,\bar{m}_{i,k}) \frac{q_{si}\bar{m}_{i,k}^{1/3} B_i^* E_d(\bar{m}_{i,k})}{K f_1(\bar{m}_{i,k}) f_2(\bar{m}_{i,k}) T} \left(\frac{L_s}{R_v T} - 1 \right) \Delta t \end{aligned} \tag{B.25}$$

where $C_{i,new}(P,T,m_i)$ is defined as $C_i(P,T,m_i)B_i$ and B_i is equal to $4\pi(\frac{3}{4\pi\rho_i})^{1/3}$; B_i^* is equal to $\left(\frac{3}{4\pi\rho_i}\right)^{1/3}$.

For other ice particle habits, the solution should be modified according to the mass-particle size relation used.

B.3 Supersaturation (specific humidity surplus) equations

Following Tzivion et al. (1989), using equations

$$q_{sw}(T) = 0.622\frac{e_{sw}(T)}{P} \tag{B.26}$$

$$\frac{de_{sw}}{dT} = \frac{L_c e_{sw}(T)}{R_v T^2} \tag{B.27}$$

$$\frac{\partial q_{sw}(T)}{\partial t} = \frac{0.622}{P}\frac{L_c e_{sw}(T)}{R_v T^2}\frac{\partial T}{\partial t} \tag{B.28}$$

$$\frac{\partial q_v}{\partial t} = -(\frac{\partial M_w}{\partial t} + \frac{\partial M_i}{\partial t})_{condensation,evaporation} \tag{B.29}$$

$$\frac{\partial T}{\partial t} = \frac{L_c}{c_p}\frac{\partial M_w}{\partial t} + \frac{L_s}{c_p}\frac{\partial M_i}{\partial t} \tag{B.30}$$

we get

$$\begin{aligned}
\frac{\partial \Delta S_w}{\partial t} &= \frac{\partial(q_v - q_{sw})}{\partial t} = -\frac{\partial M_w}{\partial t} - \frac{\partial M_i}{\partial t} - \frac{0.622 L_c e_{sw}(T)}{R_v T^2 P c_p}[L_f\frac{\partial M_w}{\partial t} + L_s\frac{\partial M_i}{\partial t}] \\
&= -(1 + \frac{0.622 L_c^2 e_{sw}(T)}{R_v T^2 P c_p})\frac{\partial M_w}{\partial t} - (1 + \frac{0.622 L_c L_s e_{sw}(T)}{R_v T^2 P c_p})\frac{\partial M_i}{\partial t} \\
&= -A(P,T)\frac{\partial M_w}{\partial t} - A_1(P,T)\frac{\partial M_i}{\partial t}.
\end{aligned} \tag{B.31}$$

Similarly, the time dependence of ΔS_i can be derived as

$$\frac{\partial \Delta S_i}{\partial t} = -A_2(P,T)\frac{\partial M_w}{\partial t} - A_3(P,T)\frac{\partial M_i}{\partial t} \tag{B.32}$$

where

$$A_2(P,T) = (1 + 0.622\frac{L_s L_c e_{si}(T)}{R_v P c_p T^2}) \tag{B.33}$$

$$A_3(P,T) = (1 + 0.622\frac{L_s^2 e_{si}(T)}{R_v P c_p T^2}). \tag{B.34}$$

Since

$$\frac{\partial M_w}{\partial t} = \int \frac{dm_w}{dt} n(m_w) dm_w \tag{B.35}$$

$$\frac{\partial M_i}{\partial t} = \int \frac{dm_i}{dt} n(m_i) dm_i \tag{B.36}$$

where $n(m)$ is the distribution function with respect to mass and the right-hand side of each equation is integrated over the whole spectrum, we get (assuming spherical ice particles)

$$\begin{aligned}
\frac{\partial \Delta S_w}{\partial t} &= -A(P,T) \int \frac{dm_w}{dt} n(m_w) dm_w - A_1(P,T) \sum_{ice\ species} \int \frac{dm_i}{dt} n(m_i) dm_i \\
&= -A(P,T) \Delta S_w \int C_{w,new}(P,T,m_w) \frac{m_w^{2/3}}{m_w^{1/3} + l_0} n(m_w) dm_w \\
&\quad -A(P,T) \frac{q_{sw} B_w^\star}{KT} \left(\frac{L_c}{R_v T} - 1 \right) \int \frac{C_{w,new}(P,T,m_w)}{f_1(m_w)} m_w^{2/3} E_d(m_w) n(m_w) dm_w \\
&\quad -A_1(P,T) \Delta S_i \sum_{ice\ species} \int C_{i,new}(P,T,m_i) \frac{m_i^{2/3}}{m_i^{1/3} + l_0} n(m_i) dm_i \\
&\quad -A_1(P,T) \frac{q_{si}}{KT} \left(\frac{L_s}{R_v T} - 1 \right) \sum_{ice\ species} B_i^\star \int \frac{C_{i,new}(P,T,m_i)}{f_1(m_i)} m_i^{2/3} E_d(m_i) n(m_i) dm_i \\
&= G_1 \Delta S_w + G_2 \Delta S_i + D_1
\end{aligned} \tag{B.37}$$

$$\begin{aligned}
\frac{\partial \Delta S_i}{\partial t} &= -A_2(P,T) \int \frac{dm_w}{dt} n(m_w) dm_w - A_3(P,T) \sum_{ice\ species} \int \frac{dm_i}{dt} n(m_i) dm_i \\
&= -A_2(P,T) \Delta S_w \int C_{w,new}(P,T,m_w) \frac{m_w^{2/3}}{m_w^{1/3} + l_0} n(m_w) dm_w \\
&\quad -A_2(P,T) \frac{q_{sw} B_w^\star}{KT} \left(\frac{L_c}{R_v T} - 1 \right) \int \frac{C_{w,new}(P,T,m_w)}{f_1(m_w)} m_w^{2/3} E_d(m_w) n(m_w) dm_w \\
&\quad -A_3(P,T) \Delta S_i \sum_{ice\ species} \int C_{i,new}(P,T,m_i) \frac{m_i^{2/3}}{m_i^{1/3} + l_0} n(m_i) dm_i
\end{aligned}$$

$$-A_3(P,T)\frac{q_{si}}{KT}\left(\frac{L_s}{R_vT}-1\right)\sum_{ice\ species}B_i^{\star}\int\frac{C_{i,new}(P,T,m_i)}{f_1(m_i)}m_i^{2/3}E_d(m_i)n(m_i)dm_i$$

$$= G_3\Delta S_w + G_4\Delta S_i + D_2 \tag{B.38}$$

where D_1 and D_2 represent the longwave radiative effects on the specific humidity surplus. Also, the dynamic term (the term representing increase/decrease in specific humidity surplus due to vertical motions) can be easily combined with D_1 and D_2.

B.4 Solution to the supersaturation equations

Equations B.37 and B.38 can be solved analytically if G_1, G_2, G_3, G_4, D_1, and D_2 are assumed constants within a timestep. For the bin-microphysics model, the changes of these variables with time are neglected within a time increment $\Delta t = t - t_0$. Thus Δt should be small enough so as to justify this assumption. A detailed discussion about this assumption is available in Tzivion et al. (1989).

In order to solve equations B.37 and B.38, we first solve for the eigenvalues of the following coefficient matrix

$$\begin{bmatrix} G_1 & G_2 \\ G_3 & G_4 \end{bmatrix}. \tag{B.39}$$

This eigenvalue problem can be easily solved and the eigenvalues are

$$\lambda_1 = \frac{(G_1+G_4)+\sqrt{(G_1+G_4)^2-4(G_1G_4-G_2G_3)}}{2} \tag{B.40}$$

$$\lambda_2 = \frac{(G_1+G_4)-\sqrt{(G_1+G_4)^2-4(G_1G_4-G_2G_3)}}{2}. \tag{B.41}$$

Then, general solutions to the homogeneous forms of B.37 and B.38 can be easily obtained and written as

$$\Delta S_w = ae^{\lambda_1 t} + be^{\lambda_2 t} \tag{B.42}$$

$$\Delta S_i = \frac{\lambda_1 - G_1}{G_2} a e^{\lambda_1 t} + \frac{\lambda_2 - G_1}{G_2} b e^{\lambda_2 t} \tag{B.43}$$

where a and b are any constants.

Now, we need to find particular solutions to B.37 and B.38 in order to completely solve these two equations. The particular solutions can be obtained by considering a and b as functions of t and solving the following two equations

$$e^{\lambda_1 t}\frac{da}{dt} + e^{\lambda_2 t}\frac{db}{dt} = D_1 \tag{B.44}$$

$$\frac{\lambda_1 - G_1}{G_2} e^{\lambda_1 t}\frac{da}{dt} + \frac{\lambda_2 - G_1}{G_2} e^{\lambda_2 t}\frac{db}{dt} = D_2. \tag{B.45}$$

These two equations can be easily solved. A solution for a and b can be written as

$$a_1 = -\frac{(\lambda_2 - G_1)D_1 - G_2 D_2}{\lambda_1(\lambda_2 - \lambda_1)} e^{-\lambda_1 t} \tag{B.46}$$

$$b_1 = -\frac{1}{\lambda_2}[D_1 - \frac{(\lambda_2 - G_1)D_1 - G_2 D_2}{\lambda_2 - \lambda_1}]e^{-\lambda_2 t}. \tag{B.47}$$

Substituting a_1 and b_1 into B.42 and B.43 for a and b, we can get the particular solutions to these two equations. The particular solutions can be written as

$$\Delta S_w^* = -\frac{(\lambda_2 - G_1)D_1 - G_2 D_2}{\lambda_1(\lambda_2 - \lambda_1)} - \frac{1}{\lambda_2}[D_1 - \frac{(\lambda_2 - G_1)D_1 - G_2 D_2}{\lambda_2 - \lambda_1}] \tag{B.48}$$

$$\Delta S_i^* = -\frac{\lambda_1 - G_1}{G_2}\frac{(\lambda_2 - G_1)D_1 - G_2 D_2}{\lambda_1(\lambda_2 - \lambda_1)} - \frac{\lambda_2 - G_1}{G_2}\frac{1}{\lambda_2}[D_1 - \frac{(\lambda_2 - G_1)D_1 - G_2 D_2}{\lambda_2 - \lambda_1}]. \tag{B.49}$$

The final solutions to B.37 and B.38 can be obtained by adding these particular solutions to B.42 and B.43 to get

$$\Delta S_w = ae^{\lambda_1 t} + be^{\lambda_2 t} + \Delta S_w^* \tag{B.50}$$

$$\Delta S_i = \frac{\lambda_1 - G_1}{G_2} ae^{\lambda_1 t} + \frac{\lambda_2 - G_1}{G_2} be^{\lambda_2 t} + \Delta S_i^*. \tag{B.51}$$

Constants a and b in the above equations can be determined from the initial conditions at the start of each time step.

REFERENCES

Clark, T.L., 1973: Numerical modeling of the dynamics and microphysics of warm cumulus convection. *J. Atmos. Sci.*, **30**, 857-878.

Feingold, G., B. Stevens, W. R. Cotton, and A. S. Frisch, 1996: The relationship between drop in-cloud residence time and drizzle production in numerically simulated stratocumulus clouds. *J. Atmos. Sci.*, **53**, 1108-1122.

Harrington, J. Y., 1997: The effects of radiative and microphysical processes on simulated warm and transition-season Arctic stratus. Ph.D. dissertation, Colorado State University, Fort Collins, Colorado, 270 pp.

Harrington, J.Y., T. Reisin, W.R. Cotton, S.M. Kreidenweis, 1999: Cloud resolving simulations of Arctic stratus. Part II: Transition-season clouds. *Atmos. Res.*, **51**, 45-75.

Olsson, P.Q., J.Y. Harrington, G. Feingold, W.R. Cotton, and S. Kreidenweis, 1998: Exploratory cloud-resolving simulations of boundary layer Arctic stratus clouds. Part I: Warm season clouds. *Atmos. Res.*, **47-48**, 573-597.

Reisin, T., 1995: A numerical study of cloud seeding in Israel using as axisymmetrical cloud model with detailed microphysics. Ph.D. dissertation, Department of Geophysics and Planetary Sciences, Tel Aviv University, 238 pp.

Reisin, T., Z. Levin, and S. Tzivion, 1996: Rain production in convective clouds as simulated in an axisymmetric model with detailed microphysics. Part I: Description of the model. *J. Atmos. Sci.*, **53**, 497-519.

Rogers, R. R. and M. K. Yau, 1989: A short course in cloud physics. Third edition, *Pergamon Press*, 293 pp.

Stevens, B., G. Feingold, W. R. Cotton, and R. L. Walko, 1996a: Elements of the microphysical structure of numerically simulated nonprecipitating stratocumulus. *J. Atmos. Sci.*, **53**, 980-1007.

Stevens, B., R. L. Walko, W. R. Cotton, and G. Feingold, 1996b: The spurious production of cloud-edge supersaturation by Eulerian model. *Mon. Wea. Rev.*, **124**, 1034-1041.

Stephens, G. L., 1983: The influence of radiative transfer on the mass and heat budgets of ice crystals in the atmosphere. *J. Atmos. Sci.*, **40**, 1729-1739.

Tzivion, S., G. Feingold, and Z. Levin, 1987: An efficient numerical solution to the stochastic collection equation. *J. Atmos. Sci.*, **44**, 3139-3149.

Tzivion, S., G. Feingold, and Z. Levin, 1989: The evolution of rain-drop spectra. Part II: Collisional collection/breakup and evaporation in a rain shaft. *J. Atmos. Sci.*, **46**, 3312-3327.

Wu, T., 1999: Numerical modeling study of the November 26, 1991 cirrus event. Ph.D. dissertation, Colorado State University, Fort Collins, Colorado, 186 pp.

List of Tables

Table 1: Bin number and particle size relation for the first 25 bins. The particle sizes are in cm.

bin #	rain	pristine ice	graupel	aggregate
1	.31250E-03	.35195E-03	.39373E-03	.53437E-03
2	.39373E-03	.44343E-03	.49606E-03	.67326E-03
3	.49606E-03	.55869E-03	.62500E-03	.84826E-03
4	.62500E-03	.70390E-03	.78745E-03	.10687E-02
5	.78745E-03	.88686E-03	.99213E-03	.13465E-02
6	.99213E-03	.11174E-02	.12500E-02	.16965E-02
7	.12500E-02	.14078E-02	.15749E-02	.21375E-02
8	.15749E-02	.17737E-02	.19843E-02	.26930E-02
9	.19843E-02	.22348E-02	.25000E-02	.33930E-02
10	.25000E-02	.28156E-02	.31498E-02	.42749E-02
11	.31498E-02	.35475E-02	.39685E-02	.53861E-02
12	.39685E-02	.44695E-02	.50000E-02	.67860E-02
13	.50000E-02	.56312E-02	.62996E-02	.85499E-02
14	.62996E-02	.70949E-02	.79370E-02	.10772E-01
15	.79370E-02	.89390E-02	.10000E-01	.13572E-01
16	.10000E-01	.11262E-01	.12599E-01	.17100E-01
17	.12599E-01	.14190E-01	.15874E-01	.21544E-01
18	.15874E-01	.17878E-01	.20000E-01	.27144E-01
19	.20000E-01	.22525E-01	.25198E-01	.34200E-01
20	.25198E-01	.28380E-01	.31748E-01	.43089E-01
21	.31748E-01	.35756E-01	.40000E-01	.54288E-01
22	.40000E-01	.45050E-01	.50397E-01	.68399E-01
23	.50397E-01	.56759E-01	.63496E-01	.86177E-01
24	.63496E-01	.71512E-01	.80000E-01	.10858E+00
25	.80000E-01	.90100E-01	.10079E+00	.13680E+00

List of Figures

Positive flux denotes radiative cooling, while negative denotes radiative warming (solid lines: longwave+shortwave; dashed lines: longwave only).

Fig. 9 Momentum flux profiles at 60 minutes of simulation time. The solid line and dotted line are for runs with and without radiative feedback, respectively.

Fig. 10 Profiles of $< \theta'_{il} W' >$ and $< r'_t W' >$ at 60 minutes of simulation time. The solid line and dotted line are for runs with and without radiative feedback, respectively.

Fig. 11 Profiles of total TKE and TKE production terms for the simulations without (top) and with (bottom) radiative feedback on particle's diffusional growth at 60 minutes of the simulation time.

Fig. 12 Profiles of solar (τ_{solar}) and infrared ($\tau_{infrared}$) optical depths at 60 minutes of simulation time. The solid line and dotted line are for runs with and without radiative feedback, respectively.

Fig. 13 Profiles of total (solid), infrared (dashed), and solar (dotted) radiative heating rates at 60 minutes of simulation time. Top: without radiative feedback on particles' diffusional growth; bottom: with radiative feedback.

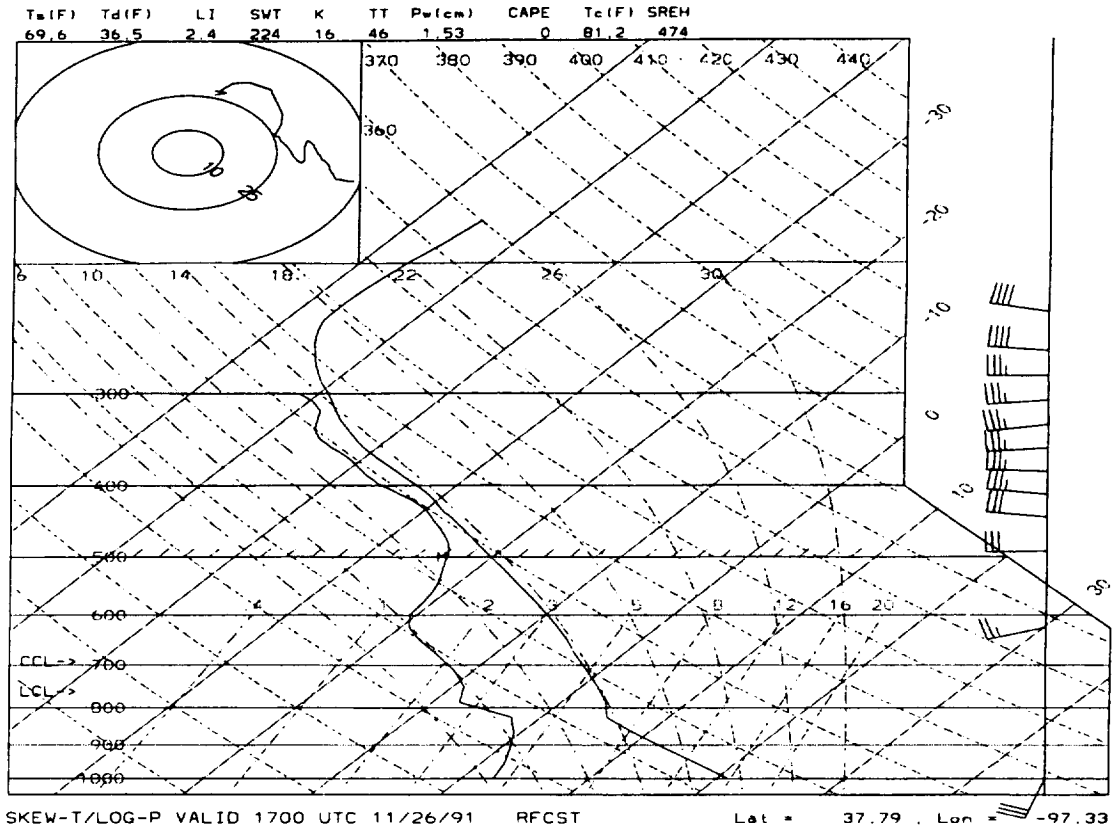
Ta(F) Td(F) LI SWT K TT Pw(cm) CAPE Tc(F) SREH
69.6 36.5 2.4 224 16 46 1.53 0 81.2 474
370 380 390 400 410 420 430 440
360
6 10 14 18 22 26 30
300
400
500
600
CCL->
700
LCL->
800
900
1000
-30 -20 -10 0 10 30
SKEW-T/LOG-P VALID 1700 UTC 11/26/91 RFCST
Lat = 37.79 , Lon = -97.33

Figure 1:

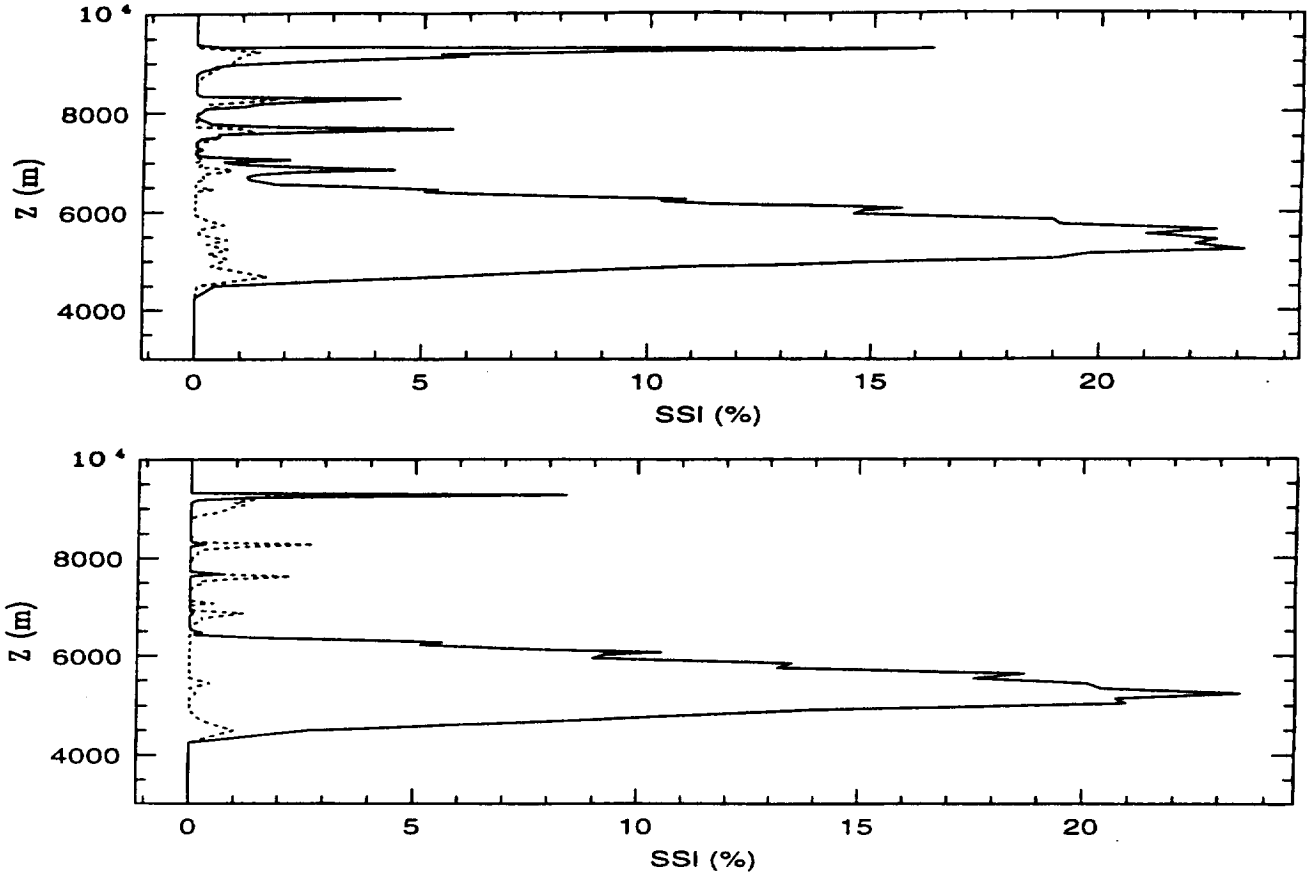
10 4
8000
6000
4000
Z (m)
0
5
10
15
20
SSI (%)
10 4
8000
6000
4000
Z (m)
0
5
10
15
20
SSI (%)

Figure 2:

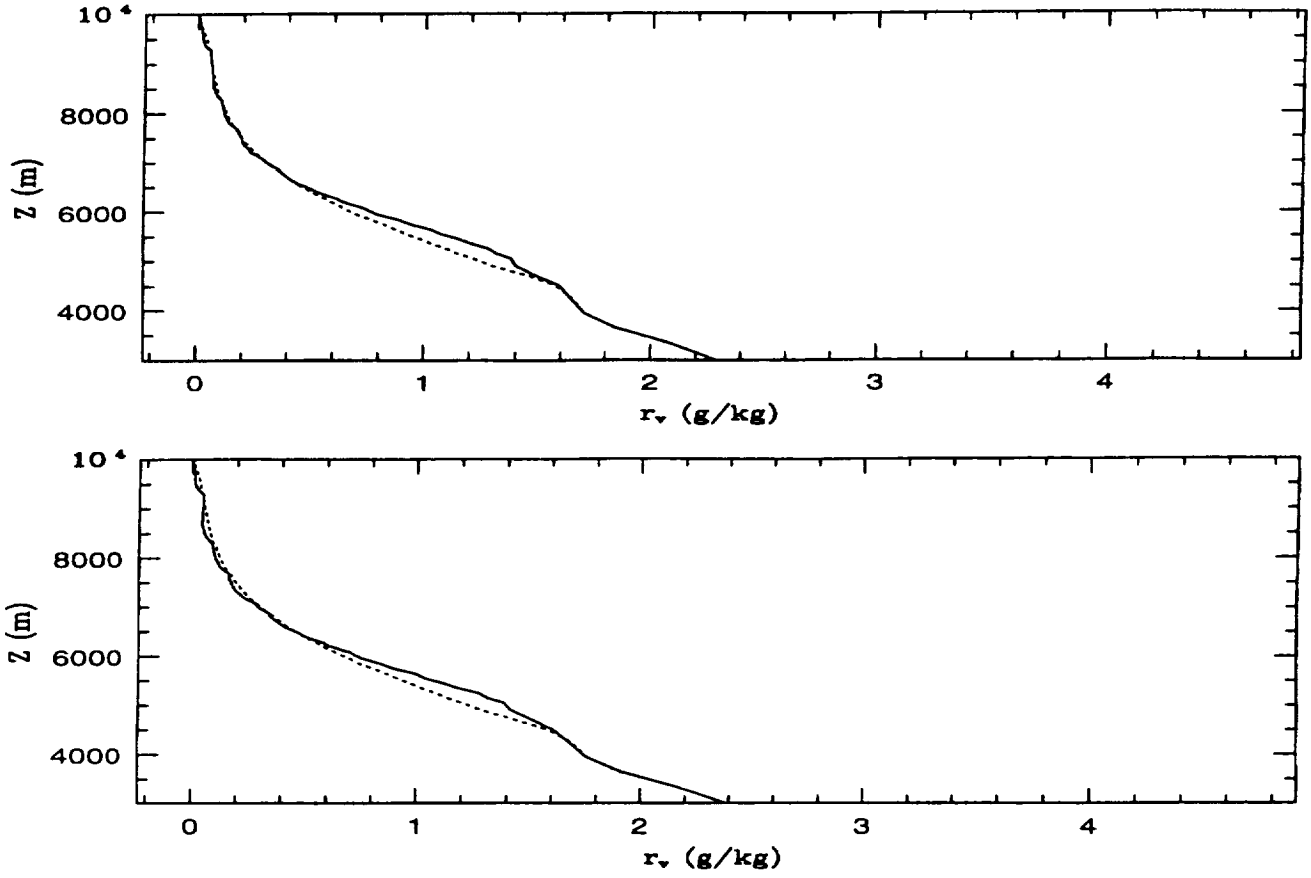
10 4
8000
6000
4000
Z (m)
0
1
2
3
4
r_v (g/kg)
10 4
8000
6000
4000
Z (m)
0
1
2
3
4
r_v (g/kg)

Figure 3:

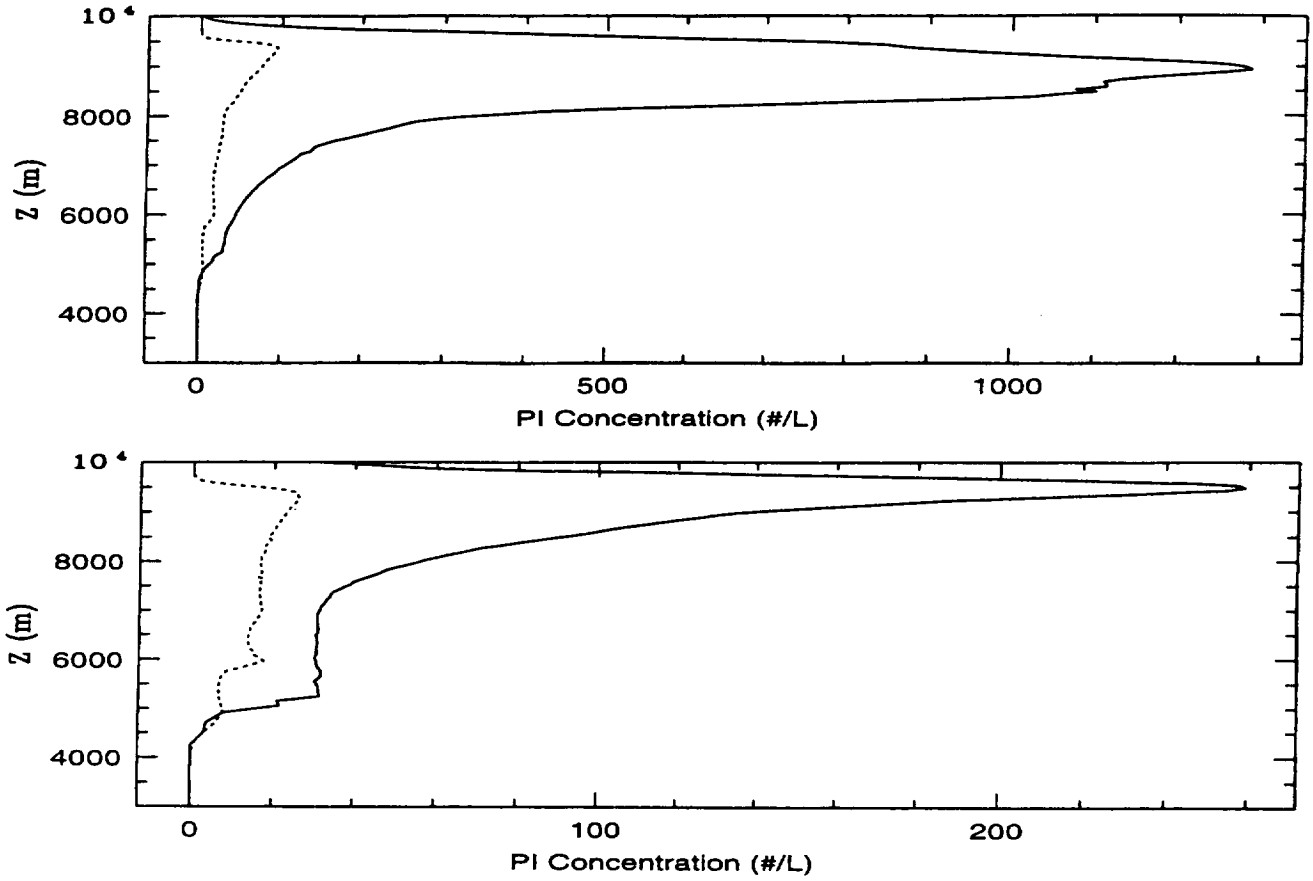
10 4
8000
6000
4000
Z (m)
0
500
1000
PI Concentration (#/L)
10 4
8000
6000
4000
Z (m)
0
100
200
PI Concentration (#/L)

Figure 4:

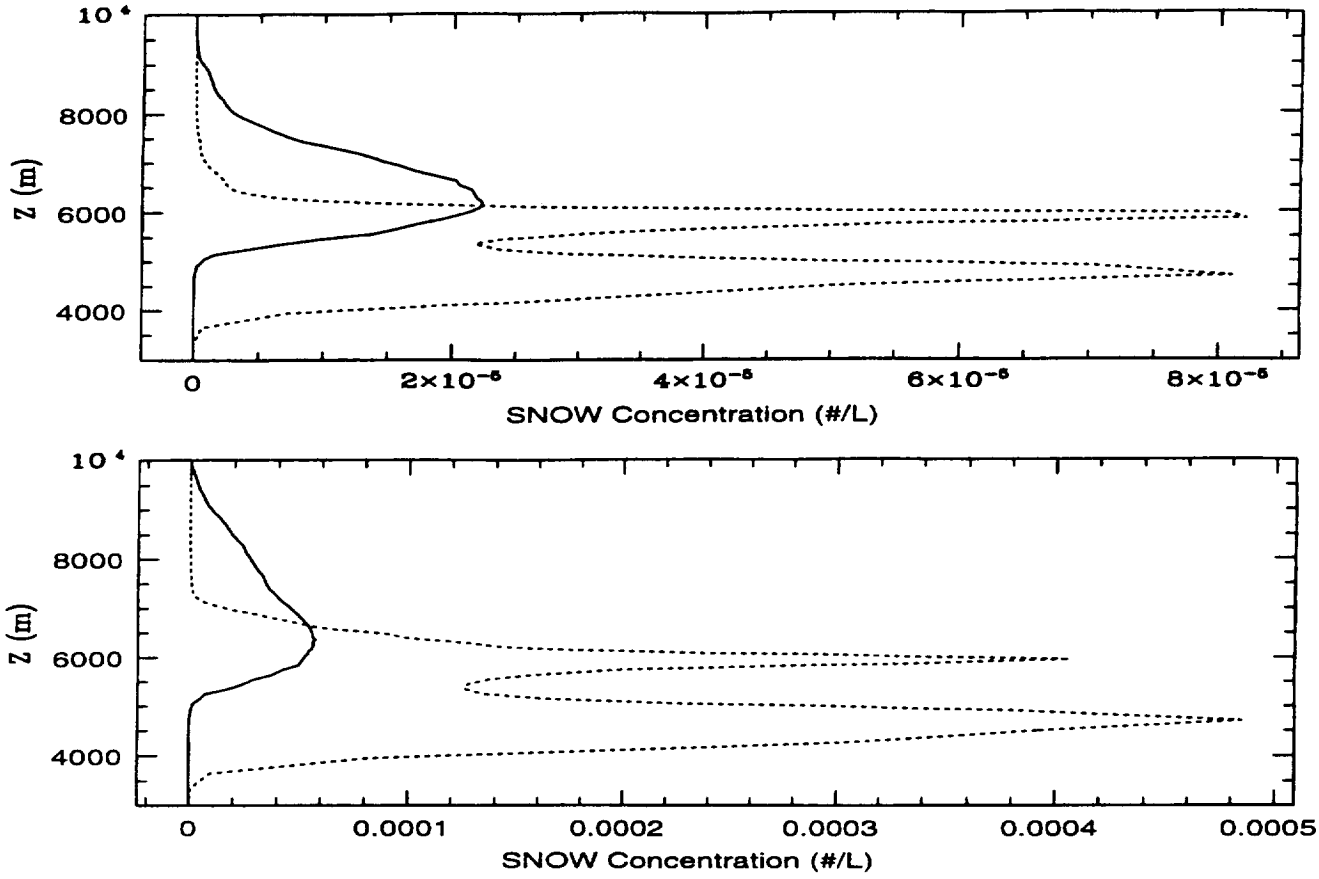
10 4
8000
6000
4000
Z (m)
0
2×10⁻⁵
4×10⁻⁵
6×10⁻⁵
8×10⁻⁵
SNOW Concentration (#/L)
10 4
8000
6000
4000
Z (m)
0
0.0001
0.0002
0.0003
0.0004
0.0005
SNOW Concentration (#/L)

Figure 5:

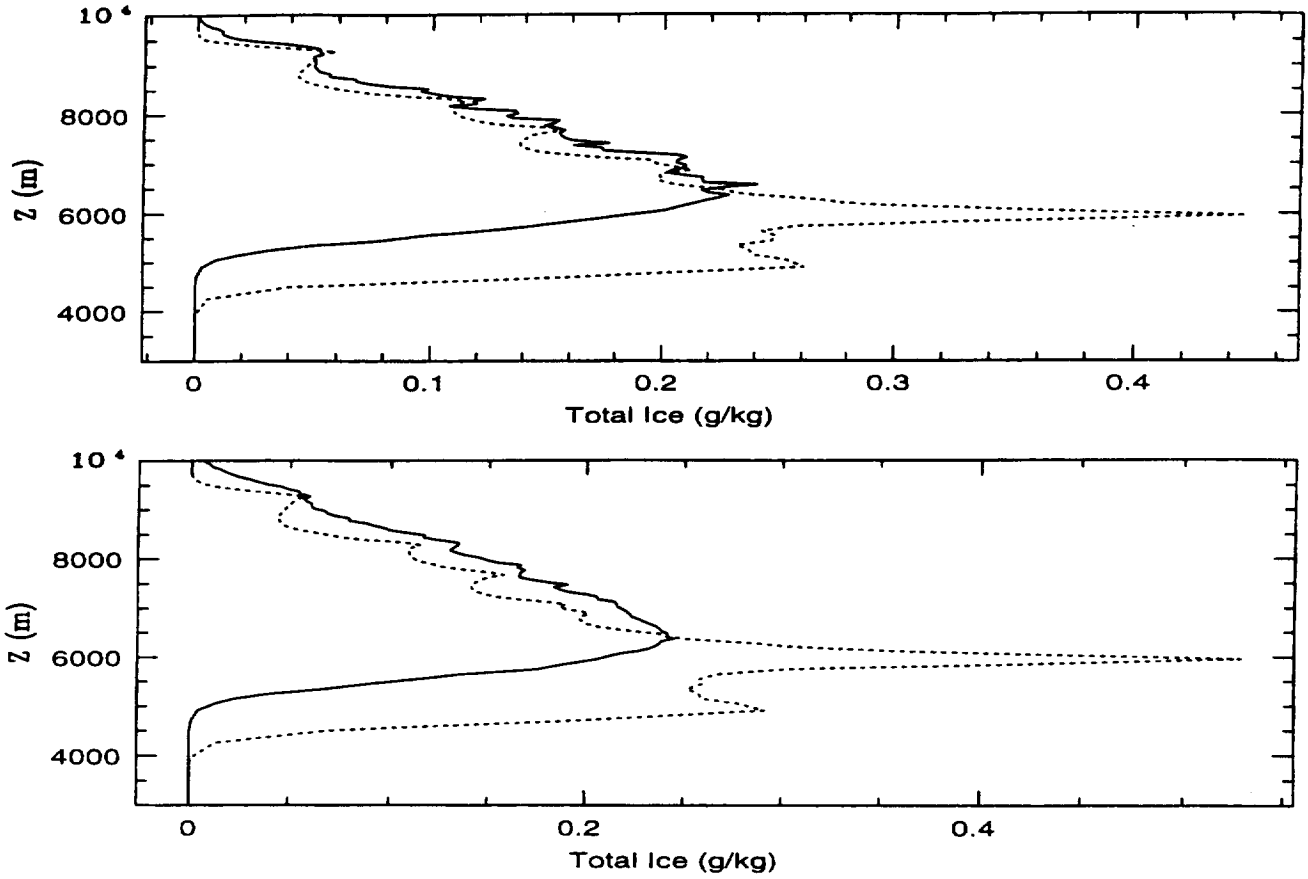
10 4
8000
6000
4000
Z (m)
0
0.1
0.2
0.3
0.4
Total Ice (g/kg)
10 4
8000
6000
4000
Z (m)
0
0.2
0.4
Total Ice (g/kg)

Figure 6:

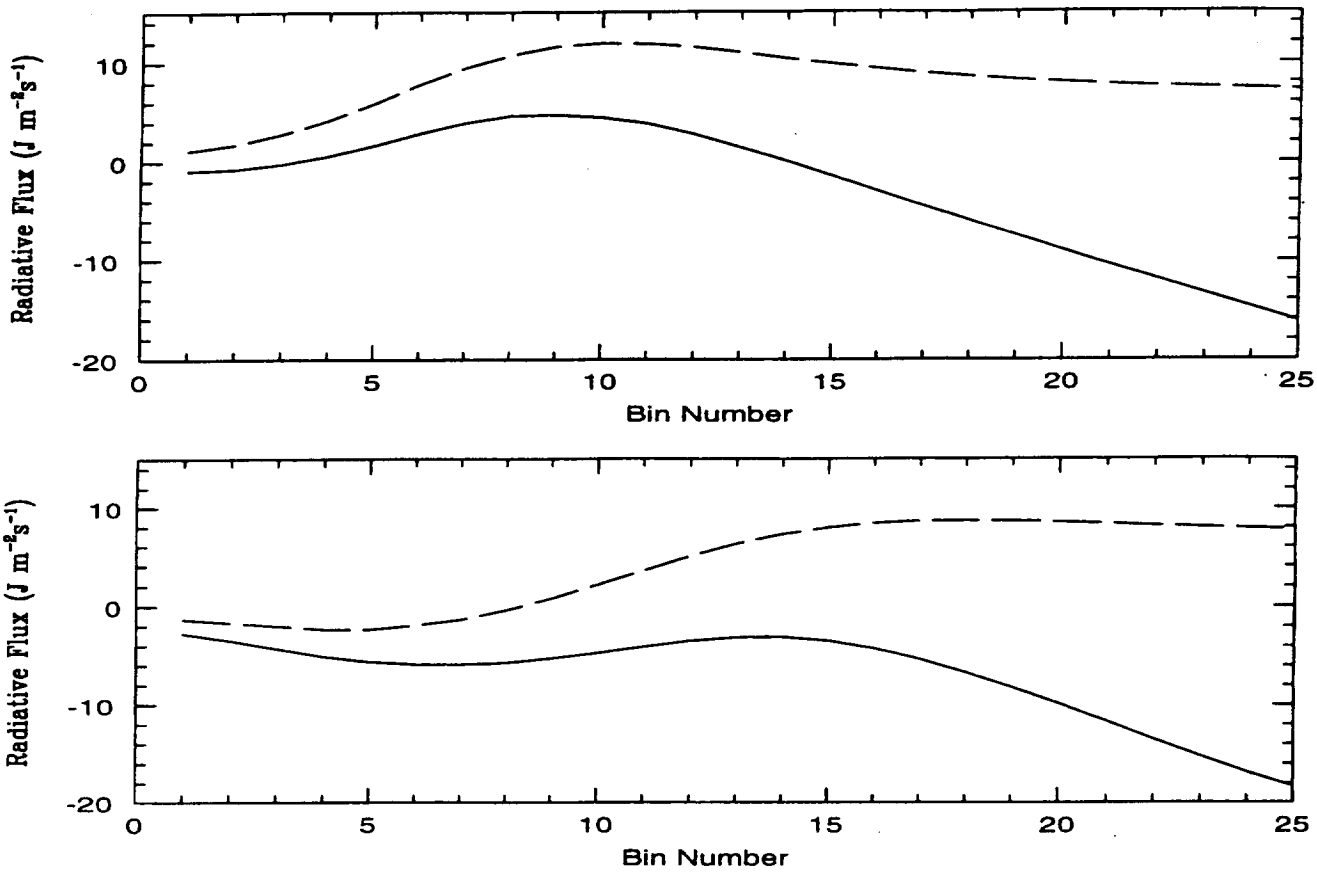
Radiative Flux (J m^{-2}s^{-1})
10
0
-10
-20
0
5
10
15
20
25
Bin Number
Radiative Flux (J m^{-2}s^{-1})
10
0
-10
-20
0
5
10
15
20
25
Bin Number

Figure 7:

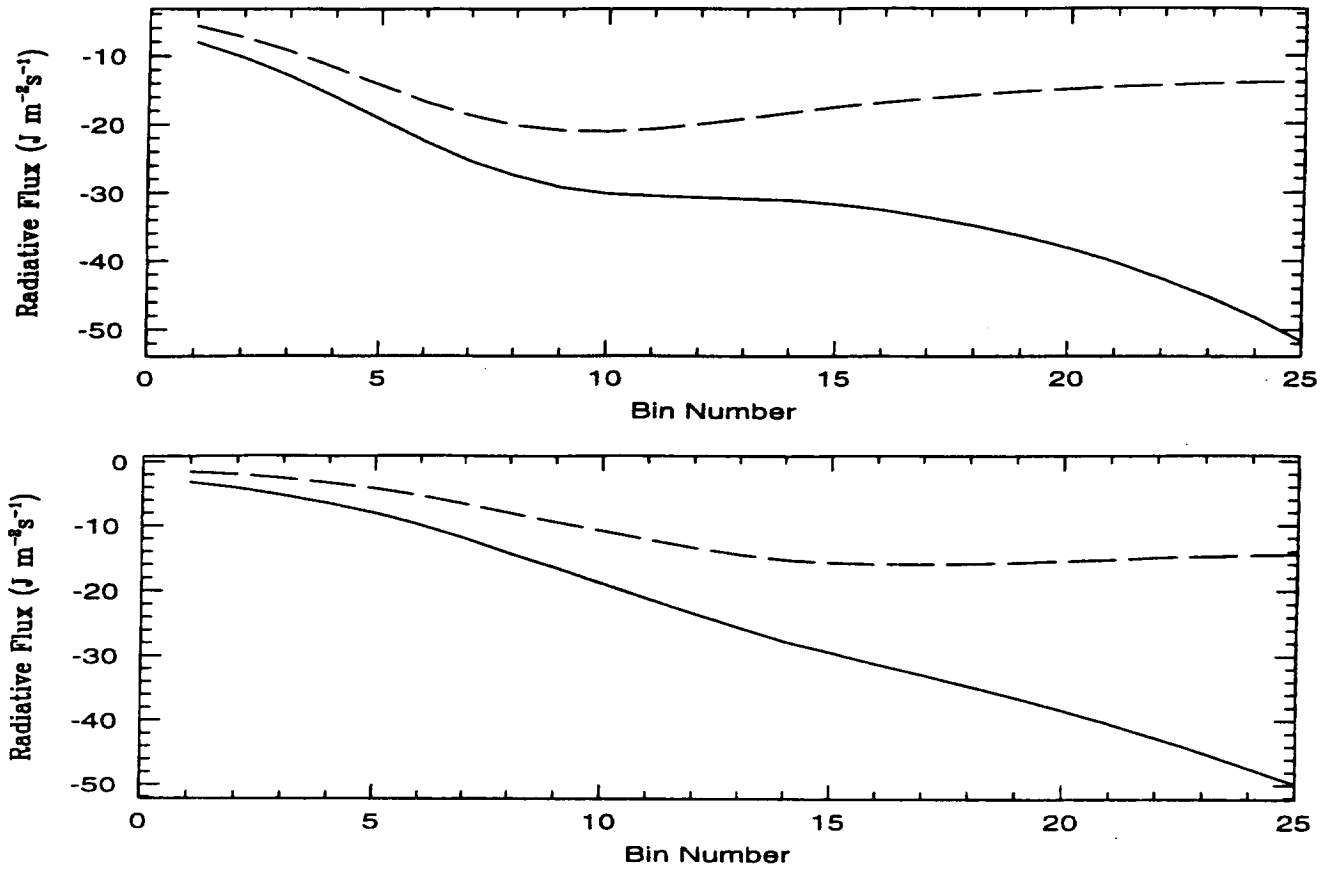
Radiative Flux (J m^{-2}s^{-1})
-10
-20
-30
-40
-50
0
5
10
15
20
25
Bin Number
Radiative Flux (J m^{-2}s^{-1})
0
-10
-20
-30
-40
-50
0
5
10
15
20
25
Bin Number

Figure 8:

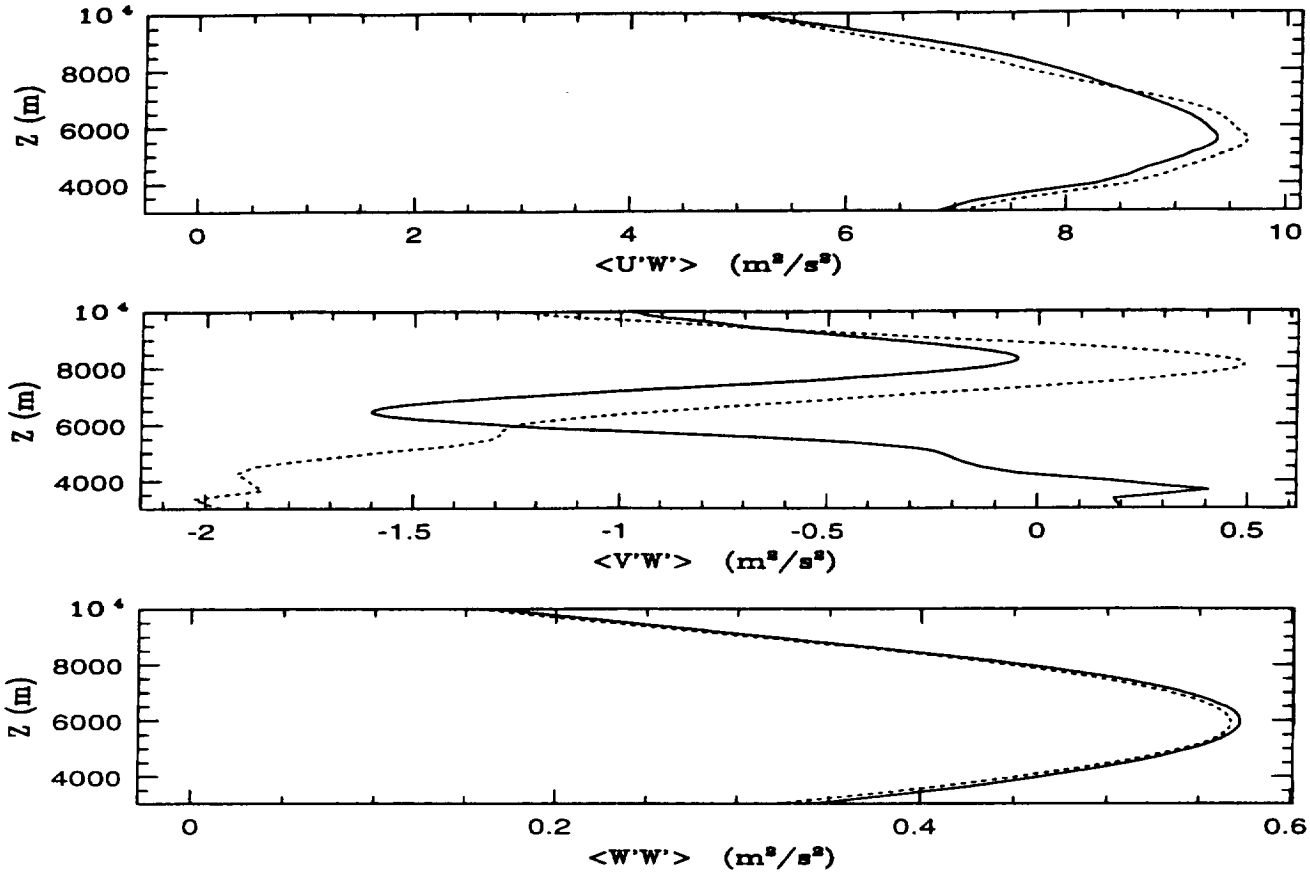
10 4
8000
6000
4000
Z (m)
0
2
4
6
8
10
<U'W'> (m²/s²)
10 4
8000
6000
4000
Z (m)
-2
-1.5
-1
-0.5
0
0.5
<V'W'> (m²/s²)
10 4
8000
6000
4000
Z (m)
0
0.2
0.4
0.6
<W'W'> (m²/s²)

Figure 9:

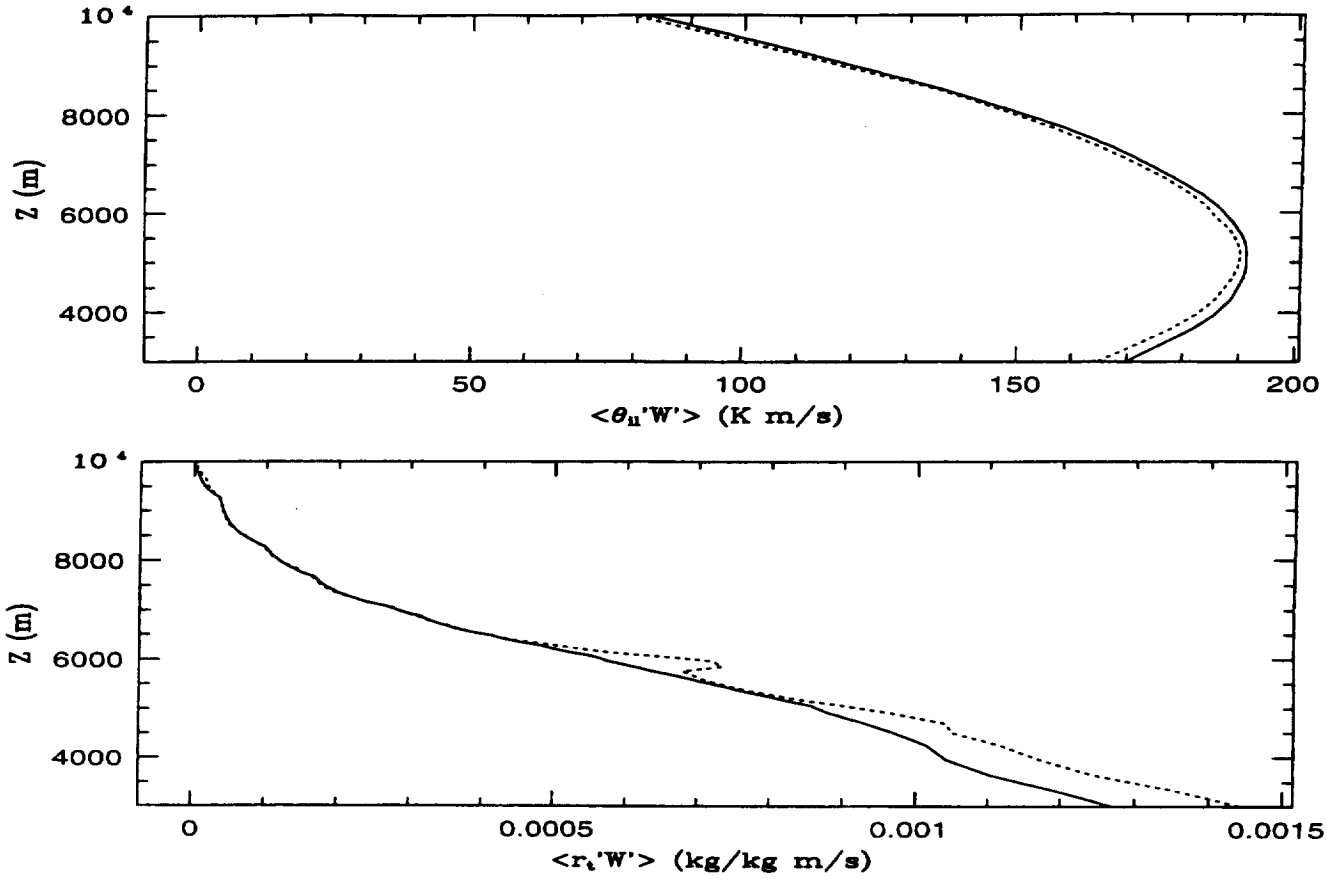
10 4
8000
6000
4000
Z (m)
0
50
100
150
200
<θil'W'> (K m/s)
10 4
8000
6000
4000
Z (m)
0
0.0005
0.001
0.0015
<rt'W'> (kg/kg m/s)

Figure 10:

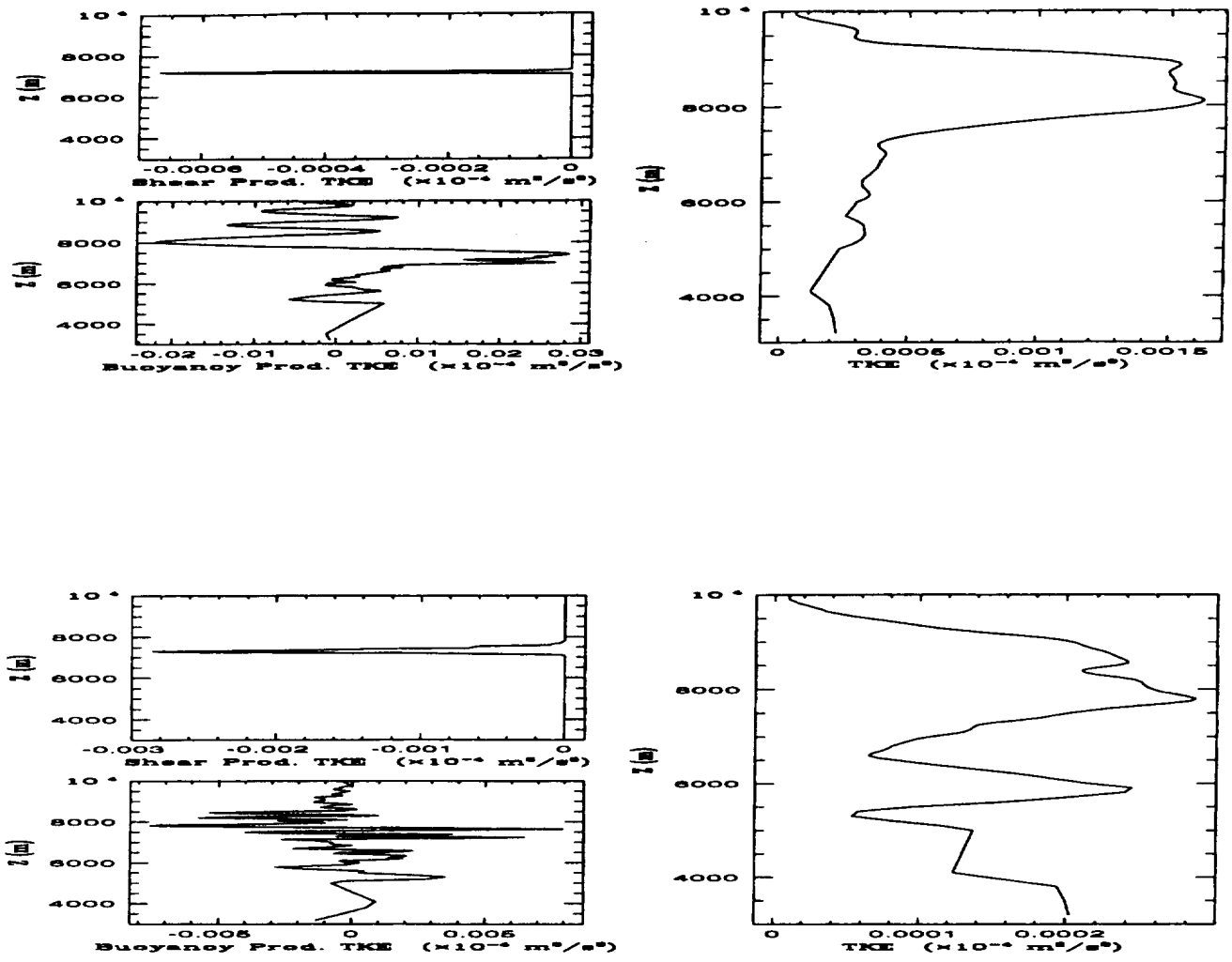
10 *
8000
6000
4000
z (m)
-0.0006 -0.0004 -0.0002 0
Shear Prod. TKE (×10⁻⁴ m²/s³)
-0.02 -0.01 0 0.01 0.02 0.03
Buoyancy Prod. TKE (×10⁻⁴ m²/s³)
0 0.0005 0.001 0.0015
TKE (×10⁻⁴ m²/s³)
-0.003 -0.002 -0.001 0
-0.005 0 0.005
0 0.0001 0.0002

Figure 11:

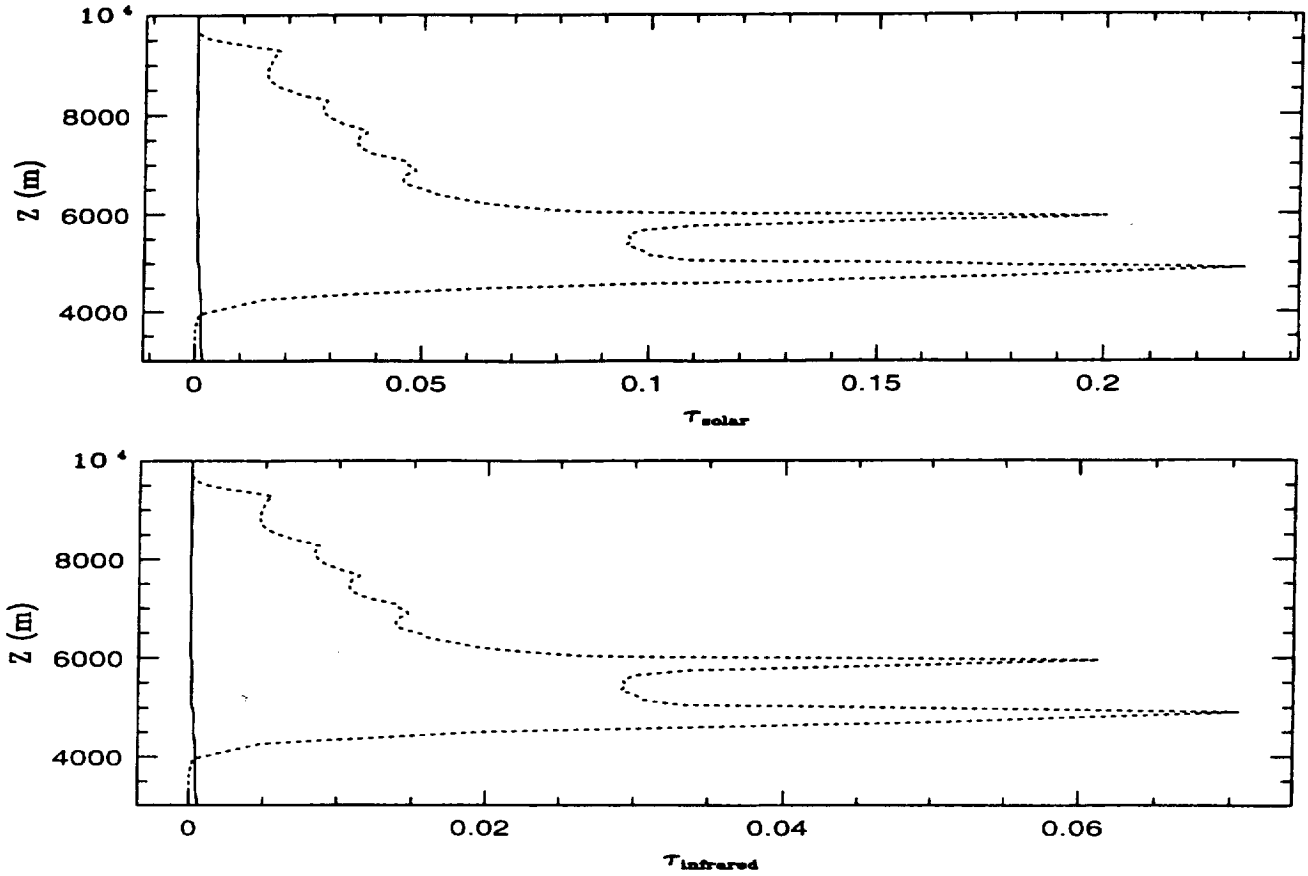
10 4
8000
6000
4000
Z (m)
0
0.05
0.1
0.15
0.2
τ solar
10 4
8000
6000
4000
Z (m)
0
0.02
0.04
0.06
τ infrared

Figure 12:

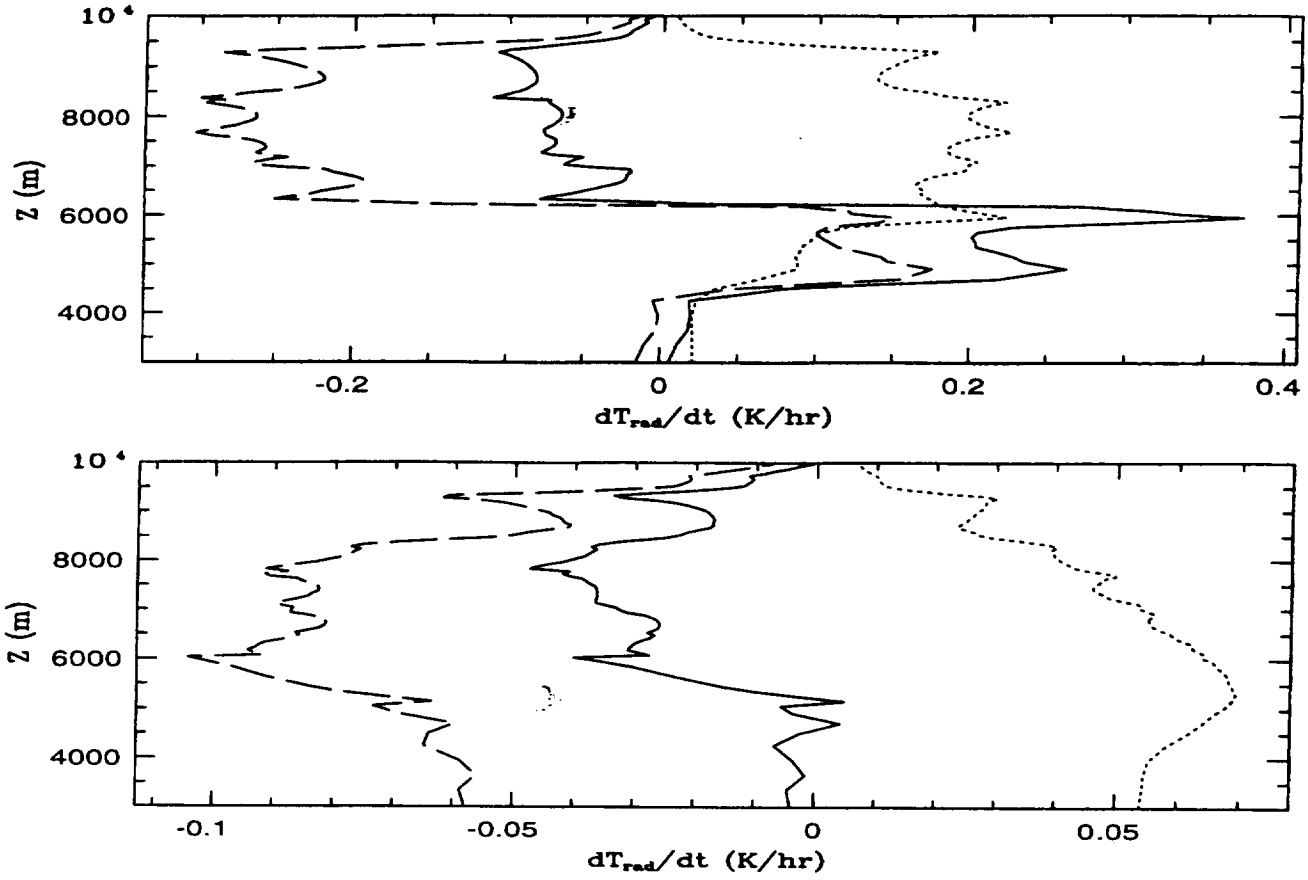
10 4
8000
6000
4000
Z (m)
-0.2
0
0.2
0.4
dT_rad/dt (K/hr)
10 4
8000
6000
4000
Z (m)
-0.1
-0.05
0
0.05
dT_rad/dt (K/hr)

Figure 13:

APPENDIX 3

Large-Eddy Simulations of the 26 November 1991 FIRE II Cirrus Case

Ting Wu, William R. Cotton,[1] and William Y. Y. Cheng

Department of Atmospheric Science

Colorado State University

Fort Collins, CO 80523

Submitted to *J. Atmos. Sci.*

July 13, 1999

[1]Corresponding author address: William R. Cotton, Department of Atmospheric Science, Colorado State University, Fort Collins, CO 80523 – e-mail: cotton@pandora.atmos.colostate.edu

Abstract

Large-eddy simulations (LES) were performed to study the dynamical, microphysical, and radiative processes in the 26 November 1991 FIRE II cirrus event. The LES model inherits the framework of the RAMS version 3b developed at Colorado State University. It includes a new radiation scheme developed by Harrington (1997) and a new subgrid scale model developed by Kosovic (1996).

The LES model successfully simulated a single cloud layer for Case 1 and a two-layer cloud structure for Case 2. The simulations demonstrated that latent heat release can play a significant role in the formation and development of cirrus clouds. For the thin cirrus in Case 1, the latent heat release was insufficient for the cirrus clouds to become positively buoyant. However, in some special cases such as Case 2, positively buoyant cells can be embedded within the cirrus layers. These cells were so active that the rising updraft induced its own pressure perturbations that affected the cloud evolution.

Vertical profiles of the total radiative and latent heating rates indicated that for well developed, deep, and active cirrus clouds, radiative cooling and latent heating could be comparable in magnitude in the cloudy layer. This implies that latent heating cannot be neglected in the construction of a cirrus cloud model.

The probability density function (PDF) of w was analyzed to assist in the parameterization of cloud-scale velocities in large-scale models. For the more radiatively-driven, thin cirrus case, the PDFs are approximately Gaussian. However, in the interior of the deep, convectively unstable case, the PDFs of w are multi-modal and very broad, indicating that parameterizing cloud-scale motions for such clouds can be very challenging.

1. Introduction

Although cirrus clouds are an important component of the climate system, they are not well understood. Cirrus clouds affect the global climate through the cloud-radiation feedback (Liou 1986). Because of our limited knowledge of the processes in cirrus clouds, numerical models of middle- and high-level clouds are useful in determining the quantitative roles of dynamics, microphysics, and radiation in the life cycle of these clouds (Cotton and Anthes 1989).

In the middle of 1980s, Starr and Cox (1985) developed a two-dimensional model for simulating the evolution of cirrus clouds. Besides dynamical and thermodynamical processes (e.g., phase changes of water), effects due to microphysical composition and radiative processes were also explicitly incorporated into their model. They found that the structure of cirrus varied dramatically from nighttime to daytime because radiative processes affected the organization and bulk properties of the cloud. Simulations of thin cirrus under midday and nighttime conditions showed that, with all other environmental factors being equal, daytime cirrus takes on a cellular structure with pockets of high ice water content (IWC) surrounded by regions of considerably lower IWC, while nighttime cirrus exhibits a more layered structure with less variation of IWC within a given layer. The simulated pattern of long-wave radiative cooling above and warming below the cirrus cloud is the key factor in modulating the vertical stability, especially for nighttime cirrus. However, for daytime cirrus, the combination of long-wave and short-wave radiation modulates not only the vertical stability but also the horizontal cloud structure because of pockets of high IWC. These high IWC pockets enhance the absorption of solar radiation, warming the high IWC pockets, thus inducing more ascending motion (leading to a more cellular structure) than at nighttime.

Lilly (1988) proposed the application of radiative-convective mixed-layer models to cirrus clouds. Lilly ignored latent heating because in cirrus clouds, radiative heating is believed to be the primary source of destablization of the cloud layer, leading to the production of turbulent kinetic energy. Using a theoretically-predicted radiative heating rate profile for a 2 km thick cloud with its top at the level of the tropical tropopause (17 km) and with an IWC of 0.02 g m^{-3}, Lilly estimated the vertical velocity and time scales for radiatively-induced cirrus turbulence. Lilly's results suggested that radiatively-induced turbulence in cirrus could be comparable to the turbulence in boundary layer clouds.

The interaction of clouds with the general circulation is generally agreed to be the most important physical process requiring improvement in today's climate models. However, the current general circulation models contain ice cloud (e.g., cirrus) parameterizations that are far too simplistic (Donner et al. 1997).

Since cirrus clouds are located high above the planetary boundary layer (PBL), turbulent kinetic energy (TKE) dissipation due to friction may not be as important as horizontal redistribution through wave activities. Vertical redistribution of TKE is suppressed due to stable stratification of the environmental atmosphere. These features may imply that the motion of cirrus clouds may be quasi-two-dimensional. Also, the turbulent parameterization schemes developed for boundary layer processes may not be applicable to cirrus clouds due to the marked difference in forcing mechanisms.

This article examines the dynamical, microphyiscal , and radiative processes in cirrus clouds using large eddy simulation (LES). In LES, the large eddies are simulated, while the small eddies are parameterized (Meong 1984). Two cases were chosen from a mesoscale simulation of a cirrus cloud event (Wu 1999) during FIRE II (Journal of Atmospheric Science special issue, December 1995).

2. Mesoscale Simulation

The cirrus event of interest occurred on 26 November 1991 during FIRE II (Mace et al. 1995). The synoptic setting of the cirrus event was characterized by a small amplitude upper-level trough-ridge system over North America on 26 November 1991, with northwesterly flow in the upper-levels ahead of the offshore ridge over the West Coast, and broad diffluent trough in the central United States. The exit region of a strong upper-level northwesterly jet, covering a third of the Western United States, contributed to the development of the cirrus cloud system in this study. A more detailed description of this cirrus event can be found in Mace et al. (1995).

Our strategy is to conduct a mesoscale simulation of the cirrus event. Once we have verified our mesoscale model results against available observations, we then use the output from the mesoscale model to provide initial and boundary conditions for the LES (to be discussed later). The mesoscale model used in this study is RAMS (Pielke et al. 1992) version 3b, with a new two-moment microphysical scheme (Harrington et al. 1995) to predict the mixing ratios and number concentrations of rain, pristine ice crystals, snow, aggregates, graupel, and hail. The model initial and boundary conditions were provided from Mesoscale Analysis and Prediction System (MAPS; Benjamin et al. 1991) and National Weather Service rawinsonde soundings. The model was initialized at 0000 UTC 26 November 1991.

Figure 1 shows the grids for the mesoscale simulations. Although Grids 1 and 2 were the same for Case A and Case B, the finer grids were different. In Case A, we attempt to capture the fine-scale features of a thin cirrus cloud located in the southeast quadrant of Grid 2, while in Case B, we attempt to capture the fine-scale features of a thicker and more convective cirrus cloud in the northwest quadrant of Grid 2. The grid configurations for Case A and Case B are given in Tables 1 and 2.

Figure 2 shows the 500-hPa geopotential height at 24 hours (0000 UTC 27 November 1991) into the simulation from Grid 1 as well as the 500-hPa geopotential height from MAPS analysis. The model captured the large-scale trough-ridge pattern reasonably well. In Figure 3, from the simulated 400-hPa snow mixing ratio of Grid 2, we can see that the model reproduced cloud bands that could be identified with high cloud visible optical depth maxima derived from satellite data (Mace et al. 1995). However, the simulated Case A (B) thin (thick) cirrus band was more to the northwest, as compared to the derived satellite data. As discussed in Wu (1999), observations have shown that the leading edge of the observed cloud system was composed of a shallow and high cloud layer (Case A), and the cloud layer to the northwest of the leading edge was deep with middle-level cloud underneath the highest cirrus cloud (Case B). Overall, RAMS showed reasonable skill in simulating the 26 November 1991 cirrus event, thus we use the mesoscale model results for the LES. Details of the mesoscale simulations are documented in Wu (1999).

3. The Subgrid-Scale (SGS) Model

The LES model inherits the framework of the Colorado State University RAMS version 3b (Pielke et al. 1992), with a radiation scheme by Harrington (1997; see also Olsson et al. 1998) and a subgrid scale model by Kosovic (1996). The subgrid-scale (SGS) model represents a critical component of a successful large-eddy simulation. The commonly used linear SGS models result in erroneous mean velocity profiles in simulations of neutrally and stably stratified atmospheric boundary layers (Kosovic 1996). In addition, linear models are absolutely dissipative, resulting in relaminarization of the flows if subjected to strong stable stratification (Kosovic 1996). Since cirrus clouds in midlatitudes are generally associated with a stably stratified and strongly sheared atmospheric environment, we felt that Kosovic's SGS model, capable of reproducing energy backscatter, as well as the effects of SGS anisotropy characteristics of shear-driven flows, was more suitable for this study.

According to Kosovic's (1996) nonlinear model, the SGS stress is defined as:

$$M_{ij} = -(C_s\Delta)^2\{2(2S_{mn}S_{mn})^{0.5}S_{ij} + C_1(S_{ik}S_{kj} - \frac{1}{3}S_{mn}S_{mn}\delta_{ij}) + C_2(S_{ik}\Omega_{kj} - \Omega_{ik}S_{kj})\} \quad (1)$$

where C_s is the traditional Smagorinsky constant which is defined as

$$C_s = (\frac{8(1+C_B)}{27\pi^2})^{0.5} \quad (2)$$

δ_{ij} is the Kronecker delta (a scalar quantity which is equal to 1 when $i = j$ and 0 otherwise), and Δ is the length scale defined by Moeng (1984):

$$\Delta = (\Delta x * \Delta y * \Delta z)^{\frac{1}{3}} \quad (3)$$

where Δx, Δy, and Δz are the grid spacings in x, y, and z directions, respectively.

Kosovic suggested that

$$C_B = 0.36. \quad (4)$$

In equation 1, S_{ij} and Ω_{ij} are strain rate tensors which are defined as

$$S_{ij} = \frac{1}{2}(\frac{\partial u_i}{\partial x_j} + \frac{\partial u_j}{\partial x_i}) \quad (5)$$

$$\Omega_{ij} = \frac{1}{2}(\frac{\partial u_i}{\partial x_j} - \frac{\partial u_j}{\partial x_i}) \quad (6)$$

where u_i and u_j are the model wind components.

The nonlinear model parameters C_1 and C_2 are determined so that the model provides the correct energy transfer and captures the normal stress effects observed in sheared flows. The following values for C_1 and C_2 are suggested by Kosovic (1996):

$$C_1 = \frac{31 C_B}{7(1 + C_B) S(k_c)} \tag{7}$$

$$S(k_c) = 0.5, C_1 = C_2. \tag{8}$$

4. Nudging the LES Model

Generally, horizontally homogeneous initialization is used in large-eddy simulation because of the small horizontal model domain. Like cloud-resolving models of tropical deep convection (Moncrieff et al. 1997), cirrus clouds are strongly influenced by larger-scale motions. We thus chose to perform a mesoscale simulation of RAMS and then nudge the LES with large-scale forcing from the mesoscale simulation.

The nudging algorithm used takes the following form:

$$u(k,i,j,t) = u(k,i,j,t-1) + F_{model} + G * (u_{obs}(k) - \bar{u}(k,t-1)) \tag{9}$$

where $u(k,i,j,t)$ is the model predicted u value at the current timestep, $u(k,i,j,t-1)$ is the model u value at the previous timestep, model-forcing terms (F_{model}) included advection, diffusion, buoyancy, etc., u_{obs} is the wind field being nudged to and is a function of the vertical index k, $\bar{u}(k,t-1)$ is the horizontal average of u at the previous timestep, and G is the inverse of the nudging time scale. Because the nudging contribution is artificial, it must not be a dominant term in the governing equations and should be scaled by the slowest physical adjustment process in the model. Of note, using $\bar{u}$ instead of u in the above equation avoids nudging out the fine scale features in the LES.

To apply nudging, u_{obs} was calculated from the mesoscale simulation outputs by using a linear interpolation method. In this study, nudging was performed for the three-dimensional wind components (u, v, and w), perturbation Exner function (π'), perturbation ice-liquid-

water potential temperature (θ'_{il}), and total water mixing ratio (r_t). In addition, nudging was only applied to the five outermost grid points on the lateral boundaries.

5. Initialization and Boundary Conditions

The LES model was initialized with a sounding taken from the mesoscale simulation described eariler. The sounding profiles used in the LES studies are shown in Figure 4. One of these two soundings was taken from a shallow cloud band near the leading edge of the simulated mesoscale cirrus cloud system (Case 1; corresponding to Case A in Figure 3), while the other sounding is taken from a deep cloud layer northwest of the simulated mesoscale cloud (Case 2; corresponding to Case B in Figure 3). The two LES runs to be discussed in this article were designed to simulate the dynamical, microphysical, and radiative processes in both shallow and deep ice cloud systems to obtain greater insight into the dynamics and physics of the observed cirrus cloud event.

A much finer grid mesh was used for the LES, with $\Delta x = \Delta y = 150$ m. Δz varied from 50 m (within the cloud layer from 6 to 10 km) to 400 m (near the surface). The model had a horizontal extent of 6×6 km^2 and a height of 11.4 km (115 vertical levels, see Table 3). The horizontal boundary conditions were cyclic. The model top was a rigid lid with a Rayleigh friction layer to prevent gravity wave reflection from the upper boundary. The lower surface, which is not as important for cirrus clouds as it is for convective storms, was a material surface across which fluxes of heat, moisture, and momentum were solved following a theory proposed by Louis (1979).

6. LES Results: Case 1-A Shallow Cloud System

a. *Simulation Overview*

The 3D LES in Case 1 covered a two-hour simulation period which was initialized with a model sounding taken at 1700 UTC 26 November 1991 (Figure 4a). Snapshots

of the vertical cross sections (at X = -0.08 km) of pristine ice (PI) number concentration, snow number concentration, and vertical velocity at 1730, 1800, and 1900 UTC are shown in Figures 5 through 7. The predicted cloud system had a single cloud layer (from r_{ice} in Figure 8), even though some secondary peaks in both PI and snow number concentrations were discernible (Figures 5 and 6). Both particle number concentration and mixing ratio were higher near the cloud top levels than in the levels below. The maximum PI concentration, PI mixing ratio, snow concentration, and snow mixing ratio were about 0.6 l^{-1}, 2.1 $\times$ 10^{-4} g kg^{-1} (figure not shown), 0.12 l^{-1}, and 8.0 $\times$ 10^{-4} g kg^{-1} (figure not shown), respectively.

As can be seen from the plots of vertical velocity (Figure 7), the cloud system was quite turbulent with cells of upward and downward activities. The horizontal extent of the cells ranged from less than 1 km to as large as 3.5 km. Vertical extent of the cells were generally less than 1 km. The greater horizontal extent of these cloud cells (bands in the horizontal cross sections) may imply that the cloud system was modulated by both shear-driven turbulence and gravity wave dynamics. The sizes of these embedded cells were similar to those found in observational studies (Gultepe et al. 1995).

Horizontally-averaged total water mixing ratio (r_t), ice-water mixing ratio (r_{ice}), ice-liquid-water potential temperature (θ_{il}), and potential temperature (θ) at 60 minutes into the simulation are shown in Figure 8. A single layer of ice water mixing ratio maximum was predicted just below 9000 m level, with a depth of slightly more than 500 m. The maximum horizontally-averaged ice water mixing ratio was on the order of 1.0 $\times$ 10^{-4} g kg^{-1} throughout the simulation (figure not shown). Below the single cloud layer, the profiles of θ_{il} and θ indicated a nearly neutral layer of about 1 km deep between 7 and 8 km levels.

Vertical profiles of horizontally-averaged turbulent kinetic energy (TKE) at 30, 60, and 120 minutes into the simulation are shown in Figure 9. As the cloud developed, the cloud layer became more turbulent in the early stage, with a peak in TKE, slightly less than 0.003 m^2 s^{-2}. The TKE decreased as the cloud evolved into its mature stage. By the end of the

simulation, the maximum horizontally-averaged TKE within the cloud layer was only about 0.0012 m^2 s^{-2}.

Infrared radiative cooling throughout the cloud layer was largely compensated by solar warming, resulting in a maximum cooling of only about 1.2 K day^{-1} near the cloud top (Figures 10 and 11). The fine ripple structure in the radiative heating rate profiles corresponded to the non-uniform cloud development. The bottom panels of these two figures also show that both solar and infrared optical depths peaked at about 8.5 km, where the maximum number concentration of ice particles was predicted. Below this level, the solar and infrared optical depths were much smaller because of the smaller ice particle number concentration and mixing ratio.

In Figure 12, vertical profiles of the horizontally-averaged heating rates due to total radiative processes and latent heat release associated with phase change of water are shown for Case 1. The latent heating rates mainly peaked at three levels, indicating a layered cloud structure commonly observed within cirrus clouds (Mace et al. 1995), especially *forced passive cirrus* (to be discussed below). The overall latent heating rate in the cloud system was much smaller in magnitude than the radiative cooling effect. No obvious net evaporation at any level was seen in this case during the first 2-hour simulation. The net radiative heating was much stronger throughout most of the cloud system than latent heating, indicating that this cirrus case was mostly driven by radiation and large-scale vertical motion. Strong radiative cooling occurred throughout most of the cloud layer with a shallow radiative warming layer centered at about 5.2 km.

b. *Probability Density Function (PDF) of w*

Since the vertical velocity distribution is critical in the parameterization of cloud-scale physics for large-scale models, such as a general circulation model (GCM), the LES study is used to determine the PDF of w. According to the mathematical definition, if

$P(w)dw$ is the probability of w in the interval from w to $w + dw$, then for a continuous w spectrum, the following expression must be satisfied:

$$\int_0^\infty P(w)dw = 1. \tag{10}$$

Since the LES model domain contains discrete grid boxes, the following definition of $P(w)$ can be used to evaluate the model-predicted distribution of vertical velocities (Mitrescu 1998):

$$P(w) = \frac{dN(w)}{dV\,dw} \tag{11}$$

where $dN(w)$ represents the number of grid cells which have vertical velocities in the interval between w and $w + dw$, dV is the total number of grid cells within the model domain, and dw is the sampling threshold. In this study, dw has a value of 0.05 m s^{-1}.

Figures 13 and 14 show the PDFs at 5400, 7700, and 9100 m AGL (above ground level) at 30 and 60 minutes into the simulation. It is apparent that the PDFs for this simulation were quite consistent throughout the cloud layer with most of the model-predicted vertical velocities falling into a narrow band between -0.1 m s^{-1} and 0.05 m s^{-1}. This is because the TKE for this cloud system was very small, thus vertical variation of TKE had no significant impact on the variation of PDFs. Also, the PDFs follow an approximately normal distribution throughout the cloud system for this simulation.

7. LES results: Case 2-A Deep Cloud System

a. *Simulation Overview*

The two-hour 3D LES for Case 2 was initialized with a sounding taken at 1930 UTC 26 November 1991 (Figure 4b). As stated previously, the sounding used in this simulation was taken from a deep and active cloud layer from the mesoscale simulation in Wu (1999).

Active cells are seen in the vertical cross sectional plots along $X = -0.08km$ (Figures 15 through 17). Generally, the cells were horizontal bands as seen in the horizontal cross sections (not shown), with horizontal extent less than 2 km and vertical extent less than 1.5 km. This range of cell sizes is comparable to the results in Gultepe et al. (1995). The comparable horizontal and vertical scales for the bands may indicate that the eddies were more buoyancy-driven than shear-driven. Also, the horizontal banded structures were probably convective cells (to be discussed later). A deep cloud system extending from 3.9 to about 9 km was simulated at 2130 UTC. A two-layer vertical cloud structure was identified at the later stage of the simulation. This compares favorably with the observations which indicated that this cloud system was composed of a middle-level cloud underneath a high cirrus layer (Mace et al. 1995). The top cloud layer, centered at about 8 km, had larger amounts of PI particles (both in number and mass), while larger snow particle number and mass were associated with the lower cloud layer which had its bottom boundary as low as 3.5 km AGL. The maximum number of PI particles nucleated at 30 minutes into the simulation was 400 l^{-1}. The maximum PI mixing ratio over the course of the simulation was 1.8×10^{-2} g kg^{-1} (figure not shown). Snow particle number concentrations were generally less than 20 l^{-1}, and snow mixing ratios were as large as 1.08×10^{-1} g kg^{-1} (figure not shown). The predicted vertical air velocities along the cross section at 30 minutes into the simulation ranged from -2.0 m s^{-1} to 0.8 m s^{-1}. This also compares very well with the available observations (Mace et al. 1995).

Shown in Figure 18 are the vertical profiles of layer-averaged r_t, r_{ice}, θ_{il}, and θ at 60 minutes into the simulation. As expected, r_t generally decreased with height, even though the profile was slightly modified due to the existence of condensates in the cloud. r_{ice} profiles displayed two distinct cloud layers with the top cirrus layer containing less total ice than in the layer below. The two-layer cloud structure indicates that the model performed very well in predicting the desired cloud system. The maximum total ice for the middle-level

cloud layer was slightly less than 0.1 g kg^{-1} at 60 minutes into the simulation. An unstable layer can be identified in the θ profile. This unstable layer was responsible for the active turbulent eddies predicted in this case.

The TKE profiles in Figure 19 show that turbulent eddies were more active in Case 2 than in Case 1. The maximum TKE in Case 2 at one hour into the simulation was about 0.55 m^2 s^{-2} which was nearly 200 times the maximum value predicted in Case 1 (Figure 9). As the simulation proceeded, transport of TKE both upward and downward can be clearly identified.

Similar to what is seen in Case 1, infrared cooling outweighed solar warming, resulting in net radiative cooling in most of the cloud system (Figures 20 and 21). The maximum net cooling near the cloud top was about three times that of Case 1. However, below 8 km, net radiative cooling or warming was very small. Because a large number of small ice particles were suspended near the cloud top, both solar optical depth and infrared optical depth peaked at 8.5 *km* AGL.

Vertical profiles of the total radiative and latent heating rates are shown in Figure 22. The change in scale of the horizontal axis between these two figures demonstrates that latent heating release played a much more significant role in Case 2 than in Case 1 (Figure 12). The maximum latent heating rate of 0.85 K h^{-1} in the early stage of the cloud development was more than two orders of magnitude greater than that for Case 1 (only about 0.05 K h^{-1}). Two regions of net diffusional growth corresponded to the two cloud layers described previously. A patch of net evaporation appeared between the two cloud layers after about one hour into the simulation. Net latent heating outweighed the net radiative effect in the cloud development. Latent heat release can destablize the cloud layer, resulting in the formation of convective cells which are very effective in transporting momentum, heat, and moisture. By the end of the simulation, net radiative cooling dominated at the cloud top region at a maximum rate of about 3.36 K day^{-1}, and the bottom levels of the cloud were

dominated by net evaporation, even though strong latent heating was still present in the top cloud layer.

b. *PDFs of w*

LES-predicted PDFs of w for this case demonstrated distinct features which differed from those in Case 1. From Figures 23 and 24, at the middle-cloud level (at 7700 m), corresponding to active turbulent motions deep in the cloud system, the PDF had a wider distribution than levels above and below. Even though the PDFs near the cloud base and top followed an approximate normal distribution with a single peak near $w = 0$, multiple peaks were found in the PDF at the middle cloud levels. It should be pointed out that the wide PDF distribution deep in the cloud system was associated with buoyancy-driven turbulence because the cloud layer between 7200 and 8500 m was unstable, especially in the early stage of the simulation. At the early stage of the simulation, the PDF at the middle cloud level covered an even wider w spectrum in the downward motion regime than that calculated later in the simulation. Although the PDF spectrum at the middle cloud levels narrowed subsequently in the simulation, the multiple peaks and fine structures indicated that turbulent eddies were very active within the cloud system because both upward and downward motions were nearly equal (Figure 24).

8. Discussion and Summary

The LES model successfully simulated a single cloud layer for Case 1 and a two-layer cloud structure for Case 2. The simulated cirrus clouds displayed properties similar to that of the *forced boundary-layer clouds* (Stull 1985) because of the similarity in their dynamics, even though cirrus clouds generally have a much larger horizontal coverage than the *forced boundary-layer clouds.* Mid-latitude cirrus clouds usually form in an stably-stratified environment with large scale forcing. In spite of the latent heat release during

phase change, there was generally insufficient heating for cirrus clouds in Case 1 to become positively buoyant. Also, the strong temperature inversion at the tropopause provided a lid to prevent cirrus clouds in Case 1 from developing into a deep cloud. As a result, the clouds in Case 1 behaved as quasi-passive tracers of the top of the troposphere. This kind of cirrus cloud can be named *forced passive cirrus* because of their similarity to their boundary layer counterpart. However, in some special cases, such as Case 2, positively buoyant cells can be embedded in the cirrus layers. These cells in Case 2 were so active that the rising updraft induced its own pressure perturbations, affecting the cloud evolution. This kind of cirrus can be classified as *forced active cirrus.*

To determine whether gravity waves were present in the simulation, we show the time-height cross section of w near the center of the domain in Figure 25. In Case 1, a slantwise propagation of the phase of w was evident in the first hour of integration, much like an internal gravity wave (Holton 1992). The gravity wave in Case 1 was probably caused by the vertical shear of the horizontal wind around 7.5 km AGL; the level of the vertical shear of the horizontal wind also corresponded to the level from where the gravity waves emanated (Figures 25a, 26a). However, in Case 2, gravity waves did not seem to be present; this was probably due to lower static stability and more turbulence in the flow. Even though there was vertical shear of the horizontal wind in Case 2, we did not detect gravity waves due to the effects of strong turbulent motion (Figures 25b, 26b).

Latent heat release can play a significant role in the formation and development of cirrus clouds (Figure 22). The release of latent heat can be an energy source for the development of upward motions which, in turn, can produce more supersaturation and cloud development. Vertical profiles of the total radiative and latent heating rates (Figures 12 and 22) indicate that for well developed, deep and active cirrus clouds, radiative cooling and latent heating can be comparable in magnitude in the cloudy layer, as in Case 2 (see bottom panel, Figure 22). This implies that latent heating cannot be neglected in the

construction of a cirrus cloud model, even though Lilly (1988) had reasonable success with his mixed-layer model in a study of anvil cirrus with latent heating ignored. However, for shallow, optically-thin cirrus clouds, as in Case 1, the latent heat release can be much smaller than the radiative cooling. In this case, the cloud development and evolution are modulated mainly by radiative effects, and latent heat effects can be safely neglected in cirrus cloud models. Gravity waves, however, may provide another uplifting mechanism for cloud development. Generally, the LES studies in this research support Starr and Cox's (1985) model calculations in which the authors showed that latent heating associated with depositional growth and sublimation of ice crystals can be a significant factor in modulating cirrus cloud evolution.

Finally, we have examined the probability density function of w with an eye towards parameterizing cirrus cloud-scale vertical velocities in larger-scale models. We find that the PDFs of w can be approximated by a normal density function for the more radiatively-driven thin cirrus case. However, in the interior of the deep, convectively unstable case, the PDFs of w are multi-modal and very broad, indicating that parameterizing cloud-scale motions for such clouds can be very challenging.

Acknowledgments

This work was supported by the NASA under contracts #NAG-1-1703 and #NAG-1-2045. The help of Brenda Thompson in preparing this manuscript is greatly appreciated, as are the comments of two anonymous reviewers. We also want to thank Prof. Gerald Mace for providing the optical depth figure.

REFERENCES

Benjamin, S. G. and co-authors, 1991: An isentropic three-hourly data assimilation system using ACARS aircraft observations. *Mon. Wea. Rev.*, **119**, 888-906.

Cotton, W. R. and R. A. Anthes, 1989: Storm and cloud dynamics. *Academic Press, Inc.*, 883 pp.

Deardorff, J. W., 1980: Stratocumulus-capped mixed layers derived from a three-dimensional model. *Boundary-Layer Meteorol.*, **18**, 495-527.

Donner, L. J. and coauthors, 1997: Large-scale ice clouds in the GFDL SKYHI general ciculation model. *J. Geophys. Res.*, **102**, 21745-21768.

Harrington, J. Y., M. P. Meyers, R. L. Walko, and W. R. Cotton, 1995: Parameterization of ice crystal conversion processes due to vapor deposition for mesoscale models using double-moment basis functions. Part I: Basic formulation and parcel model results. *J. Atmos. Sci.*, **52**, 4344-4366.

Harrington, J. Y., 1997: The effects of radiative and microphysical processes on simulated warm and transition-season Arctic stratus. Ph.D. dissertation, Colorado State University, Fort Collins, Colorado, 270pp.

Holton, J. R., 1992: An introduction to dynamic meteorology. Third edition, Academic Press, 511pp.

Kosovic, B., 1996: Subgrid-scale modeling for the large-eddy simulation of stably stratified boundary layers. Ph.D. thesis, Department of Aerospace Engineering Sciences, University of Colorado, Boulder, CO, 253 pp.

Moncrieff, M. W. and co-authors, 1997: GEWEX cloud system study (GCSS) working group 4: Precipitating convective cloud systems. *Bull. Am. Met. Soc.*, **78**, 831-845.

Lilly, D. K., 1988: Cirrus outflow dynamics. *J. Atmos. Sci.,* **45**, 1594-1605.

Liou, K. N., 1986: Influence of cirrus clouds on weather and climate process: A global perspective. *Mon. Wea. Rev.*, **114**, 1167-1199.

Louis, J. F., 1979: A parametric model of vertical eddy fluxes in the atmosphere. *Boundary Layer Meteorology,* **17**, 187-202.

Mace, G. G., D. O'C. Starr, T. P. Ackerman, and P. Minnis, 1995: Examination of coupling between an upper-tropospheric cloud system and synoptic-scale dynamics diagnosed from wind profiler and radiosonde data. *J. Atmos. Sci.,* **52**, 4094-4127.

Mitrescu, C., 1998: Cloud-resolving simulations of tropical cirrus clouds. M.S. thesis, Department of Atmospheric Science, Colorado State University, Fort Collins, CO 80523, 85 pp.

Moeng, C.-H., 1984: A large-eddy-simulation model for the study of planetary boundary-layer turbulence. *J. Atmos. Sci.,* **41**, 2052-2062.

Moeng, C.-H. and R. Rotunno, 1990: Vertical velocity skewness in the boundary layer. *J. Atmos. Sci.,* **47**, 1149-1162.

Olsson, P. Q. and co-authors, 1998: Exploratory cloud-resolving simulations of boundary-layer Arctic stratus clouds. Part I: Warm-season clouds. *Atmos. Res.*, **47-49**, 573-597.

Pielke, R. A. and co-authors, 1992: A comprehensive meteorological modeling system - RAMS. *Meteorol. Atmos. Phys.*, **49**, 69-91.

Starr, D. O'C. and S. K. Cox, 1985: Cirrus clouds. Part I: A cirrus cloud model. *J. Atmos. Sci.,* **42**, 2663-2681.

Starr, D. O'C. and S. K. Cox, 1985: Cirrus clouds. Part II: Numerical experiments on the formation and maintenance of cirrus. *J. Atmos. Sci.,* **42**, 2682-2694.

Wu, T., 1999: Numerical modeling study of the November 26, 1991 cirrus event. Ph.D. dissertation, Colorado State University, Fort Collins, Colorado, 186 pp.

List of Tables

Table 1: Model setups for Case A and Case B of the mesoscale simulations. The vertical grid spacing is the same for every grid.

	Case 1	Case 2
number of grids	4	3
x grid points	50, 50, 47, 46	50, 50, 47
y grid points	40, 42, 47, 46	40, 42, 47
z grid points	65, 65, 65, 65	65, 65, 65
horizontal grid spacings (km)	80, 20, 4, 1	80, 20, 4
vertical grid spacings (m)	200 to 500	200 to 500

Table 2: Vertical levels used in the mesoscale simulations (in m).

0.0	300.0	600.0	900.0	1200.0	1500.0
1800.0	2100.0	2400.0	2700.0	3000.0	3300.0
3600.0	3900.0	4100.0	4300.0	4500.0	4700.0
4900.0	5100.0	5300.0	5500.0	5700.0	5900.0
6100.0	6300.0	6500.0	6700.0	6900.0	7100.0
7300.0	7500.0	7700.0	7900.0	8100.0	8300.0
8500.0	8700.0	8900.0	9100.0	9300.0	9500.0
9700.0	9900.0	10100.0	10300.0	10600.0	10900.0
11200.0	11500.0	11800.0	12200.0	12600.0	13000.0
13400.0	13800.0	14200.0	14600.0	15000.0	15500.0
16000.0	16500.0	17000.0	17500.0	18000.0	

Table 3: Vertical levels used in the LES (in m).

0.0	400.0	800.0	1200.0	1600.0	2000.0
2400.0	2800.0	3200.0	3500.0	3800.0	4100.0
4400.0	4600.0	4800.0	5000.0	5100.0	5200.0
5300.0	5400.0	5500.0	5600.0	5700.0	5800.0
5900.0	6000.0	6050.0	6100.0	6150.0	6200.0
6250.0	6300.0	6350.0	6400.0	6450.0	6500.0
6550.0	6600.0	6650.0	6700.0	6750.0	6800.0
6850.0	6900.0	6950.0	7000.0	7050.0	7100.0
7150.0	7200.0	7250.0	7300.0	7350.0	7400.0
7450.0	7500.0	7550.0	7600.0	7650.0	7700.0
7750.0	7800.0	7850.0	7900.0	7950.0	8000.0
8050.0	8100.0	8150.0	8200.0	8250.0	8300.0
8350.0	8400.0	8450.0	8500.0	8550.0	8600.0
8650.0	8700.0	8750.0	8800.0	8850.0	8900.0
8950.0	9000.0	9050.0	9100.0	9150.0	9200.0
9250.0	9300.0	9350.0	9400.0	9450.0	9500.0
9550.0	9600.0	9650.0	9700.0	9750.0	9800.0
9850.0	9900.0	9950.0	10000.0	10100.0	10200.0
10300.0	10400.0	10600.0	10800.0	11000.0	11200.0
11400.0					

List of Figures

Fig. 1 The mesoscale grid configuration for a) Case A and b) Case B.

Fig, 2 a) 24-h predicted 500-hPa geopotential height (at contour intervals of 30 m) superposed with 500-hPa wind vectors (m s^{-1}) from Grid 1 of the mesoscale simulation (0000 UTC 27 November 1991). Inset indicates the scale of the horizontal wind vectors (m s^{-1}); b) 500-hPa geopotential height (at contour intervals of 30 m) from MAPS analysis at 0000 UTC 27 November 1991.

Fig. 3 a) 18-h predicted 400-hPa snow mixing ratio from Grid 2 of the mesoscale simulation (1800 UTC 26 November 1991), at contour intervals of 10 X 10^{-3} g kg^{-1}; b) high cloud visible optical depths derived from GOES data at 1800 UTC 26 November 1991 (panel b taken from Mace et al. 1995).

Fig. 4 Skew T-log p diagram for temperature (^{o}C), dew point temperature (^{o}C), and wind (m s^{-1}) at a) 1700 UTC 26 November 1991 and b) 1930 UTC 26 November 1991 at 37.79^o N and 97.33^o W from the mesoscale simulation of Wu (1999). The soundings in a) and b) are the initial conditions of Case 1 and Case 2 (LES), respectively.

Fig. 5 Vertical $y - z$ cross section (at x = -0.08 km) of pristine ice number concentration (at contour intervals of 0.3 l^{-1}) for Case 1 (LES) at a) 30 minutes, b) 60 minutes, and c) 120 minutes into the simulation.

Fig. 6 Vertical $y - z$ cross section (at x = -0.08 km) of snow particle number concentration for Case 1 (LES) at a) 30 minutes (at contour intervals of 6 X 10^{-5} l^{-1}) , b) 60 minutes (at contour intervals of 6 X 10^{-5} l^{-1}), and c) 120 minutes (at contour intervals of 0.06 l^{-1}) into the simulation.

Fig. 7 Vertical $y - z$ cross section (at x = -0.08 km) of vertical velocity (w; at contour intervals of 1 cm s^{-1}) for Case 1 (LES) at a) 30 minutes, b) 60 minutes, and c) 120 minutes into the simulation.

Fig. 8 Profiles of horizontally-averaged a) total water mixing ratio (r_t), b) pristine ice + snow mixing ratios (r_{ice}), c) ice-liquid-water potential temperature (θ_{il}), and d) potential temperature (θ) at 60 minutes into the simulation for Case 1 (LES).

Fig. 9 Profiles of horizontally-averaged turbulent kinetic energy (TKE) at 30 (solid), 60 (dotted), and 120 minutes (dashed) into the simulation for Case 1 (LES).

Fig. 10 a) Profiles of radiative heating rate (solid line: total; dashed line: IR; dotted line: solar) and b) solar (τ_{solar}) and infrared ($\tau_{infrared}$) optical depths (dashed line: IR; dotted line: solar) at 60 minutes into the simulation for Case 1 (LES).

Fig. 11 a) Profiles of radiative heating rate (solid line: total; dashed line: IR; dotted line: solar) and b) solar (τ_{solar}) and infrared ($\tau_{infrared}$) optical depths (dashed line: IR; dotted line: solar) at 120 minutes into the simulation time for Case 1 (LES).

Fig. 12 Profiles of total radiative (solid) and latent (dotted) heating rates at a) 30 minutes, b) 60 minutes, and c) 120 minutes into the simulation for Case 1 (LES).

Fig. 13 PDF of w at a) 5400 m, b) 7700 m, and c) 9100 m above ground level (AGL) at 30 minutes into the simulation for Case 1 (LES).

Fig. 14 PDF of w at a) 5400 m, b) 7700 m, and c) 9100 m above ground level (AGL) at 60 minutes into the simulation for Case 1 (LES).

Fig. 15 Vertical $y - z$ cross section (at x = -0.08 km) of pristine ice number concentration for Case 2 (LES) at a) 30 minutes (at contour intervals of 100 l^{-1}), b) 60 minutes (at

contour intervals of 50 l^{-1}), and c) 120 minutes (at contour intervals of 5 l^{-1}) into the simulation.

Fig. 16 Vertical $y - z$ cross section (at x = -0.08 km) of snow particle number concentration for Case 2 (LES) at a) 30 minutes (at contour intervals of 3 l^{-1}), b) 60 minutes (at contour intervals of 6 l^{-1}), and c) 120 minutes (at contour intervals of 6 l^{-1}) into the simulation.

Fig. 17 Vertical $y - z$ cross section (at x = -0.08 km) of vertical velocity (w) for Case 2 (LES) at a) 30 minutes (at contour intervals of 40 cm s^{-1}), b) 60 minutes (at contour intervals of 40 cm cm s^{-1}), and c) 120 minutes (at contour intervals of 10 cm s^{-1}) into the simulation.

Fig. 18 Profiles of horizontally-averaged a) total water mixing ratio (r_t), b) pristine ice + snow mixing ratios (r_{ice}), c) ice-liquid-water potential temperature (θ_{il}), and d) potential temperature (θ) at 60 minutes into the simulation for Case 2 (LES).

Fig. 19 Profiles of horizontally-averaged turbulent kinetic energy (TKE) at 30 (solid), 60 (dotted), and 120 minutes (dashed) into the simulation for Case 2 (LES).

Fig. 20 a) Profiles of radiative heating rate (solid line: total; dashed line: IR; dotted line: solar) and b) solar (τ_{solar}) and infrared ($\tau_{infrared}$) optical depths (dashed line: IR; dotted line: solar) at 60 minutes into the simulation for Case 2 (LES).

Fig. 21 a) Profiles of radiative heating rate (solid line: total; dashed line: IR; dotted line: solar) and b) solar (τ_{solar}) and infrared ($\tau_{infrared}$) optical depths (dashed line: IR; dotted line: solar) at 120 minutes into the simulation time for Case 2 (LES).

Fig. 22 Profiles of total radiative (solid) and latent (dotted) heating rates at a) 30 minutes, b) 60 minutes, and c) 120 minutes into the simulation for Case 2 (LES).

Fig. 23 PDF of w at a) 5400 m, b) 7700 m, and c) 9100 m above ground level (AGL) at 30 minutes into the simulation for Case 2 (LES).

Fig. 24 PDF of w at a) 5400 m, b) 7700 m, and c) 9100 m above ground level (AGL) at 60 minutes into the simulation for Case 2 (LES).

Fig. 25 The height-time cross section of w (in cm s^{-1}) at x,y = -0.08 km of the model domain for a) Case 1 (LES) at contour intervals of 0.4 cm s^{-1} and b) Case 2 (LES) at contour intervals of 10 cm s^{-1}. Solid (dashed) contours represent positive (negative) values, and zero-contours are suppressed.

Fig. 26 The height-time cross section of the horizontal wind (in m/s) at x,y= -0.08 km of the model domain for a) Case 1 (LES) and b) Case 2 (LES). The scales of the u and v component of the wind are given at the top of the figure.

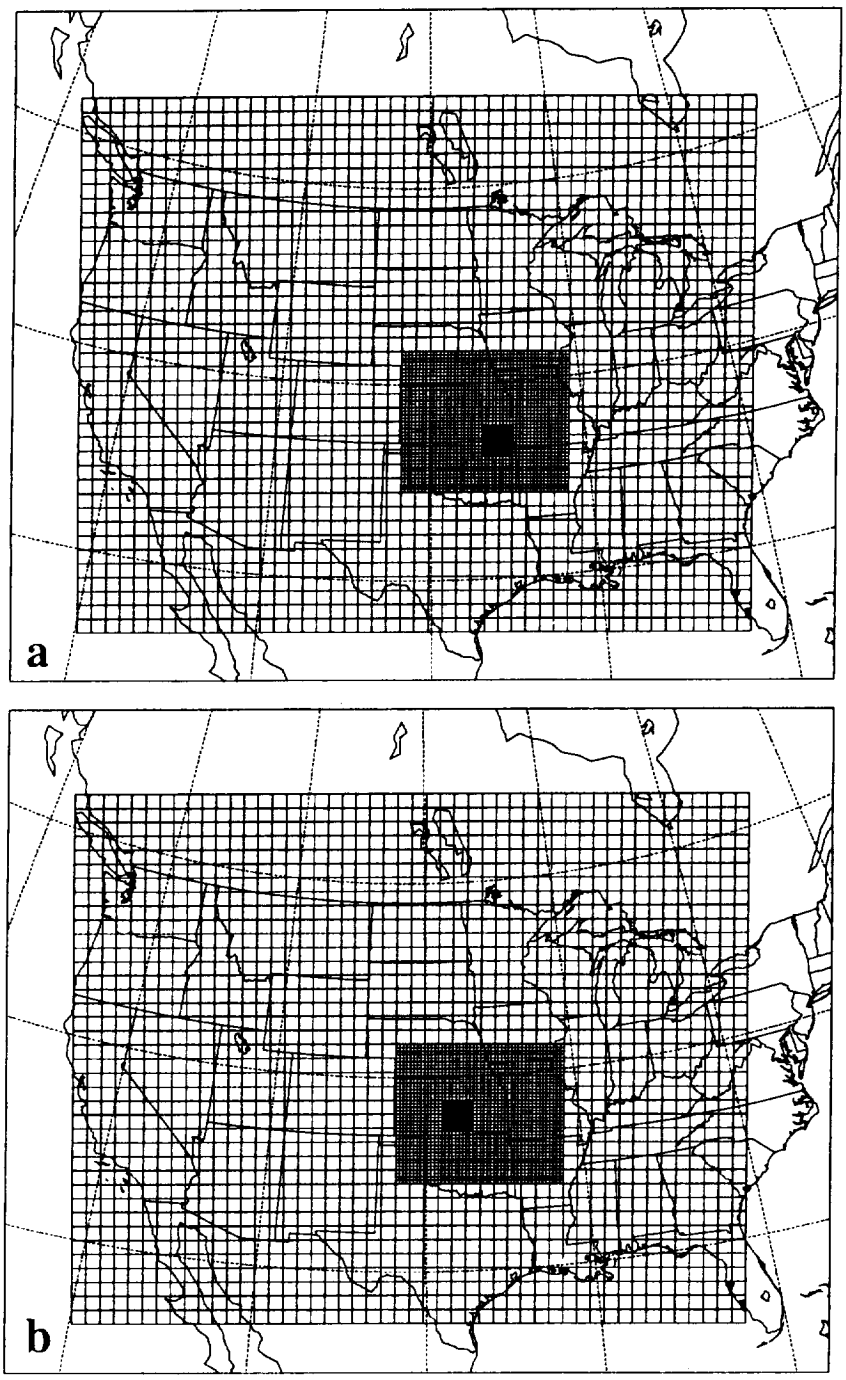

Figure 1 The mesoscale grid configuration for a) Case A and b) Case B.

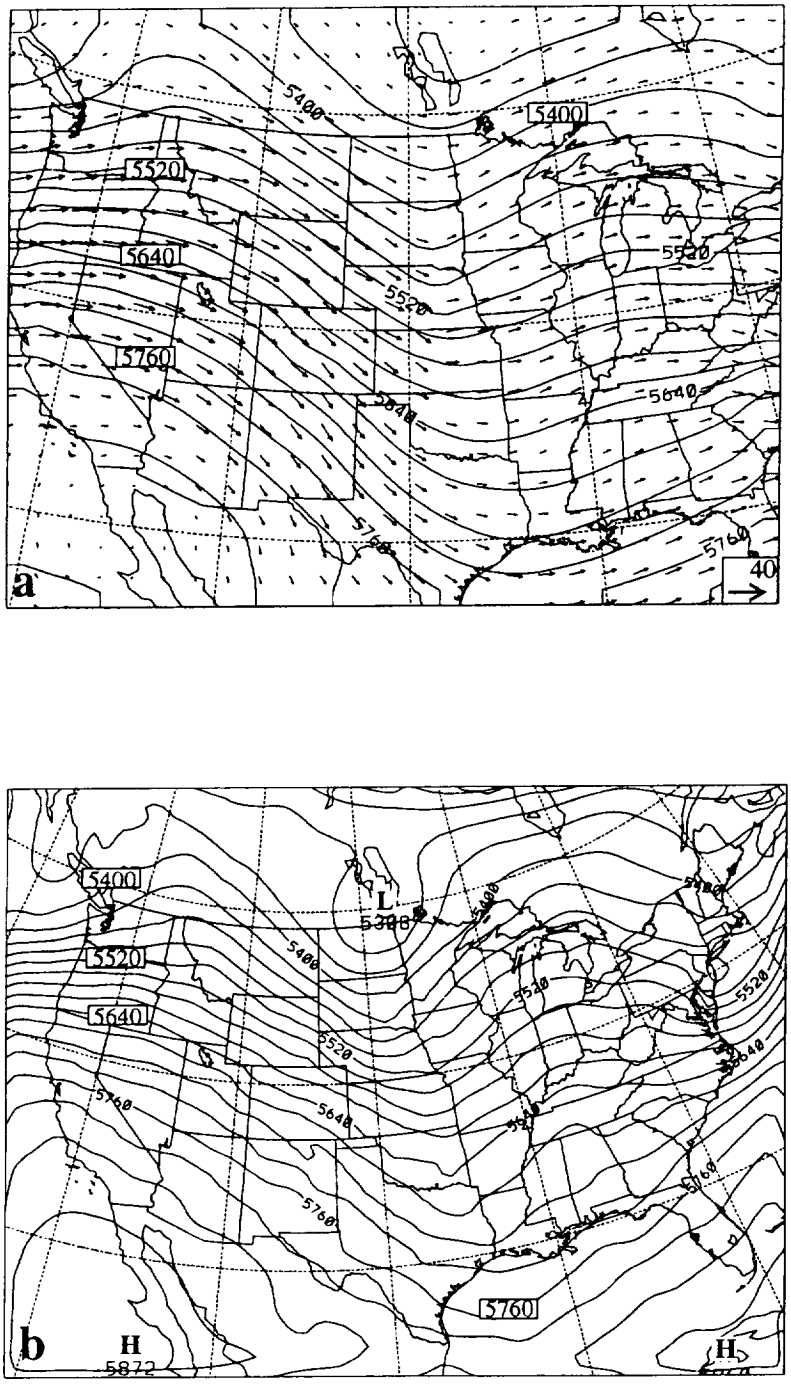

Figure 2 a) 24-h predicted 500-hPa geopotential height (at contour intervals of 30 m) superposed with 500-hPa wind vectors (m s^{-1}) from Grid 1 of the mesoscale simulation (0000 UTC 27 November 1991). Inset indicates the scale of the horizontal wind vectors (m s^{-1}); b) 500-hPa geoptential height (at contour intervals of 30 m) from MAPS analysis at 0000 UTC 27 November 1991.

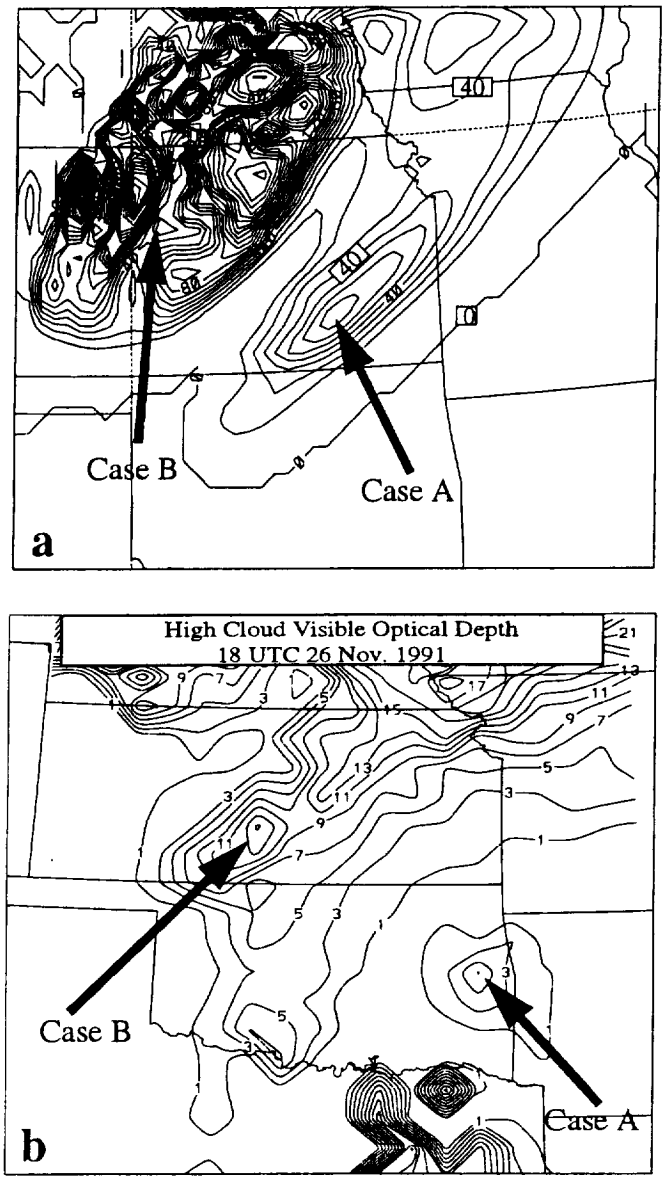

Figure 3 a) 18-h predicted 400-hPa snow mixing ratio from Grid 2 of the mesoscale simulation (1800 UTC 26 November 1991), at contour intervals of 10 X 10^{-3} g kg^{-1}; b) high cloud visible optical depths derived from GOES data at 1800 UTC 26 November 1991 (panel b taken from Mace et al. 1995).

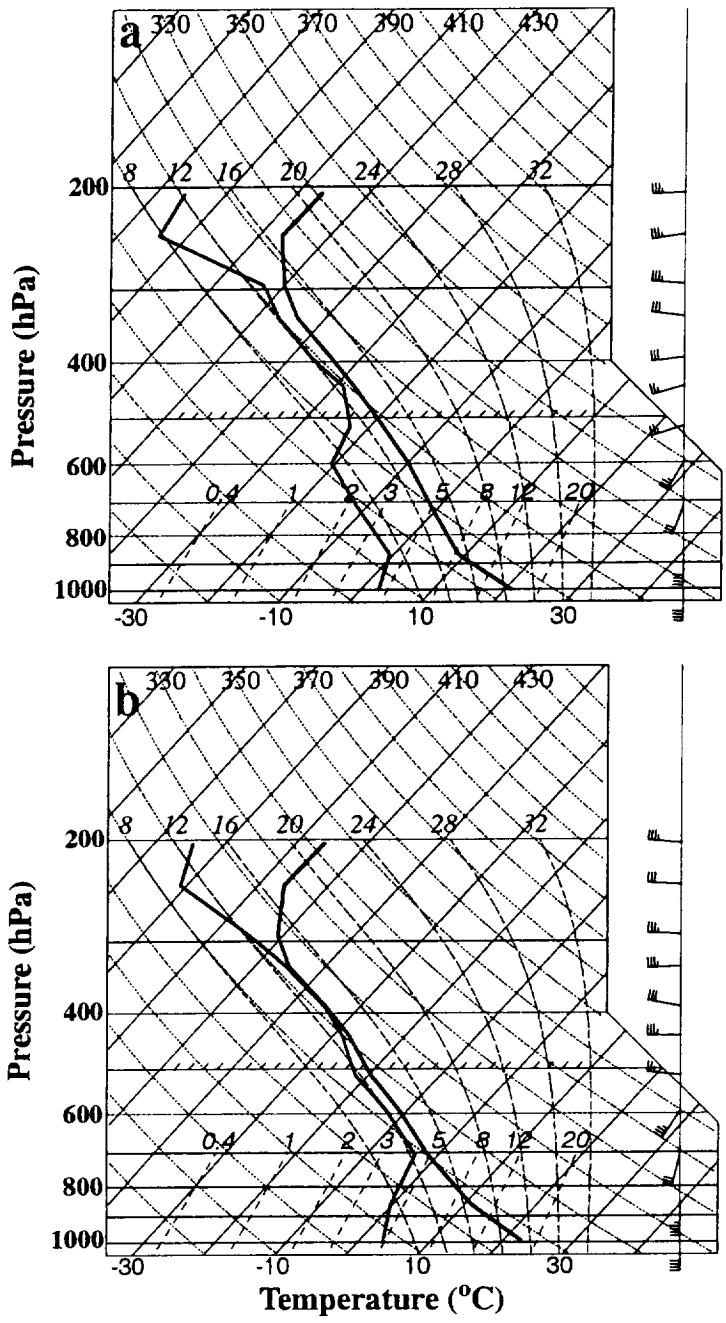

Figure 4 Skew T-log p diagram for temperature (°C), dew point temperature (°C), and wind (m s^{-1}) at a) 1700 UTC 26 November 1991 and b) 1930 UTC 26 November 1991 at 37.79° N and 97.33°W from the mesoscale simulation of Wu (1999). The soundings in a) and b) are the initial conditions of Case 1 and Case 2 (LES), respectively.

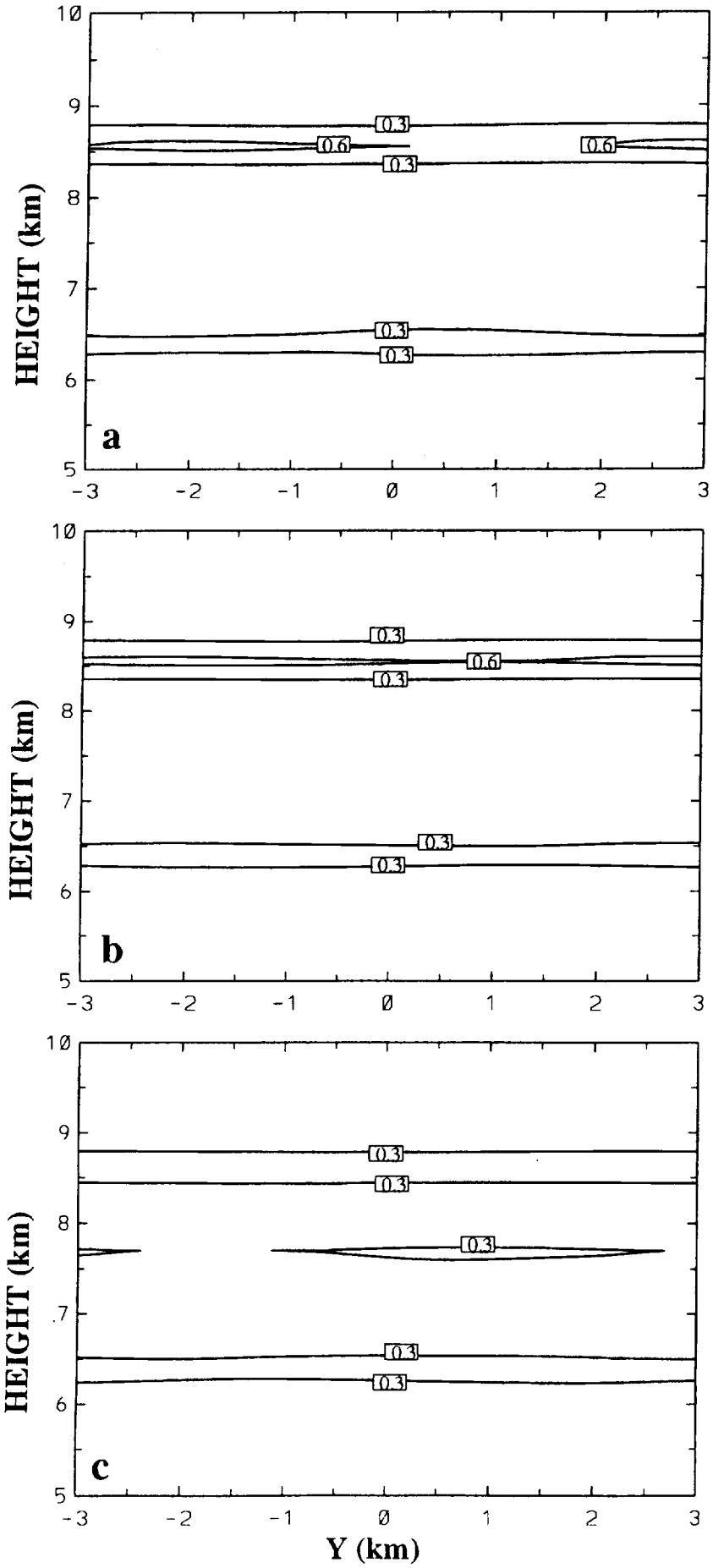

Figure 5 Vertical y-z cross section (at x = -0.08 km) of pristine ice number concentration (at contour intervals of 0.3 l^{-1}) for Case 1 (LES) at a) 30 minutes, b) 60 minutes, and c) 120 minutes into the simulation.

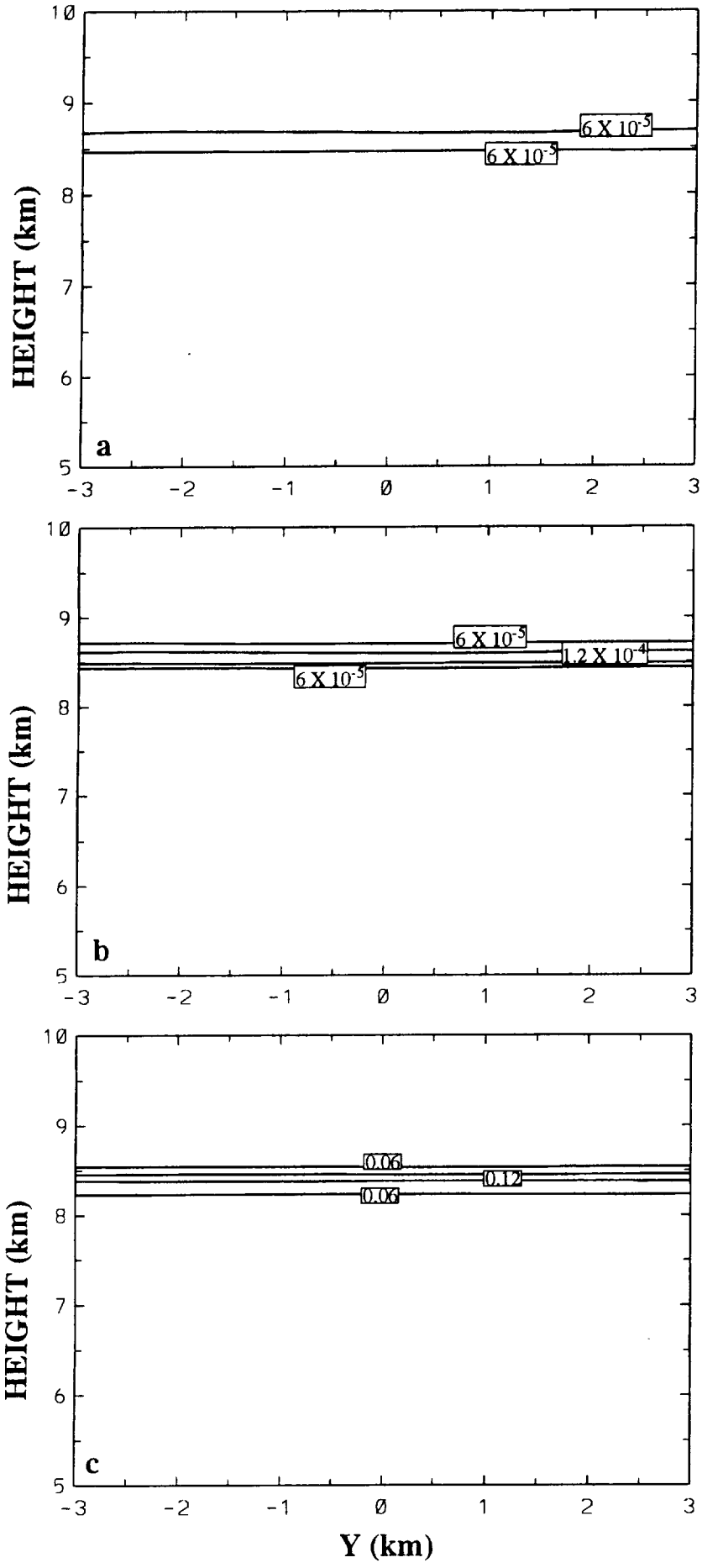

Figure 6 Vertical y-z cross section (at x = -0.08 km) of snow particle number concentration for Case 1 (LES) at a) 30 minutes (at contour intervals of 6 X 10^{-5} l^{-1}), b) 60 minutes (at contour intervals of 6 X 10^{-5} l^{-1}), and c) 120 minutes (at contour intervals of 0.06 l^{-1}) into the simulation.

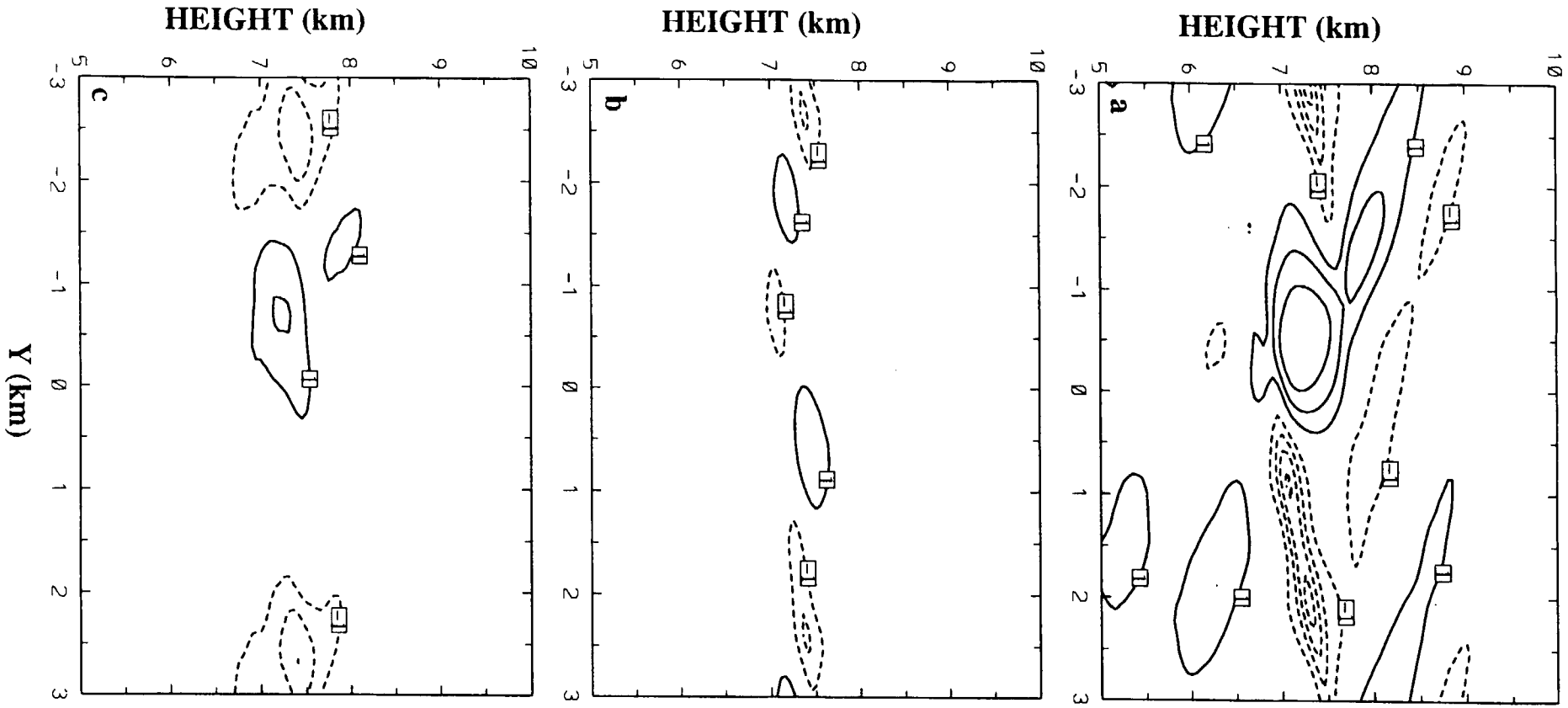

Figure 7 Vertical y-z cross section (at x = -0.08 km) of vertical velocity (w; at contour intervals of 1 cm s^{-1}) for Case 1 (LES) at a) 30 minutes, b) 60 minutes, and c) 120 minutes into the simulation.

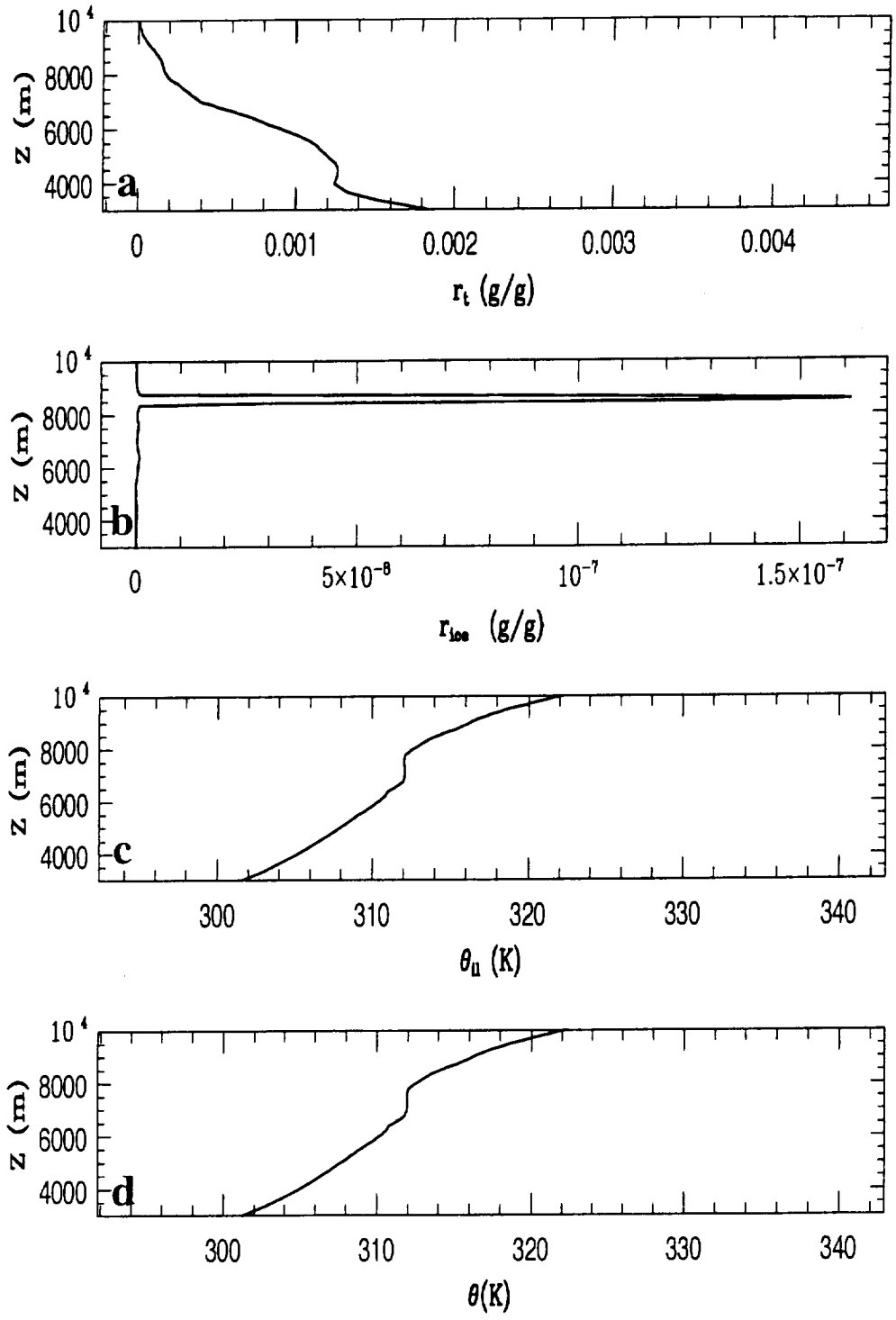

Figure 8 Profiles of horizontally-averaged a) total water mixing ratio (r_t), b) pristine ice + snow mixing ratios (r_{ice}), c) ice-liquid-water potential temperature (θ_{il}), and d) potential temperature (θ) at 60 minutes into the simulation for Case 1 (LES).

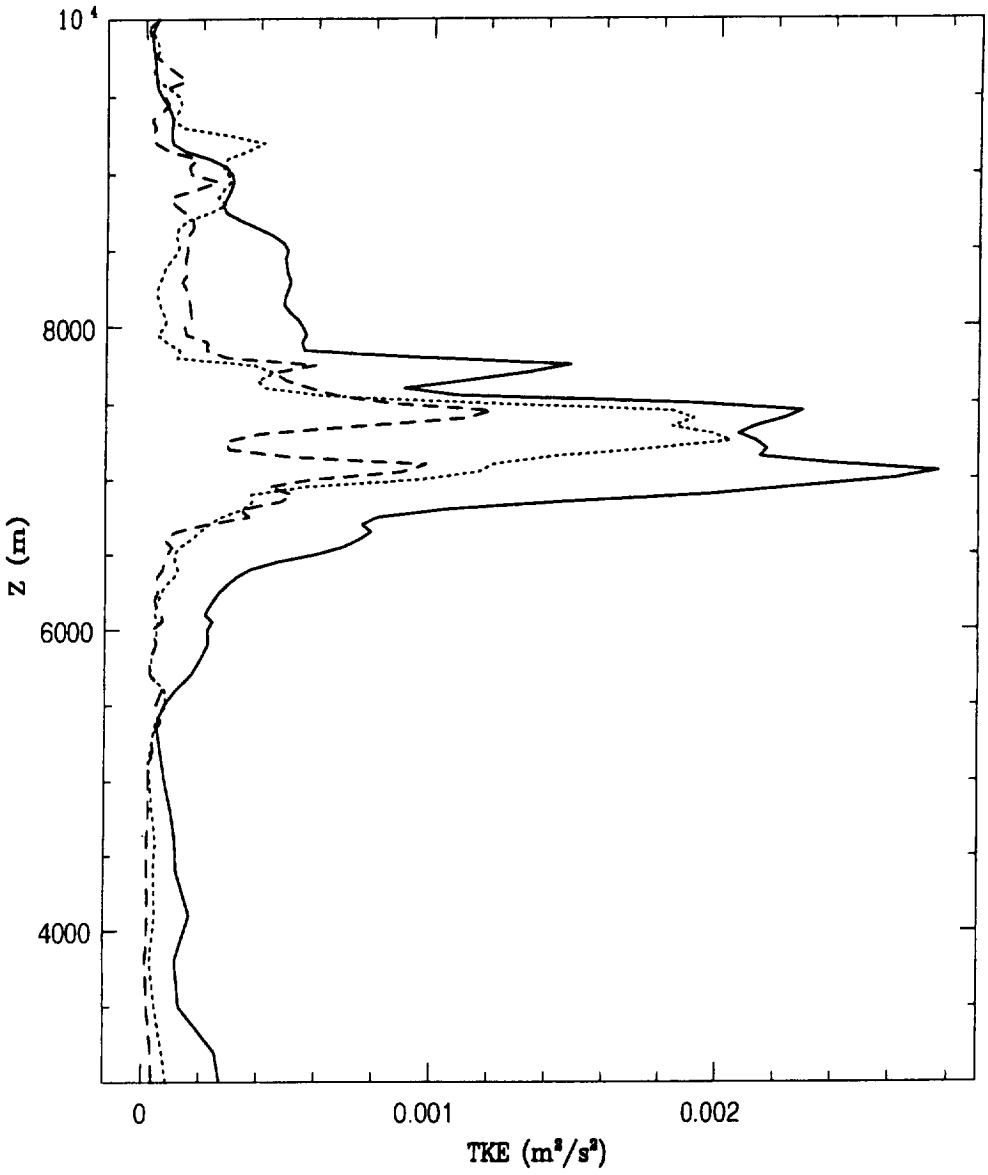

Figure 9 Profiles of horizontally-averaged turbulent kinetic energy at 30 (solid), 60 (dotted), and 120 minutes (dahsed) into the simulation for Case1 (LES).

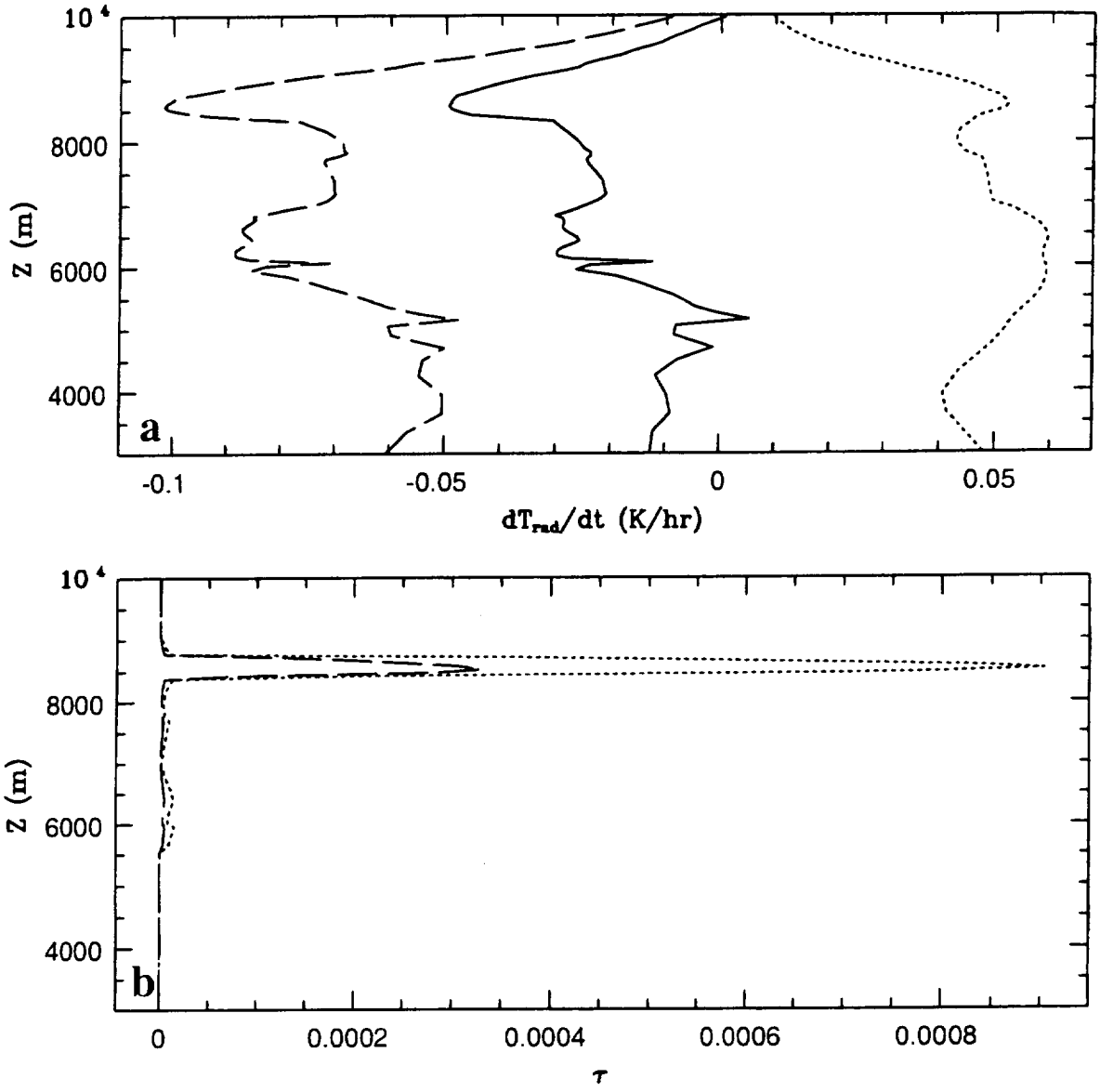

Figure 10 a) Profiles of radiative heating rate (solid line: total; dashed line: IR; dotted line: solar) and b) solar (τ_{solar}) and infrared ($\tau_{infrared}$) optical depths (dashed line: IR; dotted line: solar) at 60 minutes into the simulation for Case 1 (LES).

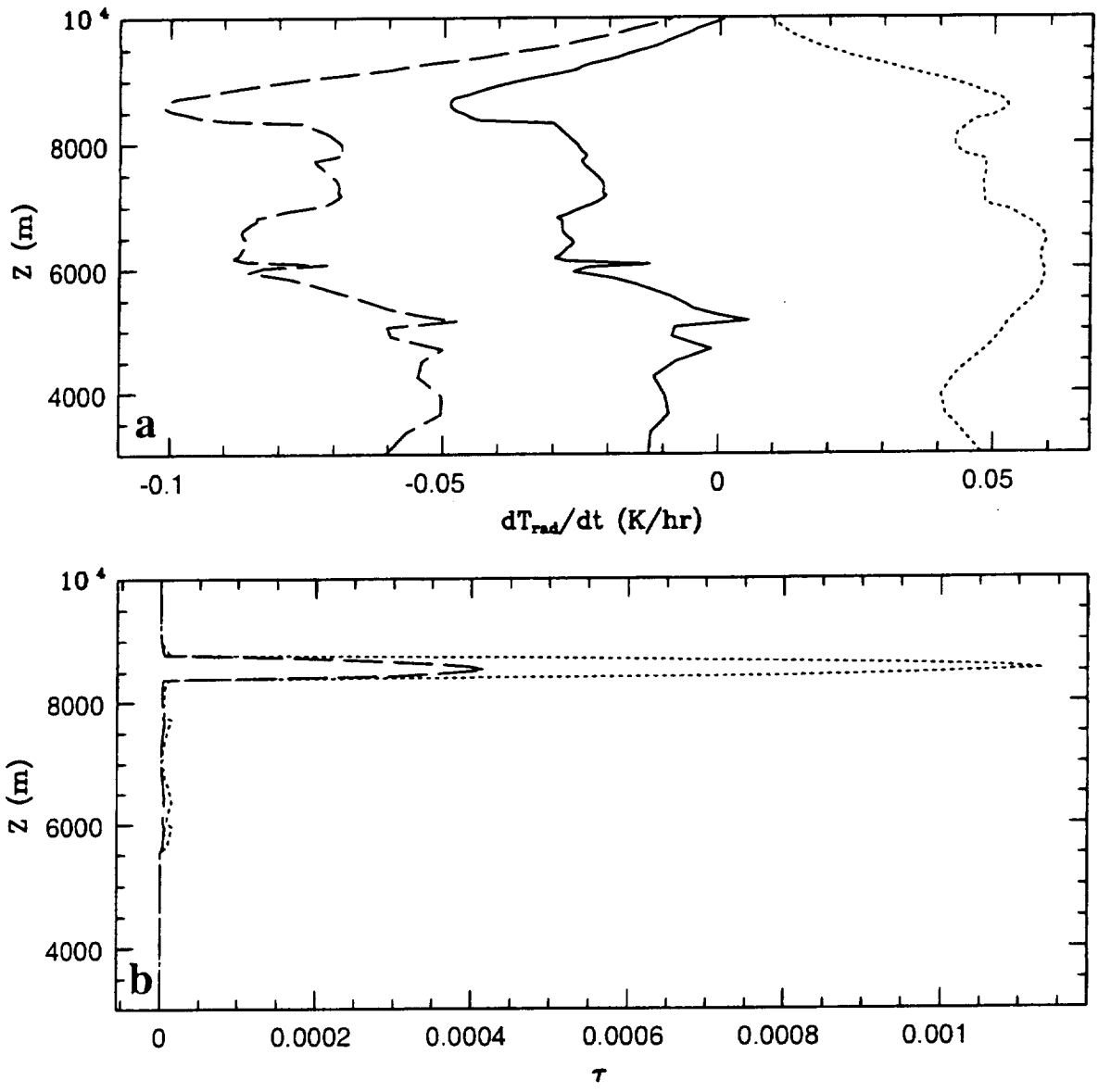

Figure 11 a) Profiles of radiative heating rate (solid line: total; dashed line: IR; dotted line: solar) and b) solar (τ_{solar}) and infrared ($\tau_{infrared}$) optical depths (dashed line: IR; dotted line: solar) at 120 minutes into the simulation for Csae 1 (LES).

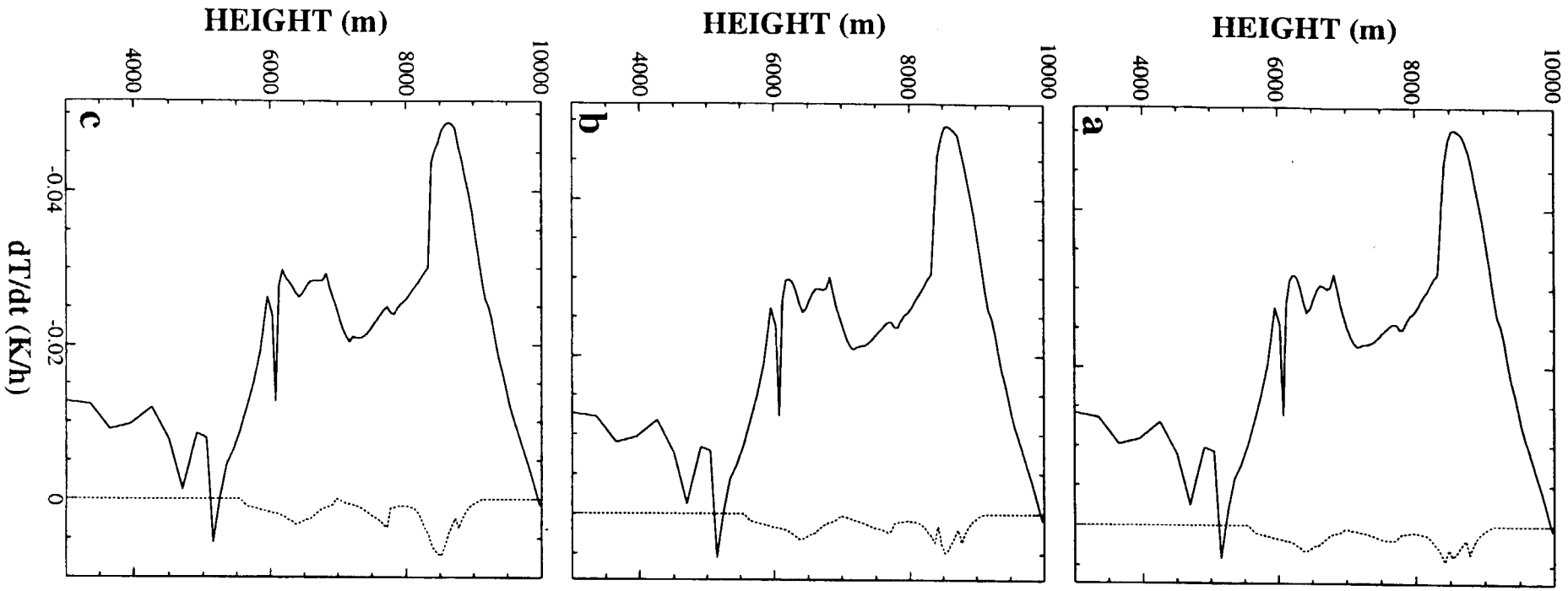

Figure 12 Profiles of total radiative (solid) and latent (dotted) heating rates at a) 30 minutes, b) 60 minutes, and c) 120 minutes into the simulation for Case 1 (LES).

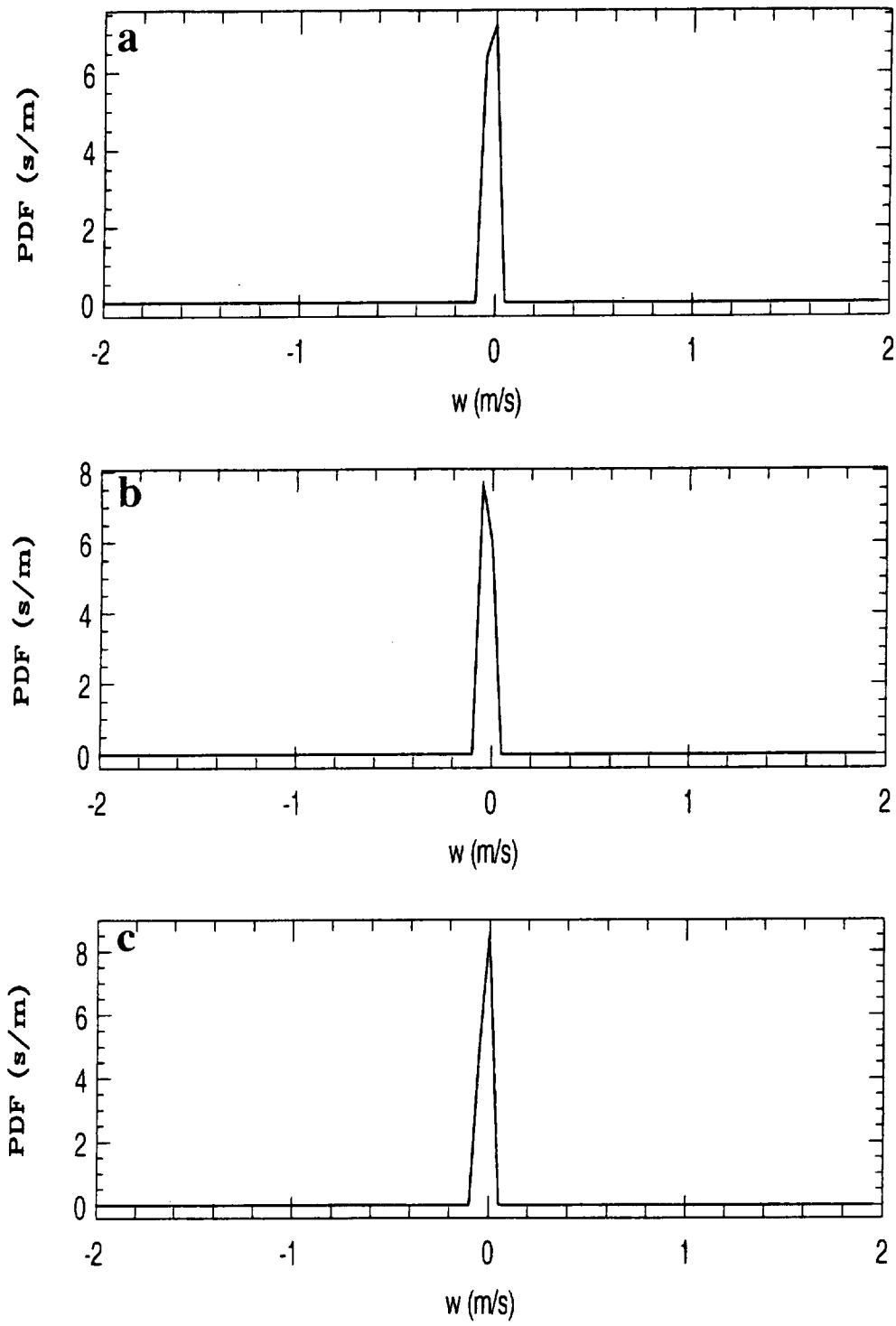

Figure 13 PDF of w at a) 5400 m, b) 7700 m, and c) 9100 m above ground level (AGL) at 30 minutes into the simulation for Case 1 (LES).

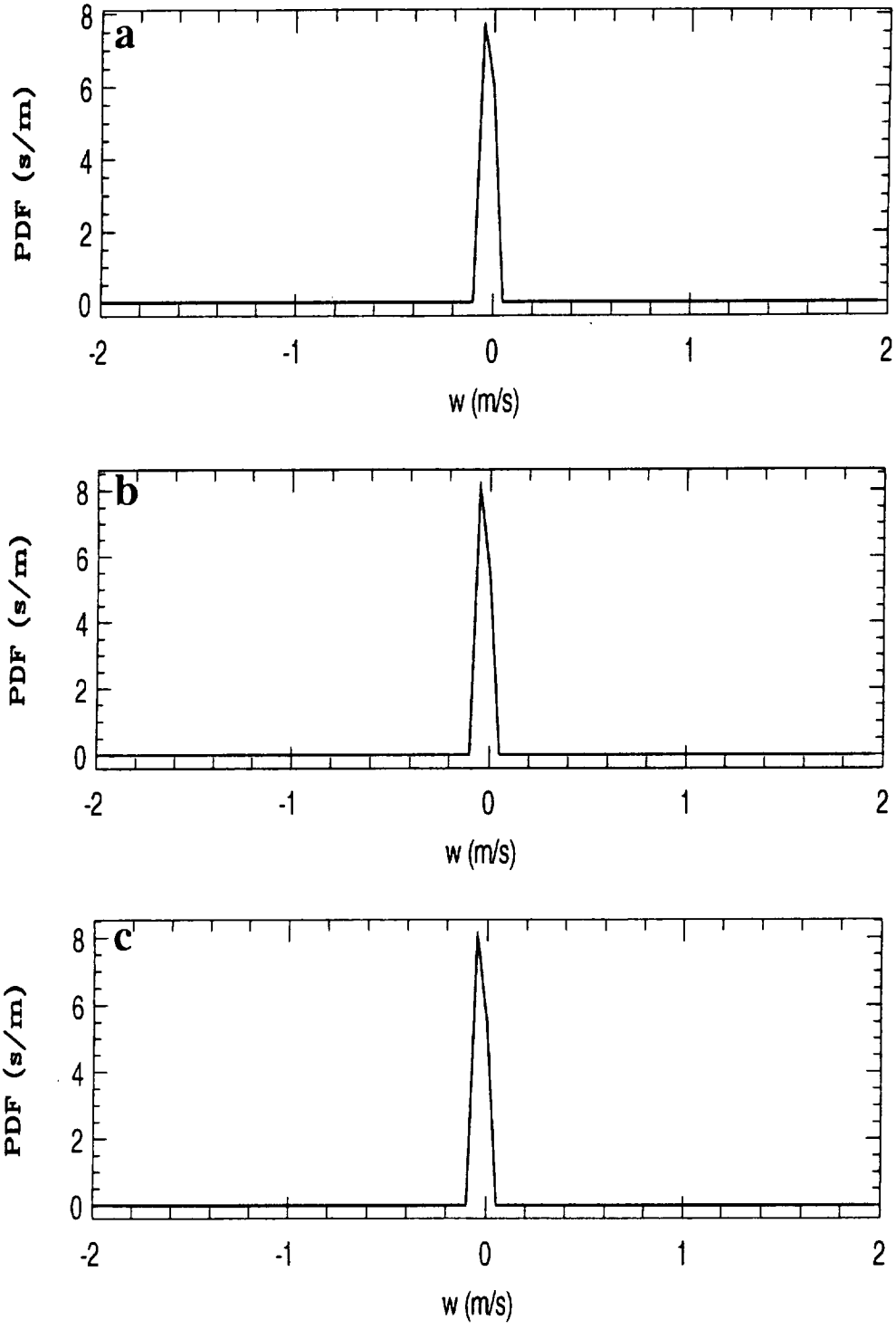

Figure 14 PDF of w at a) 5400 m, b) 7700 m, and c) 9100 m above ground level (AGL) at 60 minutes into the simulation for Case 1 (LES).

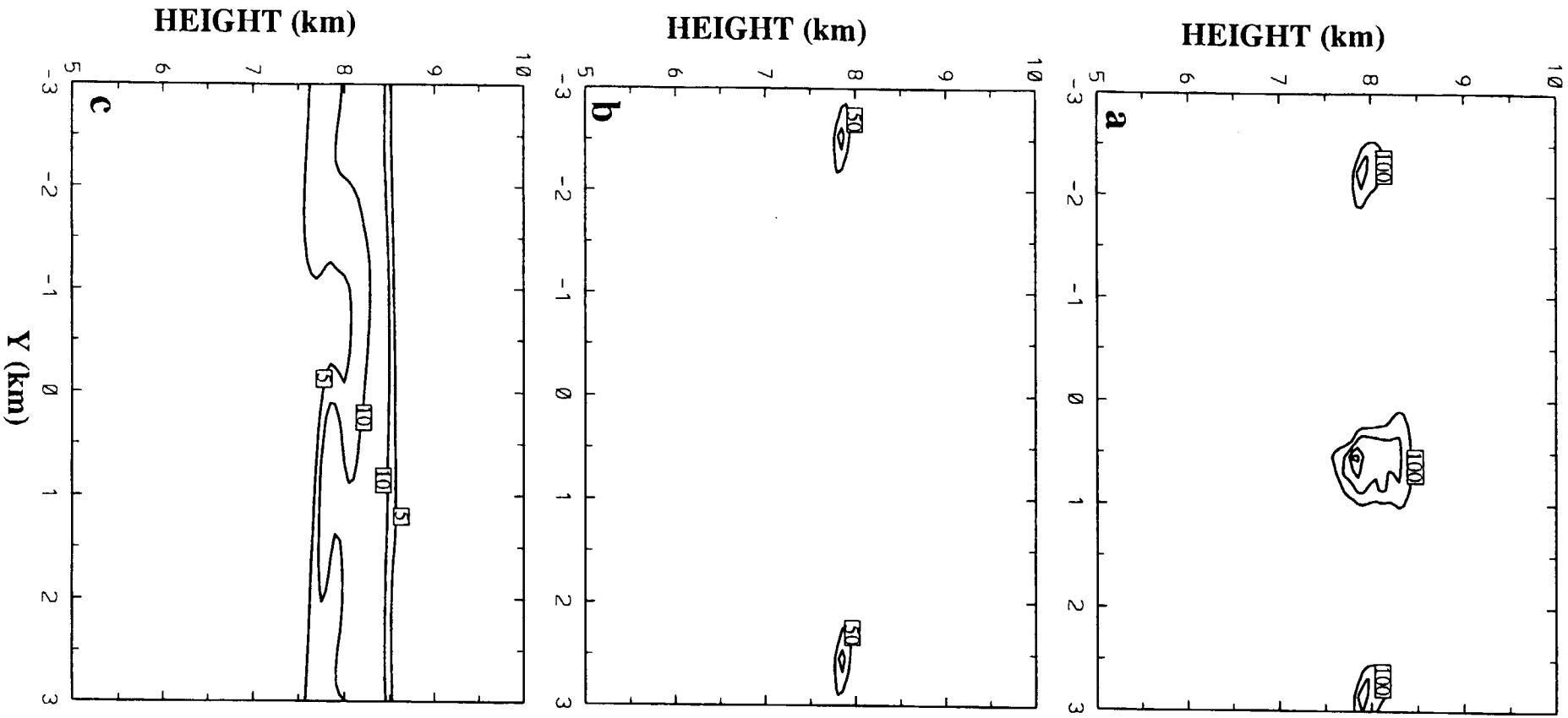

Figure 15 Vertical y-z cross section (at x = -0.08 km) of pristine ice number concentration for Case 2 (LES) at a) 30 minutes (at contour intervals of 100 l^{-1}), b) 60 minutes (at contour intervals of 50 l^{-1}), and c) 120 minutes (at contour intervals of 5 l^{-1}) into the simulation.

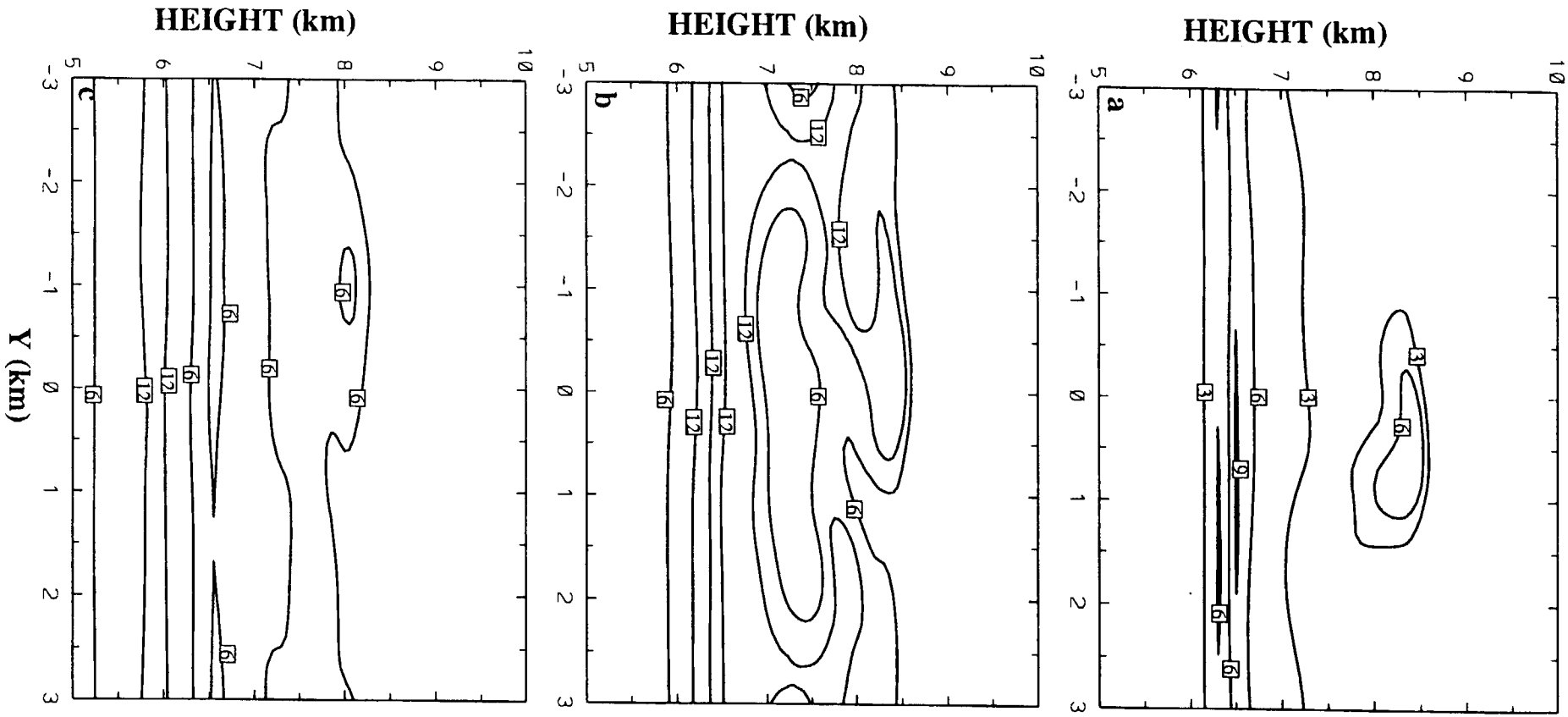

Figure 16 Vertical y-z cross section (at x = -0.08 km) of snow particle number concentration for Case 2 (LES) at a) 30 minutes (at contour intervals of 3 l^{-1}), b) 60 minutes (at contour intervals of 6 l^{-1}), and c) 120 minutes (at contour intervals of 6 l^{-1}) into the simulation.

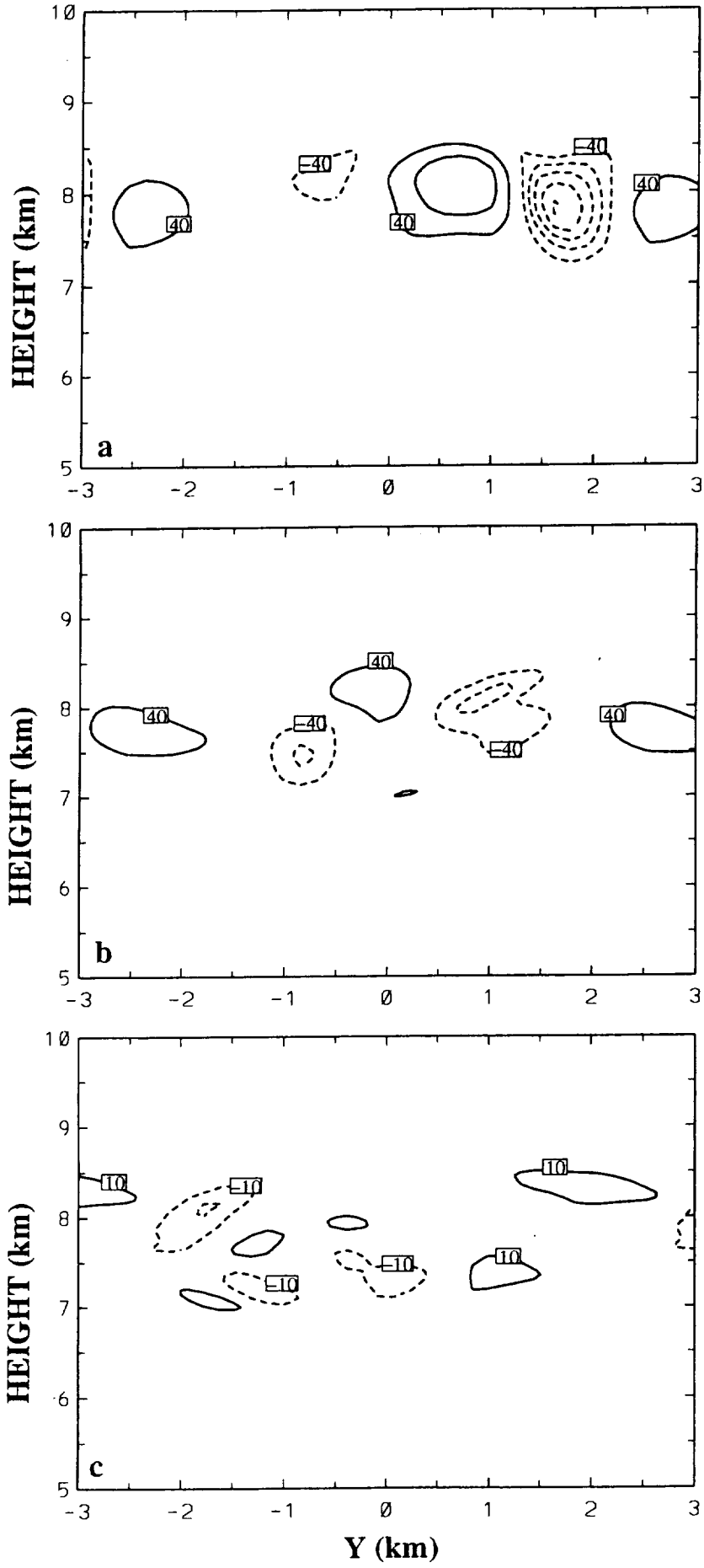

Figure 17 Vertical y-z cross section (at x = -0.08 km) of vertical velocity (w) for Case 2 (LES) at a) 30 minutes (at contour intervals of 40 cm s^{-1}), b) 60 minutes (at contour intervals of 40 cm s^{-1}), and c) 120 minutes (at contour intervals of 10 cm s^{-1}) into the simulation.

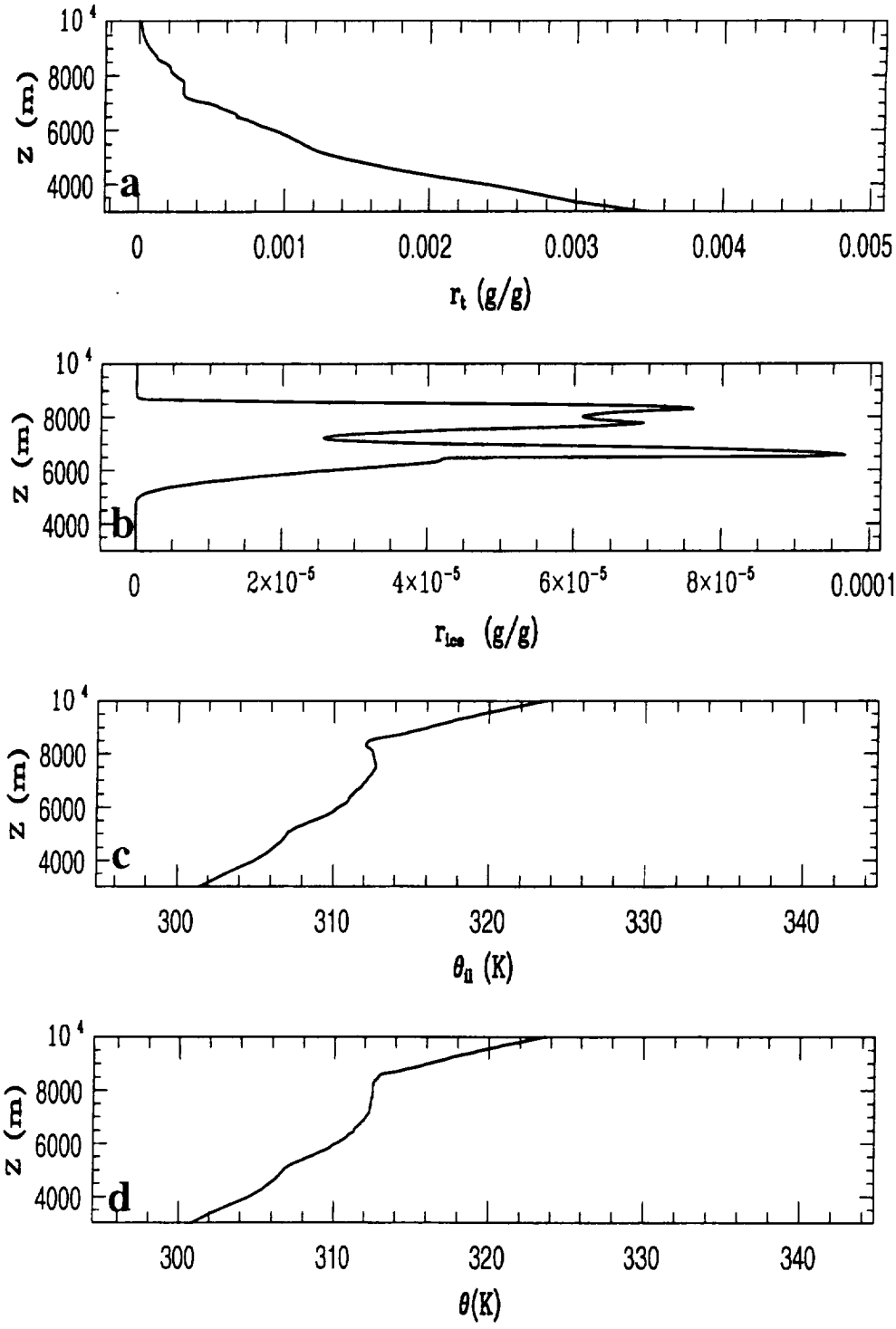

Figure 18 Profiles of horizontally-averaged a) total water mixing ratio (r_t), b) pristine ice + snow mixing ratios (r_{ice}), c) ice-liquid-water potential temperature (θ_{il}), and d) potential temperature (θ) at 60 minutes into the simulation for Case 2 (LES).

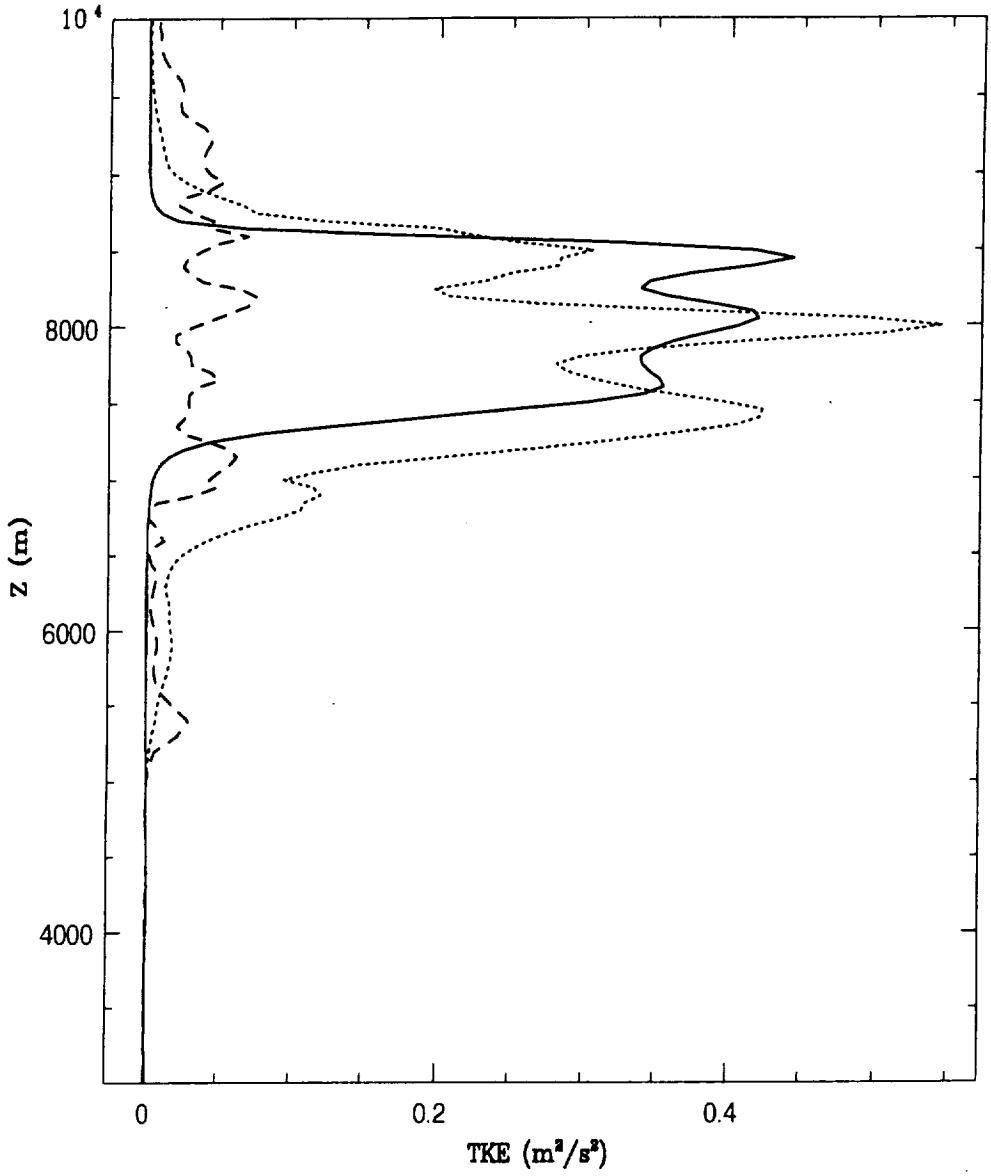

Figure 19 Profiles of horizontally-averaged turbulent kinetic energy at 30 (solid), 60 (dotted), and 120 minutes (dahsed) into the simulation for Case 2 (LES).

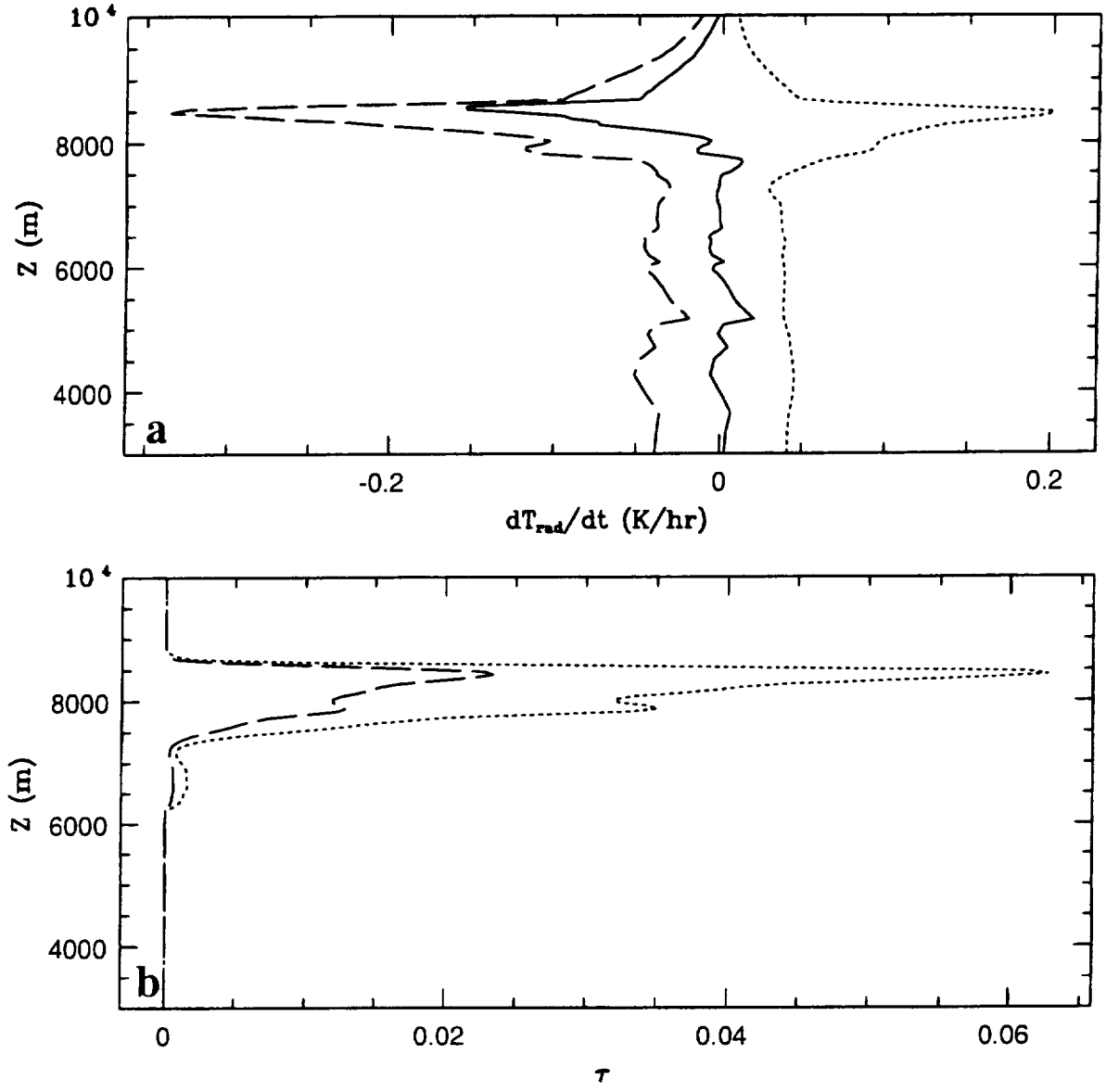

Figure 20 a) Profiles of radiative heating rate (solid line: total; dashed line: IR; dotted line: solar) and b) solar (τ_{solar}) and infrared ($\tau_{infrared}$) optical depths (dashed line: IR; dotted line: solar) at 60 minutes into the simulation for Csae 2 (LES).

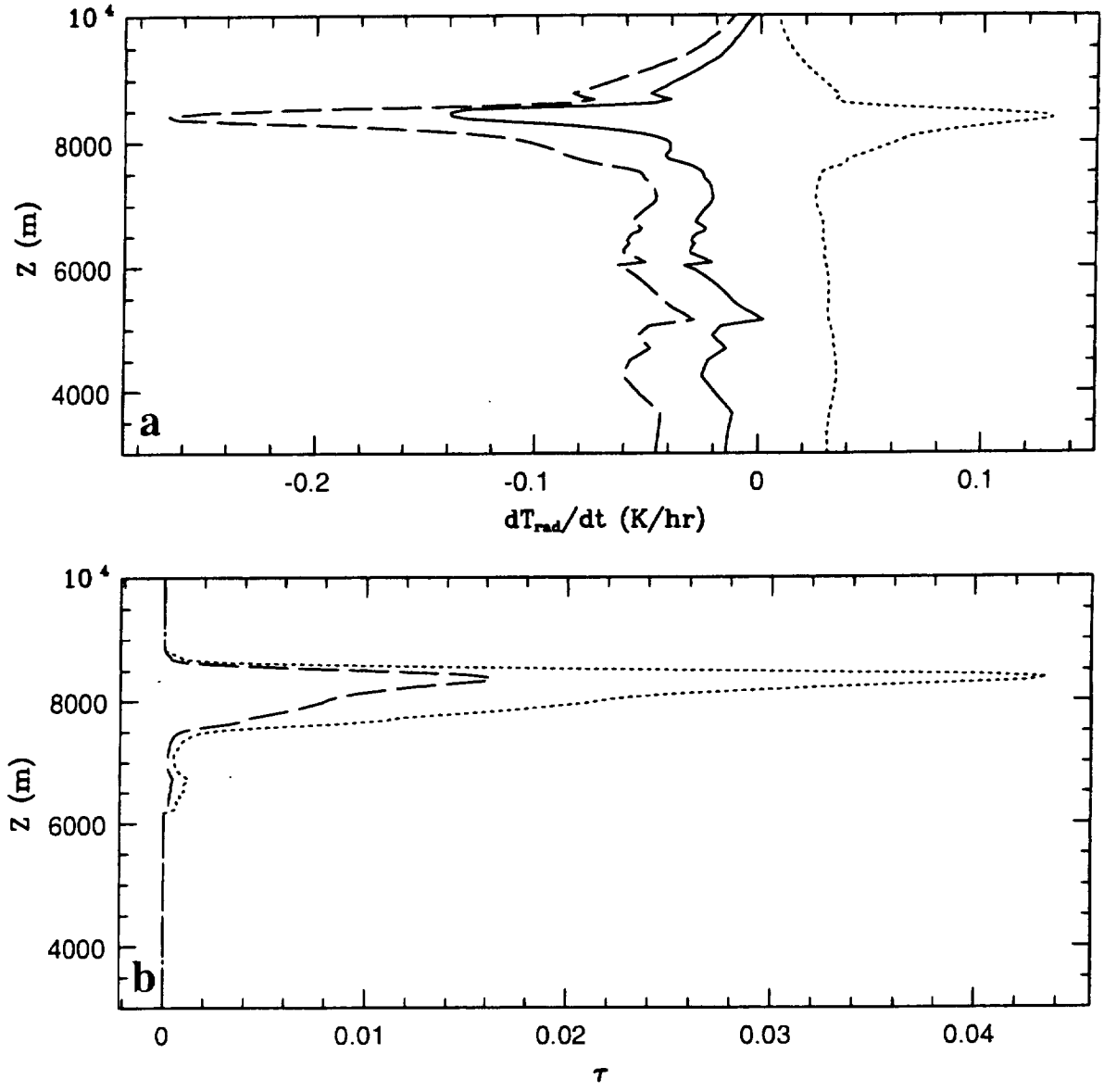

Figure 21 a) Profiles of radiative heating rate (solid line: total; dashed line: IR; dotted line: solar) and b) solar (τ_{solar}) and infrared ($\tau_{infrared}$) optical depths (dashed line: IR; dotted line: solar) at 120 minutes into the simulation for Csae 2 (LES).

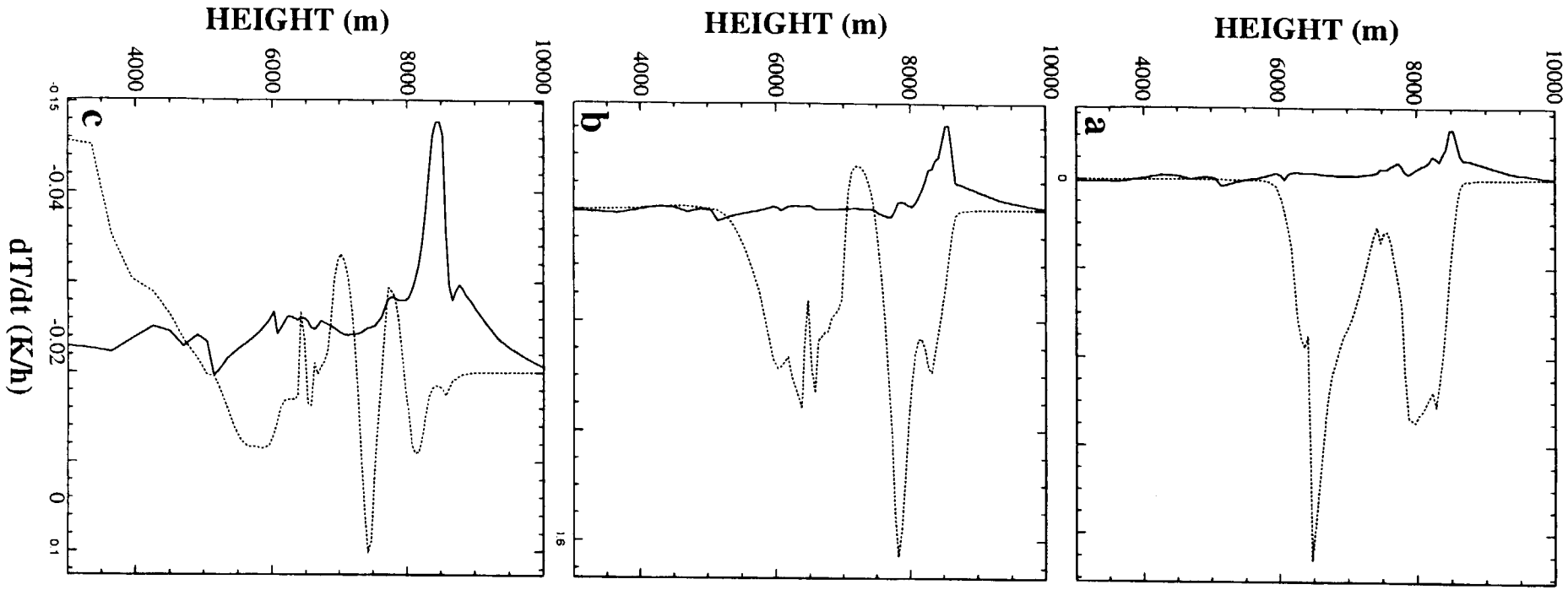

Figure 22 Profiles of total radiative (solid) and latent (dotted) heating rates at a) 30 minutes, b) 60 minutes, and c) 120 minutes into the simulation for Case 2 (LES).

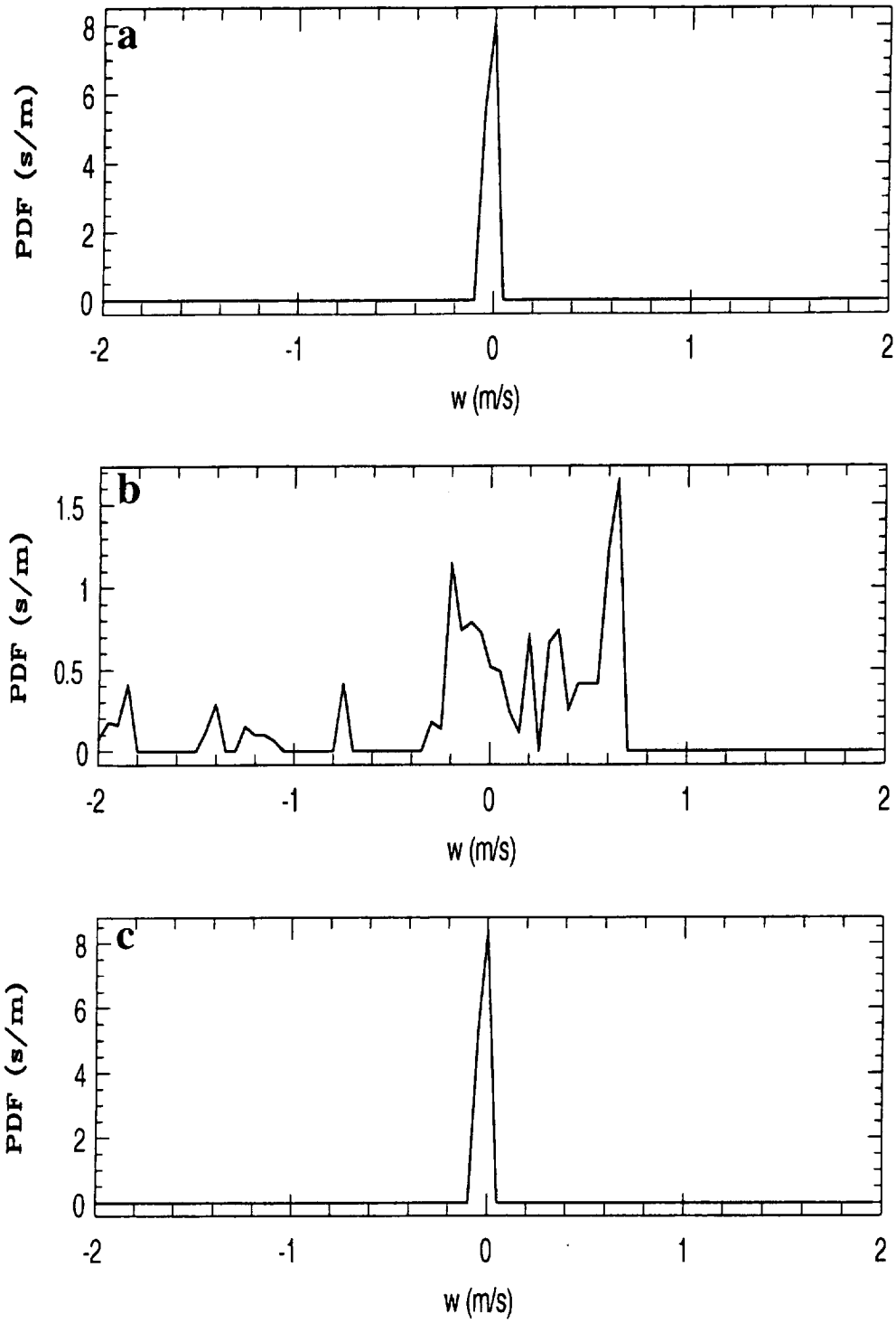

Figure 23 PDF of w at a) 5400 m, b) 7700 m, and c) 9100 m above ground level (AGL) at 30 minutes into the simulation for Case 2 (LES).

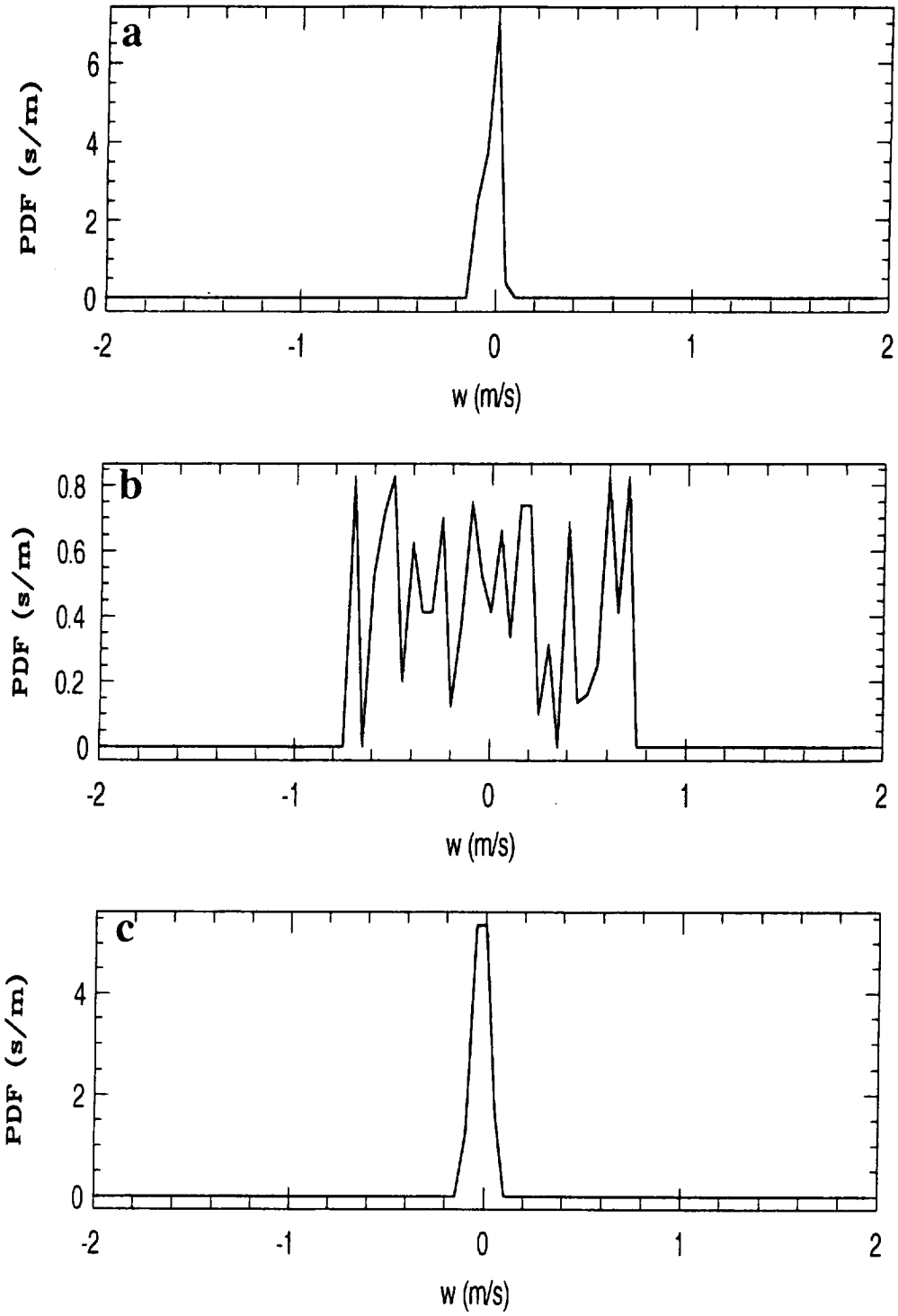

Figure 24 PDF of w at a) 5400 m, b) 7700 m, and c) 9100 m above ground level (AGL) at 60 minutes into the simulation for Case 2 (LES).

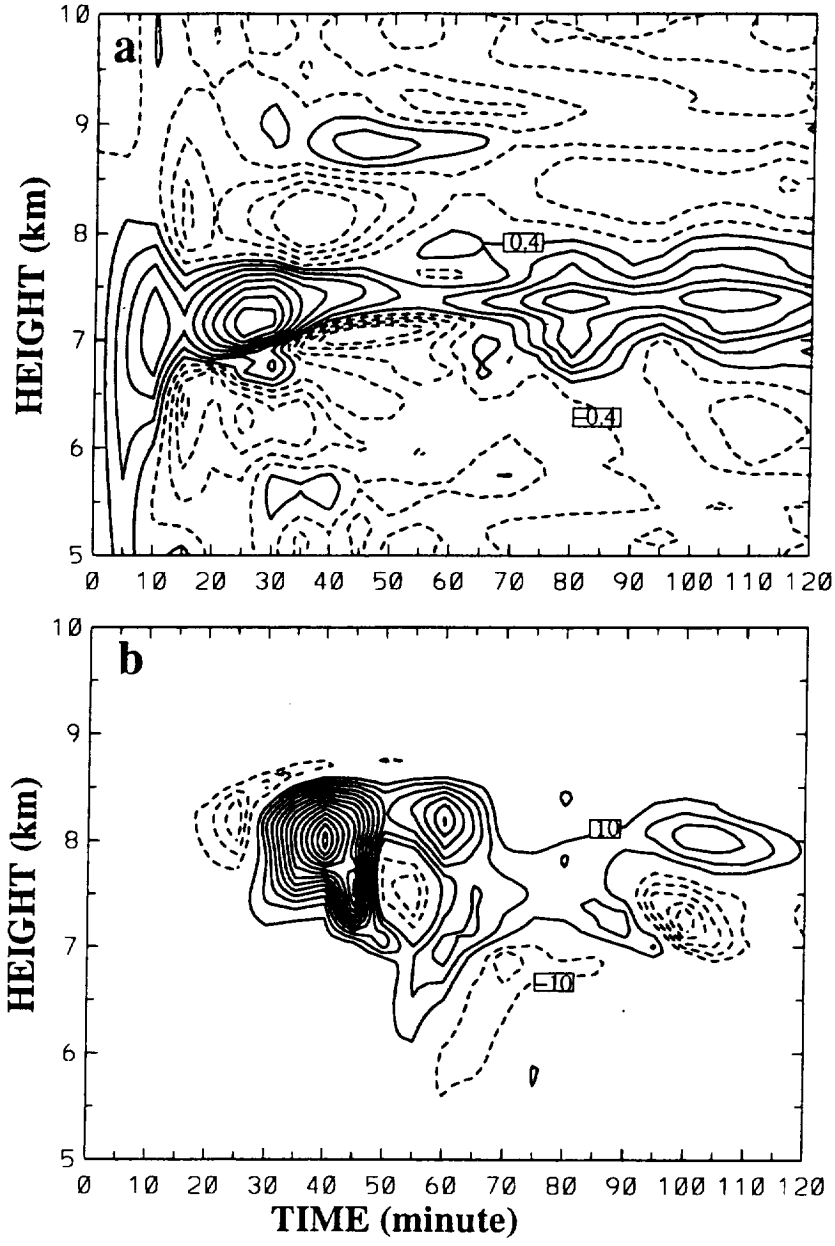

Figure 25 The height-time cross section of w (in cm s^{-1}) at x,y=-0.08 km of the model domain for a) Case 1 (LES) at contour intervals of 0.4 cm s^{-1} and b) Case 2 (LES) at contour intervals of 10 cm s^{-1}. Solid (dashed) contours represent positive (negative) values, and zero-contours are suppressed.

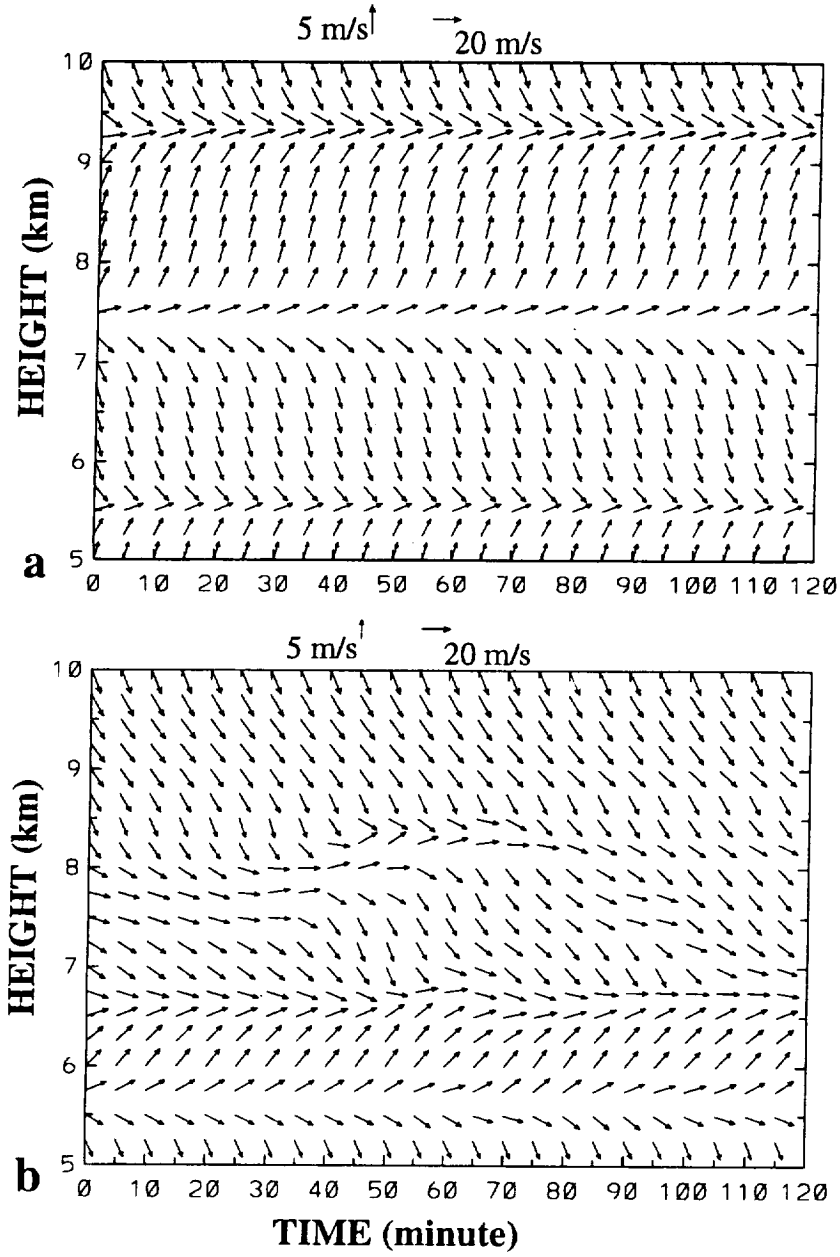

Figure 26 The height-time cross section of the horizontal wind (in m s^{-1}) at x,y=-0.08 km of the model domain for a) Case 1 (LES) and b) Case 2 (LES). The scales of the u and v components of the wind are given at the top of the figure.